SAPIENZA
UNIVERSITÀ DI ROMA

DOTTORATO DI RICERCA IN ENERGIA E AMBIENTE
*PhD Program in ENERGY and ENVIRONMENT*

*XXXVIII Cycle*

# System Thermal-Hydraulic Analyses Supporting the Development of Lead-cooled Fast Reactors

*PhD Thesis*

Scuola di Dottorato in Scienze e Tecnologie per l'Innovazione Industriale
Facoltà di Ingegneria Civile e Industriale
Dipartimento di Ingegneria Astronautica, Elettrica ed Energetica

**Giorgio Khalil Youssef**

Advisor
Prof. Fabio Giannetti

Co-Advisor/Tutor
Eng. Marco Caramello
Dr. Cristiano Ciurluini

A.A. 2024-2025

*(Page intentionally left blank)*

# SOMMARIO

L'urgente necessità di decarbonizzare il sistema energetico globale, in risposta alla crisi climatica, ha rilanciato l'interesse per l'energia nucleare come fonte affidabile, a basse emissioni di carbonio e programmabile. L'energia nucleare, già oggi uno dei principali contributori alla produzione di elettricità senza emissioni, ha il potenziale per svolgere un ruolo centrale nel raggiungimento degli obiettivi di decarbonizzazione profonda.

In questo contesto, il Generation IV International Forum (GIF) ha promosso lo sviluppo di concetti avanzati di reattori in grado di superare le limitazioni delle tecnologie attualmente in uso. Tra questi, i reattori veloci raffreddati a piombo (Lead-cooled Fast Reactors, LFR) si sono affermati come una delle opzioni più promettenti. Gli LFR operano con uno spettro neutronico veloce, utilizzando piombo liquido o eutettico piombo-bismuto (LBE) come refrigerante primario. L'impiego di combustibili avanzati, come il MOX (Mixed Oxide Fuel), costituito tipicamente da ossido di plutonio miscelato con ossido di uranio impoverito o naturale, consente il riciclo del plutonio proveniente dal combustibile esausto, riducendo l'accumulo di materiali fissili stoccati e contribuendo così agli obiettivi di non proliferazione e sostenibilità. Inoltre, operare in spettro veloce permette agli LFR di aumentare l'utilizzo del combustibile, abilitando l'impiego di isotopi fertili come l'uranio-238 e il torio-232 per la generazione di isotopi fissili (rispettivamente plutonio-239 e uranio-233). Questa capacità consente di estrarre una maggiore quantità di energia per unità di uranio naturale e di ridurre la necessità di estrazione di nuovo combustibile. Inoltre, lo spettro veloce è particolarmente efficace nella trasmutazione degli attinidi minori a lunga vita (come nettunio, americio e curio) in isotopi a vita più breve o stabili, mediante fissione. Questo processo di trasmutazione riduce significativamente la radiotossicità e il carico termico a lungo termine dei rifiuti nucleari, affrontando uno dei principali ostacoli all'accettazione pubblica dell'energia nucleare e alla progettazione dei depositi geologici. La scelta dei metalli pesanti liquidi (Heavy Liquid Metals, HLM) come refrigeranti conferisce ulteriori vantaggi di scambio termico e chimici rispetto ai refrigeranti tradizionali. Il loro altissimo punto di ebollizione (circa 1740 °C per il piombo e 1670 °C per l'LBE) permette il funzionamento del reattore a pressione atmosferica, eliminando la necessità di recipienti in pressione e riducendo i rischi legati a guasti indotti da sovrapressione. Le ottime proprietà termofisiche degli HLM—come l'elevata densità e conducibilità termica—favoriscono la rimozione passiva del calore e permettono design compatti del nocciolo con un trasferimento termico efficiente. L'impiego degli HLM consente di operare a temperature più elevate, migliorando l'efficienza termodinamica e contribuendo alle prestazioni complessive degli LFR. Inoltre, gli HLM sono chimicamente inerti rispetto ad aria e acqua, eliminando il rischio di reazioni violente come la generazione di idrogeno, un problema rilevante nei reattori veloci al sodio (Sodium-cooled Fast Reactors, SFR) e nei reattori ad acqua leggera (Light Water Reactors, LWR).

Nonostante i numerosi vantaggi, l'impiego degli HLM come refrigeranti primari introduce una serie di sfide tecniche che devono essere attentamente affrontate per garantire un funzionamento sicuro e affidabile del reattore. Una delle problematiche più critiche è la corrosione: alle alte temperature, piombo e LBE sono chimicamente aggressivi verso i materiali strutturali, in particolare gli acciai, causando la progressiva degradazione dei componenti a contatto con il refrigerante. La formazione di strati protettivi di ossido sulla superficie degli acciai può mitigare la corrosione, ma la loro stabilità è altamente sensibile alla concentrazione di ossigeno nel refrigerante. È quindi essenziale mantenere livelli di ossigeno precisi e stabili, richiedendo l'implementazione di sistemi robusti di controllo e monitoraggio dell'ossigeno.

Una problematica correlata è l'erosione e il trasporto di massa, soprattutto nelle aree soggette a elevate velocità di flusso o forti gradienti termici, dove gli strati protettivi possono essere rimossi meccanicamente, accelerando ulteriormente la degradazione dei materiali. Un'altra sfida rilevante riguarda l'attivazione del refrigerante e la produzione di polonio, in particolare nel caso dell'LBE, che contiene Bismuto-209, il quale può essere trasmutato in Polonio-210 sotto irraggiamento neutronico. Il Polonio-210 è un emettitore alfa altamente radiotossico con un'emivita relativamente breve (~138 giorni), che comporta seri rischi radiologici durante operazioni di manutenzione, esercizio e smantellamento. Questo aspetto richiede strategie rigorose di contenimento e l'impiego di sistemi di manipolazione remota. L'impiego di piombo puro mitiga il problema del polonio, riducendone in modo sostanziale la quantità prodotta; rimangono tuttavia altre difficoltà legate al peso maggiore dei metalli liquidi rispetto all'acqua e al più elevato punto di congelamento, che impongono ulteriori vincoli progettuali ed operativi. Inoltre, l'opacità degli HLM complica la visualizzazione del flusso e la strumentazione interna, limitando la disponibilità di dati sperimentali dettagliati per lo sviluppo di modelli e la validazione dei codici.

La termoidraulica degli HLM coinvolge fenomeni complessi come la transizione da circolazione forzata a naturale, la stratificazione termica nelle piscine e il congelamento del refrigerante. Il congelamento è una preoccupazione significativa: il piombo solidifica a circa 327 °C e l'LBE a circa 125 °C, rendendo necessario il riscaldamento continuo del refrigerante e dei componenti anche durante fermate o manutenzioni, per prevenire la solidificazione e le conseguenti occlusioni. Questo impone complessità aggiuntive ai sistemi di rimozione del calore di decadimento, che devono essere progettati per operare in modo affidabile su un ampio intervallo di temperature. Infine, il comportamento termoidraulico e la modellazione degli HLM pongono sfide uniche. La loro elevata densità e il basso numero di Prandtl portano a caratteristiche di flusso e di scambio termico significativamente diverse rispetto all'acqua, richiedendo notevoli sforzi in attività di ricerca e sviluppo (R&D). In assenza di reattori operativi a scala reale, la progettazione e la valutazione di sicurezza degli LFR devono basarsi fortemente su simulazioni numeriche ad alta fedeltà supportate da dati sperimentali in impianti in scala ridotta. La qualificazione dei modelli numerici e dei codici di termoidraulica di sistema (System Thermal-Hydraulic, STH), così come la validazione dei sistemi di sicurezza in condizioni rappresentative, restano passaggi fondamentali nello sviluppo di questa classe di reattori.

Questa ricerca di dottorato contribuisce all'avanzamento tecnologico degli LFR attraverso un'estesa campagna di analisi termoidrauliche di sistema mirate a supportare la progettazione, la qualifica e la dimostrazione di sicurezza di diversi concetti LFR in fase di sviluppo nel mondo. Lo strumento di simulazione principale impiegato è RELAP5, un codice per la System Thermal Hydraulics (STH) validato principalmente per i reattori ad acqua. La tesi si articola su tre progetti principali: ALFRED, il Westinghouse-LFR (WEC-LFR) e MYRRHA

Nel caso di ALFRED, è stata condotta un'ampia serie di studi, tra cui un'analisi PIRT (Phenomena Identification and Ranking Table), per identificare le principali criticità tecniche e orientare la priorità delle attività di R&D. Per valutare il comportamento del reattore in condizioni nominali e incidentali, sono state effettuate simulazioni accoppiate NK-TH (cinetica neutronica e termoidraulica), focalizzandosi su transitori non protetti. Particolare attenzione è stata dedicata al sistema innovativo di rimozione del calore di decadimento (DHR), che si basa sulla degradazione dei meccanismi di condensazione a causa della presenza di gas incondensabili. Questo approccio mira a conciliare due obiettivi contrastanti: rimuovere efficacemente il calore residuo mantenendo al contempo il refrigerante primario al di sopra del punto di congelamento. Per supportare e valutare questo concetto, è stato utilizzato l'impianto sperimentale SIRIO, su cui sono state condotte analisi termoidrauliche sia sperimentali che numeriche. Ulteriori indagini sono state eseguite per

studiare la condensazione in condizioni pure e in presenza di gas incondensabili, e per validare i modelli e le correlazioni implementate in RELAP5.
Il lavoro sul WEC-LFR ha coinvolto due impianti sperimentali principali. Il PHRF, dedicato allo studio del sistema passivo di rimozione del calore (PHRS) del WEC-LFR, il cui principio si basa sulla transizione del trasferimento di calore da acqua ad aria con conseguente degradazione della rimozione termica, è stato modellato e analizzato in profondità. Il secondo impianto è la Versatile Lead Facility (VLF), che rappresenta il sistema di raffreddamento del reattore (RCS), analizzato attraverso una pre-test analysis sia in condizioni nominali che accidentali. Inoltre, la presenza nel VLF di componenti chiave del RCS del WEC-LFR ha portato a un'analisi approfondita di due elementi critici: lo scambiatore di calore primario (PHE) e il simulatore di fascio di barre di combustibile (FPBS). Il PHE, uno scambiatore innovativo a microcanali, rappresenta una tecnologia emergente per la quale la letteratura e l'esperienza industriale sono ancora limitate. Per questo motivo è stato condotto uno studio comparativo utilizzando sia un codice STH (RELAP5) sia uno strumento CFD (Ansys CFX). Il FPBS, invece, è un componente rappresentativo di un elemento di combustibile del WEC-LFR. Per valutarne le prestazioni è stata condotta un'analisi di sotto-canale tramite il codice DASSH, seguita da un confronto con RELAP5 per verificare la coerenza della modellazione e individuare eventuali limiti dei codici.

Infine, per il reattore MYRRHA, la ricerca si è concentrata sul sistema secondario di raffreddamento, studiato tramite l'impianto sperimentale HEXACOM. L'obiettivo principale è stato applicare e affinare una procedura di qualifica dei modelli numerici STH degli impianti sperimentali, finalizzata a migliorare l'accuratezza della modellazione e supportare i futuri processi autorizzativi. È stato sviluppato un modello completo in RELAP5, calibrato e validato tramite dati sperimentali e specifiche progettuali. I risultati delle simulazioni hanno fornito importanti indicazioni sul comportamento del circuito idraulico e hanno contribuito alla qualifica del modello termoidraulico.

Il lavoro futuro dovrebbe concentrarsi sull'ampliamento del dominio di validazione dei codici STH tramite l'acquisizione di dati sperimentali di alta qualità, in particolare in condizioni transitorie e incidentali. L'accoppiamento tra codici STH e strumenti ad alta fedeltà come CFD o codici di sotto-canale dovrebbe essere ulteriormente esplorato per migliorare la risoluzione dei fenomeni locali nei componenti critici. Inoltre, l'integrazione di approcci multi-fisici, comprendenti feedback strutturali, neutronici e termoidraulici, sarà essenziale per aumentare l'accuratezza delle valutazioni di sicurezza. Dal punto di vista sperimentale, ulteriori campagne di prova su impianti avanzati come SIRIO, PHRF, VLF e HEXACOM saranno necessarie per affinare le strategie di modellazione e ridurre le incertezze in condizioni rilevanti per la progettazione. Queste direzioni di sviluppo contribuiranno in modo significativo alla qualificazione e al processo di licensing degli LFR, sostenendo il loro impiego sicuro e sostenibile nei futuri sistemi energetici nucleari.

# ABSTRACT

The urgent need to decarbonize the global energy system, in response to the climate crisis, has revitalized interest in nuclear power as a reliable, low-carbon, and dispatchable energy source. Nuclear energy, already a major contributor to carbon-free electricity generation, has the potential to play a central role in achieving deep decarbonization targets.

To this end, the Generation IV International Forum (GIF) has promoted the development of advanced reactor concepts that aim to overcome the limitations of current technologies. Among these, Lead-cooled Fast Reactors (LFRs) have emerged as one of the most promising options. LFRs operate in a fast neutron spectrum by relying on liquid lead or lead-bismuth eutectic as the primary coolant and the deployment of advanced fuel types such as Mixed (MOX) fuel, typically composed of plutonium oxide blended with depleted or natural uranium oxide, allows for the recycling of plutonium recovered from spent nuclear fuel, thereby reducing the accumulation of fissile material in storage and supporting non-proliferation and sustainability goals. Additionally, operating in a fast neutron spectrum allows LFRs to enhance the fuel utilization enabling the use of fertile isotopes such as Uranium-238 and Thorium-232 for breeding fissile material (respectively Plutonium-239 and Uranium-233). This capability extends the energy extracted per unit of natural uranium and reducing the need for fresh uranium mining. Moreover, the fast spectrum is particularly effective in transmuting long-lived minor actinides (such as neptunium, americium, and curium) into shorter-lived or stable isotopes through fission. This transmutation process significantly reduces the long-term radiotoxicity and heat load of nuclear waste, addressing one of the key challenges facing nuclear energy in terms of public acceptance and repository requirements. The choice of Heavy Liquid Metals (HLM) as reactor coolant offers a series of heat transfer and chemical advantages over traditional coolants. Their extremely high boiling point (around 1740 °C for lead and 1670 °C for LBE) permits reactor operation at atmospheric pressure, eliminating the need for pressurized vessels and reducing the risk of pressure-induced failures. The good thermophysical properties of HLMs namely the high density and thermal conductivity enhance passive heat removal capabilities and enable compact core designs with efficient heat transfer. The employment of HLMs enables operation at higher temperatures, improving the thermodynamic efficiency and contributing to the performances of LFRs. Additionally, HLMs are chemically inert with respect to air and water, eliminating the potential for violent reactions such as hydrogen generation, which is a major concern in Sodium-cooled Fast Reactors (SFRs) or Light Water Reactors (LWRs) designs.

Despite their many advantages, the use HLMs as primary coolants introduces a series of technical challenges that must be carefully addressed to ensure safe and reliable reactor operation. One of the most critical issues is corrosion: at high temperatures, lead and LBE are chemically aggressive toward structural materials, particularly steels, leading to progressive degradation of components exposed to the coolant. The formation of protective oxide layers on the surface of steels can mitigate corrosion, but their stability is highly sensitive to the oxygen concentration in the coolant. Maintaining a precise and stable oxygen level is therefore essential, requiring the implementation of robust oxygen control and monitoring systems. A related concern is erosion and mass transfer, especially in regions of high flow velocity or thermal gradients, where protective oxide layers may be mechanically removed, further accelerating material degradation. Another major challenge involves coolant activation and polonium production, particularly for LBE, which contains Bismuth-209 that can be transmuted into Polonium-210 under neutron irradiation. Polonium-210 is a highly radiotoxic alpha emitter with a relatively short half-life (~138 days), posing significant radiological hazards during maintenance, operation, and decommissioning.

This issue demands stringent containment strategies and remote handling capabilities. Pure lead avoids the polonium problem but remains heavier and has higher melting and freezing points, which introduces its own operational constraints. Moreover, the opacity of HLMs complicates flow visualization, instrumentation, and refuelling operations. Moreover, HLM Thermal-Hydraulics (TH) involves complex phenomena such as transition from forced to natural circulation, pool thermal stratification and freezing. Coolant freezing is also a considerable concern: lead freezes at around 327 °C and LBE at about 125 °C, necessitating continuous heating of the coolant and system components even during shutdown or maintenance phases to prevent solidification and blockages. This imposes complexity to decay heat removal systems, which must be designed to operate reliably across a wide range of temperatures. Finally, the TH behaviour and simulation of HLMs presents unique modelling difficulties. Their high density and low Prandtl number result in flow and heat transfer characteristics that differ significantly from those of water, requiring significant efforts in Research and Development (R&D) activities. In the absence of full-scale operational reactors, the design and safety assessment of LFRs must rely heavily on high-fidelity numerical simulations supported by data from scaled experimental facilities. The qualification of numerical models and System Thermal-Hydraulic (STH) codes, and the validation of safety systems under representative conditions, remain critical steps in the development of this reactor class.

This doctoral research contributes to the advancement of LFR technology through an extensive campaign of system-level TH analyses aimed at supporting the design, qualification, and safety demonstration of several LFR concepts under development in the world. The primary simulation tool used throughout the work is RELAP5, a STH code validated primarily for LWRs. The thesis is articulated around three key projects: ALFRED, the Westinghouse-LFR (WEC-LFR), and MYRRHA.

In the case of ALFRED, a series of in-depth studies—including a Phenomena Identification and Ranking Table (PIRT) analysis—were performed to pinpoint the main technical challenges and to guide the prioritization of R&D activities. To assess reactor behaviour under both normal and accidental conditions, coupled Neutron Kinetic (NK) and TH simulations were conducted, focusing on unprotected transients. Particular attention was devoted to ALFRED's innovative Decay Heat Removal (DHR) system, which relies on degradation of condensation mechanisms affected by the presence of non-condensable gases. This approach aims to conjugate two competing objectives: efficient decay heat removal and maintaining the primary coolant above its freezing point. To support and evaluate this concept, the SIRIO facility was involved in this work performing both experimental and numerical TH analyses. Additional extensive investigations were carried out to study the condensation process—both in pure conditions and with non-condensable—and to validate the TH models and correlations implemented in RELAP5.

The work on the WEC-LFR involved two major facilities. The PHRF which is dedicated to study and test the Passive Heat Removal System (PHRS) of the WEC-LFR. The PHRS is based on water-to-air transition heat transfer regime causing the decreasing of heat removal. The PHRF was modelled and deeply analysed. The other experimental facility involved within this framework is the VLF, representing the Reactor Cooling System (RCS), was analysed performing a pre-test analysis to gain enough understanding of this facility both in nominal and accidental conditions. Furthermore, the inclusion of key components of the WEC-LFR's RCS within the VLF experimental facility prompted detailed stand-alone analyses of two critical elements: the Primary Heat Exchanger (PHE) and the Fuel Pin Bundle Simulator (FPBS). The PHE, an innovative microchannel heat exchanger, represents a novel solution for which limited experience and literature exist within the nuclear industrial. As such, a comparative study was carried out using both a STH code (RELAP5) and a Computational Fluid Dynamics (CFD) tool (Ansys CFX) to better understand its behaviour.

The FPBS, on the other hand, is a representative model of the WEC-LFR Fuel Assembly. To evaluate its performance, a subchannel analysis was performed using the DASSH code, followed by a comparative assessment between DASSH and RELAP5 to verify modelling consistency and identify code-specific limitations.

Finally, for the MYRRHA reactor, a PIRT analysis has been performed in parallel with ALFRED, in the framework of R&D activities supporting the development of LFRs in Europe. Next, the research focused on the secondary cooling system, investigated through the HEXACOM experimental facility. This work primarily aimed at applying and refining a qualification procedure for STH numerical models of experimental facilities, with the goal of enhancing modelling accuracy and supporting future licensing processes. A comprehensive RELAP5 model of the system was developed, calibrated, and validated using both experimental data and nominal design specifications. The simulation results offered important insights into the behaviour of the water loop and played a key role in the qualification of the thermal-hydraulic model.

Future work should focus on extending the validation domain of STH codes through additional high-quality experimental data, particularly under transient and accident conditions. The coupling of STH codes with high-fidelity tools such as CFD or subchannel analysis codes should be further explored to improve the resolution of local phenomena within critical components. Moreover, the integration of multi-physics approaches—including structural, NK and TH feedback—will be essential to enhance the accuracy of safety assessments. On the experimental side, additional test campaigns on advanced facilities such as SIRIO, PHRF, VLF, and HEXACOM are necessary to refine modelling strategies and reduce uncertainties in design-relevant conditions. These future directions are expected to contribute significantly to the qualification and licensing of LFRs, ultimately supporting their safe and sustainable deployment in future nuclear energy systems.

# TABLE OF CONTENTS

# LIST OF FIGURES

# LIST OF TABLES

# LIST OF ABBREVIATIONS

| | |
|---|---|
| ADS | Accelerator Driven System |
| ALFRED | Advanced Lead Fast Reactor European Demonstrator |
| AMR | Advanced Modular Reactor |
| ANL | Argonne National Laboratory |
| ATHENA | Advanced Thermal-Hydraulic Experiment for Nuclear Application |
| ATWS | Anticipated Transient Without SCRAM |
| AZ | Active Zone |
| BAF | Bottom of Active Fuel |
| BEIS | UK department for Business, Energy & Industrial Strategy |
| BoC | Beginning of Cycle |
| BREST | Bystryj reaktor so svincovym teplonositelem, Lead-cooled Fast Reactor |
| BT | Bayonet Tube |
| CANDLE | Constant Axial shape of Neutron flux, nuclide densities, and power shape During Life of Energy production |
| CB | Core Barrel |
| CC | Core Compaction |
| CDF | Cumulative Damage Function |
| CFD | Computational Fluid Dynamics |
| CIRCE | CIRCulation of Eutectic |
| COMPLOT | COMPonents LOop Testing |
| CR | Control Rod |
| CRS | Core Restraint System |
| CTC | Coolant Temperature Coefficient |
| DA | Dummy Assembly |
| DASSH | Ducted Assembly Steady-State Heat transfer |
| DBA | Design Basis Accident |
| DEC | Design Extended Condition |
| DES | Detached Eddy Simulation |
| DHR | Decay Heat Removal |
| DIA | DIAphragm |
| EBT | Emergency Boration Tank |
| ELF | Electrical Long-running Facility |
| ENEA | Italian National Agency for New Technologies, Energy, and Sustainable Economic Development |
| EoC | End of Cycle |
| FA | Fuel Assembly |
| FADF | Fuel Assembly Distribution Factor |
| FALCON | Fostering ALFRED Construction |
| FIV | Flow-Induced Vibration |
| FOAK | First-Of-A-Kind |
| FoM | Figure of Merit |
| FPBS | Fuel Pin Bundle Simulator |
| FPDF | Fuel Pin Distribution Factor |

| | |
|---|---|
| FSI | Fluid–Structure Interaction |
| FTC | Fuel Temperature Coefficient |
| Gen-IV | Generation-IV |
| GHG | Green-House Gases |
| GIF | Generation IV International Forum |
| GP | Guard Plate |
| GRNSPG | Gruppo di Ricerca Nucleare di San Piero a Grado |
| GV | Guard Vessel |
| HELENA | Heavy Liquid metal Experimental loop for advanced Nuclear Applications |
| HELIOS | Heavy Liquid Metal Oxygen Conditioning System |
| HEXACOM | Heat EXchAnger at COMplot |
| HLM | Heavy Liquid Metal |
| HMTA | Heat and Mass Transfer Analogy |
| HP | Heating Plate |
| HS | Heat Structure |
| HX | Byphass Heat eXchanger |
| IAEA | International Atomic Energy Agency |
| INL | Idaho National Laboratory |
| IS | Internal Structure |
| ISF | Internal Structure Failure |
| ITF | Integral Test Facilities |
| IV | Inner Vessel |
| IVFHM | In-Vessel Fuel Handling Machine |
| KAIST | Korea Advanced Institute of Science and Technology |
| LCOE | Levelized Cost Of Electricity |
| LEADER | Lead European Advanced DEmonstrator Reactor |
| LES | Large Eddy Simulation |
| LFR | Lead-cooled Fast Reactor |
| LLNL | Lawrence Livermore National Laboratory |
| LOCA | Loss Of Coolant Accident |
| LOFA | Loss Of Flow Accident |
| LOHS | Loss Of Heat Sink |
| LP | Lower Plenum |
| LWR | Light Water Reactor |
| M&S | Modelling and Simulation |
| MCHE | Microchannel Heat Exchanger |
| MEXICO | Mass EXchange In Continuous Operation |
| MOX | Mixed Oxide |
| MYRRHA | Multi-purpose hYbrid Research Reactor for High-tech Applications |
| NACIE-UP | NAtural CIrculation Experiment UPgrade |
| NG | Non-condensable Gas |
| NGT | Non-condensable Gas Tank |
| NK | Neutron Kinetic |
| NRC | Nuclear Regulatory Commission |
| P&ID | Piping and Instrumentation Diagrams |

| | |
|---|---|
| P&T | Partitioning and Transmutation |
| PCS | Power Conversion System |
| PEACER | Proliferation-resistant, Environment-friendly, Accident-tolerant, Continual, and Economical Reactor |
| PHE | Primary Heat Exchanger |
| PHRS | Passive Heat Removal System |
| PHX | Primary Heat eXchanger |
| PIRT | Phenomena Identification and Ranking Table |
| PLD | Pulsed Laser Deposition |
| PLOOP | Protected Loss Of Off-site Power |
| PP | Primary Pump |
| QA | Quality Assurance |
| R&D | Research and Development |
| RANS | Reynolds-Averaged Navier-Stokes |
| RC | Reactor Cover |
| RCP | Reactor Coolant Pump |
| RCS | Reactor Cooling System |
| RELAP5 | Reactor Excursion and Leak Analysis Program (version no. 5) |
| RP | Reactor Plate |
| RV | Reactor Vessel |
| RZ | Radial Zone |
| SBO | Station Black Out |
| SEALER | Swedish Advanced Lead Reactor |
| SET | Separate Effects Tests |
| SFR | Sodium-cooled Fast Reactor |
| SG | Steam Generator |
| SGTR | Steam Generator Tube Rupture |
| sH2O | Supercritical water |
| SIRIO | SIstema di RImozione del calore di decadimento per reattori nucleari innOvativi |
| SMR | Small Modular Reactor |
| SNETP | Sustainable Nuclear Energy Technology Platform |
| SNU | Seoul National University |
| SoT | Start of Transient |
| SPS | Spark Plasma Sintering |
| SR | Safety Rod |
| SSE | Safe Shutdown Earthquake |
| SSTAR | Small, Secure Transportable Autonomous Reactor |
| STC | Structure Temperature Coefficient |
| STH | System Thermal-Hydraulic |
| TH | Thermal-Hydraulics |
| TMDPJUN | TiMe-DePendent JUNction |
| TMDPVOL | TiMe-DePendent VOLume |
| TW | Time Window |
| ULOF | Unprotected Loss of Flow |
| ULOHS | Unprotected Loss of Heat Sink |

| | |
|---|---|
| UNIROMA1 | Sapienza University of Rome |
| UP | Upper Plenum |
| URANUS | Ubiquitous, Rugged, Accident-forgiving, Nonproliferating, and Ultra-lasting Sustainer |
| UTOP | Unprotected Transient Over-Power |
| V&V | Verification and Validation |
| VLF | Versatile Loop Facility |
| WEC | Westinghouse Electric Company |
| ZPA | Zero-Period Acceleration |

# LIST OF SYMBOLS

## Latin symbols

| | |
|---|---|
| a | Neutron temperature feedback coefficient [pcm/K] |
| A | Area [m²] |
| C | Delayed neutron precursor [n/m²s] |
| e | Error (process value – setpoint) |
| f | Fraction of delayed neutrons [-] |
| g | Gravity acceleration [m/s²] |
| H | Elevation [m] |
| h | Convection heat transfer coefficient [W/m²K] |
| K | Constant [-] or pressure loss coefficient [-] |
| k | Thermal conductivity [W/mK] |
| M | Molecular weight [kg/mol] |
| n | Number [-] |
| Nu | Nusselt number [-] |
| p | Pressure [Pa] |
| Pr | Prandtl number [-] |
| $\dot{Q}$ | Thermal power [W] |
| q" | Heat flux [W/m²] |
| r | Reactivity [$] |
| Re | Reynolds number [-] |
| S | External neutron source [n/m²s] |
| SF | Scaling Factor [-] |
| s | Valve stem position [-] or thickness [m] |
| T | Temperature [°C] |
| t | Time [s] |
| U | Overall heat transfer coefficient [W/m²K] |
| V | User-defined control variables as reactivity contributions |
| x | Flow quality [-] |
| Z | Shah correlating parameter [-] |

## Greek symbols

| | |
|---|---|
| β | Effective delayed neutron fraction [-] |
| Γ | Mass flow rate [kg/s] |
| Δ | Quantity variation |
| δ | Liquid film thickness [m] |
| ε | Rugosity [m] |
| λ | Decay constant [$s^{-1}$] |
| Λ | Prompt neutron generation time [s] |
| μ | Dynamic viscosity [Pa s] |
| ν | Cinematic viscosity [m²/s] |

| | |
|---|---|
| ρ | Density [kg/m³] |
| σ | Stress [MPa] |
| φ | Neutron flux [n/m²s] |
| ω | Angular velocity [rad/s] |

## Subscripts and superscripts

| | |
|---|---|
| b | Bulk condition |
| eff | Effective |
| F | Fuel |
| g | Gas phase |
| $H_2O$ | Water-side |
| i | i-th neutron precursor group or volume or heat structure |
| l | Liquid phase |
| Pb | Lead-side |
| r | Reduced value (ratio of pressure or temperature to the critical pressure or temperature) |
| W | Coolant |

# 1. INTRODUCTION

Meeting the energy demands of a growing global population while simultaneously reducing Green-House Gas (GHG) emissions remains one of the greatest challenges of the 21st century [1]. In response to the escalating climate crisis, nations around the world have committed to ambitious decarbonization goals aimed at achieving net-zero emissions within the coming decades [2]. Electricity generation, as one of the primary sources of global carbon emissions, is a major focus of these efforts. While renewable energy sources such as solar and wind have seen rapid growth, their intermittency and variability necessitate the integration of stable, dispatchable, and low-carbon alternatives. In this context, nuclear energy stands out as a proven and scalable solution capable of delivering large quantities of carbon-free electricity with high reliability. Figure 1 illustrates the projected global temperature rise based on different energy mix scenarios. Each dot represents a specific scenario, color-coded by the estimated temperature increase. The figure highlights that higher shares of both renewable and nuclear energy are essential to effectively limit global warming.

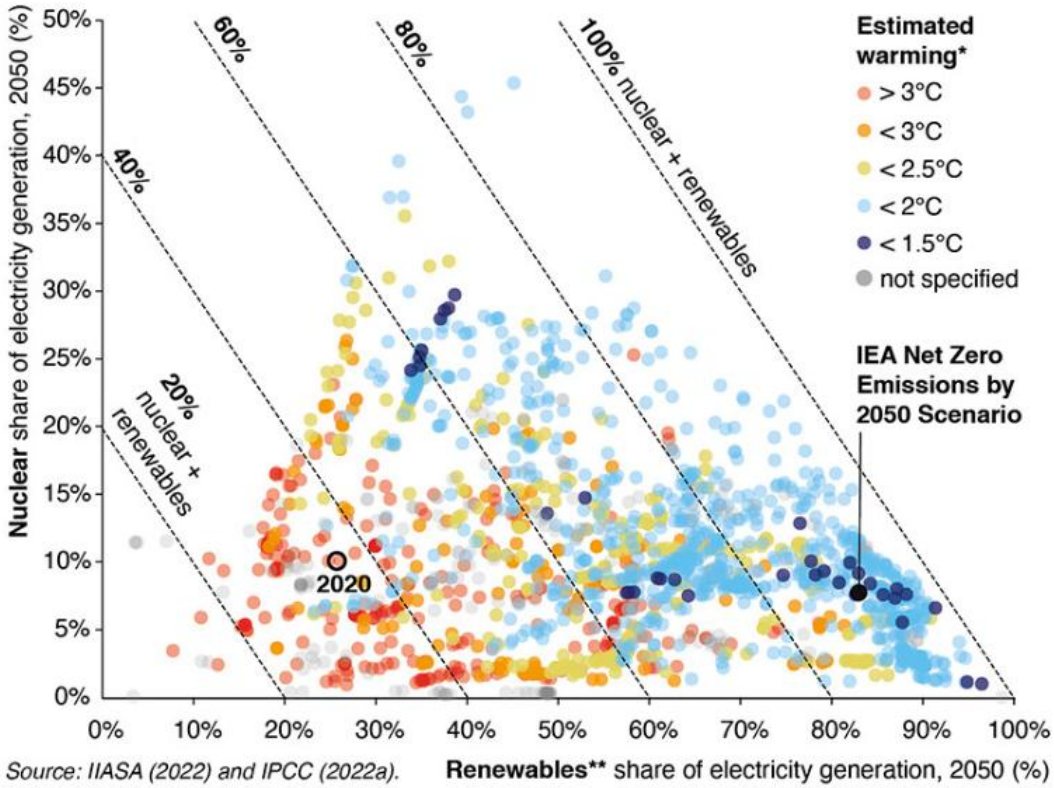


***Figure 1 Shares of nuclear and renewable energy in the electricity generation mix and corresponding climate warming across IPCC AR6 scenarios [2]***

Currently, nuclear power provides roughly 10% of the world's electricity and over one-quarter of all low-carbon electricity. In many developed economies—such as France, the United States, South Korea, and Canada—nuclear power plants constitute a substantial share of the energy [3]. More recently, a growing number of countries in Asia, Eastern Europe, and the Middle East are investing in nuclear infrastructure to meet their energy and environmental targets. According to the International Atomic Energy Agency (IAEA), more than 50 countries are exploring the use of nuclear energy, and over 60 reactors are under construction globally as of 2024 [4]. This renewed global interest is further driven by energy security concerns, fossil fuel price volatility, and the need for resilient energy systems in the face of climate extremes.

## 1.1. Generation IV reactors and LFRs

The growing and persistent demand for safe and sustainable energy has driven the ongoing advancement of nuclear technology. Generation IV (Gen-IV) reactors represent the most recent stage in this development, featuring innovative designs aimed at overcoming the challenges and limitations of earlier reactor generations [5]. Within this framework, the Generation IV International Forum (GIF) was established as an international collaborative initiative aimed at advancing the research required to evaluate the feasibility and performance of Gen IV nuclear reactors, with the goal of enabling their industrial deployment by 2030. To guide this development, GIF defined a set of ambitious goals that Gen-IV systems must meet to ensure their long-term viability. These include improvements in sustainability, economics, safety and reliability and proliferation resistance [6]. Among the six reactor technologies identified by the GIF, Lead-cooled Fast Reactors (LFRs) [7] are widely recognized as one of the most promising technologies capable of addressing the objectives set by the GIF.

From a sustainability perspective, LFRs leverage the neutronic properties of lead, which has a low neutron absorption cross-section and poor moderating capabilities. These features enable the reactor to operate effectively in a fast neutron spectrum, favouring the achievement of near-unitary breeding ratios. This means that fertile (e.g., $U^{238}$ or $Th^{232}$) can be efficiently converted into fissile (respectively $Pu^{239}$ and $U^{233}$), contributing to a closed fuel cycle and improved resource utilization. Moreover, the fast spectrum allows the transmutation and burning of minor actinides which are the main contributors to the long-term radiotoxicity of spent nuclear fuel. By significantly reducing the radiological burden of high-level waste, LFRs enhance the overall sustainability of the nuclear fuel cycle.

In terms of economic performance, LFRs benefit from the favourable thermo-physical properties of lead. Most notably, the very high boiling point at atmospheric pressure of lead and LBE (respectively 1737 °C and 1670 °C) enables reactor operation at high temperatures and low system pressures. This allows for a simplification of the reactor's design, reducing the need for complex pressure control systems and large containment structures typically required to manage high-pressure conditions in conventional reactors. As a result, construction times and capital investment can be reduced. Furthermore, the primary components of an LFR—including the core, heat exchangers, and primary pumps—can be housed within a single vessel, further minimizing plant footprint and system complexity. The high core outlet temperatures (up to ~550 °C) achievable with LFRs also allow for more efficient thermodynamic cycles than those used in traditional Light Water Reactors (LWRs), potentially leading to better electricity generation performance. However, several technological challenges must be addressed for commercialization. These include the development of systems to keep lead or LBE above their freezing point (respectively 327 °C and 125 °C) during shutdown and maintenance phases, and the implementation of corrosion-resistant coatings for structural materials exposed to molten lead. While the absence of commercial-scale LFRs limits direct cost comparisons with LWRs, recent reviews [8] suggest that, aside from the First-Of-A-Kind (FOAK) deployments, LFRs are likely to become economically competitive with existing nuclear technologies.

With regard to safety and reliability, LFRs offer several inherent and passive safety features. The high atomic number and density of lead provide excellent shielding against gamma radiation, reducing radiation doses to personnel and facilitating maintenance. Additionally, the coolant's favourable neutronic and thermo-physical characteristics allow for larger spacing between fuel rods (i.e., high pitch-to-diameter ratios), resulting in lower pressure drops and reduced pumping requirements.

These design features are crucial for maintaining effective core cooling, especially under accident conditions, where natural circulation mechanisms can suffice for decay heat removal without reliance on active safety systems. In severe accident scenarios, the high density of lead facilitates passive dispersion of molten fuel, helping to prevent abnormal conditions and enabling more robust accident management strategies. Lead's physical properties also mitigate other accident phenomena, such as steam entrainment in the case of a Steam Generator Tube Rupture (SGTR), by avoiding steam to reach the core which causes a positive reactivity insertion.

Lastly, proliferation resistance and physical protection are intrinsic advantages of the LFR design. The use of MOX (Mixed Oxide) fuel, which combines plutonium and uranium oxides along with other minor actinides, makes the fuel unattractive for diversion or dual use, as it contains isotopic compositions unsuitable for weapons-grade material. Additionally, the long refuelling intervals and high burnup rates in LFRs limit opportunities to extract usable plutonium during the reactor's operational cycle. From a physical protection standpoint, the use of lead as a coolant enhances resilience: lead does not pose fire or explosion hazards when exposed to air and water, reducing the risk associated with external attacks or internal failures. The lack of significant internal pressure within the reactor system also prevents large-scale containment pressurization in the event of sabotage or catastrophic failure.

## 1.2. State of the art on LFRs

LFRs have attracted increasing attention in recent decades as one of the most viable Generation IV reactor concepts. Their development draws from both historical experience with fast reactors and more recent innovations in materials, safety systems, and fuel cycle strategies. Several projects worldwide are advancing LFR designs [9], including, but not limited to, the BREST-OD-300 [10] (Bystryj reaktor so svincovym teplonositelem, Lead-cooled Fast Reactor) which is supported and funded by the Russian government and currently represents the most advanced LFR project. Other notable efforts include the URANUS [11] (Ubiquitous, Rugged, Accident-forgiving, Nonproliferating, and Ultra-lasting Sustainer) developed by Seoul National University (SNU) in collaboration with the Korea Advanced Institute of Science and Technology (KAIST); the SEALER [12] (Swedish Advanced Lead Reactor) designed by the Swedish company Blykalla and the SSTAR [13] (Small, Secure Transportable Autonomous Reactor) designed by Argonne National Laboratory (ANL) and Lawrence Livermore National Laboratory (LLNL). Table 1 summarizes the main quantities of the LFRs mentioned above.

***Table 1 Key parameters of LFRs concepts***

| **Parameter** | **BREST** | **URANUS** | **SEALER** | **SSTAR** |
|---|---|---|---|---|
| **Core power [$MW_{th}$]** | 700 | 100 | 140 | 45 |
| **Nuclear fuel** | PuN-UN | $UO_2$ | UN | TRUN |
| **Electrical power [$MW_e$]** | 300 | 40 | 55 | 20 |
| **Primary system type** | Pool | Pool | Pool | Pool |
| **Primary coolant** | Lead | LBE | Lead | Lead |

| | | | | |
|---|---|---|---|---|
| **Core inlet temperature [°C]** | 420 | 300 | 400 | 420 |
| **Core outlet temperature [°C]** | 540 | < 450 | 550 | 564 |
| **Secondary cycle** | Superheated steam | Superheated steam | Superheated steam | Supercritical $CO_2$ |
| **Net efficiency [%]** | 42 | 40 | 36 | 44 |
| **Turbine inlet pressure [bar]** | 180 | 80 | 130 | 200 |
| **Feedwater temperature [°C]** | 340 | 250 | 340 | 402 |
| **Turbine inlet temperature [°C]** | 505 | 360 | 530 | 550 |

### *1.2.1. BREST-OD-300 reactor*

The BREST-OD-300 [14] is a next-generation LFR developed by Russia as part of its national initiative to close the nuclear fuel cycle [15]. This strategy aims to significantly reduce long-lived radioactive waste by enabling the reprocessing and reuse of spent fuel. With a power output of 300 MWe, the reactor is designed to achieve high standards of safety, sustainability, and fuel efficiency. It employs lead as the coolant and a uranium-plutonium nitride (PuN-UN) fuel, which offers excellent thermal conductivity, compatibility with advanced cladding materials like chromium ferritic-martensitic steel, and high breeding potential. The core operates with a breeding ratio equal to or greater than one, enabling in-core fuel regeneration and minimizing the need for fresh fissile material. Additionally, the reactor maintains a very low excess reactivity ($\Delta\rho < \beta_{eff}$), enhancing its intrinsic safety.

Passive safety is a cornerstone of the design. Due to lead's thermal and physical properties, the reactor remains stable even under severe conditions, such as rapid reactivity insertion or complete loss of forced circulation, without exceeding fuel damage thresholds. The fuel assembly layout is engineered to promote lateral coolant overflow in case of damage, mitigating the risk of local overheating.

The BREST-OD-300 adopts a loop-in-a-pool-type configuration: the core and primary components are housed within a central cavity, surrounded by four peripheral compartments inside a steel-lined concrete vessel. The central area contains the core, neutron reflector, control and protection rods, and space for spent fuel assemblies. The peripheral sections accommodate the Steam Generator and Reactor Coolant Pump modules (SG-RCP), along with emergency heat exchangers and other support systems. To optimize heat removal and core performance, fuel assemblies are arranged with varying rod diameters—smaller in the centre and larger toward the periphery—creating a power distribution that matches the coolant flow profile.

Unlike conventional reactors, the BREST-OD-300 does not require high-pressure operation or intermediate cooling loops, simplifying system design and improving economic viability. As a prototype, it is intended to demonstrate safe and flexible operation while supporting the broader deployment of medium-scale fast reactors for a sustainable nuclear future.

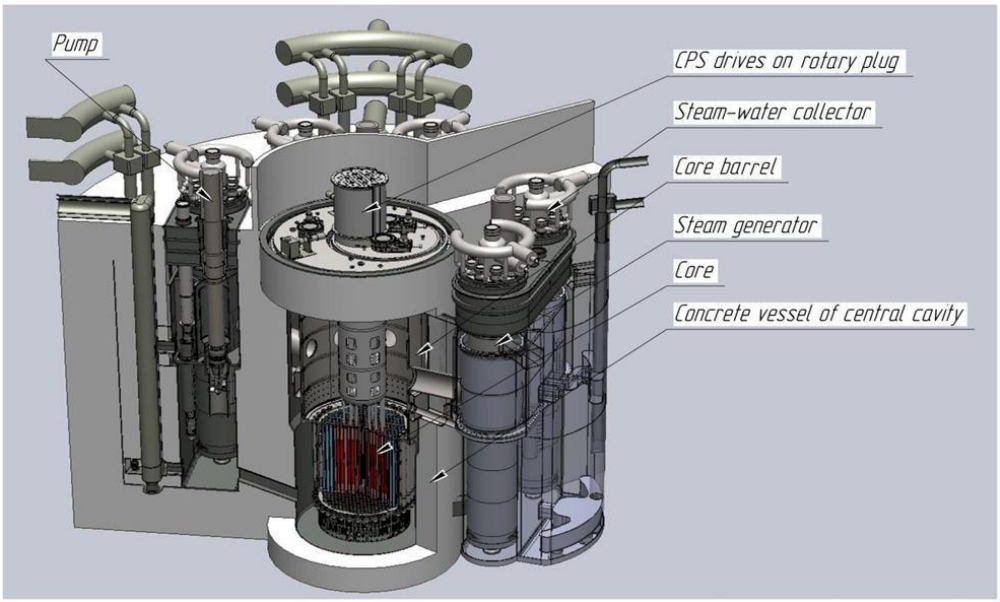


***Figure 2 BREST-OD-300 overview [14]***

### *1.2.2. URANUS reactor*

URANUS-40 [11] is a Korean-designed LBE-cooled Small Modular Reactor (SMR) developed at Seoul National University (SNU), with a thermal power output of 100 $MW_{th}$ and an electric output of 40 $MW_e$. It belongs to the fast reactor class and adopts a compact, pool-type configuration entirely based on passive safety principles and natural circulation, eliminating the need for primary coolant pumps.

The core consists of uranium dioxide ($UO_2$) fuel, arranged in a hexagonal lattice with two enrichment zones (9.25% and 17.75%) to optimize power distribution and minimize peaking factors. The reactor is designed for a long operational cycle of 20 years without refuelling, supported by durable structural materials such as T-91 cladding overlaid with Al-containing ferritic steel. The system includes an advanced oxygen control mechanism to manage corrosion in the LBE environment, ensuring material longevity and operational safety. URANUS-40 employs eight shell-and-tube type steam generators immersed in the reactor pool, enabling natural circulation on both the primary and secondary sides. The core operates with an inlet temperature of 300 °C and an outlet temperature of up to 450 °C, ensuring high thermal efficiency while maintaining conservative margins for structural integrity. The steam generators are designed to efficiently couple with a Rankine cycle for power production, with potential for cogeneration applications.

Safety is a cornerstone of the URANUS design. It includes multiple redundant shutdown mechanisms: a primary system using active control rods, a secondary gravity-driven rod system, and a tertiary ultimate shutdown device triggered by melting mechanisms. The reactor vessel is double-walled and features a seismic base isolation system, capable of withstanding seismic events up to 0.5 g. The entire facility is housed underground, significantly enhancing resistance to external threats such as aircraft impact, sabotage, or natural disasters.

Overall, URANUS-40 combines inherent safety, long-term fuel sustainability, compactness, and modularity, making it particularly suitable for deployment in isolated regions, industrial sites, or as a reliable source of clean energy for electricity and heat cogeneration. Its design philosophy emphasizes simplicity, robustness, and resistance to severe accident scenarios without reliance on external power or active intervention.

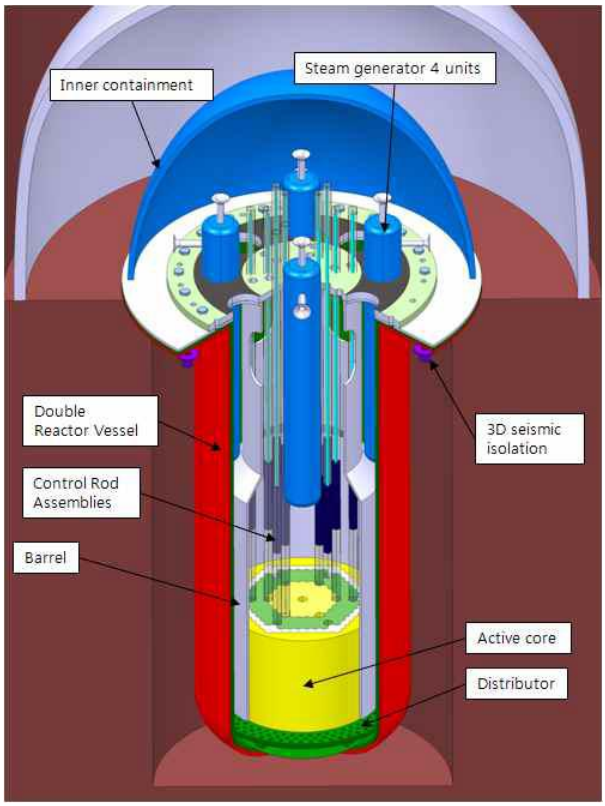


***Figure 3 URANUS-40 reactor module scheme [11]***

### *1.2.3. SEALER reactor*

SEALER is a 55 MW compact, passively safe small modular reactor (SMR) developed by the Swedish company Blykalla for commercial electricity generation [12]. Its design emphasizes long operational life, safety, and modularity. The reactor features a 25-year fuel residence time, enabling continuous operation without refuelling. This extended core life significantly lowers fuel management costs and is made possible using uranium nitride (UN) fuel, which possesses a uranium density approximately 40% higher than that of conventional uranium dioxide ($UO_2$). This higher density not only allows for a longer fuel cycle but also enhances thermal safety margins, as uranium nitride exhibits thermal conductivity approximately seven times greater than $UO_2$. Consequently, the reactor operates more than 1500°C below the fuel melting point, greatly improving safety.

Manufacturing uranium nitride, however, presents technical challenges when using conventional fabrication techniques. Blykalla addresses this by employing Spark Plasma Sintering (SPS) combined with hot pressing. This method allows for the direct conversion of enriched uranium hexafluoride ($UF_6$) into sintered fuel pellets through a reaction with streaming ammonia ($NH_3$), representing a novel and efficient fuel production process.

SEALER is designed with an emphasis on passive safety. Decay heat removal is achieved through natural convection of the lead coolant, eliminating reliance on active systems. In the event of a severe accident, such as core disruption, volatile fission products are retained within the lead, preventing their release into the environment and thus avoiding the necessity of evacuating the surrounding population. The compact nature of the reactor core reduces the amount of residual heat, which further facilitates passive heat removal and supports the development of scalable and replicable reactor units.

A major technological challenge in lead-cooled systems is the corrosive and erosive behaviour of the coolant. Blykalla has responded by developing a series of advanced aluminium-alloyed steels to protect different reactor components. These include alloys suitable for cladding tubes, reactor vessels, and pump impellers, resisting lead corrosion and long-term structural integrity under high-temperature conditions.

The company's first reactor, named SEALER-One, will act as a demonstrator and will also be used for non-electric applications such as pyrolysis and steam generation. The licensing process for SEALER-One is currently underway, with construction planned at Nyköping, the location of the Studsvik research facility. Initial criticality is expected by 2029. The commercial model, SEALER-55, is designed for modular, factory-based production, allowing reactors to be manufactured centrally and transported to their final installation sites. Serial production of SEALER-55 is projected to commence in the early 2030s.

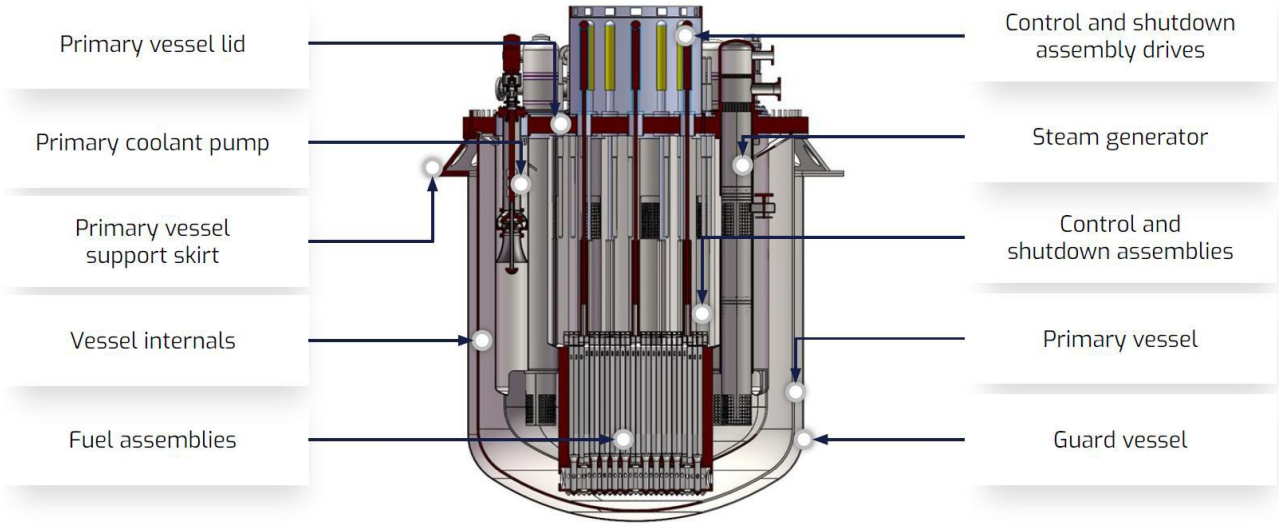


***Figure 4 SEALER primary system layout [16]***

### *1.2.4. SSTAR reactor*

SSTAR [13] is a compact LFR concept developed in the United States under the Generation IV framework. It is designed to address the energy and infrastructure needs of developing nations and remote regions through a highly self-sufficient and proliferation-resistant architecture. With a nominal electrical output of 20 $MW_e$ (45 $MW_{th}$), SSTAR is optimized for autonomous operation over extremely long core lifetimes, targeting up to 30 years without refuelling. The core operates in a fast neutron spectrum and is cooled by natural circulation of liquid lead, removing the need for mechanical pumps and thereby enhancing passive safety and system reliability.

A defining feature of SSTAR is its sealed cartridge core, which is shipped as a prefabricated unit and returned to a central facility at the end of its lifetime. This approach supports strong non-proliferation goals by eliminating on-site refuelling and reducing access to nuclear materials. The core is fuelled with transuranic nitride fuel, offering high thermal conductivity and fissile content, while maintaining structural integrity at elevated temperatures.

The reactor operates with a conversion ratio close to unity, allowing it to maintain fissile self-sufficiency over its entire operational life. Heat removal and electricity generation are achieved via a supercritical $CO_2$ Brayton cycle, enabling thermal conversion efficiencies up to 44%, which is notably high for small-scale nuclear systems.

SSTAR incorporates autonomous load following capabilities without the need for control rod motion, relying instead on passive thermo-structural feedback to modulate power output. Its simplified operational requirements allow it to function with minimal staffing, and its compact form factor enables transport by ship or land, facilitating deployment in isolated areas lacking developed infrastructure. The core and primary system are housed in a pool-type vessel, approximately 12 meters in height and 3.2 meters in diameter, allowing for modular manufacturing and ease of installation.

Overall, SSTAR exemplifies a new generation of distributed nuclear energy systems that prioritize security, flexibility, and minimal environmental and operational footprints. Its design philosophy aligns with the broader objectives of international deployment, offering energy security to nations without domestic fuel cycle infrastructure, and contributing to sustainable nuclear development in regions that would otherwise remain underserved by conventional large-scale reactors.

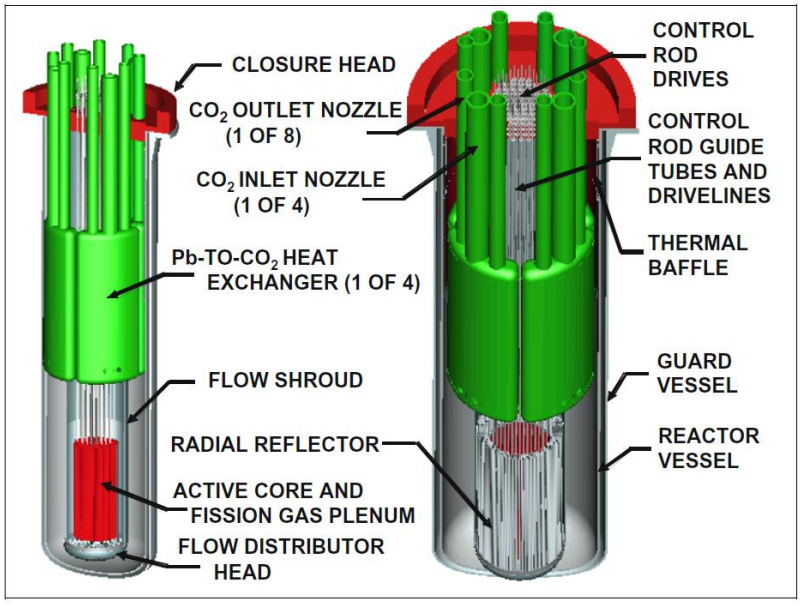


***Figure 5 Pre-conceptual 20 $MW_e$ (45 $MW_{th}$) SSTAR reactor [13]***

## 1.3. Experimental facilities supporting the development of LFRs

The development and deployment of LFRs require a robust and sustained program of experimental research to address the unique challenges associated with this Generation IV technology. LFRs operate with heavy liquid metal coolants, which exhibit distinct thermophysical, chemical, and neutronic behaviours. Moreover, each innovative system approaching toward the state-of-the-art of nuclear industry must undergo thorough verification and the acquisition of operational experience. As a result, the qualification of design concepts, safety systems, structural materials, and thermal-hydraulic models demands extensive validation through dedicated experimental facilities [17]. These facilities are essential to generate high-quality data under representative operating conditions and to support the verification and validation (V&V) of numerical codes used in safety analysis, particularly STH, subchannel, and CFD models [18].

At the international level, numerous R&D activities have been undertaken over the past two decades to advance the maturity of LFR technology. These efforts are especially concentrated in countries such as Russia, China, the United States, and several EU member states [19]. Within Europe, the strategic development of experimental infrastructures has been guided by coordinated programs and funding mechanisms under the EURATOM framework, often in synergy with the GIF and the Sustainable Nuclear Energy Technology Platform (SNETP).

The experimental facilities dedicated to LFR development are designed to investigate a wide range of key scientific and engineering issues which are related to the following topics:

- **Neutronics:** one of the primary concerns lies in the accurate prediction of neutron flux distribution, reactivity coefficients, and transmutation rates within a fast neutron spectrum. This is particularly critical given the use of dense fuels (e.g., MOX or nitride) and the hard neutron flux typical of lead-cooled systems, which can significantly affect core behaviour and long-term fuel evolution. Precise modelling of these phenomena is essential for core design, fuel cycle optimization, and burnup credit assessments.
- **Materials:** another critical challenge, as structural components in LFRs must withstand prolonged exposure to high temperatures, intense neutron irradiation, and the corrosive environment of liquid lead or LBE. The development and qualification of corrosion-resistant steels, such as alumina-forming alloys or chromium-based ferritic-martensitic steels, remain active areas of R&D. In addition, mechanical integrity under thermal cycling and radiation-induced swelling must be rigorously evaluated.
- **Chemistry:** maintaining a stable oxygen concentration is fundamental to forming and preserving protective oxide layers on steel surfaces. However, fluctuations in oxygen levels or interactions with impurities can destabilize these films, leading to accelerated corrosion. Moreover, the management of activated products, such as $Po^{210}$ in LBE, introduces radiological safety and maintenance challenges that require advanced purification and containment strategies.
- **Thermal-Hydraulics:** related at the core of reactor safety and efficiency. The high density and low Prandtl number of heavy liquid metals lead to flow and heat transfer characteristics significantly different from those of water or sodium. Key phenomena include natural circulation behaviour, thermal stratification in pools, coolant freezing risks, and the performance of passive decay heat removal systems. Accurate modelling of these effects is crucial for both nominal operation and transient scenarios. Additionally, a detailed characterization of Fuel Assembly subchannels from heat transfer and hydraulic points of view is required.

- **Instrumentation:** substantial limitations due to the opaque, corrosive, high-temperature environment of the coolant must be addressed. Conventional optical or ultrasonic sensors are often ineffective, requiring the development of robust, radiation-tolerant instrumentation capable of withstanding immersion in lead or LBE. This includes thermocouples, flowmeters, pressure sensors, and neutron detectors adapted for harsh conditions.

Within this framework, the Italian National Agency for New Technologies, Energy, and Sustainable Economic Development (ENEA) advances in heavy liquid metal technologies through EURATOM projects [20]. Key facilities include CIRCE (CIRCulation of Eutectic), a pool system for integral testing, and NACIE-UP (NAtural CIrculation Experiment UPgrade), focused on thermal-hydraulics and heat transfer in LBE-cooled rod bundles. HELENA (Heavy Liquid metal Experimental loop for advanced Nuclear Applications), another ENEA facility, tests components like pumps and heat exchangers under realistic LFR conditions.

The CIRCE facility [21], is the world's largest LBE pool installation, designed to investigate natural and enhanced circulation, thermal-hydraulics of fuel assemblies and components, and system behaviour under accident conditions. It consists of three main tanks, with the central experimental vessel containing up to 90,000 kg of LBE and capable of hosting full-scale test sections. In the context of MYRRHA support activities, CIRCE has been adapted to test SGTR scenarios through a dedicated test section. This configuration allows the reproduction of core phenomena such as rupture propagation, fission product retention, and impurity transport. The system includes jet pump-driven circulation, flow meters, filtering systems, and separators that reproduce MYRRHA's diaphragm behaviour. SGTR experiments are carried out under conservative thermal conditions (350 °C), with controlled tube rupture positions, to validate the safety systems and response of LFRs under severe transient events.

NACIE-UP [22] is a rectangular loop facility to support experimental research on thermal-hydraulics, fluid dynamics, heat transfer, chemistry control, and corrosion in heavy liquid metal-cooled systems. The loop, approximately 8 meters high and 2 meters wide, operates with lead or LBE up to 550 °C and 10 bar. It features a 19-pin wire-spaced FPBS with up to 250 kW power, designed to replicate MYRRHA-like core conditions. Heat removal is achieved through a shell-and-tube heat exchanger connected to a secondary pressurized water loop (16 bar), enabling long transient studies. Gas-lift enhanced circulation is supported by an argon injection system. The facility is equipped with precise flow meters, pressure drop sensors, and extensive thermocouple instrumentation (67 sensors) for detailed temperature and heat transfer measurements. NACIE-UP is essential for validating design correlations and STH models under both natural and mixed convection regimes relevant to Gen-IV LFRs.

The HELENA loop [23] is a versatile experimental facility designed to support the technological development of LFRs. It operates with pure lead and is configured to test thermal-hydraulics, heat transfer, chemistry control, corrosion, and component qualification under realistic conditions. The primary circuit includes a centrifugal pump (10–40 kg/s), a shell-and-tube heat exchanger (10–250 kW), a corrosion test section, and a high-power fuel pin simulator (19 pins, 250 kW). The loop can operate at temperatures up to 500–550 °C and includes instrumentation for flow, pressure, and oxygen control. A dedicated test section is used to assess erosion and corrosion behaviour of structural materials and components like pump impellers, isolation valves, and sensors. An advanced oxygen control system ensures coolant chemistry stability. HELENA enables experimental validation of CFD, and STH codes and supports the qualification of key technologies for future LFR demonstrators such as ALFRED and MYRRHA.

In parallel, the development of ALFRED is supported through a collaborative effort within FALCON [24] (Fostering ALFRED Construction), a consortium of European institutions that includes ANSALDO NUCLEARE, ENEA, RATEN ICN. In particular, a dedicated research infrastructure [25] is currently under construction in Romania. As shown in Figure 6, six experimental facilities make-up the research infrastructure.

Among these, ATHENA (Advanced Thermal-Hydraulic Experiment for Nuclear Application) [25] stands out as a large-scale pool facility specifically designed to replicate the thermal-hydraulic conditions of ALFRED. With a diameter of 3.2 meters and a height of 10 meters—matching the vertical scale of the reactor—it will host approximately 800 tons of liquid lead, making it the largest pool-type heavy liquid metal facility in the world. ATHENA is dedicated to testing large to full-scale components under representative conditions, focusing on phenomena such as thermal-hydraulics in the reactor pool, heat transfer in the bypass region of a multi-assembly core, primary pump performance, forced-to-natural circulation transition, steam generator tube rupture (SGTR), and partial blockage within fuel assemblies.

Closely connected to ATHENA is ChemLab [25], a dedicated chemistry laboratory supporting research in heavy liquid metal coolant behaviour and material science. Its primary objectives include the study of oxygen control and monitoring in lead, as well as the chemical interactions between the coolant and structural materials. ChemLab is divided into two main sections: one for experimental investigations on oxygen solubility, corrosion, and coolant chemistry control, and the other as a metallographic laboratory for post-experiment analysis of materials and dissolved metal content following lead exposure.

To explore severe accident phenomena and radionuclide behaviour, the Meltin'Pot platform [25] plays a central role. This unique research facility, hosted in a dedicated hot cell, consists of four experimental modules focused on key safety-relevant phenomena: fuel–coolant interactions, fuel dispersion and relocation in lead during core degradation scenarios, retention of fission products within the coolant or their migration to the cover gas, and behaviour of polonium isotopes in liquid lead. Meltin'Pot is specifically designed to support the safety assessment and licensing of ALFRED under hypothetical severe accident conditions.

The HELENA-2 loop facility [25] is aimed at studying the thermal-hydraulic behaviour of ALFRED's fuel assemblies under both forced and natural circulation regimes. It also includes provisions for conducting Flow-Induced Vibration (FIV) experiments and for qualifying control rod drive mechanisms under realistic conditions.

The Hands-ON facility [25] is a pool-type setup intended for validating ALFRED's fuel handling operations. It simulates handling procedures for both standard and deformed subassemblies and serves as a testbed for demonstrating the reliability and performance of the reactor's fuel handling equipment.

Finally, ELF (Electrical Long-running Facility) [25] is a large-scale pool-type facility designed to carry out long-duration tests and reliability assessments of ALFRED's primary components. It features a 5 MW core simulator, three steam generators, three pumps, and three decay heat removal (DHR) loops. ELF supports steady-state thermal-hydraulic investigations, long-term evaluation of component performance, and validation of lead–material compatibility under extended operation. It also enables the demonstration of an active oxygen control system for the primary loop and the simulation of accidental scenarios such as the transition from forced to natural circulation during a protected Loss Of Heat Sink (LOHS) coupled with a Loss Of Flow Accident (LOFA).

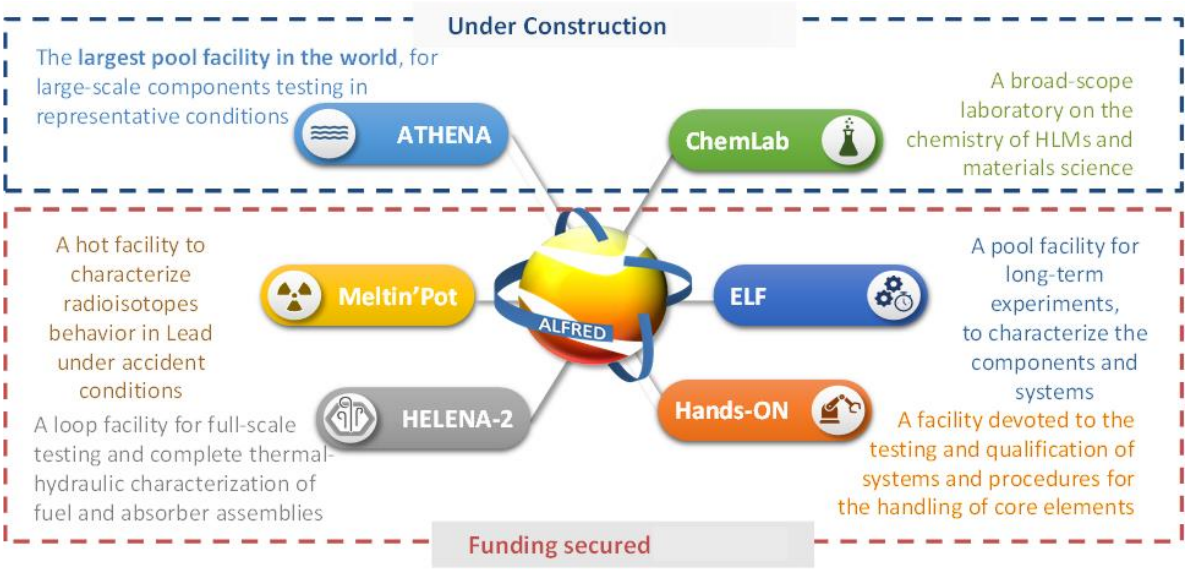


***Figure 6 ALFRED Research Infrastructure [25]***

The Belgian Nuclear Research Centre (SCK CEN) has launched a strong R&D programme to address the main design and licensing challenges, particularly those related to the use of liquid LBE as reactor coolant. In this frame SCK CEN has constructed and commissioned various LBE test facilities [26].

The COMPLOT (Components Loop Testing) facility [26] is an isothermal experimental loop specifically designed to investigate the hydraulic and hydrodynamic behaviour of heavy liquid metal systems, with a focus on full-scale reactor core components. Standing approximately 12 meters tall, the loop enables real-scale hydraulic testing under representative flow conditions. It operates with 9 tons of LBE within a temperature range of 200 °C to 400 °C, and supports a wide mass flow rate spectrum, ranging from 3.5 kg/s to 104.8 kg/s. The system is equipped with active coolant chemistry control to ensure stable and accurate simulation of reactor-relevant conditions. LBE-COMPLOT provides essential experimental data for the validation of core component designs and for the qualification of flow dynamics in lead-based fast reactor systems.

The MEXICO (Mass Exchange in Continuous Operation) facility [26] is a specialized experimental platform designed to test and evaluate oxygen control systems and filtration technologies in LBE environments. It contains approximately 7 tons of LBE and operates within a temperature range of 200 °C to 450 °C, with the capability to be upgraded up to 550 °C. MEXICO enables the assessment of filtration system performance, focusing on the removal of oxide particulates and the long-term stability and efficiency of purification components. The facility plays a critical role in supporting the chemistry control strategies necessary for the safe and reliable operation of LFRs and other HLM-cooled systems.

The HELIOS (Heavy Liquid Metal Oxygen Conditioning System) facility [26] is a dedicated LBE conditioning and storage setup developed to investigate and optimize oxygen control strategies in heavy liquid metal environments. Operating at a temperature of 450 °C, HELIOS supports the study of conditioning systems essential for maintaining chemical stability in lead-bismuth eutectic coolants. The facility also enables research into calamity mitigation strategies, particularly in scenarios involving steam ingress, which can compromise coolant chemistry and reactor safety. Additionally, HELIOS is used to test spargers and impeller inserts designed for gas bubbling applications, which are critical for active oxygen control and mixing efficiency in LFR systems.

## 1.4. PhD objectives and workflow activities

The development of LFRs involves multidisciplinary challenges that require the integration of experimental research, numerical modelling, and system-level analysis. This doctoral research has been dedicated to the TH investigation of LFRs, with a focus on supporting their design, safety assessment, and experimental validation through advanced numerical simulations and comparative analysis. The work has been developed in parallel with the ongoing R&D efforts on key LFR projects such as ALFRED, the Westinghouse-LFR, and MYRRHA, as well as their associated experimental facilities (respectively SIRIO, PHRF and VLF, HEXACOM). The thesis is structured to reflect the methodological progression and application of the research.

Chapter 2 presents the V&V methodology followed for the qualification of TH simulations and introduces the computational tools adopted throughout the research, including RELAP5, ANSYS-CFX, and DASSH. This forms the foundation for the system-level analyses performed in later chapters.

Chapter 3 focuses on the ALFRED reactor, beginning with a design overview followed by a PIRT analysis aimed at identifying safety-relevant areas characterized by significant uncertainty and limited modelling accuracy. This process was supported by coupled NK-TH simulations of unprotected transients. The chapter also presents an extensive study on the SIRIO facility, used to experimentally assess ALFRED's DHR system. Given that SIRIO was originally scaled to the older LEADER design, a rescaling analysis was conducted to align it with the updated FALCON configuration. Based on this revised version, a pre-test analysis was performed to verify the consistency and fidelity of the scaling strategy by comparing results with the full-scale reactor. In parallel, the condensation process—both in pure steam and with non-condensable gases—was thoroughly investigated. RELAP5 models and correlations were reviewed, source code modifications were implemented, and a broad validation campaign was carried out to enhance the code's predictive capability.

Chapter 4 presents the investigation conducted on the Westinghouse-LFR, beginning with a reactor overview and continuing with detailed analyses of the PHRF and VLF. The former is dedicated to study the behaviour and performance of the full scale PHRS. The latter arises to test the key components of Westinghouse-LFR. For both experimental setups, pre-test was performed using RELAP5, and in the case of VLF, dedicated component-level studies were conducted to evaluate the performance of the PHE using RELAP5 and ANSYS-CFX and the FPBS using RELAP5 and DASSH.

Chapter 5 addresses the MYRRHA system, with particular focus on its secondary loop and the associated experimental facility, HEXACOM. A PIRT analysis was carried out on MYRRHA to identify and prioritize key safety-relevant phenomena, guiding the overall thermal-hydraulic investigation. Both experimental data and numerical modelling were employed to investigate the transient thermal-hydraulic behaviour of the system. In this context, a qualification procedure developed by SCK CEN was also applied to validate and qualify the RELAP5 input deck for HEXACOM, ensuring the robustness and reliability of the simulation results for safety analysis and design support

Finally, Chapter 6 summarizes the main outcomes of the research and outlines future perspectives, including experimental needs, modelling improvements, and multi-physics integration.

The flowchart in Figure 7 visually summarizes the research activities undertaken and their logical progression throughout the thesis.

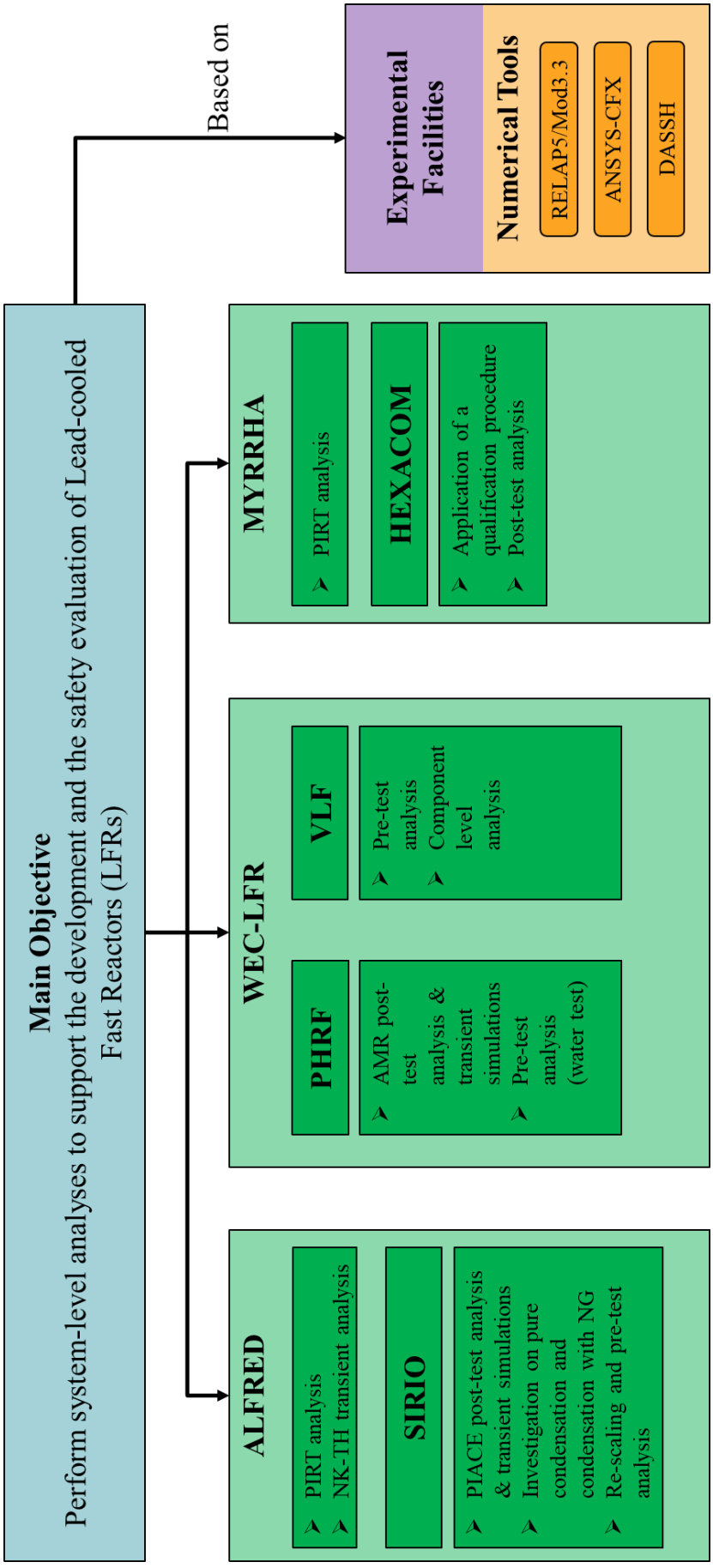


***Figure 7 Flowchart of the thesis***

# 2. METHODOLOGY AND NUMERICAL TOOLS

STH analysis plays a critical role in supporting the design, safety demonstration, and licensing of LFRs by simulating the behaviour of the primary and secondary systems under both nominal and accidental conditions. The methodology adopted for STH analyses relies on the use of one-dimensional, best-estimate system codes, and, when necessary, coupling with higher-fidelity tools or models related to other physics. The modelling approach typically includes the development of detailed nodalizations of full-scale reactors or experimental facilities, identification of key phenomena and execution of steady-state and, upon that, transient simulations are performed (both accidents and operational transient e.g., start-up and shut-down). To ensure reliability, simulation results are subjected to rigorous Verification & Validation (V&V) procedures according to the IAEA guidelines [18], including benchmarking, validation against experimental data, sensitivity analyses, and code qualification workflows. In parallel, in case in which experimental data are not available, a pre-test analysis can be performed in order to better understand the TH behaviour and to fully characterize the system under observation. This systematic approach allows the thermal-hydraulic behaviour of LFR systems to be characterized with sufficient accuracy to support design decisions and inform the development of passive safety strategies and decay heat removal systems.

## 2.1. Phenomena Identification and Ranking Table analysis

The Phenomena Identification and Ranking Table (PIRT) analysis [27] is a structured and expert-driven methodology developed to systematically identify and prioritize the physical phenomena that govern the behaviour of nuclear systems under normal and accidental conditions [28]. It is a critical element of the safety assessment process, particularly when dealing with advanced reactor concepts such as LFRs, for which the operational database and regulatory framework are still evolving. The approach supports the identification of research needs, informs the definition of experimental campaigns, and provides a foundation for the qualification and validation of numerical tools.

In the context of this doctoral research, a comprehensive PIRT analysis was carried out for two of the most advanced LFR designs currently under development in Europe: ALFRED and MYRRHA. The activity was conducted within the framework of a collaborative European project focused on the safety evaluation and modelling of HLM reactors. The primary goal was to identify and rank the phenomena that most significantly impact the safety margins of the two reactor concepts, under a representative set of Design Basis Accidents (DBAs) and Design Extension Conditions (DECs).

The PIRT process was initiated by establishing the reference configurations of ALFRED and MYRRHA and selecting a set of initiating events for each reactor concept. These events usually include unprotected transients, loss-of-heat-sink scenarios, and other conditions that could challenge the reactor's safety functions. Each transient was broken down into discrete phases to facilitate the identification of phenomena influencing the plant response at each stage.

Next, a set of Figures of Merit (FoMs) was defined, representing key performance indicators aligned with the fundamental safety functions: reactivity control, heat removal, and confinement of radioactive materials. Examples of FoMs include peak cladding temperature, primary system pressure, coolant inventory retention, and integrity of structural barriers. These FoMs served as reference points for assessing the relevance of each phenomenon under consideration.

A multidisciplinary panel of experts was assembled, including specialists in thermal-hydraulics, materials science, neutronics, chemistry, and system design. The panel included representatives from design organizations, research institutions, and universities with extensive experience in LFR technology. During a series of structured workshops and expert elicitation sessions, the panel identified the key phenomena expected to influence the plant's response to the selected transients. These included both general nuclear safety phenomena (e.g., decay heat removal, flow instability, fuel pin heat-up) and HLM-specific issues (e.g., gas entrainment, stratification in large pools, freezing of the coolant, corrosion-erosion, and non-condensable gas effects on heat transfer).

Each phenomenon was then scored using a qualitative ranking system based on two parameters: the importance to safety (IMP) and the state of knowledge (SOK). The IMP rating reflects the degree to which a given phenomenon affects the FoMs, while the SOK rating indicates the maturity of current knowledge, including the availability of experimental data, validated models, and the degree of consensus among experts. Typically, a three-level scale was adopted, e.g., High (H), Medium (M), Low (L) for both dimensions, and the combination of these two rankings formed the basis of the final prioritization (see Figure 8).

| Gap Identification → Priority R&D effort | | | |
|---|---|---|---|
| Rank of SOK (data) | Rank of IMP (impact on FoM) | | |
| | High | Medium | Low |
| High | | | |
| Medium | GAP | | |
| Low | GAP | GAP | |

***Figure 8 Proposed GAP identification grid***

Importantly, this ranking process is iterative. In cases where uncertainty or disagreement arose among panellists—either due to lack of data or conflicting modelling results—targeted numerical simulations and sensitivity analyses were performed using established tools such as Monte Carlo, STH, and CFD codes. These simulations were carried out in close collaboration with reactor designers and safety analysts to clarify the physical behaviour and reduce uncertainty. This feedback loop between expert judgment and computational analysis ensured that the final rankings were evidence-based and traceable.

The outcomes of the PIRT analysis included not only a prioritized list of critical phenomena for ALFRED and MYRRHA but also the identification of synergies and common challenges across both designs. Despite differences in power level, configuration, and mission objectives, both systems share common safety concerns related to the use of liquid lead or LBE as coolant, such as freezing, oxygen control, and complex flow regimes in pool-type reactors.

Moreover, the PIRT results provided a clear roadmap for future R&D efforts, highlighting areas where experimental data are lacking, model development is needed, or validation is required. These results also informed the qualification strategy for system thermal-hydraulic codes and supported the definition of test matrices for existing and future experimental facilities.

In summary, the PIRT analyses performed for ALFRED and MYRRHA established a rigorous and transparent framework for identifying and prioritizing the phenomena that must be addressed to ensure reactor safety. These analyses play a key role in the broader effort to demonstrate the viability of LFRs and contribute to their safe and effective deployment in future nuclear energy systems.

## 2.2.V&V process and STH qualification procedure

In nuclear safety analysis, numerical modelling plays a central role in informing design decisions, supporting licensing procedures, and evaluating accidental scenarios. With growing reliance on STH codes to simulate complex transients, the need for rigorous and standardised model qualification procedures has become increasingly important [29]. Widely used codes are capable of simulating both steady-state and transient conditions, but the accuracy of their predictions is strongly tied to the quality and validation of the input models. Regulatory authorities now require comprehensive model qualification to ensure that simulations credibly represent the physical behaviour of the systems being analysed.

STH codes form the backbone of thermal-hydraulic analysis in both industry and research, enabling the simulation of fluid flow and heat transfer in advanced nuclear systems. Developed over decades by regulatory agencies, national laboratories, and international collaborations, these codes—based on the one-dimensional conservation equations for mass, momentum, and energy—have been extensively validated through benchmark campaigns involving Separate Effects Tests (SETs), Integral Test Facilities (ITFs), and actual plant data. However, even a well-validated code cannot deliver meaningful results without a well-qualified application model. This recognition has led to the development of systematic qualification methodologies that go beyond standard verification and validation. These methodologies ensure the model's suitability for its intended use by evaluating the fidelity of geometric representation, boundary and initial conditions, sensitivity to key parameters, and the assumptions underpinning the simulation.

Such structured approaches are particularly important when modelling experimental facilities or advanced reactor concepts, where system conditions often exceed the original validation envelope of the code. Modern qualification practices emphasize modularity, traceability, and transparency. To this end, Quality Assurance (QA) is increasingly integrated into the modelling workflow through version control of input decks, standard test procedures, documentation protocols, and peer review processes. These QA practices enhance reproducibility, support long-term model maintenance, and ensure compliance with international best practices and regulatory standards.

This section presents a typical qualification procedure applied in this work, which is a revision and adaptation of the methodology developed by UNIPI-GRNSPG [30][31]. The proposed procedure has been developed at SCK CEN [32]. This methodology is adapted from and builds upon previous work by UNIPI-GRNSPG, with enhancements to address the specific needs of modern experimental infrastructures. A nodalization is considered "qualified" when it satisfies a set of predefined criteria that assess both its geometric fidelity and its capability to reproduce thermal-hydraulic phenomena under steady-state and transient conditions.

To properly apply the nodalization qualification procedure, a set of fundamental reference documents must be available. These include the Piping and Instrumentation Diagrams (P&IDs) and descriptive documentation of the experimental facility or test section, detailed as-built drawings of all components, piping, insulation, and their support structures—including geometrical data required for weight estimation—as well as comprehensive charts of instrumentation and valves with corresponding dimensions, connections, and structural supports.

Additionally, the procedure requires at least one steady-state test under nominal operating conditions for comparison with the STH code, one transient test (e.g., start-up or shutdown) for dynamic validation, and one steady-state test specifically for heat loss assessment. Incomplete or missing documentation may compromise the ability to achieve qualification or necessitate model tuning.

When data are only partially available, such limitations must be explicitly noted in the final nodalization report. Beyond this minimum, it is recommended to construct a graphical representation of the nodalization showing hydrodynamic and thermal components as well as defined regions. Although not mandatory, several general modelling guidelines are advised, based on established literature and STH code user manuals. These include the selection of the minimum number of hydrodynamic control volumes and heat structure mesh points sufficient to capture the key physical phenomena of interest. Control volumes should be grouped into regions defined by consistent unitary node lengths, which are selected to ensure Courant stability across the model and to balance geometric fidelity with numerical efficiency.

Typically, a node length-to-diameter ratio significantly greater than one is used, except in vessels where axial and radial dimensions are comparable. For systems involving two-phase flow and/or natural circulation, a "sliced" nodalization approach is recommended. The relative variation in length between adjacent nodes should not exceed ±50%; larger changes must be implemented using transitional nodes. For new applications or cases where results may be sensitive to spatial discretization, a posteriori sensitivity study is advised: the model should be run with node lengths reduced to 50% and increased to 150%, and the effect on steady-state parameters should be evaluated. The node length is considered adequate if further refinement does not lead to significant changes in the results. The procedure consists of 17 steps which can be divided into five main areas [32]:

- Hydraulic parameters
- Heat transfer parameters
- Exceptions
- Testing of the input deck
- Heat losses assessment

### 2.2.1. Hydraulic qualification

The geometric and hydraulic verification of the nodalization begins with a series of local and global checks comparing the model with the as-built drawings of the facility. These checks are necessary to ensure accurate physical representation of the system and adherence to predefined acceptability margins. The hydraulic qualification involves 7 steps which include both global and local limit.

*STEP 1: Hydrodynamic component length*

This step involves verifying the length of each hydrodynamic component, defined as its geometric extension along the primary flow direction. The modelled length must match the as-built reference within ±50% of the selected unitary node length, ensuring consistency with the chosen spatial discretization.

*STEP 2: Hydrodynamic component orientation*

This step focuses on the orientation of hydrodynamic components, interpreted as the vertical angle relative to the flow direction. Each component's orientation must agree with the as-built drawings within a tolerance of the maximum between ±1° and ±3.5%, thus ensuring accurate gravity effects and natural circulation modelling.

*STEPS 3 - 4: Relevant elevation change and control point*

These steps address global elevation constraints. In STEP 3, the user identifies relevant elevation changes, defined as height differences that significantly influence thermal-hydraulic behaviour—such as those driving natural circulation by affecting the height between thermal centres. In STEP 4, control points are defined as minor elevation changes or geometric details that, while less impactful on system behaviour, must still be tracked. Acceptability criteria are set to ±0.5% for relevant elevation changes and ±1.0% for control points, relative to as-built references. If these limits are not met, components that previously passed local checks (i.e., in STEP 1) must be revised to meet global consistency.

*STEPS 5 - 6: Hydrodynamic component volume and local flow area / hydraulic diameter*

These steps focus on the local volume and hydraulic characteristics of the nodalized components. In STEP 5, the total free volume of each hydrodynamic component—including non-flowing regions—must agree with the as-built configuration within ±1.5%. In STEP 6, the local flow area and hydraulic diameter—defined as average values for each computational node—must fall within ±2% of the design specifications. Special considerations apply to vessel heads, where geometry may be difficult to characterize or approximated in STH codes. For such cases, the acceptance margin can be extended to ±5% for the average flow area, if STEP 5 is satisfied. Additionally, the hydraulic diameter may be adjusted to compensate for deviations from ideal cylindrical geometry.

*STEP 7: Hydrodynamic total volume of the nodalization*

Finally, this step defines a global constraint on the total volume of the entire nodalization. The summed volume of all components must agree with the value derived from engineering drawings within ±1%. If this criterion is not met, the user must revisit the modelling choices made in STEPS 1, 5, and 6 to reconcile the discrepancy and bring the overall nodalization into compliance.

### 2.2.2. Heat Transfer qualification

The thermal qualification of the nodalization includes both local and global checks to ensure that thermal masses and heat transfer surfaces are accurately represented. These verifications are based on detailed comparisons with the as-built documentation, including flanges, connections, instrumentation, and insulation.

*STEP 8: Thermal component mass*

This step addresses the mass of individual thermal components, which must correspond to the values derived from engineering drawings within a tolerance of ±2.5%. This mass should include not only the core structure of the component but also any attached elements that contribute to thermal inertia.

*STEP 9: Thermal component heat transfer surface*

This step focuses on the heat transfer surface area of each thermal component. Two levels of accuracy are specified: surfaces in direct contact with the main working fluid (e.g., water, steam, lead, or LBE) must be modelled within ±1.5% of the reference value, while surfaces exchanging heat with secondary media, such as ambient air, must be represented within ±5.0%.

*STEP 10: Thermal total mass of the nodalization*

This step introduces a global constraint on the total mass of the nodalization. The cumulative thermal mass must match the reference value from the as-built configuration within ±2.0%. If this criterion is not satisfied, the user must revise the thermal representation of one or more components previously assessed in STEP 8 to restore consistency.

*STEP 11: Total heat transfer surface of the nodalization*

This step imposes a global limit on the total heat transfer surface area of the nodalization. The aggregated surface area for components exchanging heat with the main fluid must be within ±1.0%, while that for components exchanging with external fluids must lie within ±4.0% of the reference values. Deviations beyond these limits necessitate revision of the modelling performed in STEP 9.

*STEP 12: Material properties*

The material properties used for thermal structures must be verified. These include the temperature-dependent functions for density, specific heat capacity, and thermal conductivity. The modeller is required to document the source of these data—such as bibliographic references, manufacturer datasheets, or other credible sources—and describe the method by which these properties have been implemented in the model.

### 2.2.3. Exceptions qualification

Certain components within the system cannot be fully characterized through standard geometric or thermal assessments, as their behaviour is strongly influenced by modelling choices and specific code implementations. These components must undergo a standalone qualification, in which their behaviour is validated under boundary conditions representative of the facility's actual operating conditions.

*STEP 13: Exceptions*

Typical examples of such components include control valves, where the correct representation of the flow coefficient (Cv) is critical; pumps, which require implementation of homologous performance curves; and non-conventional heat exchangers—such as air or oil coolers—that operate outside the standard water/steam

domain and thus require dedicated modelling. Additionally, large pools must be validated when thermal stratification or natural circulation mechanisms play a significant role in system behaviour. The results of these standalone assessments must confirm that the model adequately reproduces the expected component performance.

### *2.2.4. Testing qualification*

After successfully completing the first 13 qualification steps, the numerical model is tested by performing simulations representative of relevant experimental tests selected by the user.

*STEP 14: Code capabilities*

As a preliminary step in the testing phase, the user must identify the key thermal-hydraulic phenomena expected to occur during the operation of the system. Based on this list, the most relevant physical sub-models and empirical correlations required to represent these phenomena should be determined. The next step is to verify whether the selected thermal-hydraulic code includes appropriate models and correlations for these phenomena. Three possible outcomes may arise from this comparison:

- If a necessary sub-model or correlation is not implemented in the code, this constitutes a warning, indicating that the model may inadequately represent the system's behaviour.
- If the sub-model or correlation is implemented and its domain of validity includes the operating range of the facility, the model is expected to reliably reproduce the relevant physical behaviour.
- If the operating conditions lie outside the validated range of the code's implemented models or correlations, the simulation results may only partially reflect the actual system behaviour, and additional caution must be exercised.

In cases where such detailed assessment is not feasible, the user may alternatively apply a PIRT methodology to evaluate the adequacy of the code in addressing key physical processes.

*STEP 15: Steady-state test*

The user must select a relevant steady-state test case, preferably one representing nominal operating conditions of the facility, from the available experimental dataset. The goal is to evaluate the code’s capability to reproduce key system parameters under steady-state conditions. The acceptance criteria for the nodalization should be defined by the user but must meet at least the following minimum standards—assuming appropriate instrumentation is available:

- The overall thermal power balance must be captured within ±2.0%, or within the experimental uncertainty if this exceeds 2%.
- Measured temperatures must be reproduced within ±3 °C, or within the associated experimental uncertainty if higher.
- Measured flow rates must fall within ±6% of experimental values, unless larger uncertainties are reported.
- Measured pressures must be captured within ±0.1%, or within experimental uncertainty if larger.

These acceptance bands serve as general guidance and may be adapted on a case-by-case basis depending on the facility characteristics and test quality.

*STEP 16: Transient test*

In addition to steady-state validation, the user must select a representative transient test case—such as a start-up or shutdown procedure—from the experimental database. The objective is to verify the model's ability to reproduce dynamic system behaviour during operational transients. The criteria for acceptance must be defined by the user and tailored to the specifics of the selected transient. Comparisons should focus on time-dependent parameters such as temperatures, pressures, flow rates, and timing of system responses. A combination of qualitative trend matching and quantitative error metrics is encouraged to comprehensively evaluate the model's performance.

### *2.2.5. Heat Losses assessment*

Heat losses represent a critical aspect in accurately modelling the thermal behaviour of experimental facilities. However, their quantification and representation in system codes are subject to significant uncertainties, stemming from several contributing factors. These include variations in ambient environmental conditions over different timescales (daily, seasonal), non-uniform distribution of insulation materials around components, the presence of thermal bridges at structural supports, and the influence of geometrical features—such as chimney-like effects—on convective heat transfer. Additionally, minor undetected leaks or other unidentified sources may contribute to discrepancies in the heat balance.

*STEP 17: Heat losses assessment*

Considering these challenges, it is considered acceptable that the nodalization reproduces the total heat losses under steady-state conditions within a tolerance of ±10% relative to experimentally measured values. This allowance reflects the practical limitations of modelling real-world thermal losses while maintaining an adequate level of accuracy for system-level simulations.

The procedure is fully summarized in Table 2.

***Table 2 Procedure for qualification of STH code nodalization***

| STEP | Category | Item | Description | Additional note |
|---|---|---|---|---|
| **1** | Hydraulic | Hydrodynamic component length | Acceptability: ±50% of unitary node length | Compare to AB drawing |
| **2** | | Hydrodynamic component orientation | Acceptability: max [±1°; ±3.5%] | Compare to AB drawing |
| **3** | | Relevant elevation change | Define relevant elevation changes. Acceptability: ±0.5% | Relevant elevation changes have to be defined by the user of this procedure in order to be applied at proper locations. Compare to AB drawing |
| **4** | | Control point | Define other elevation changes acceptability ±1% | Compare to AB drawing |
| **5** | | Hydrodynamic component volume | Acceptability: ±1.5% | Compare to AB drawing |
| **6** | | Hydrodynamic component node flow area / hydraulic diameter | Acceptability: ±2% ±5% for special cases | Compare to AB drawing |
| **7** | | Nodalization total volume | Acceptability: ±1% | Compare to AB drawing |
| **8** | Heat Transfer | Thermal component mass | Acceptability: ±2.5% | Compare to AB drawing |
| **9** | | Thermal component HT surface | Acceptability: ±1.5% / ±5.0% | Compare to AB drawing |
| **10** | | Nodalization total mass | Acceptability: ±2.0% | Compare to AB drawing |
| **11** | | Nodalization total HT surface | Acceptability: ±1.0% / ±4.0% | Compare to AB drawing |
| **12** | | Material properties | Provide reference | Conductivity, density and heat capacity need to be referenced |
| **13** | Exceptions | Standalone qualification | Qualify special components | Procedure for standalone qualification is defined by the user. The list currently includes control valves, pumps, non-conventional heat exchanger, large pool |
| **14** | Testing | Code capabilities | Define the relevant | Validation range of correlations needs to be checked against the |

| | | | | |
|---|---|---|---|---|
| | | | phenomena and compare to the correlations adopted in the code | range addressed in the model. If an important correlation is applied out of range or is not implemented in the code has to be stated at this step |
| **15** | | Check steady state | Define a steady state case of relevance and check relevant parameters against experiment | Acceptability according to a minimum set of parameters provided |
| **16** | | Check transient | Define a transient case of relevance and check relevant parameters against experiment | Acceptability is user defined |
| **17** | Heat Losses test | Heat Losses | Heat Losses acceptability: ±10%. Check against experiment | -- |

## 2.3. Computer codes

This section presents the computational tools employed throughout the TH investigations conducted in this research. Three primary codes were used: RELAP5, a well-established STH code used for transient and steady-state analysis of nuclear systems; ANSYS-CFX, a high-fidelity CFD tool suited for detailed local flow and heat transfer analysis; and DASSH, a subchannel analysis code specifically developed for advanced reactor cores. Each code was selected based on its capabilities, validation status, and applicability to specific modelling tasks, ranging from system-level safety analysis to component-level qualification and subchannel behaviour. The following subsections provide a brief overview of these tools and their roles within the research framework.

### *2.3.1. RELAP5*

RELAP5 (Reactor Excursion and Leak Analysis Program) [33] is a well-established STH code developed at the Idaho National Laboratory (INL) for the U.S. Nuclear Regulatory Commission (NRC). Originally designed to simulate transients in LWRs, RELAP5 has evolved into a highly versatile tool widely used in both industry and research for the best-estimate simulation of normal and off-normal conditions in nuclear power plants. The code is the result of decades of continuous development, benchmarking, and validation through international collaboration and is still assessed and improved by numerous institutions worldwide.

RELAP5 is primarily written in FORTRAN 77 and is based on a one-dimensional, non-homogeneous, and non-equilibrium two-phase flow model. It solves the conservation equations of mass, momentum, and energy for both liquid and vapor phases using a semi-implicit finite difference method. The steam phase may contain a non-condensable gas component, which is treated as being in thermal and mechanical equilibrium with the vapor, allowing the simulation of steam–gas mixtures relevant to various accident scenarios.

The hydraulic domain is discretized into control volumes, which represent homogeneous fluid zones, connected by junctions where fluid flow occurs. Scalar quantities (pressure, density, internal energy, void fraction) are calculated at the centre of control volumes, while vector quantities (velocity) are calculated at the junctions. The spatial arrangement accounts for 1D conservation laws, with limited treatment of gravity effects in vertical segments—often referred to as a “1.5D” modelling approach. RELAP5 includes specific models for form losses, choked flow, area changes, phase separation, non-condensable gas transport, and boron tracking, among others.

Heat transfer is modelled through one-dimensional heat structures, which simulate conduction across solid walls and convective heat exchange with adjacent fluid volumes. Typical applications include the modelling of fuel rods, pipe walls, and heat exchanger surfaces. The user defines thermal coupling between fluid volumes and solid regions, selecting from predefined convective boundary conditions that reflect the hydraulic geometry and flow regime.

RELAP5 includes a point neutronic kinetics model, enabling coupled NK-TH simulations, especially relevant for reactivity-initiated transients. The code can simulate a wide range transients, including, but not limited to, Loss Of Coolant Accident (LOCA), Anticipated Transient Without SCRAM (ATWS), Station Black Out (SBO), and Loss Of Heat Sink (LOHS) scenarios.

The numerical scheme employs a user-defined initial timestep, which is adaptively reduced during the simulation to ensure convergence. If convergence cannot be maintained below a minimum threshold, the code terminates the calculation. The structured modelling approach used in RELAP5 allows for modular system representation, which is crucial in large-scale simulations of complex facilities or advanced reactor designs.

Although it was originally developed for LWRs, RELAP5 has been successfully applied to non-LWR systems. The version of RELAP5/Mod3.3 employed in this research has been specifically modified to incorporate the thermophysical properties of HLM [34], namely pure lead and LBE, along with the corresponding state-of-the-art heat transfer correlations [35]. The newly heat transfer correlations for HLM implemented in RELAP5 are Seban-Shimazaki [36] suitable for pipe internal flows and Mikityuk [37] suitable for tube bundles.

These enhancements were introduced to improve the code's applicability and accuracy in simulating LFR systems and experimental facilities operating with HLM coolants. The modified version has been successfully applied in both post-test analyses and benchmarking exercises [38], demonstrating its capability to accurately reproduce the main thermal-hydraulic phenomena observed during experiments involving liquid lead and LBE. In particular, the code has shown good agreement with experimental trends for key operating parameters, confirming its reliability and predictive capabilities under conditions relevant to advanced reactor designs.

### *2.3.2. ANSYS-CFX*

ANSYS CFX [39] is an advanced CFD software developed by Ansys Inc., renowned for its reliability and precision in simulating complex fluid dynamics and heat transfer processes. Its capabilities make it particularly suitable for nuclear engineering applications, where it is employed to analyse coolant flow patterns, thermal mixing, and heat transfer under both steady-state and transient conditions. CFX has been widely adopted in both industrial and academic contexts, especially in projects involving HLM systems and innovative reactor concepts.

The software uses a cell-vertex, mixed finite volume/finite element approach to solve the full Navier-Stokes equations in three dimensions. It supports simulations using structured or unstructured meshes, making it highly adaptable to intricate geometries. For time-dependent problems, CFX implements an implicit time integration scheme, ensuring numerical stability even for small timesteps. Its coupled solver approach, combined with false timestep algorithms and preconditioning techniques, allows for efficient and fast convergence.

A key advantage of CFX is its advanced turbulence modelling capability. It supports various models such as Reynolds-Averaged Navier-Stokes (RANS), Large Eddy Simulation (LES), and Detached Eddy Simulation (DES), enabling the accurate simulation of turbulent flows. Furthermore, CFX includes multiphase flow models, which are essential for nuclear systems that involve gas-liquid interactions or immiscible fluids like lead and water. Heat transfer is modelled through conduction, convection, and radiation, with built-in boundary condition models adapted to diverse flow regimes.

CFX is also fully integrated with the broader Ansys simulation environment, allowing for multiphysics simulations in combination with tools like Ansys Mechanical. This integration enables Fluid–Structure Interaction (FSI) analyses, where mechanical deformation due to fluid forces and thermal stresses is taken into account. The software includes user-friendly tools for geometry preparation, mesh generation, result visualization, and process automation through scripting.

Thanks to its computational efficiency, parallel processing capabilities, and extensive library of physical models, ANSYS CFX is a powerful and versatile tool for detailed thermal-hydraulic analyses. It is particularly valuable in the design and safety assessment of nuclear components operating under demanding conditions, such as those found in LFRs.

### *2.3.3. DASSH*

DASSH (Ducted Assembly Steady-State Heat transfer) [40] is a computational tool developed at Argonne National Laboratory (ANL) for performing steady-state thermal-fluid analyses of reactor cores composed of ducted, hexagonally gridded assemblies. The software is specifically designed to provide efficient and reasonably accurate assessments of pressure drops and temperature distributions in the coolant, duct walls, and fuel pins, based on user-defined mass flow rates and power profiles. DASSH is intended to support the early design phase of reactor systems, particularly when detailed geometrical specifications are not yet finalized. Its intermediate-fidelity modelling framework allows for rapid thermal-hydraulic assessments with relatively low computational cost, while still capturing the dominant heat transfer phenomena relevant to ducted assemblies.

Each assembly is divided into subchannels, representing the fluid regions bounded by fuel pins and structural walls. The tool applies an energy balance formulation to determine coolant temperatures within each subchannel, relying on empirical correlations for friction and turbulent mixing. Rather than solving the full coupled momentum and energy conservation equations, DASSH employs approximations that reduce computational effort while preserving the key physical behaviour. The axial heat transfer is treated through forced advection, while radial transport is modelled using a modified conduction term that accounts for turbulence-induced mixing, particularly in wire-wrapped fuel bundles.

The core thermal power distribution is provided either by polynomial user input or generated internally based on axial profiles assigned to each pin and subchannel. The user specifies the coolant inlet temperature and either the mass flow rate or the temperature rise across each assembly. With these inputs, DASSH calculates the resulting temperature distributions in the coolant and structural components.

Heat transfer between coolant and duct walls occurs via convection and conduction. Radial energy transport between subchannels is handled using enhanced thermal diffusivity, derived from geometry- and flow-based mixing correlations. Axial conduction is neglected, with the assumption that axial heat transfer is dominated by advection. To solve the energy equation, DASSH uses a forward-difference marching scheme along the axial direction, where the temperature at each axial plane depends solely on the upstream plane. The duct wall temperature is lagged by one axial step to decouple assemblies and avoid the need for a global solution algorithm. While simple and computationally efficient, this scheme imposes a constraint on the axial mesh resolution to ensure numerical stability.

The physical model assumes a steady-state, incompressible fluid with homogeneous and isotropic thermophysical properties. The effects of compressibility, viscosity, and gravity are neglected. Heat conduction through the wire-wrap and across solid pin-to-pin interfaces is also omitted, as their influence is considered secondary in the context of subchannel-level modelling.

# 3. ANALYSES TO SUPPORT THE DEVELOPMENT OF ALFRED

ALFRED (Advanced Lead Fast Reactor European Demonstrator) has emerged as a key reference design for future fast reactor demonstrators [41]. Its main goal is to demonstrate both the technical feasibility and economic viability of LFRs, serving as a critical milestone toward the commercial deployment of Generation IV nuclear systems. ALFRED addresses essential challenges including material corrosion resistance, fuel cycle optimization, and the implementation of passive safety systems, embodying the core principles of sustainability, safety, and innovation that define Generation IV designs.

The conceptual design of ALFRED was initially developed under the LEADER project (Lead European Advanced DEmonstrator Reactor) [42] within the European 7th Framework Programme (FP7), leveraging extensive research activities and collaborative efforts supported by the European Commission. Recently, ALFRED reactor has been revised through a collaborative effort within FALCON (Fostering ALFRED CONstruction), a consortium of European institutions that includes ANSALDO NUCLEARE, ENEA, and RATEN ICN [43].

Both conceptual scheme of LEADER and FALCON configurations of ALFRED are depicted respectively in Figure 9 and Figure 10.

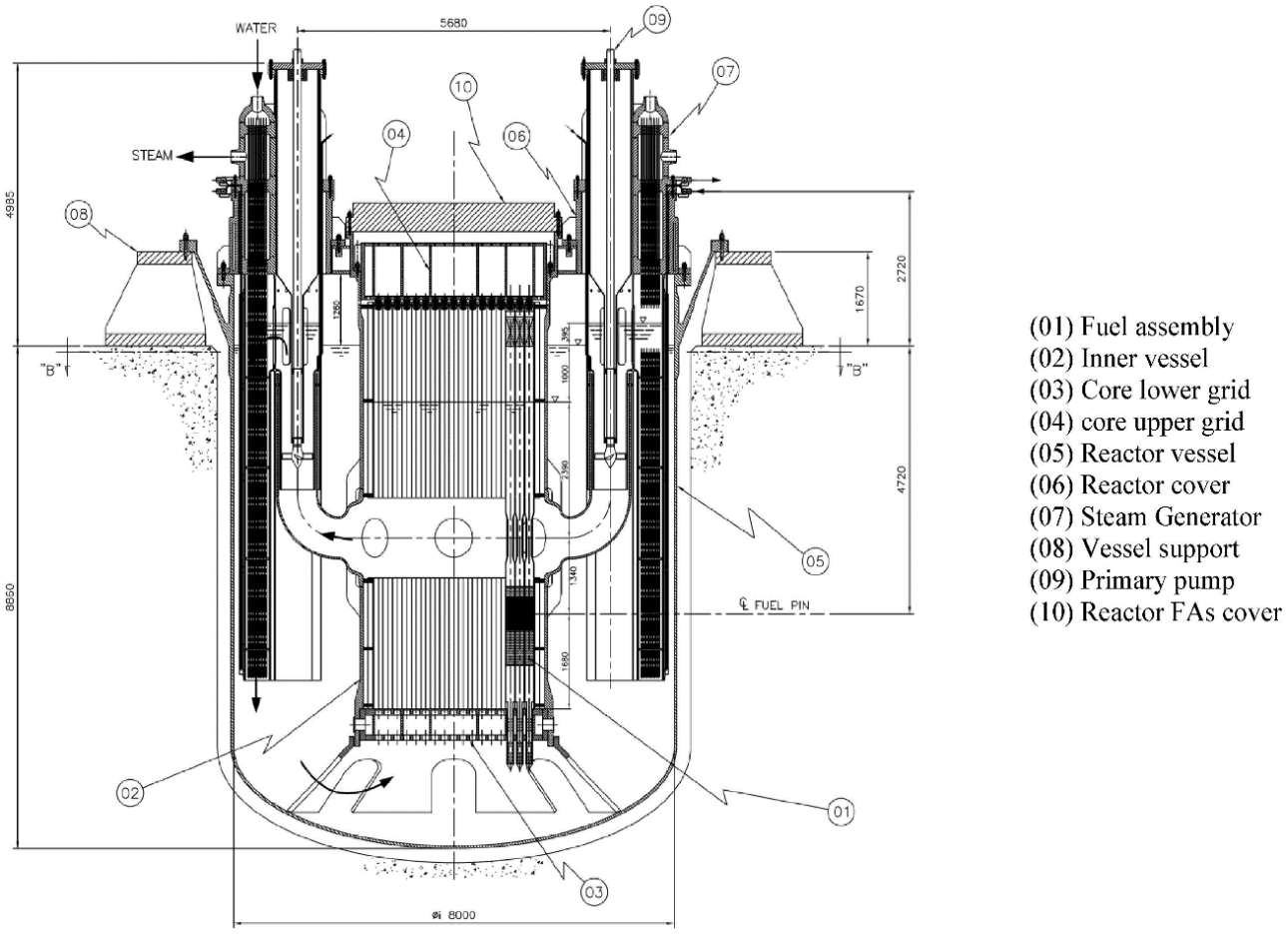


***Figure 9 ALFRED layout LEADER version [42]***

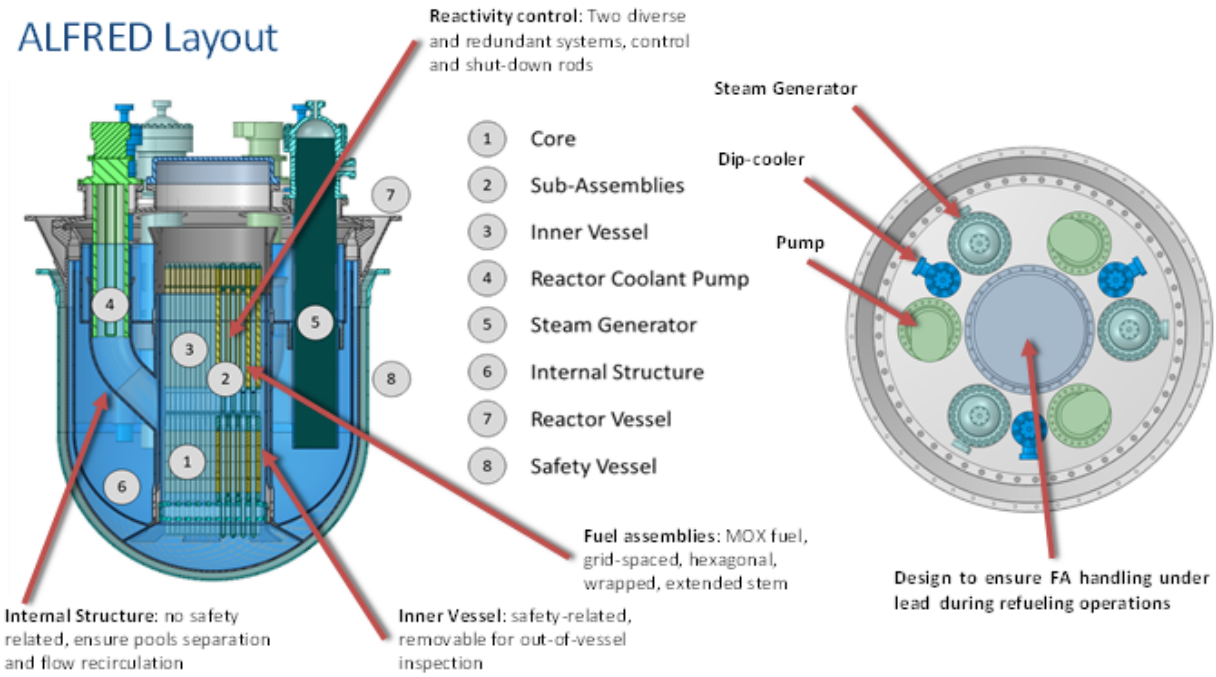


*Figure 10 ALFRED layout FALCON version [43]*

## 3.1.Reactor design overview

One of the leading concepts in the development of LFR technology is ALFRED depicted in Figure 11 [44].

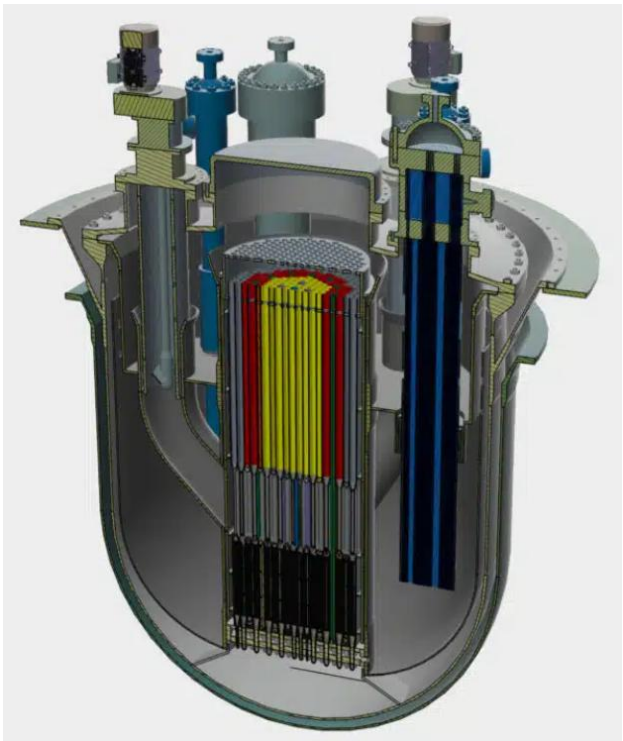

*Figure 11 RCS of ALFRED scheme [44]*

To pursuit the main target of ALFRED reactor, a staged approach summarised in Table 3 is foreseen in order to progressively gain operating experience and face validation issues [44].

***Table 3 ALRED main parameters in the stages of operation [44]***

| Parameter | Unit | STAGE 0 | STAGE 1 | STAGE 2 | STAGE 3 |
|---|---|---|---|---|---|
| **Core inlet temperature** | °C | 390 | 390 | 400 | 400 |
| **Core outlet temperature** | °C | 390 | 430 | 480 | 520 |
| **Core thermal power** | MW | 0 | 100 | 200 | 300 |
| **Steam line pressure** | bar | / | 170 | 175 | 180 |
| **Steam line temperature** | °C | / | 420 | 435 | 450 |

The concept involves commencing operations at low power and temperature, gradually ramping up both using the reactor itself to validate subsequent operational phases and the concurrent advancement of the R&D program. Three power levels are foreseen (100, 200, and 300 $MW_{th}$), at constant primary flow rate and increasing temperature. The RCS is composed of key components, including the reactor core, 3 RCPs and 3 SGs.

The FALCON design foresees an Internal Structure (IS, depicted in green in Figure 12) incorporated within the Reactor Vessel (RV) to direct the cold lead from the SG towards the lead-free level [45]. From there, the lead flows through openings in the IS and descends through the annular space between the IS and the RV before entering the core.

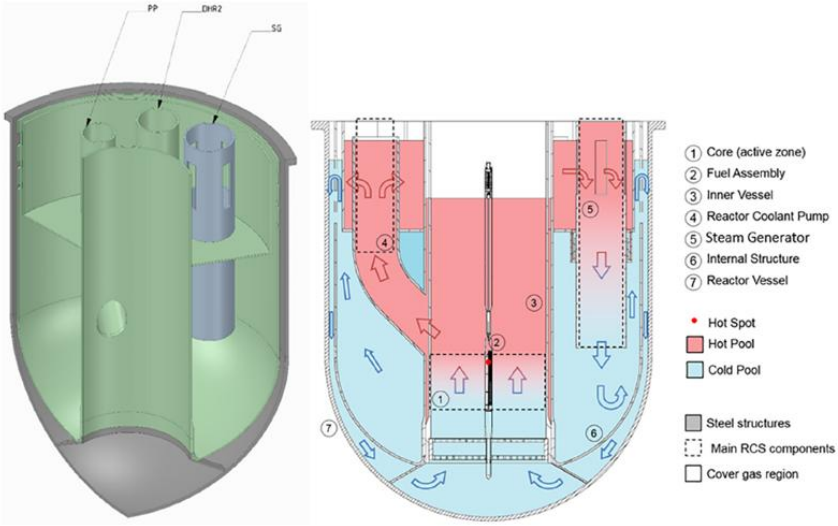


***Figure 12 Internal view of the ALFRED revised configuration and sketch of the primary flow path [45]***

This flow arrangement prevents coolant stagnation in the upper pool region under both forced and natural circulation, mitigating thermal stratification. In the event of a SGTR, steam is carried along the primary flow path to the free surface and discharged into the cover gas system, preventing water ingress into the reactor core which could result in a reactivity insertion due to the water moderation and lead density variations effects. Finally, a Hot Pool (HP) has been introduced in the upper region to separate the RCPs from the SGs, enhancing lead distribution at the SG inlet [45]. The main geometrical data of the RV and IS are summarised in Table 4 [44].

*Table 4 RV and IS geometry [44]*

| Parameter | Value | Unit |
|---|---|---|
| **Inner diameter** | 8300 | mm |
| **Height** | 10000 | mm |
| **Vessel thickness** | 50 | mm |
| **RV-IS gap** | 150 | mm |
| **IS thickness** | 50 | mm |
| **IS-HP gap** | 150 | mm |
| **Material** | AISI-316L | - |
| **Corrosion protection measure** | Oxygen control | - |

While maintaining several of the main geometrical parameters of the previous core configuration [46], the new design introduces several adjustments aimed at improving neutronic and thermal-hydraulic performance and enabling in-core testing. The revised core, illustrated in Figure 13 consists of 134 Fuel Assemblies (FAs) [47]. The active region is divided into two zones: the inner and outer regions, containing 56 and 78 FAs, respectively. The inner region has MOX with an enrichment of 20.5 wt. % in PuO1.97 while the outer region is enriched to 26.2 wt.%.

The chosen concentrations and zoning guarantee operability in a 5-batches strategy with a criticality swing during a 1-year long equilibrium irradiation sub-cycle equal to 2200 pcm (STAGE 3). 126 fuel pins are arranged in a hexagonal wrapper to make up the FA [48], around a central position hosting a dummy pin for additional in-core instrumentation. FAs are surrounded by 102 Dummy Assemblies (DAs), arranged in two concentric rings.

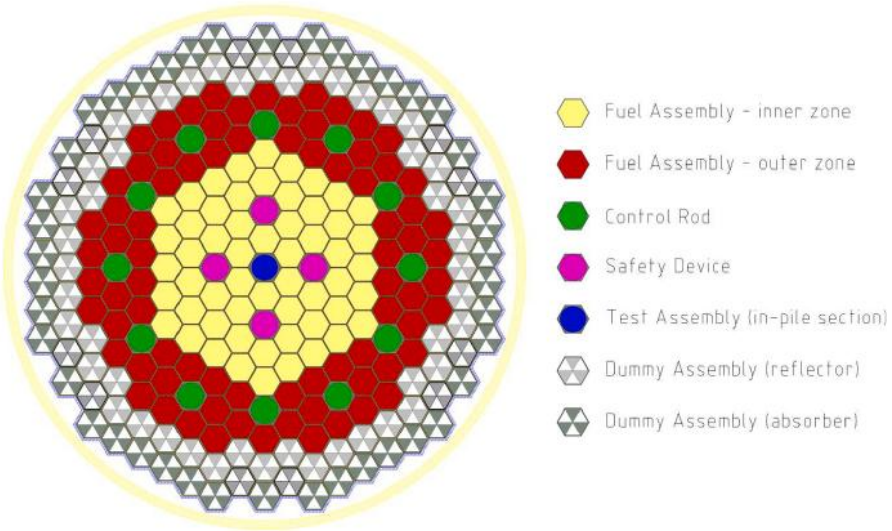


*Figure 13 ALFRED core [47]*

The inner ring serves to reflect leaking neutrons back into the core, while the outer ring provides radiation shielding for the inner vessel. The core central position is dedicated to in-pile irradiation experiments, allowing the testing of fuel assemblies and materials to be used in subsequent stages under neutron irradiation at temperature conditions representative of future stages. The control and shutdown functions are ensured by 12 Control Rods (CRs) and 4 Safety Devices (SDs).

Table 5 presents the power peaking factors at the Beginning and End of an equilibrium sub-Cycle (BoC and EoC, respectively) for the newly implemented configuration. In the table, both the FA Distribution Factor (FADF) and the Fuel Pin Distribution Factor (FPDF) are reported. The former relates to the power distribution across the entire core on an assembly-by-assembly basis, while the latter details the power distribution within the hottest assembly of the inner and outer zones on a pin-by-pin level. Finally, the axial profile peak factor is also included in Table 5. The table also highlights the shift of the peak FADF from the inner to the outer zone, influenced by the partial insertion of the control rods at BoC.

***Table 5 Power distribution factors at BoC and EoC for the two fuel zones [47]***

| **Power distribution factors** | **Inner zone** | | **Outer zone** | |
|---|---|---|---|---|
| | BoC | EoC | BoC | EoC |
| **Core wise – assembly by assembly (FADF) (A)** | 1.292 | 1.162 | 1.154 | 1.164 |
| **Assembly – wise pin by pin (FPDF) (B)** | 1.011 | 1.012 | 1.057 | 1.059 |
| **Core – wise pin by pin (A*B)** | 1.306 | 1.175 | 1.219 | 1.232 |
| **Pin – wise axial (C)** | 1.168 | 1.157 | 1.240 | 1.172 |
| **Total peaking factor (A*B*C)** | 1.526 | 1.360 | 1.512 | 1.445 |

The core is hosted inside the inner vessel (IV), whose functional requirement is to support and restraint the core, maintaining its geometry for criticality purposes. The pin is made of a stack (810 mm tall) of fuel pellets. Moreover, fuel pins are hollowed in order to decrease the thermal gradient, to mitigate the maximum fuel temperature and to accommodate the fuel swelling expected at the design burnup of 100 MWd/kgHM. The geometry of the fuel pin and the FA is shown in Figure 14.

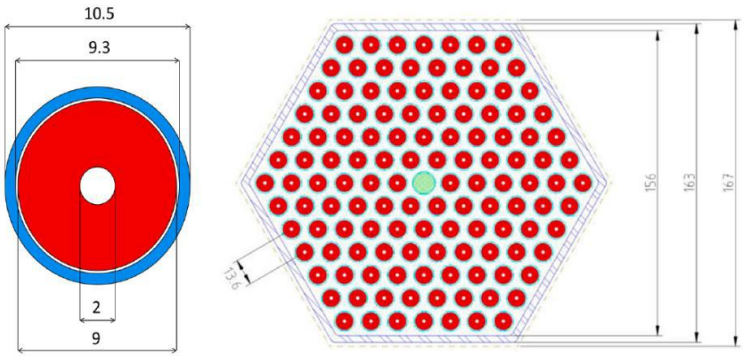


***Figure 14 Fuel Pin and Fuel Assembly sketch [44]***

The SGs adopt Bayonet Tubes (BTs), with an active length of 6 meters, designed to interface the RCS with the secondary system.

A system of coaxial tubes is employed to ensure efficient heat transfer. The feedwater supplied from the Balance of Plant (BoP) flows downward through the innermost tube, which crosses the steam header, until it reaches the bottom, where the third tube is sealed by a welded hemispherical end cap. From this point, the water ascends through the annular region formed between the second and third concentric tubes. As it rises, it removes heat from the surrounding liquid lead in a purely counter-current configuration, maximizing heat transfer efficiency.

Earlier SG configuration featured a double-walled external tube structure to minimize the risk of direct interaction between water and lead in the event of a SGTR [42]. This design aimed to prevent reactivity insertion accidents caused by neutron moderation from water droplets or steam bubbles entering the core. However, despite its safety benefits, the simultaneous failure of both tube walls, although highly unlikely, could not be entirely excluded.

In the current design, this safety function has been transferred to IS, which forces the lead to rise to the free surface level before returning to the core. This arrangement ensures that any water or steam entering the system is effectively purged into the cover gas space, enhancing safety. Additionally, the removal of the double-walled tubes significantly improves the thermal performance of the steam generator, leading to higher efficiency and simpler construction. The ALFRED SG drawings is depicted in Figure 15.

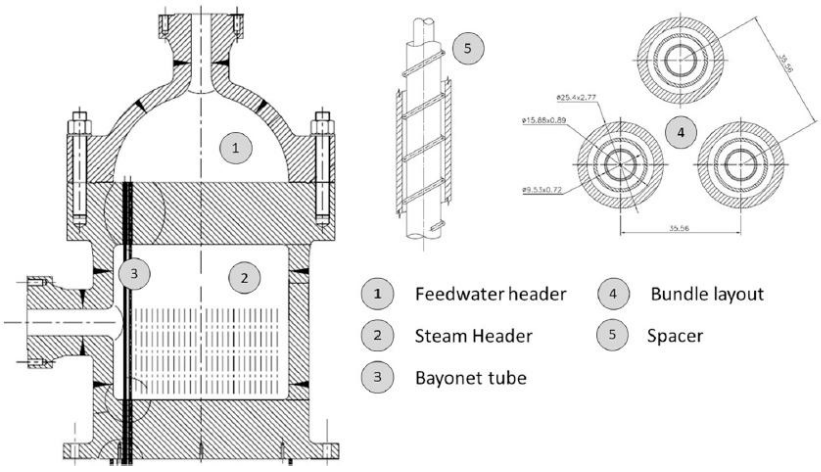


***Figure 15 ALFRED SG details [44]***

The RCP is hosted in a duct of the IS connecting the core outlet plenum with the HP and thus experiences highest reactor temperatures. In addition, the operating conditions of the component entail high speeds and variations in the momentum of the fluid, thus requesting protection methods against both corrosive and erosive attack by molten lead. The RCP does not suffer from thermal gradients and is not subject to neutron irradiation during operation. the installation of the component in the ducts of the IS guarantees simplicity in the extraction, which might be anticipated to be more frequent than other components due to the severe operating conditions related to the impeller material. The main parameters of the ALFRED RCP are shown in Table 6 [44].

*Table 6 ALFRED RCP main data [44]*

| Parameter | Value | Unit |
|---|---|---|
| **Nominal flow rate** | 1908 | $m^3/h$ |
| **Nominal head** | 1.5 | m |
| **Specific speed** | 2.97 | - |
| **Minimum / Maximum flow rate** | 900/1980 | $m^3/h$ |
| **Pump type** | Axial/mixed flow | - |
| **Rotational speed** | 289 | rpm |
| **Hydraulic efficiency** | 73 | % |
| **Power supply** | 108.15 | kW |
| **Motor supply** | 200 | kW |

Finally, the passive Decay Heat Removal (DHR) system (category D according to [49], see Figure 16) is composed of 3 loops connected to the SGs and removes decay heat from the primary coolant thanks to dedicated heat exchangers (Isolation Condensers, ICs). In the event of a loss of heat sink, the DHR system ensures that the primary coolant temperatures remain within acceptable limits. In the FALCON design, Non-condensable Gases (NGs) are introduced to passively reduce the power removed by the DHR system [50]. This new configuration includes a nitrogen tank connected to the IC, improving power removal and delaying coolant freezing in the long term after a generic postulated initiating event. The system operates in a way that limits the depressurization rate, thereby delaying primary coolant freezing. The main data of the IC are reported in Table 7.

*Table 7 IC reference data [50]*

| Parameter | Value | Unit |
|---|---|---|
| **Number of tubes** | 16 | - |
| **Inner diameter** | 32.1 | mm |
| **Outer diameter** | 38.1 | |
| **Length** | 2000 | mm |
| **Headers outer diameter** | 560 | mm |
| **Headers thickness** | 60 | mm |
| **Material** | Inconel 600 | - |

If an initiating event inhibits normal heat removal from the primary coolant, the DHR intervenes, starting with the closure of feedwater and steam-line isolation valves. With the fluid now confined and continuously absorbing heat, it begins to boil, leading to a gradual increase in pressure. Once the pressure reaches approximately 190 bar, the safety system inlet valve opens, allowing steam to be vented into the IC.

During the initial phase of this transient, the pressure of the steam exceeds that of the non-condensable gases, pushing the nitrogen into its dedicated tank connected to the lower head of the IC. Meanwhile, the steam passing through the IC condenses, forming a water level inside the condenser. When the IC downstream valve is subsequently opened, the condensate returns to the SG by gravity, thus establishing natural circulation. In this loop, water absorbs decay heat from the lead within the SG, exits, and then condenses again in the IC, completing the passive heat removal process.

As time progresses, decay heat decreases, and the power removed by the IC may exceed the heat supplied by the SG, resulting in a gradual depressurization of the system. When the steam partial pressure drops below the partial pressure of the non-condensable gases, these gases begin to expand and migrate back into the IC. The presence of non-condensable gases reduces heat transfer efficiency, thereby decreasing the thermal power removed by the IC and slowing the depressurization rate.

The system is specifically designed to maintain a minimum pressure of at least 123 bar, corresponding to the saturation pressure at the lead freezing temperature. This ensures that the liquid lead does not solidify. Additionally, an orifice placed downstream of the bottom isolation valve in the safety system is engineered to maintain a liquid water column in the piping below the IC, thus limiting nitrogen ingress into the SG.

The hydraulic diameter of this orifice (10 mm) was optimized through detailed sensitivity analyses to ensure reliable natural circulation flow. It is important to note that condensation within the IC occurs at the water's partial pressure, which depends on the local concentration of nitrogen in the condenser bundle, further affecting the overall heat removal performance.

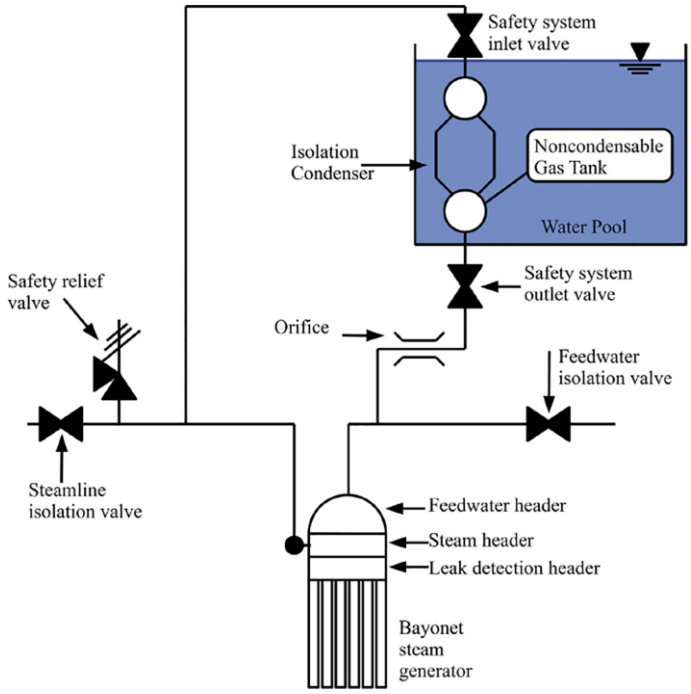


***Figure 16 DHR layout [50]***

## 3.2. PIRT analysis

In the framework of the European project ANSELMUS [51], specifically within Work Package 1, Task 1.1, a PIRT analysis was conducted for the ALFRED reactor. The starting point is based on Ref. [52] by defining a well-characterized reference design configuration and systematically partitioning the system into its key components to enable focused evaluation of safety-relevant phenomena. The components constituting ALFRED partitioning are Core, Reactor Vessel, Steam Generator, Primary Coolant and DHR.

Next, a set of representative accident scenarios was then selected, reflecting the most critical events that could challenge the reactor's integrity and operational safety. Specifically, three main transients were identified: Steam Generator Tube Rupture (SGTR), Core Compaction (CC), and Internal Structure Failure (ISF). These events were selected on the basis of engineering judgement so to include in the PIRT discussion most of the expected physical phenomena, possibly simplifying the identification of those having lower knowledge. Each scenario was systematically dissected into distinct phases, and corresponding Figures of Merit (FoMs) were established to guide safety assessments.

The SGTR scenario involves a single tube rupture leading to the injection of steam (in choked flow conditions) at high pressure into the primary lead circuit. Assuming a break located in the lower part of the tube, the escaping water discharges through both the downcomer tube and the steam riser, with internal structures preventing steam entrainment into the core and instead directing it toward the cover gas. This transient was divided into three phases: the initial critical flow discharge phase, the transport of steam to the cover gas and subsequent pressurisation of the expansion volume, and the long-term condition in which the system stabilises under passive cooling via the DHR system. Critical phenomena considered included steam-lead interaction, precipitation of lead oxides, chemical and mechanical effects, and eventual steam condensation and fission product stripping. The associated FoMs focused on maintaining the integrity of the primary system barrier and controlling the transport of radioactive material beyond the reactor coolant system.

In the CC scenario, an earthquake-induced uniform reactivity insertion of 250 pcm over 10 seconds leads to an increase in core power. The event phases encompass the initial rapid reactivity rise and local thermal maxima, the intermediate transition toward a new equilibrium between power production and removal, and the final long-term steady-state until operator intervention. The FoMs for this event targeted the maximum fuel temperature relative to melting thresholds and the time-to-rupture of cladding, defining crucial safety limits to prevent fuel damage.

The ISF scenario envisages a break in pump ducting, causing a low-pressure, high-temperature suction area to communicate with the high-pressure, low-temperature cold pool. The resulting influx of cold lead into the pump duct induces complex flow redistribution: part of the flow bypasses the core, reducing core cooling, while another portion is redirected through intact loops. This transient involves an initial forced flow reduction phase, a subsequent transition marked by oscillatory flow behaviour as the system shifts to natural circulation, and a final long-term phase where decay heat is passively removed by the DHR system. Key FoMs for this scenario included cladding integrity and overall primary system barrier integrity.

Following the identification of scenarios and FoMs, a comprehensive mapping of relevant physical phenomena was carried out. The careful integration of these phenomena into the PIRT framework allowed for a robust prioritization of safety issues, ultimately guiding the definition of future experimental investigations, model development needs, and targeted validation activities for ALFRED’s design evolution.

The extensive PIRT analysis process culminated in the consolidation of expert evaluations into a clear and comprehensive consensus regarding the phenomena most critical to ALFRED's safety under the examined accident scenarios. Through iterative discussions, numerical studies, and engineering judgement, the panellists reached unanimous agreement on the relative IMP and SOK associated with each phenomenon. This consensus is meticulously summarized and documented in Table 8, Table 9 and Table 10, which respectively present the ranked lists for the SGTR, CC, and ISF events. The prioritization reflected in these tables provides a robust foundation for guiding targeted experimental campaigns, refining numerical models, and defining future R&D priorities.

***Table 8 SGTR PIRT results***

| Component | Phenomenon | IMP | | | SOK |
|---|---|---|---|---|---|
| | | I | II | III | |
| Core | Oxides precipitation | | M | | M |
| | Convection heat transfer | L | M | M | M |
| | Gap conductance between fuel and cladding | L | L | L | M |
| | Clad conductivity | L | L | L | M |
| | Fuel thermal properties | L | L | L | M |
| | Fuel mechanical properties | L | L | L | M |
| | Decay heat | | | M | H |
| | Fission reaction | L | | | H |
| | Doppler effect | L | | | H |
| | Coolant density reactivity feedback | L | | | M |
| | Core geometry reactivity feedback | L | | | M |
| | Pressure losses | L | L | M | M |
| Reactor Vessel | Pressure losses | L | L | M | M |
| Steam Generator | Flashing | M | | | M |
| | Direct interphase heat transfer (between water & steam) | L | | | M |
| | Direct contact heat transfer between the two fluids | M | | | M |
| | Rise and propagation of pressure waves | M | | | H |
| | Mechanical Stresses | M | | | M |

| | | | | | |
|---|---|---|---|---|---|
| | Choked flow | M | | | H |
| | Pressure losses | M | L | L | M |
| **Primary Coolant** | Primary coolant freezing (blockage and volumetric variation) | L | | | M |
| | Build-up of metal oxides debris | L | | | M |
| | Oxides precipitation | L | | | M |
| | Chemical interactions | | H | | L |
| | Steam entrainment and transport in liquid lead | | M | | M |
| | Steam + Fission Product interaction | M | M | L | M |
| | Polonium trapping | M | M | M | M |
| **DHR** | Heat transfer | | | M | M |
| | Condensation | | | M | M |
| | Condensation with non-condensable gases | | | M | M |
| | Pool Boiling (inside tubes) | | | L | M |
| | Pressure losses | | | H | H |

***Table 9 CC PIRT results***

| **Component** | **Phenomenon** | **IMP** | | | **SOK** |
|---|---|---|---|---|---|
| | | **I** | **II** | **III** | |
| **Core** | Chemical Fission Gas mass transfer | | | L | L |
| | Corrosion material on the cladding | | | M | L |
| | Retention of volatile fission products | | | L | M |
| | Hydraulic fission Gas mass transport | | | L | M |
| | Convection heat transfer | M | M | M | M |
| | Gap conductance between fuel and cladding | M | L | L | M |
| | Clad conductivity | L | L | L | M |
| | Fuel thermal properties | H | H | H | M |

| | | | | | |
|---|---|---|---|---|---|
| | Fuel mechanical properties | M | M | L | M |
| | Decay heat | | | M | H |
| | Fission reaction | M | | | H |
| | Doppler effect | M | M | | H |
| | Coolant density reactivity feedback | M | M | | M |
| | Core geometry reactivity feedback | M | M | | M |
| | Fuel/Clad melt and relocation reactivity feedback | H | H | | M |
| | PCMI (Pellet-Cladding Mechanical Interaction) | H | H | | M |
| | Fission gas release mechanism | M | L | | M |
| | Pressure losses | L | L | L | M |
| **Reactor Vessel** | Corrosion material | | L | | M |
| | Liquid Metal Embrittlement | | L | | M |
| | Creep effect | | L | L | M |
| | Pressure losses | L | L | L | M |
| **Steam Generator** | Pressure losses | L | L | | M |
| **Primary Coolant** | Convection heat transfer | L | | | M |
| | Hydraulic fission gas mass transport | | | L | L |
| | Chemical fission gas mass transport | | | L | M |
| | Retention of volatile fission products | | | L | M |
| | Polonium trapping | L | L | L | M |
| | Coolant fuel interaction | L | L | L | L |
| **DHR** | Heat transfer | | | M | M |
| | Condensation | | | M | M |
| | Condensation with non-condensable gases | | | M | M |
| | Pool Boiling (inside tubes) | | | L | M |
| | Pressure losses | | | H | H |

***Table 10 ISF PIRT results***

| Component | Phenomenon | IMP | | | SOK |
|---|---|---|---|---|---|
| | | I | II | III | |
| **Core** | Convection heat transfer | H | M | M | M |
| | Gap conductance between fuel and cladding | H | M | M | M |
| | Clad conductivity | H | M | M | M |
| | Fuel thermal properties | M | M | M | M |
| | Fuel mechanical properties | M | M | M | M |
| | Decay heat | | | H | H |
| | Fission reaction | H | | | H |
| | Doppler effect | H | | | H |
| | Coolant density reactivity feedback | M | | | M |
| | Core geometry reactivity feedback | M | | | M |
| | Pressure losses | H | M | M | M |
| **Reactor Vessel** | Thermal stratification | L | M | M | M |
| | Creep effect | | M | | M |
| | Pressure losses | H | H | H | M |
| **Steam Generator** | Pressure losses | L | M | H | M |
| **Primary Coolant** | Polonium trapping | L | L | L | M |
| **DHR** | Heat transfer | | | H | M |
| | Condensation | | | M | M |
| | Condensation with non-condensable gases | | | M | M |
| | Pool Boiling (inside tubes) | | | L | M |
| | Pressure losses | | | H | H |

## 3.3. Neutronic and Thermal-Hydraulic transient analysis

In this context, a dedicated numerical model of ALFRED was developed with the objective of comprehensively investigating the reactor's behaviour under both steady-state and abnormal conditions during accidental transients. This numerical effort also supports the PIRT analysis discussed previously, in particular within the framework of the ANSELMUS project (Work Package 1, Task 1.3) [51].

Three unprotected transients were investigated: Unprotected Loss of Flow (ULOF), Unprotected Transient Over-Power (UTOP), and Unprotected Loss of Heat Sink (ULOHS). These scenarios were originally studied in the context of the earlier ALFRED LEADER design [53]; in this work, they have been revisited and applied to the updated ALFRED FALCON configuration to evaluate its performance and safety characteristics under challenging conditions.

The analysis aims to assess the effectiveness of the revised ALFRED design while simultaneously identifying potential modelling issues that could impact safety evaluations. By leveraging neutronic-thermal hydraulic coupling techniques, this study provides a preliminary assessment of ALFRED's dynamic response, enhancing the understanding of its inherent safety features and informing both future experimental validations and design optimizations. Furthermore, this investigation contributes to the refinement of the reactor's safety case and supports the prioritization of R&D activities as indicated by the PIRT outcomes.

### *3.3.1. Numerical model*

The numerical model of ALFRED [54] was developed employing RELAP5/Mod3.3, which was specifically adapted to incorporate the thermophysical properties of liquid lead [34] and the corresponding heat transfer correlations [35]. This enhanced version has been successfully utilized in post-test analyses and numerical benchmark exercises [38], demonstrating its capability to accurately capture key phenomena observed in liquid lead experiments and to reliably predict the main trends of operational parameters. The numerical model is illustrated in Figure 17.

Although ALFRED features a three-loop pool-type configuration, in this study the model has been simplified by collapsing all three loops into a single equivalent loop, in line with established best practices for code modelling [55]. This approximation is justified as long as the transients under investigation do not involve asymmetric behaviours between the loops, which is not the focus of this work.

In Figure 17, the control volumes coloured in green represent the ALFRED RCS, while those in blue correspond to the in-containment sections of the secondary loops, defined between the isolation valves. The DHR system is also included in the model and is depicted by cyan-coloured control volumes, whereas orange volumes represent the pool side of the ICs.

The first digit of the hydrodynamic components number identifies a specific system as follows:

- "1XX" for the RCS.
- "4XX" for the secondary loop and the DHR system.
- "7XX" for the pool side of the IC.

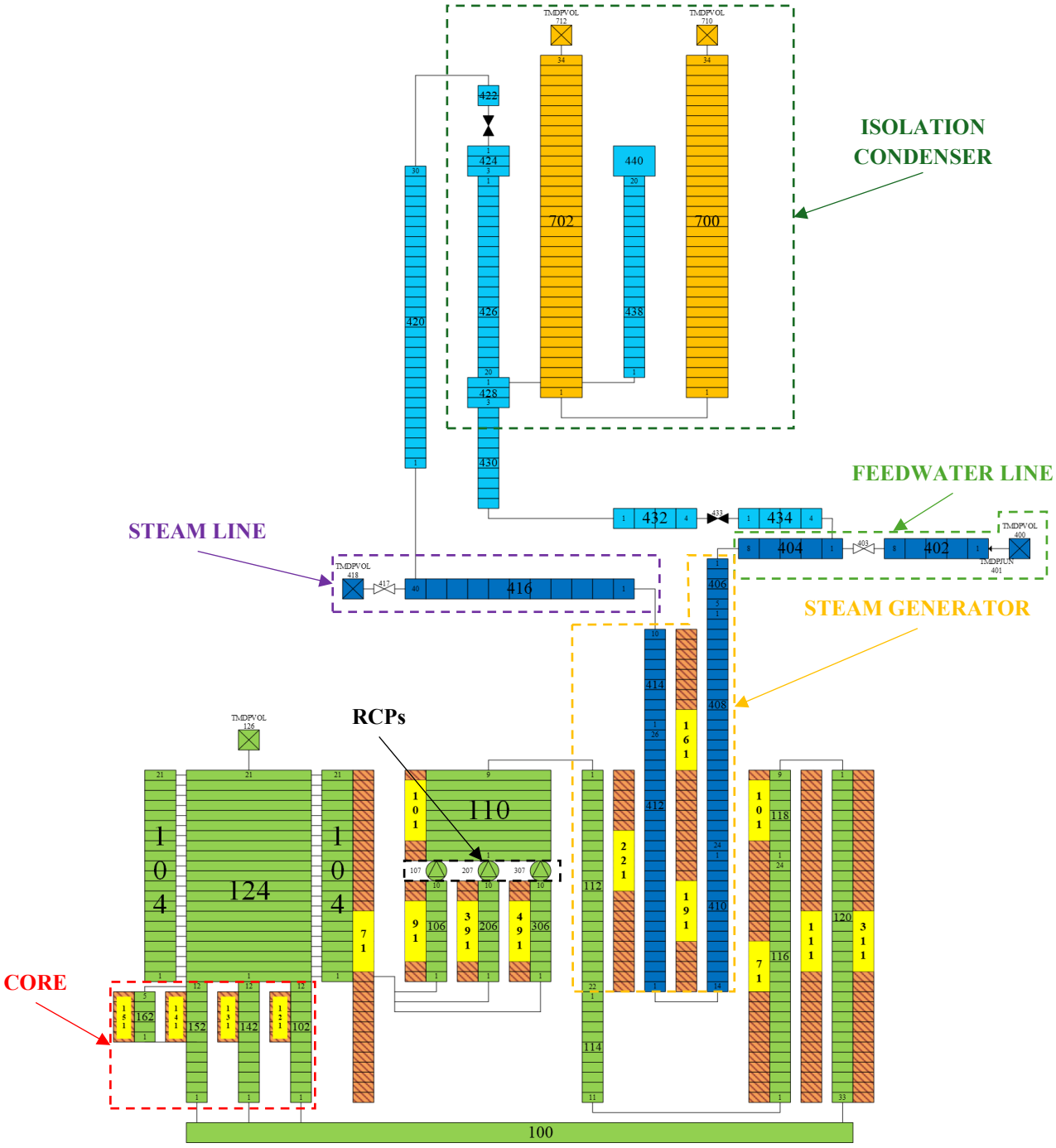


***Figure 17 R5 nodalization scheme of ALFRED***

The reactor core is modelled using three equivalent PIPE components, numbered 102, 142, and 152. PIPE 102 represents all the reflector dummy assemblies combined, PIPE 142 models the average fuel assembly behaviour—representing all core assemblies except the hottest one—and PIPE 152 corresponds to the hottest fuel assembly. Additionally, PIPE 162 is included in parallel with PIPE 152 to simulate the subchannel adjacent to the hottest pin.

From the thermal perspective, Heat Structures (HSs) are associated with the average assemblies, the hottest assembly, and the hottest pin (as shown in Figure 17). The first two HSs are divided into 10 axial nodes, of which five nodes represent the active length of the core with a total height of 810 mm (162 mm per mesh), as reported in [44]. The heat structure for the hottest pin focuses exclusively on the active length.

The total reactor power is distributed among these three HSs based on radial peak factors provided in [47], and within each HS, the power is axially distributed following the specified axial profile reported in [47]. The thermophysical properties of the materials used in these heat structures—MOX fuel [56], 15-15 Ti alloy for the cladding [57], and helium in the gap [58]—have been implemented in the numerical model.

Given that the simulated transients involve several neutronic phenomena, the NK model within RELAP5 has been activated. In the version adopted here, the available NK model is the 0-D point kinetics approach. The NK equations employed are the following:

$$\frac{d}{dt}\varphi(t) = \frac{r(t)-\beta}{\Lambda}\varphi(t) + \sum_{i=1}^{N_d} \lambda_i \, C_i(t) + S \qquad 1)$$

$$\frac{d}{dt}C_i(t) = \frac{\beta f_i}{\Lambda}\varphi(t) - \lambda_i \, C_i(t) \qquad 2)$$

$$r(t) = r_o - r_B + \sum_{i=1}^{n_s} r_{si}(t) + \sum_{i=1}^{n_c} V_{ci}(t) + \sum_{i=1}^{n_\rho} a_{Wi} T_{Wi}(t) + \sum_{i=1}^{n_F} a_{Fi} T_{Fi}(t) \qquad 3)$$

where:

- $t$ is time
- $\varphi$ is the neutron flux
- $C_i$ are the delayed neutron precursors of group $i$
- $\beta$ is the effective delayed neutron fraction
- $\Lambda$ is the prompt neutron generation time
- $r$ is the reactivity
- $f_i$ is the fraction of delayed neutrons of group $i$
- $\lambda_i$ is the decay constant of group $i$
- $S$ is the external neutron source
- $r_o$ is the user-defined initial reactivity
- $r_B$ is the bias reactivity
- $r_{si}$ are the input tables of reactivity curves vs time
- $n_s$ is the number of input tables
- $V_{ci}$ are the user-defined control variables as reactivity contributions
- $n_c$ is the number of control variables
- $T_{Wi}$ is the volume averaged temperature of the coolant in the volume $i$
- $a_{Wi}$ is the coolant temperature coefficient for the volume $i$
- $n_\rho$ is the number of hydrodynamic volumes in the core
- $T_{Fi}$ is the volume averaged temperature of the fuel in the heat structure $i$
- $a_{Fi}$ is the fuel temperature coefficient for the heat structure $i$
- $n_F$ is the number of heat structures in the core

The point kinetics model is used to calculate the power behaviour in a nuclear reactor by employing a space-independent approximation. This method assumes that power can be separated into spatial and temporal components, and it is suitable for scenarios where the spatial distribution of the neutron flux remains relatively constant. The adoption is justified by the nature of the transients considered, where the reactor dynamics are primarily governed by global reactivity effects and thermal-hydraulic feedback. In such cases, detailed spatial resolution of the neutron flux is not required, and the point kinetics approximation provides an adequate level of accuracy for capturing the core's global response. This approach allows for an efficient yet conservative evaluation of key safety parameters, such as temperature evolution and power excursion.

The model calculates both the prompt fission power, and the power generated from the decay of fission products. The prompt power is released immediately during fission, including the energy from the kinetic motion of fission fragments and neutron moderation. Decay power, on the other hand, results from the radioactive decay of fission products and it is calculated assuming an infinite operating time using ANS94-4 data [59] which require the fuel isotopic composition namely $^{235}$U, $^{238}$U, $^{239}$Pu, and $^{241}$Pu. The inclusion of these isotopes in the ANS 94-4 dataset makes it suitable for application to MOX fuel.

Equation 1) and Equation 2) compute the neutron population ($\varphi(t)$) and delayed neutron precursors ($C_i(t)$) and thus the generation of immediate fission power. Since the neutron population is also a function of the reactivity, this quantity ($r(t)$) can be evaluated by Equation 3). This is the so-called separable model which defines the reactivity as the sum of separate contributions. The quantity $r_o$ is the value given in input by the user and representing the initial reactor reactivity, usually assumed equals to zero. The quantity $r_B$ is the bias reactivity. After input processing, it is used by the code to compensate the other contributes, the ones in Equation 3) characterized by the summation sign and explained in the following, and to ensure that $r(t = 0) = r_o$.

The quantities $r_{si}$ represent time-dependent reactivity insertions defined through a set of user-provided tables. The parameter $n_s$ indicates the number of these tables. This approach allows the simulation of multiple reactivity insertion in the core during a transient. For example, one table may represent a sudden positive reactivity insertion, while another may simulate a negative reactivity insertion corresponding to a SCRAM curve. The $V_{ci}$ values represent $n_c$ control variables that can be user-defined to represent reactivity contributions, e.g., fuel axial expansion, coolant expansion, etc.

$T_{Wi}(t)$ is the spatially averaged temperature of volume $i$, and $a_{Wi}$ is the temperature coefficient (excluding density effects) for volume $i$. The number of hydrodynamic volumes considered in the reactor core is $n_\rho$. This approach allows the user to compute a weighted coolant temperature coefficient based on the temperature levels in different part of the core. It is important to note that the weighting factors are included within the calculation of the $a_{Wi}$ coefficients. The implementation of the fuel temperature coefficient is treated in a similar way. the quantity $T_{Fi}(t)$ is the average fuel temperature in heat structure $i$, while $a_{Fi}$ is the corresponding fuel temperature coefficient. The number of the considered heat structures in the reactor core is $n_F$. The reactor physics input data required to solve the NK problem represented by Equation 1), 2) and 3) have been provided by ENEA, which designed the ALFRED core [47].

The ERANOS code in the 2.3N available from the Nuclear Energy Agency software database has been used for the calculations of all neutronic-related parameters along with nuclear data coming from ENDF/B-VIII.0 tapes [60]. The computed parameters are the delayed neutron fraction ($\beta$), the delayed neutron yield ratio for each group ($f_i$, six groups are considered), the delayed neutron decay constant for each group ($\lambda_i$) and prompt neutron generation time ($\Lambda$). Since no neutron sources are present in the reactor, the '$S$' term in Equation 1) can be neglected.

For the ALFRED transient analysis, several NK feedbacks have also been considered in the input deck. The Fuel Temperature Coefficient (FTC), which comprises the Doppler effect and the fuel expansion, and the Coolant Temperature (i.e., density) Coefficient associated with the Active Zone (CTC-AZ) have been implemented by using the approach considering $a_{Wi}$ and $a_{Fi}$ coefficients. The hydrodynamic volumes and heat structures related to the core active zone (see Figure 17) have been accounted for. Instead, the coolant temperature coefficient referred to the upper plenum (CTC-UP), lower plenum (CTC-LP) and Radial Zone (CTC-RZ) around the active region have been introduced by means of control variables ($V_{ci}$).

The same methodology has been adopted for the Structural Temperature Coefficients, accounting for the metallic structures within the active zone (STC-Clad), the diagrid (STC-Dia), the expansion pads (STC-Pads), and the control and safety rods (STC-CRs). The latter consists of two different contributions. Considering that CRs and SRs enter the core from the bottom, during heating transients, when the stems that hold these components in position axially expand, the CRs and SRs are gradually extracted from the core, resulting in positive reactivity feedback (labelled STC-CRs-STEM).

What effectively rules this feedback is the axial temperature profile of the stem going approximately from the Bottom of Active Fuel (BAF) to the top of the hot pool. Considering the low mass and volume of the stem, in the current simplified NK model based on nodal kinetics, its inertia is neglected, and the average coolant temperature is computed in this axial region and adopted as controlling parameter for this reactivity feedback. In addition, it must be considered that the core is supported by the lower support plate anchored to the IV (see Figure 12)

During heating transients, when the IV axially expands in the downwards direction, it carries with it also the support plate and the core leaning over. Since the CRs and SRs are hanging from above, they do not move with the rest of the core structure. In conclusion, the downwards displacement of the core produces an insertion of the CRs/SRs, resulting in negative reactivity feedback (labelled STC-CRs-IV). Also in this case, it is the axial temperature profile associated with the IV steel structure that rules the reactivity feedback (from approximately BAF to top of reactor). For this, the related average temperature is computed and used as controlling parameter. The logic associated with the implemented control variables, is shown below:

$$V_{ci}(t) = a_i\,(T_i - T_{0i}) \qquad 4)$$

It corresponds to a linear reactivity variation as function of the temperature difference with respect to a nominal value ($T_{0i}$). Equation 4) is implemented by using a table, centred at the steady state conditions corresponding to the desired power level, to have null feedback in those conditions. For each NK feedback, the $a_i$ coefficient in Equation 4) is shown in Table 11.

***Table 11 NK feedback implemented in the input deck***

| NK Feedback | Reactivity Coefficient (pcm/K) | Reference Temperature (description) |
|---|---|---|
| **FTC** | -0.698 | Average fuel temperature within the AZ |
| **CTC-AZ** | +0.078 | Average Pb temperature within the AZ |
| **CTC-LP** | -0.094 | Average Pb temperature below the AZ |
| **CTC-UP** | -0.142 | Average Pb temperature above the AZ |
| **CTC-RZ** | -0.080 | Average Pb temperature around the AZ |
| **STC-Clad** | +0.084 | Average clad temperature within the AZ |
| **STC-Dia** | -0.260 | Average core inlet temperature |
| **STC-Pads** | -0.623 | Average core outlet temperature |
| **STC-CRs-IV** | -0.822 | IV average steel temperature between BAF and top of reactor |
| **STC-CRs-STEM** | +0.775 | Average Pb temperature between BAF and top of hot pool |

The feedback coefficients were computed with ERANOS combining the pertinent feedback effects as described in [61]. The feedback effects have been calculated via variations to the reference parameters (taken in their STAGE 3 value), meaning fuel temperature, lead density in various regions of the system, steel density, fuel density, active height, absorber height and FA pitch exactly as in [61].

Finally, an important aspect to be highlighted is that the NK feedback associated with the pads radial expansion is a threshold effect. This means that if the core outlet temperature is below a critical value, this reactivity feedback is neglected. For sake of clarity, the implemented logic is reported in Equation 5):

$$\begin{cases} T_{Pb\ out\ core} \leq T_{crit} \quad \rightarrow \quad \Delta\rho_{Pads} = 0 \\ T_{Pb\ out\ core} > T_{crit} \quad \rightarrow \quad \Delta\rho_{Pads} = a_i \left(T_{Pb\ out\ core} - T_{Pb\ out\ core,ref}\right) \\ T_{crit} = 520 + 0.977 * (T_{Pb\ in\ core} - 400) \end{cases} \qquad 5)$$

This logic was selected to properly simulate the pads NK effect. These components consist in outward protrusions machined on the FAs wrapper tube. They are designed to enter in contact when the core works in STAGE 3 nominal conditions. Indeed, retrieving the STAGE 3 data from Table 3, it is possible to see that, if core inlet temperature coincides with the nominal value, the critical temperature ($T_{crit}$) approaches the nominal core outlet temperature and the pads NK feedback ($\Delta\rho_{Pads}$) is equals to zero.

When the core outlet temperature exceeds the nominal value, the pads radially expand provoking an increase of the core radius and of the coolant volume fraction (at the expenses of the fuel one), i.e., negative reactivity feedback.

However, to properly account for this phenomenon, the pads radial expansion must be compared with the one occurring at the core bottom and due to the diagrid, caused by an increase in the core inlet temperature. It is the relative radial expansion of the pads with respect to the diagrid that actually rules FA outwards flowering and thus this NK feedback. For this a threshold is inserted in Equation 5) and this threshold is proportional to the core inlet temperature increase with respect to its nominal value.

The ALFRED primary system model comprises three pumps, one SG and several PIPE components that simulate the lead volumes within the RV, as shown Figure 12. The three RCPs are simulated with RELAP5 PUMP components. The component nominal data (see Table 6), as well as homologous curves have been implemented according to the information provided by ANSALDO.

Several passive HSs have been introduced in the input deck to simulate the main steel structures present in the reactor layout. HS 71 represents the IV. HSs 91, 391 and 491 model the pump ducts. HSs 101 and 111 represent the IS and finally HS 311 simulates the RV (see Figure 12). These HSs are fundamental to properly model the reactor thermal inertia during transient conditions.

On the other hand, in the secondary loop, the feed water flow is simulated by the TMDPVOL 400 which imposes the pressure and temperature conditions at the SG inlet, and by the TMDPJUN 401 which imposes the desired feed water mass flow rate. The feedwater enters the SG and exits as superheated steam which then moves toward the turbines represented by the TMDPVOL 418.

The bayonet tube SG is modelled as follows: PIPE 406 and PIPE 414 represent the feedwater and steam headers, respectively; PIPE 408 and PIPE 410 simulate the tubes downcomer section, where the regenerative heat transfer with the riser section occurs. Finally, the riser of the SG tube bundle is modelled by PIPE 412 which is thermally coupled with the liquid lead that flows in the SG shell side represented by PIPE 112. Primary and secondary sides are thermally coupled by means of HS 221 (see Figure 17). Additionally, the HS 161 and HS 191 models the regenerative heat transfer between the riser and the downcomer. Finally, the thermal properties for the bayonet tube steel (i.e., AISI316L) are derived from [62] and the heat transfer coefficient in the lead side is evaluated by Mikityuk correlation [37] suitable for fuel and tube bundles.

For the primary loop, from the hydraulic point of view, the friction factor associated with the distributed pressure drops is computed by Colebrook correlation [63]. Instead, the K-loss coefficients related to concentrated head losses must be given in input by the user. They have been evaluated according to the formulas indicated in the Idelchik hydraulic handbook [64].

In addition, concentrated pressure drops at the bottom of PIPEs 142, 152 and 162, have been used to simulate the FA inlet orifice. They have been tuned to obtain the proper core gagging scheme. The goal is to keep the maximum clad temperature below the limit indicated in [53]. Clearly, the reference scenario is STAGE 3, where the core temperature level is higher (see Table 3)

Finally, the three RCPs on the primary system and the TMDPJUN 401 on the secondary loop are provided with an integral control system given by Equation 6) and Equation 7) to regulate the pump velocity in the primary loop and the mass flow rate of the secondary side respectively:

$$\Delta\omega = K_I \int_0^t e(\tau)\, d\tau \quad (6)$$

$$\Delta\Gamma = K_I \int_0^t e(\tau)\, d\tau \quad (7)$$

in which:

- $\Delta\omega$ is the primary pump velocity variation
- $\Delta\Gamma$ is the secondary (feedwater) mass flow rate variation
- $K_I$ is the integral constant
- $e(\tau)$ is the error based on a setpoint

The integral controllers were used during the steady state calculations to obtain the nominal reactor parameters, according to indications provided in Table 3 [44]. The setpoints of the RCPs and the TMDPJUN 401 with which the errors are computed are the core outlet and inlet temperatures, respectively. In this way, the primary loop thermal cycle is correctly reproduced for each reactor operational stage that is simulated.

The integral controllers were selected (with respect to other controller options, i.e., proportional, derivative or combination of them) since, even if with higher computational times, they tend to the given setpoint with smoother trends, avoiding oscillations around the desired value and ensuring the stability of the numerical solution obtained.

Finally, it is worth to be mentioned that the heat losses were not explicitly modelled over the entire numerical model of ALFRED reactor. This is a conservative assumption for the transient analysis since one heat sink of the primary system is neglected (even if it represents a minor aspect). Indeed, given the reactor layout, the vessel insulation thickness can be sized such that heat losses remain negligible compared to the reactor power, while remaining consistent with acceptable insulation costs. As such, this is a design-related aspect that does not jeopardize the transient results obtained and discussed in this work.

### *3.3.2. Description of selected unprotected transients*

The analysis of DEC transients is performed based on ALFRED steady-state calculations (see Section 3.3.3). The safety analysis follows a deterministic approach, employing a methodology similar to that used for LWRs [65]; namely, evaluating the consequences of selected PIEs that could occur in the ALFRED reactor. Three accidental transients were investigated with the aim to understand the reactor behaviour under abnormal conditions. The selected PIEs are Loss of Flow, Over-Power Transient and Loss Of Heat Sink.

These scenarios were primarily studied to gain insight into the intrinsic safety features of ALFRED and to preliminarily assess the adequacy of the core and plant design solutions. In all three cases, the postulated DEC includes the failure of the reactor SCRAM, leading to unprotected transients. Additionally, the failure of the DHR system was also assumed as an aggravating condition.

In the ULOF scenario, the transient involves the loss of core coolant flow due to failure of the RCPs, caused by a loss of their electrical power supply. However, the secondary loop is assumed to remain in normal operation, with the feedwater mass flow rate kept constant at its nominal value.

In the UTOP case, a reactivity insertion of 250 pcm within 10 s is assumed. This insertion is intended to conservatively envelop the effects of potential voiding in part of the active core region—regardless of the cause, including SGTR, core compaction (in support of PIRT analysis, see Section 3.2), FA blockage, etc.—in line with the assumptions in [53]. The primary and secondary loops are assumed to remain in normal operation, i.e., the forced circulation is kept in both systems.

For the ULOHS scenario, the loss of feedwater to the SGs is postulated. In this case, forced circulation in the primary system is maintained.

In all the considered scenarios, the integrity of the fuel pellet and the clad were preliminary verified. As far as the fuel is concerned, its corresponding maximum temperature was monitored during all the transient evolutions and compared with its relative melting temperatures which is 2800 °C according to its isotopic composition [66].

With regard to the clad, its maximum temperature was monitored and compared to its melting temperature which is 1417 °C [57]. In addition, its creep resistance can be preliminarily evaluated with the correlation provided in [67] and reported in Eq. 8), even though additional dedicated mechanical calculations should be performed to ensure the absence of other failure phenomena.

$$t_{failure} = 10^{\frac{1520-\sigma_{eff}}{0.086T}-13} \quad 8)$$

In the previous, $\sigma_{eff}$ is the effective stress in the cladding expressed in MPa, $T$ is the clad temperature expressed in K and $t_{failure}$ is the time-to failure expressed in hours. A first-tentative value for the $\sigma_{eff}$ was calculated in [67] using TEMIDE [68] and it was used in the current work. It corresponds to 36 MPa. In accordance with [67], this preliminary $\sigma_{eff}$ value is independent from the maximum cladding temperature. However, in the future development of the activity, a more valuable estimation of this parameter will be obtained by performing a dedicated thermomechanical analysis.

### *3.3.3. Simulation results*

This numerical activity started from steady state numerical simulations that represent the normal operation of ALFRED both at STAGE 2 and STAGE 3. At STAGE 2, the core produces a fission power of 200 MW, which is removed by a liquid lead coolant flow rate of approximately 17000 kg/s. The coolant enters the core at 400 °C and exits at 480 °C. The thermal power is then transferred to the secondary loop through the steam generators. In the secondary loop, this power is removed by a water flow rate of around 133 kg/s, with the fluid entering at 335 °C and exiting at 435 °C. During STAGE 2, the secondary loop operates at a pressure of 175 bar. Table 12 summarizes the key results of the full power steady state calculation. Parameters indicated with '(BC)' are the ones imposed as boundary conditions for the current calculation.

In Table 12, a slight deviation worth to be discussed is the one associated with the primary mass flow.

As discussed in Section 3.3.1 , the core inlet temperature is set to the nominal value by adjusting the SG secondary feedwater flow. In addition, the primary pump speed is regulated to obtain the nominal core outlet temperature. Indeed, for both these parameters, the associated error is negligible in Table 12.

Given the core power, that is imposed as BC, and the correct inlet/outlet temperatures, for the core power balance, the only possible source of deviation in the primary mass flow evaluation are the liquid metal thermophysical properties, e.g., the lead heat capacity. This is because the empirical correlations used in RELAP5 [34], are slightly different from the ones used to calculate the parameters in Table 3.

Finally, another small deviation can be detected in the SG secondary feedwater flow and, consequently in the steam outlet temperature. Indeed, the former is a little higher than its nominal value and, accordingly, the latter a bit lower (i.e., the thermal power exchanged by the SG is the nominal one). This is related to the fact that RELAP5 slightly underestimates the heat transfer within the component.

Thus, to exchange the SG nominal power, the control system must increase the feedwater flow. However, the discrepancy is very limited (0.5%). If it seems higher when it comes to steam outlet temperature is only because, for superheated steam, the temperature is very sensitive with the fluid enthalpy. Thus, even a small difference in the latter causes a higher deviation in the former (of the order of some degrees).

***Table 12 STAGE 2 full power calculations: steady-state results***

| Parameter | Unit | Nominal Data [44] | RELAP5 | Deviation |
|---|---|---|---|---|
| **Thermal power (BC)** | MW | 200 | 200 | / |
| **Total lead mass flow rate** | kg/s | 16845.6 | 17218.2 | +2.2% |
| **Core inlet temperature** | °C | 400 | 400.0 | 0 °C |
| **Average core outlet temperature** | °C | 480 | 480.0 | 0 °C |
| **II SG inlet temperature (BC)** | °C | 335 | 335 | / |
| **II SG outlet temperature** | °C | 435 | 431.8 | -3.2 °C |
| **II SG pressure (BC)** | bar | 175 | 175 | / |
| **II SG mass flow rate** | kg/s | 132.9 | 133.7 | +0.6% |
| **Max. Fuel temperature** | °C | - | 1402.4 | / |
| **Max. Clad temperature** | °C | - | 500.9 | / |

On the other hand, at STAGE 3, the core produces a fission power of 300 MW. Primary mass flow is the same of STAGE 2. The coolant enters the core at 400 °C and exits at 520 °C. In the steam generators, the thermal power is removed by a water flow rate of around 192 kg/s, with the fluid entering at 335 °C and exiting at 450 °C. During STAGE 3, the secondary loop operates at a pressure of 180 bar. Table 13 summarizes the key results of the full power steady state calculation.

Here, the same slight deviation of Table 12 related to the liquid lead mass flow can be detected. As expected, passing from STAGE 2 to STAGE 3, clad and fuel maximum temperatures increase significantly. It should be noted that, for both stages, the maximum clad temperature associated with the heat structure simulating the hottest pin (i.e., HS 151 in Figure 17) is below or equals to the limit value indicated for this parameter during normal operations in [53].

This has been obtained by increasing the flow rate through the subchannel that interfaces with this heat structure (i.e., PIPE 162 in Figure 17). By design, the average mass flow cooling each pin is nearly 1 kg/s (compare data in Section 3.1 and Table 13). Instead, according to simulation results, a mass flow of about 130% of the average value is needed in STAGE 3 to keep the clad maximum temperature below the limit.

To reach this goal, the concentrated pressure drops at the inlet of PIPEs 142, 152 and 162, simulating the FA inlet orifice, have been accordingly tuned. However, this has been done by preserving the total core pressure drops that have been aligned to the design value of 1 bar, indicated in [53].

***Table 13 STAGE 3 full power calculations: steady-state results***

| Parameter | Unit | Nominal Data [44] | RELAP5 | Deviation |
|---|---|---|---|---|
| **Thermal power (BC)** | MW | 300 | 300 | / |
| **Total lead mass flow rate** | kg/s | 16845.6 | 17268.9 | 2.5% |
| **Core inlet temperature** | °C | 400 | 400.0 | 0 °C |
| **Average core outlet temperature** | °C | 520 | 520.0 | 0 °C |
| **II SG inlet temperature (BC)** | °C | 335 | 335 | / |
| **II SG outlet temperature** | °C | 450 | 449.0 | -1.0 °C |
| **II SG pressure (BC)** | bar | 180 | 180 | / |
| **II SG mass flow rate** | kg/s | 192.5 | 193.4 | 0.5% |
| **Max. Fuel temperature** | °C | - | 1954.5 | / |
| **Max. Clad temperature** | °C | - | 550.9 | / |

ULOF TRANSIENT

The PIE associated with this scenario is the loss of power supply to all primary pumps. Both the reactor SCRAM and the ALFRED DHR are supposed to fail. Instead, the secondary loop is assumed to operate in normal operation with no control of the feedwater mass flow rate. After the PIE, the RCPs decelerate according to the torque-inertia equation and the component moment of inertia. In the mid-long term, they become an additional concentrated head loss along the liquid lead primary flow path. The extent of this pressure drop is consistent with the homologous curves provided by ANSALDO. After the RCPs coast down, the natural circulation establishes in the primary loop. As visible in Figure 18, the mass flow trend is independent from the initial reactor stage since the pump component is the same and the mass flow rate in steady-state conditions is the same. However, in case of STAGE 3, the new steady state value is higher (29% vs 25% of nominal value, see Table 12 and Table 13) due to the increased average temperature level in the primary circuit.

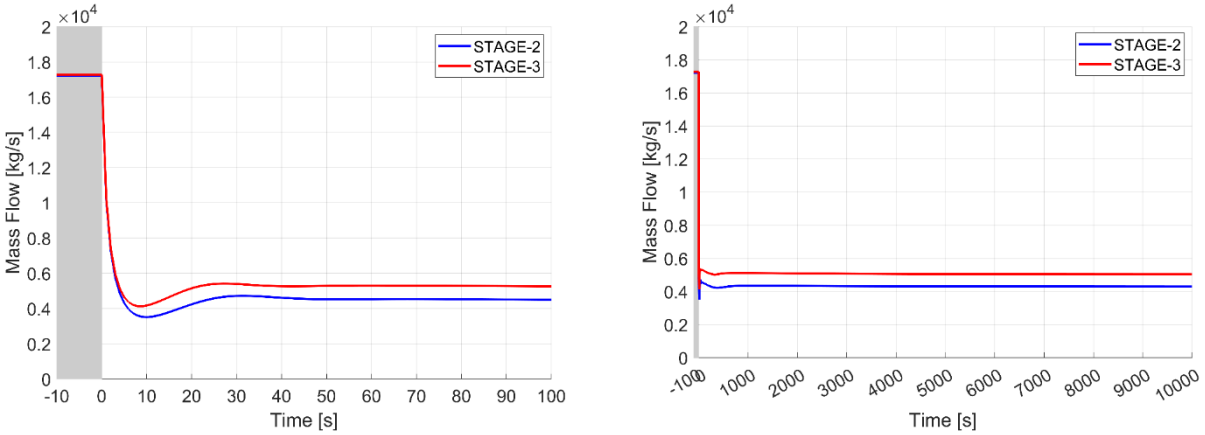


***Figure 18 ULOF transient: RCS mass flow rate in short-term (left) and long-term (right)***

The relative reactor power trends are shown in Figure 19a. From the figure, it can be seen that in the short-term, for both stages the power decreases rapidly to 50% of nominal power, with a slightly faster slope for STAGE 3. This is because the reactivity in STAGE 3 reduces earlier than in STAGE 2, due to the threshold behaviour of the STC-Pads: in STAGE 3, they provide a non-zero feedback immediately after the PIE, whereas in STAGE 2, the pads take approximately 5 seconds to reach the temperature threshold and give a non-zero feedback. Then for both stages, the reactor power stabilizes nearly at 65% of the nominal power.

The power trend is consistent with the one of the total reactivity (Figure 19b), where, after the perturbation following the PIE, the zero value is restored after about 25 minutes (i.e., 1500 s). Even more information can be deduced by the NK feedbacks reported in Figure 19c and Figure 19d, for STAGE 2 and STAGE 3 respectively. To understand these figures, the acronyms defined in Section 3.3.1 must be recalled.

In the short term, as expected, the NK feedbacks provoking the sharp power decrease is the FTC and STC-Pads (red and dark green dashed lines in Figure 19c and Figure 19d). Indeed, the pad system has been designed to quickly intervene in overtemperature transients to radially expand the core and, consequently, to introduce negative reactivity feedback (i.e., smoothing the power peak). In the mid-term (i.e., hundreds of seconds), the FTC changes sign and becomes positive due to the drop of the fuel temperature.

Nevertheless, this contribution is overcome by the negative reactivity feedback due to coolant density coefficient in the upper plenum and the radial expansion of the core pads. For this, the reactor power keeps decreasing. In fact, in this time scale, the temperature change can be only detected in the core itself and at the

core outlet (i.e., upper plenum). After nearly 400 s, the lower plenum and, thus, the core inlet, is reached by the colder fluid coming from the steam generators. Indeed, within these components, the drop of the lead mass flow, produces a consequent decrease of the SG primary outlet temperature (i.e., the primary temperature difference increases). This triggers the positive NK feedback associated with the diagrid contraction (pink dotted line in Figure 19c and Figure 19d). In addition, in the long term (i.e., thousands of seconds), temperature effects become also detectable in the reactor hot pool and IV. Thus, they are also visible related to the CRs feedback, positive for STC-CRs-STEM (magenta dashed/dotted line) and negative for STC-CRs-IV (orange dashed/dotted line), as discussed in Section 3.3.1.

Together with the FTC, they restore the equilibrium, leading the total reactivity to zero. The NK transient is very similar when considering both STAGE 2 and STAGE 3. The only slight deviation is visible in the short-mid-term, and it is due to the timing needed to the cold lead exiting the steam generator to propagate up to the lower plenum and, thus, the core inlet, producing the positive NK feedback associated with the diagrid contraction.

The power-to-mass ratio differs in the two cases, leading to a different thermal inertia of the system when withstanding this accidental scenario. In STAGE 2, this ratio is lower and, thus, the reactor thermal inertia is higher. This smooths the main transient oscillations visible in the power trend in both the short (between 20 and 40 s) and mid-term (up to 400 s). After, the cold lead reaches the lower plenum, the transient proceeds in a common way in both the calculations. From this moment onwards, the effect of the thermal inertia is negligible.

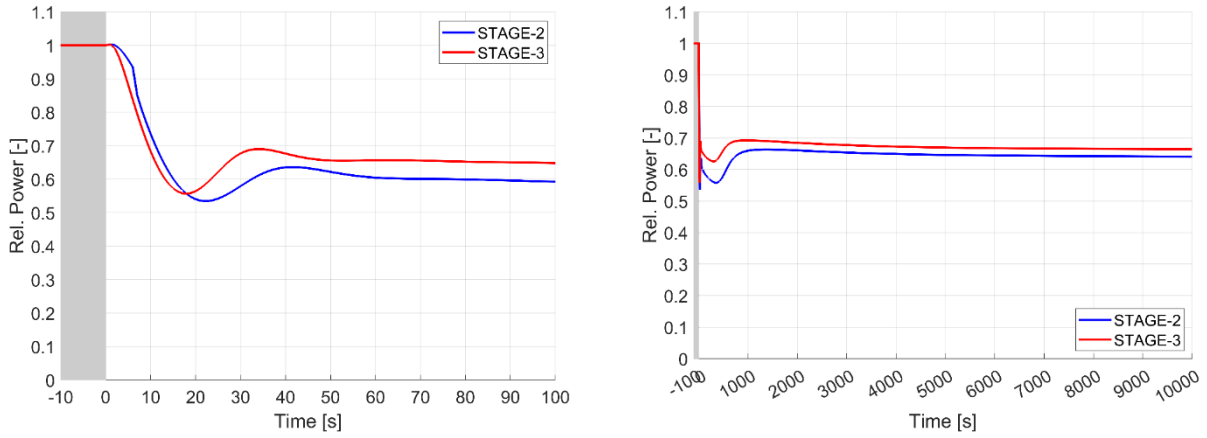


**(a)**

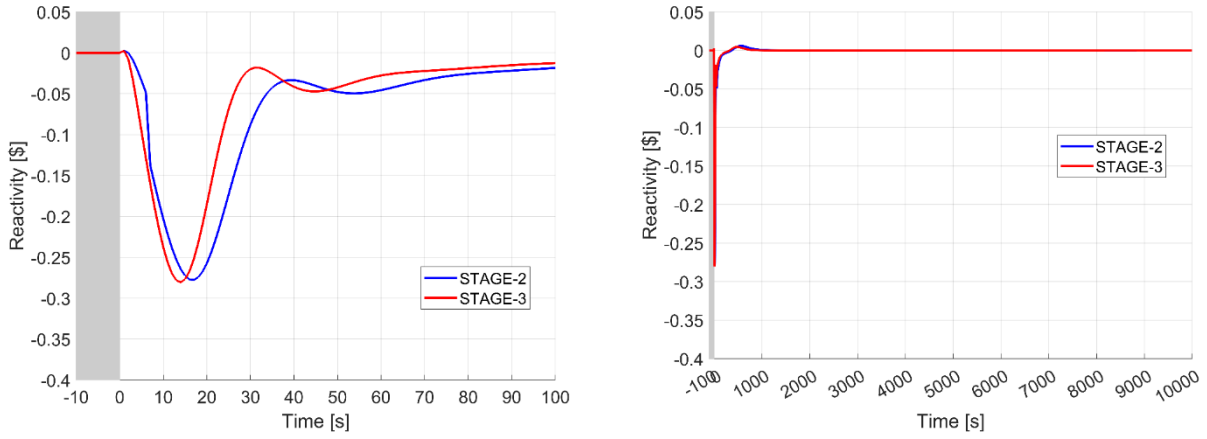


**(b)**

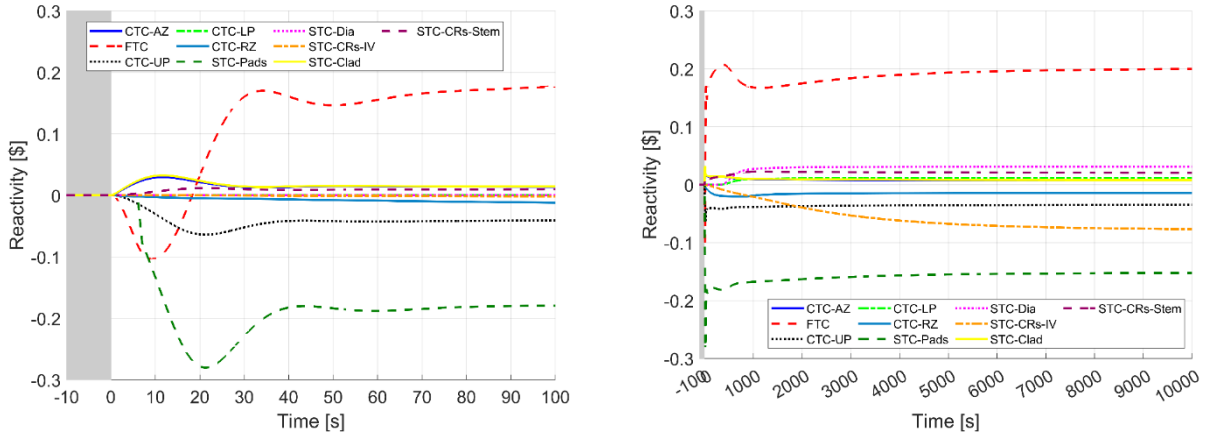


**(c)**

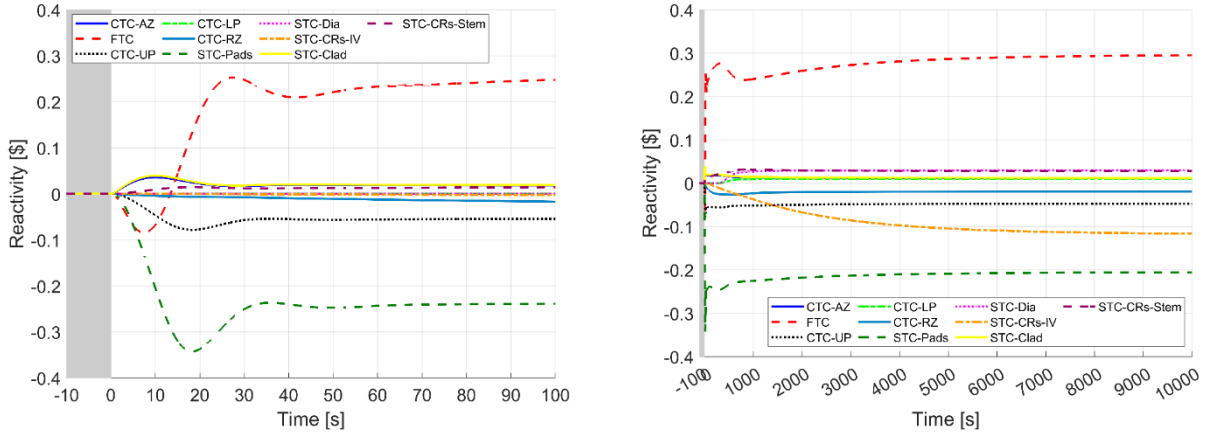


**(d)**

***Figure 19 ULOF transient: relative reactor power (a), total reactivity (b), STAGE 2 (c) and STAGE 3 (d) NK feedback, in short-term (left) and long-term (right).***

Figure 20a shows the core inlet (dashed lines) and outlet (solid lines) temperatures for STAGE 2 (blue lines) and STAGE 3 (red lines). As already pointed out, the inlet temperature reduces only in the long-term. This is due to the reduction in the primary system mass flow and the degradation of the SGs heat transfer performance. On the other hand, the core coolant outlet temperature increases after PIE due to the mismatch between the generated thermal power and the core flow rate.

The short-term peak for STAGE 2 and STAGE 3 corresponds to 655 °C and 735 °C, i.e., 136% and 141% of the nominal value (Table 12 and Table 13). The final value of the core inlet temperature for both stages are approximately 360 °C, while the outlet temperatures are 565 °C and 635 °C respectively for STAGE 2 and STAGE 3, i.e., 118 and 122% of the nominal values in Table 12 and Table 13.

Particular attention must be paid to the primary system minimum temperature. Due to the absence of dedicated modelling for heat losses, the evaluation of the freezing margin is limited. Nonetheless, this aspect is considered of secondary importance in the context of the present transient scenario. Apart from the previous issue, coolant core inlet and outlet temperatures are not strictly related to any safety criteria, but they are useful to quickly understand in a quantitative way the deviation of the primary fluid system from the nominal state occurring after the PIE.

Figure 20b shows the trend of the maximum clad temperature where a sudden increase occurs due to the failure to remove the thermal power caused by the interruption of forced circulation. The peak temperatures for both stages are about the 146% of the nominal ones and the final values are 119% (consistent with the core outlet temperature).

Finally, of particular importance is to check the integrity of the second barrier (i.e., the clad). The clad integrity is preliminarily verified by the fact that the clad peak temperatures (which are 723 °C for STAGE 2 and 823 °C for STAGE 3) are lower than the melting point of 1417 °C, derived from [57]. Therefore, there is no clad failure due to melting.

Additionally, according to Equation 8), the clad time-to-failure is estimated to be more than 2 years (875 days) for STAGE 2 and about 23 days for STAGE 3. The maximum fuel temperature evolution is depicted in Figure 20c from which it can be seen that it follows the same trend as the power generated in the core. Therefore, as expected, no peaks are detected. For both stages, the final value is about 78% of the nominal value (see Table 12 and Table 13).

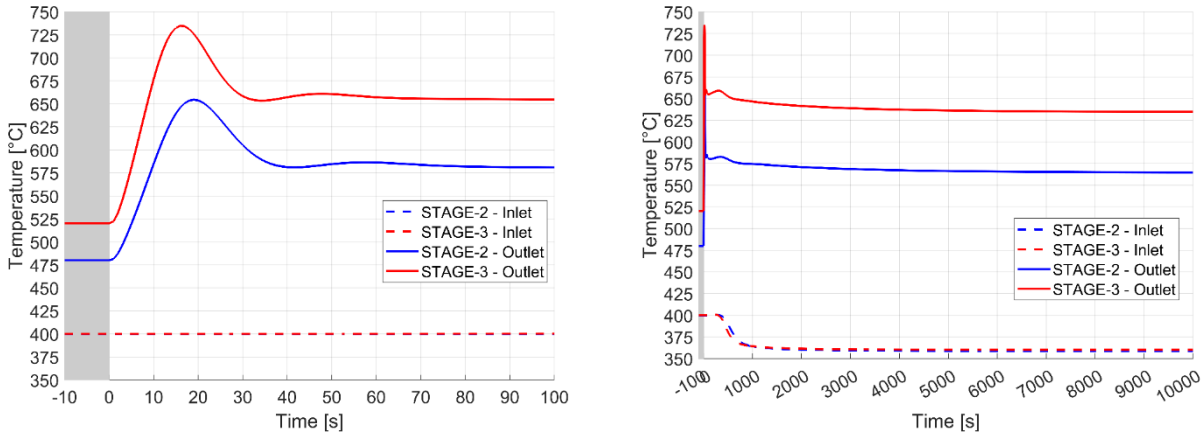


**(a)**

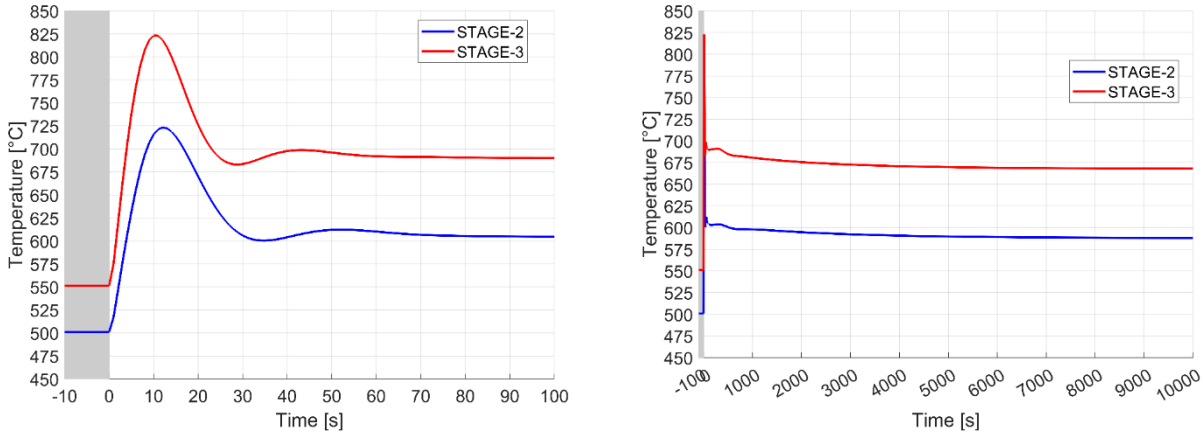


**(b)**

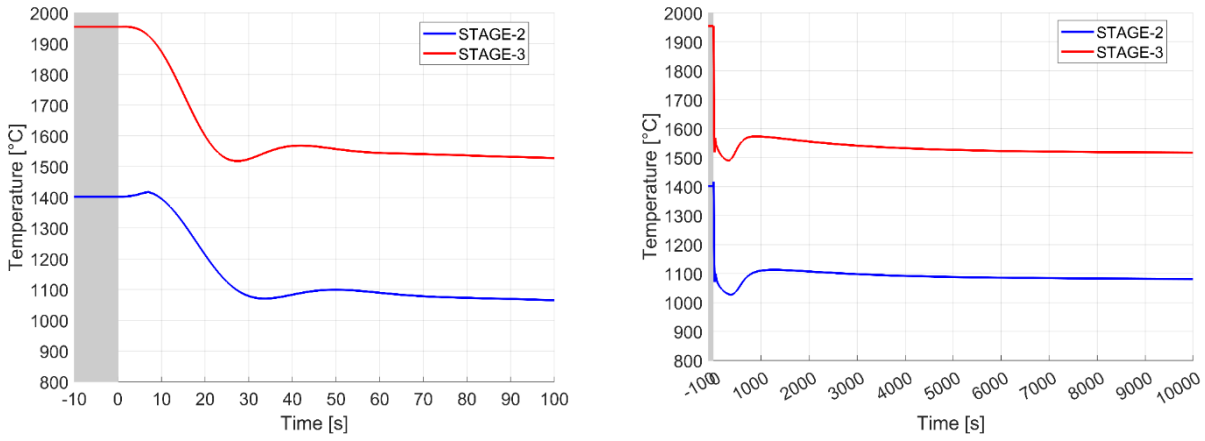


**(c)**

***Figure 20 ULOF transient: core inlet/outlet temperatures (a), maximum clad temperature (b) maximum fuel temperature (c), in short-term (left) and long-term (right).***

UTOP TRANSIENT

As far as the UTOP is concerned, the initiating event consists in an unforeseen reactivity insertion of 250 pcm in 10 seconds. The reactivity trend is assumed linear during the considered time window. The PIE features were selected according to the indications provided for this scenario in [53]. Both the primary and secondary loops are assumed to remain in normal operation with no control of the corresponding mass flow rate. In this transient, no reactor SCRAM and no DHR intervention are postulated (they are assumed to fail).

After PIE, the core relative power shows a maximum of 215% and 172% for respectively STAGE 2 and STAGE 3 (see Figure 21a). As expect the peak occurs at the end of the insertion time window, i.e., 10 s after the start of transient. The magnitude of the relative power spike is different between the two stages. In STAGE 2, the relative extent of the power excursion is higher. This can be justified looking at Figure 21c and Figure 21d, gathering the NK feedbacks for STAGE 2 and STAGE 3, respectively.

As visible, for STAGE 3 two main contributions counterbalance the positive reactivity insertion, i.e., FTC and STC-Pads (red and green dashed lines in Figure 21d). Instead, for STAGE 2, the occurrence of the STC-Pads NK feedback is delayed (green dashed line in Figure 21c), and this leads to a high relative power peak. Its initial absence is due to the logic implemented for this reactivity feedback, reflecting the physics behind this phenomenon, (see Section 3.3.1).

This NK feedback has a threshold effect based on the relative radial expansion between the pads (at core outlet) and the diagrid (at core inlet). In STAGE 3, the core nominal temperature level is higher and, consequently, the margin with respect to the temperature threshold that activates the STC-Pads feedback is reduced. Thus, a lower relative power excursion is needed to approach the limit.

Instead, in STAGE 2, the rector works with lower temperature values, and a higher relative power excursion is needed to activate the pads NK feedback. However, in both stages, the power spike is dampened in about 15 seconds. For both stages, a new equilibrium is reached in the mid-long term, characterized by a power level equals to 120% of the nominal value.

The reactor power trend is consistent with that of total reactivity, which is plotted in Figure 21b. It can be noticed the maximum peak in the short term caused by the imposed positive reactivity insertion, which is then

dampened in 15 seconds. The zero-value reactivity is restored in about 30 minutes. Regarding the different reactivity feedbacks, they are plotted in Figure 21c and Figure 21d for STAGE 2 and STAGE 3, respectively.

As visible, in the short-term after PIE, the external reactivity insertion is mainly counterbalanced by the prompt negative FTC (red dashed line in Figure 21c and Figure 21d). Instead, in the mid-long term, the fuel temperatures decrease (see Figure 22c), and the magnitude of the FTC lowers accordingly (with respect to the short-term peak value). However, the increase of the lead primary thermal cycle (see Figure 22a) leads to the occurrence of other negative reactivity feedbacks, mainly the ones related to the IV axial expansion and the pads radial expansion (orange dotted-dashed line and green dashed line Figure 21c and Figure 21d, respectively). Together, these three contributions counterbalance the positive reactivity insertion.

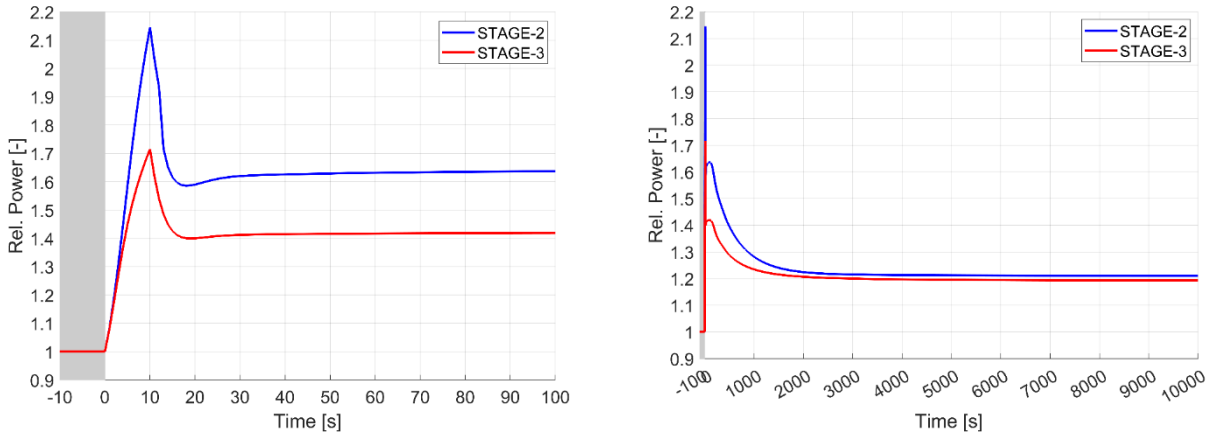


**(a)**

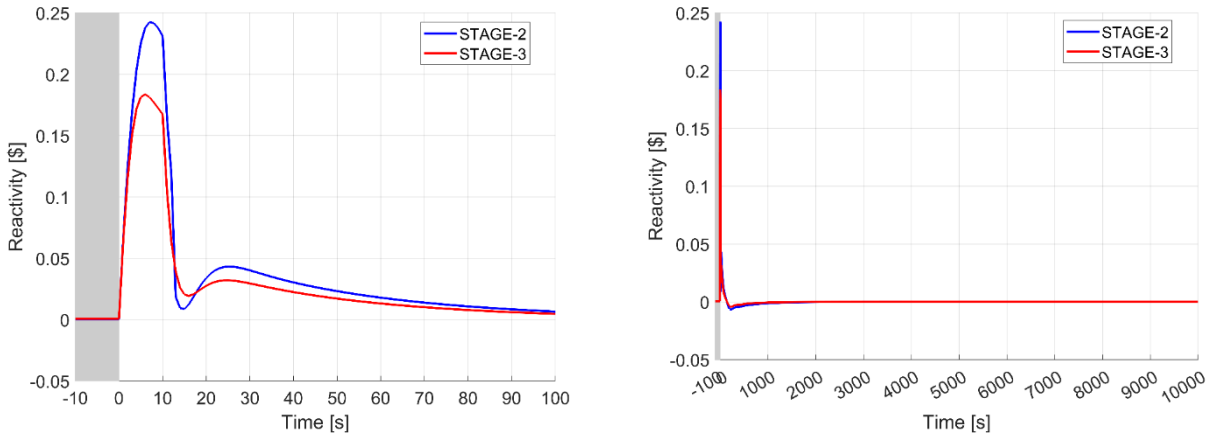


**(b)**

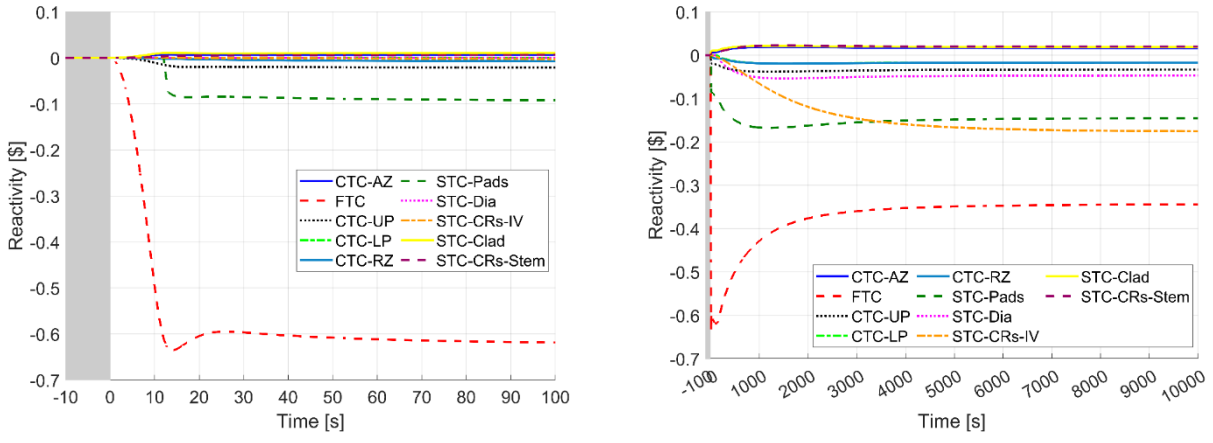

**(c)**

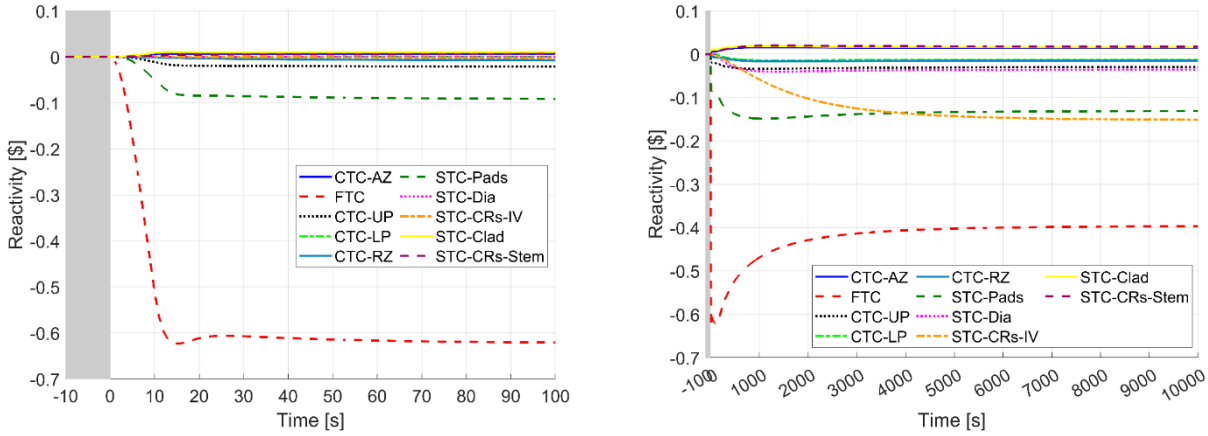


**(d)**

***Figure 21 UTOP transient: relative reactor power (a), total reactivity (b), STAGE 2 (c) and STAGE 3 (d) NK feedback, in short-term (left) and long-term (right).***

The core inlet/outlet temperature evolutions are plotted in Figure 22a. The core outlet temperature experiences two different surges. The first occurs in the short term and is related to the sudden reactivity insertion (first 10 seconds after PIE). The second is experienced in the mid-term when also the lower plenum temperature, i.e., the core inlet temperature starts to rise.

This second one is smoother than the first one. The timing of this second increase depends on the thermal-hydraulic feedback provided by the steam generators. In the long term, i.e. after about 100 minutes, the core temperatures stabilize again. The primary average temperature increases of 71 °C and 60 °C for STAGE 2 and STAGE 3, respectively.

In addition, in this new steady state characterizing the end of transient, the primary temperature difference corresponds to 99 °C and 146 °C for STAGE 2 and STAGE 3, corresponding to 123% and 121% of the nominal value (see Table 12 and Table 13). The increase in this parameter is due to the fact that the primary flow is kept constant during the overall transient. Thus, the power-to-flow ratio correspondingly increases.

Referring to the maximum clad temperature (Figure 22b), it follows the trend of the core outlet temperature. The peak temperature is reached at about 17 minutes in both stages and corresponds to 599 °C and 640 °C for STAGE 2 and STAGE 3, i.e., 120% and 116% of the nominal value in Table 12 and Table 13. These temperature levels are far below the melting point [57].

In addition, according to Equation 8), the time-to-failure is of 836 years and 101 years respectively for STAGE 2 and STAGE 3. Of course, if fuel and clad are into contact before the transient the ensuing contact pressure could lead to clad failure due to plastic deformations rather than creep ones; notwithstanding the modest values reached by the clad temperature in this scenario, more detailed thermomechanical analysis should thus be performed to understand whether clad failure can occur and the corresponding driving mechanism.

Finally, concerning the maximum fuel temperature, the trend for both stages is consistent with the reactor power evolution. After a sharp increase, a new equilibrium point is reached, higher than the nominal one. An important aspect to consider is the assessment of the integrity of the fuel itself. For this check, the maximum fuel temperature for both stages were compared to the melting temperature according to [66].

The maximum fuel temperature peak for STAGE 2 and STAGE 3 are respectively 2096 °C and 2525 °C. Given the isotopic composition of ALFRED fuel, indicated in [47], the melting point is close to 2800 °C. Thus, in the case of a reactivity insertion whose magnitude approaches the prompt-criticality, no fuel melting occurs. However, the adopted trend (i.e., linear ramp in 10 seconds) is not the more conservative. In the future developments of the activity, other shapes will be considered and investigated.

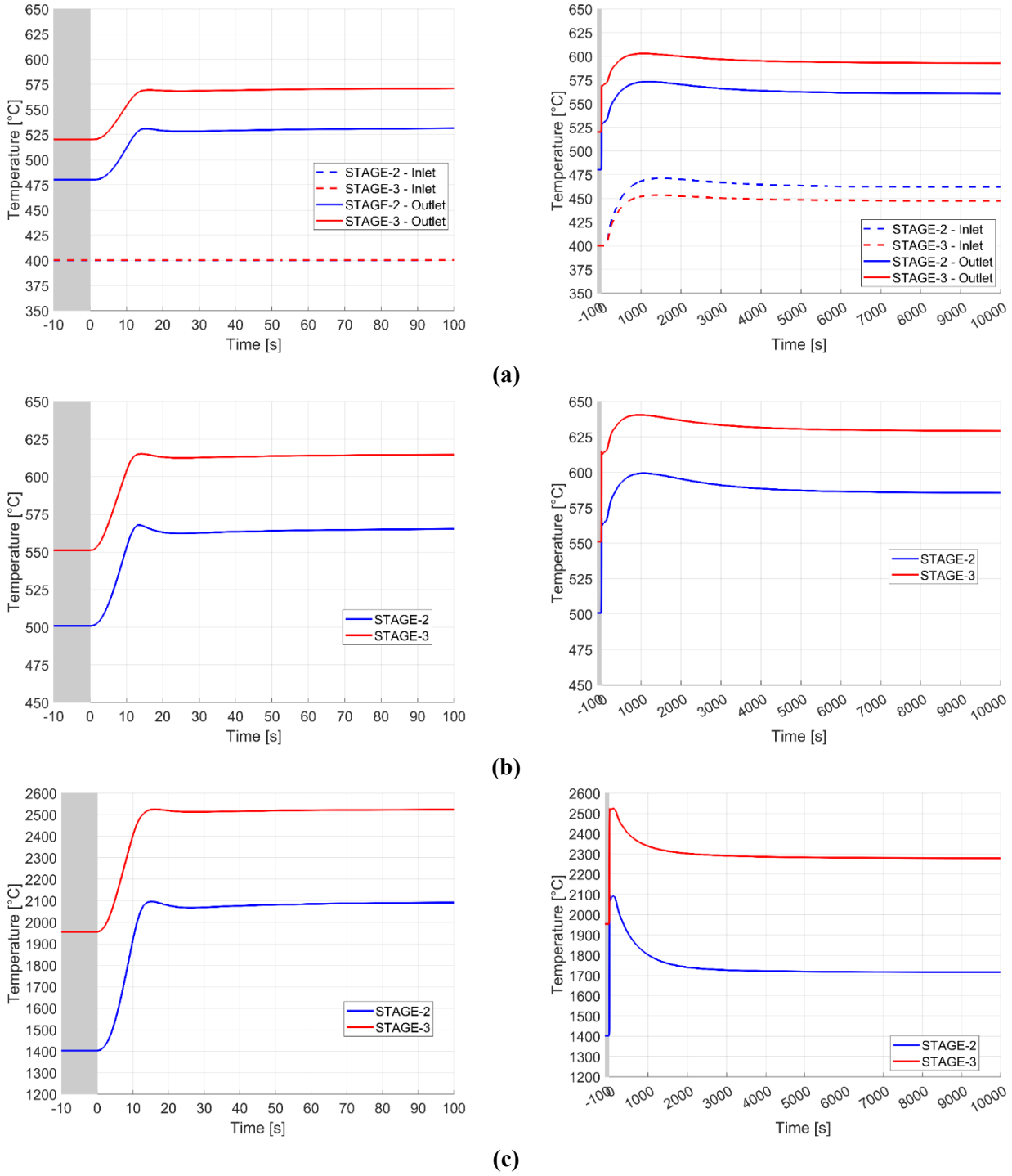


***Figure 22 UTOP transient: core inlet/outlet temperatures (a), maximum clad temperature (b) maximum fuel temperature (c), in short-term (left) and long-term (right).***

ULOHS TRANSIENT

This transient is initiated by the simultaneous loss of all feedwater pumps. Also in this case, both SCRAM and DHR are supposed to fail. Instead, the primary loop is assumed to operate in normal operation with no control of the RCS mass flow rate. As discussed in Section 3.3.1, the feedwater pumps are modelled by TMDPJUN 401 (see Figure 17). This component allows the user to simulate any mass flow trend by providing the corresponding timetable. To model the secondary pump coast down the following equation was used, derived from [69]:

$$\bar{\Gamma} = \frac{t_{\frac{1}{2}}}{t + t_{\frac{1}{2}}} \quad 9)$$

Where:

- $\bar{\Gamma}$ is the relative mass flow rate, normalized with respect to the nominal value (see Table 12 and Table 13).
- $t$ is the variable of time
- $t_{\frac{1}{2}}$ is the mass flow rate halving time which is set to 0.01 seconds

The halving time of the secondary flow rate was set based on typical feedwater pumps. For these components, the usual duration of the coast down transient swings from 1 to 5 seconds, according to the IAEA indications provided in [70]. The accidental evolution was investigated without postulating the SGs isolation. Thus, the valves on the feedwater and steam lines are both open.

This accidental sequence is different from the two already discussed. Indeed, given the loss of the heat sink and the unprotected nature of the transient, the reactor experiences a persistent power unbalance. Due to the BCs associated with the scenario considered, the reactor cannot reach a new steady state configuration, as in the previous two cases.

The power trend associated with the ULOHS is shown in Figure 23a. The reactor power monotonically decreases towards the decay heat, that is the only source term still present after about 42 minutes. This is consistent with the trend of the total reactivity (Figure 23b). It experiences a significant drop resulting in continuous negative reactivity feedback due to the system transient behaviour. This produces the shutdown of the fission reaction within the core. More in detail, the loss of the SGs and the unavailability of the DHR system cause an increase in the primary system temperatures. This provokes the occurrence of the corresponding negative reactivity feedback.

The main contributes are the STCs (see Figure 23c and Figure 23d for STAGE 2 and STAGE 3, respectively). A deviation can be detected in Figure 23 between the two stages. The difference is due to the lack in STAGE 2 of the STC-Pads NK feedback. This is because the FA radial pads are designed to be in contact at the STAGE 3 nominal conditions (see Table 3) and to introduce negative reactivity feedback when experiencing a radial expansion greater than the one of the diagrid at the core inlet.

During the ULOHS transient, both inlet and outlet core temperatures increase with a comparable slope due to the heating of the whole primary system. This consideration is valid for both the stages (see Figure 24a). If STAGE 3 is considered, before the PIE occurrence, the pads are already in contact.

Thus, during the accidental evolution, the core temperatures increase produces a relative radial expansion of these components and the occurrence of the corresponding NK feedback (green dashed line in Figure 23d). Instead, when it comes to STAGE 2, the core nominal temperatures are lower, and the pads are not in contact before the PIE occurrence.

For this, even if the core temperatures increase with the same slope of STAGE 3, the rise is not enough to produce the relative radial expansion needed to the pads to fill the gap (reminding that the diagrid is contemporarily expanding at the core inlet).

Consequently, the STC-Pads is always zero (see green dashed line in Figure 23c). Another aspect to be commented is related to the FTC. For both the stages, this contribute is initially positive due to the power decrease, resulting in a drop of the fuel temperature (see Figure 24c). Then, in the mid-long term, this parameter restarts to rise due to the heating of the whole primary system. For this, the FTC inverts its trend and begins to decrease. At the end of transient, it is negative for both the calculations and, thus, contributes to the total negative reactivity. However, this aspect is irrelevant since in the long-term the only source term still active is the decay heat, that is unaffected by the NK feedback.

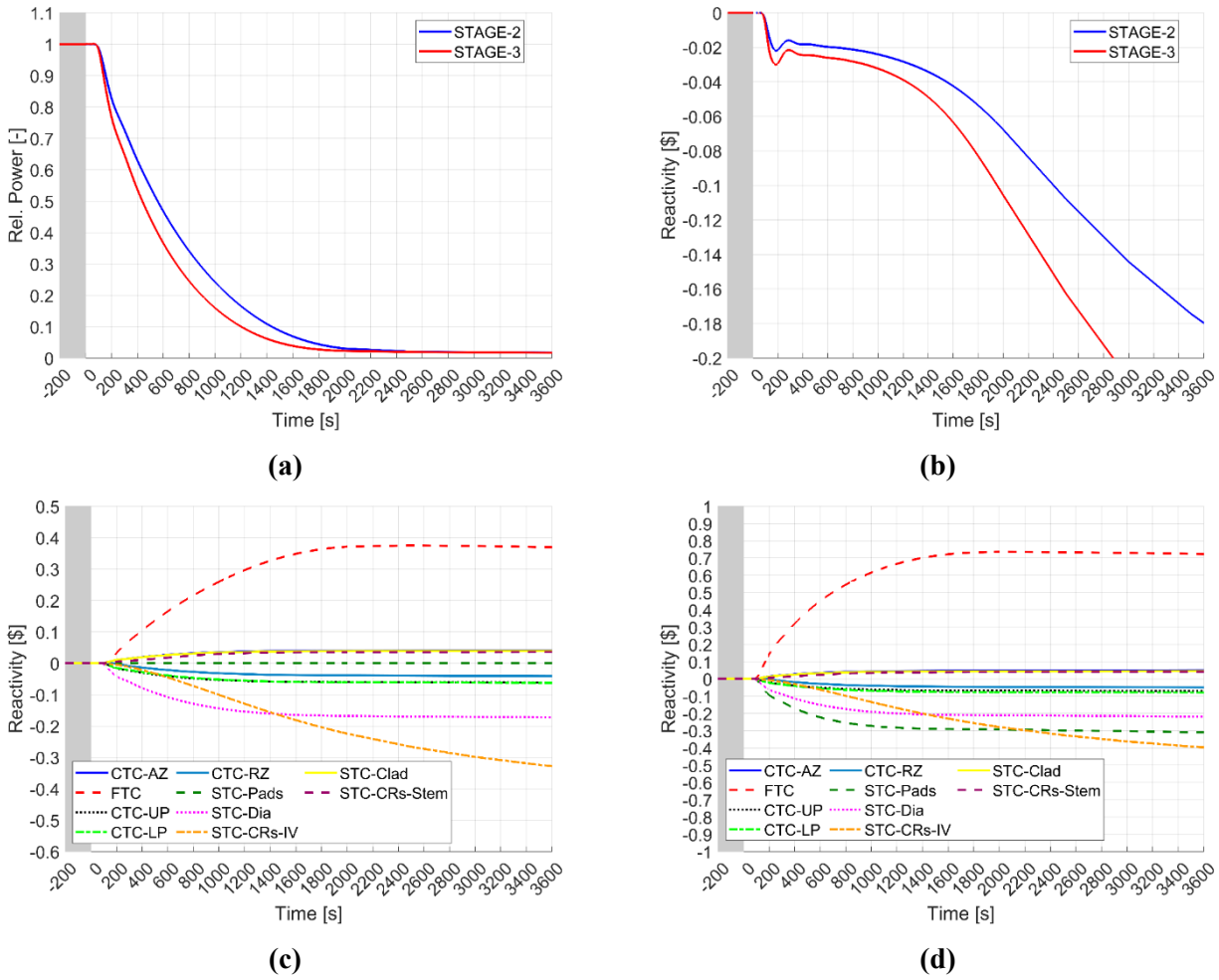


***Figure 23 ULOHS transient: relative reactor power (a), total reactivity (b), STAGE 2 (c) and STAGE 3 (d) NK feedback, in the short/mid-term.***

As depicted in Figure 24a, due to the reduction of the reactor power the lead temperature difference across the core becomes negligible. For the same reason, clad (Figure 24b) and fuel (Figure 24c) temperatures approach the coolant ones.

For what concerns the lead and clad temperatures, the main effect is the loss of the heat sink (i.e., both the SGs and the DHR system) and the consequent heating of the whole primary system. For this, the associated time trends monotonically rise.

Instead, referring to the fuel temperature, it initially drops due to the reactor shutdown. Once approached the other system temperatures, i.e., coolant and clad, it experiences the same heating. Nevertheless, for the whole simulation time considered for the two cases (i.e., the grace time related to the clad CDF), this parameter keeps well below its nominal value.

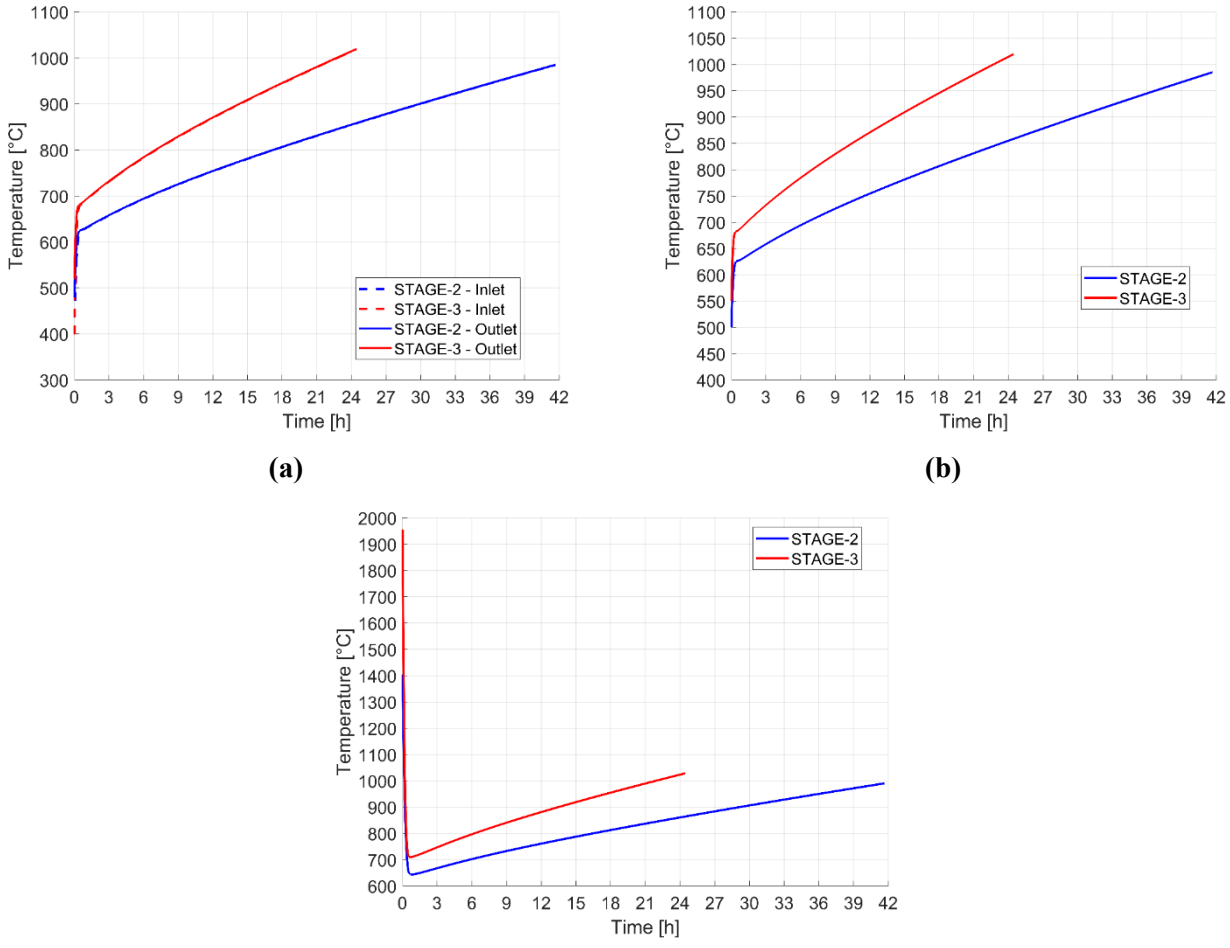


***Figure 24 ULOHS transient: core inlet/outlet temperatures (a), maximum clad temperature (b) maximum fuel temperature (c).***

As shown before, the SGs cannot remove the long-term thermal power generated within the core due to the decay heat, and the DHR system is not available as postulated in this transient. Thus, the primary system average temperature constantly increases. For this accident, to evaluate the thermal creep behaviour of the cladding steel, a Cumulative Damage Function (CDF) approach has been adopted. This is a widely spread and validated criterion to assess the steel failure [71]. The CDF can be defined as follows:

$$\mathrm{CDF} = \sum_i \frac{\Delta t_i}{t_{R,i}} \qquad 10)$$

Where:

- $\Delta t_i$ is the simulation time-step.
- $t_{R,i}$ is the rupture time (calculated with Equation 8).

The reactor grace time related to this accident was preliminarily defined as the time required for the CDF to reach the unity. As already said, $t_{R,i}$ was computed with Equation 8), where the maximum cladding temperature (shown in Figure 24b) was used.

With this methodology, the reactor grace time is equal to approximately 42 hours for STAGE 2 and 23 hours for STAGE 3. The calculations were stopped when the simulation time approaches these values. The time evolution of the CDF is shown in Figure 25. For both cases, the CDF profile has an exponential trend. In addition, the one of STAGE 3 shows a steeper slope, due to the higher temperatures characterizing this scenario.

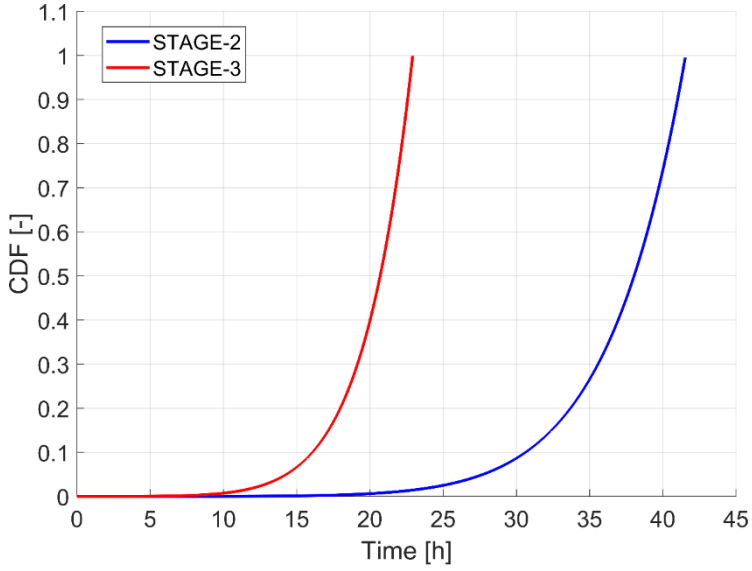


***Figure 25 ULOHS transient: time evolution of the clad CDF***

## 3.4.SIRIO

As part of the development of Generation IV reactors, passive safety systems have become a focal point due to their inherent reliability and independence from active components [49]. These systems rely on natural physical mechanisms—such as gravity, natural circulation, and thermal expansion—to maintain reactor safety during abnormal conditions. In the case of ALFRED, the design and implementation of a passive DHR system are particularly critical due to the high freezing point of the primary coolant, liquid lead (327 °C). Effective removal of decay heat is essential to avoid coolant freezing and ensure system integrity during postulated accident scenarios.

To meet this challenge, an innovative self-regulating DHR system was developed for ALFRED (for more details see Section 3.1). Its operating principle is based on the controlled degradation of condensation efficiency caused by the presence of non-condensable gases, which serves as a self-limiting mechanism for the heat removal process. In support of this concept, the SIRIO experimental facility was designed and constructed to investigate the performance and underlying physics of this novel passive safety system. The results from SIRIO contribute to both the experimental validation and the refinement of numerical modelling approaches for ALFRED's passive DHR design.

### *3.4.1. Description of the facility*

The SIRIO facility [72] (SIstema di RImozione della potenza di decadimento per reattori nucleari innOvativi, Decay heat removal system for innovative nuclear reactors), owned by ENEA and located at the SIET laboratories in Piacenza (Italy), was originally designed and constructed within the SIRIO project [73] to experimentally investigate passive DHR systems for advanced nuclear reactors.

The innovative DHR concept tested in SIRIO aims to ensure safe and long-term cooling of the RCS without relying on external power sources or operator intervention. It achieves this through passive control of the heat removal rate via the self-actuated injection of NGs into the IC tubes in response to the declining decay heat over time. As decay power decreases, the reduction in steam pressure inside the loop allows the NGs—stored in the Non-condensable Gas Tank (NGT)—to progressively enter the IC. Their increasing partial pressure within the tubes degrades condensation heat transfer, thereby reducing the removed power and passively balancing it with the residual core power. This mechanism also helps maintain the IC outlet temperature at sufficiently high levels, preventing the ingress of cold water that could otherwise cause premature lead solidification in the steam generator. This strategy is particularly relevant for LFRs, where effective cooling must be ensured while preventing the early freezing of lead, which has a high melting point.

The design of SIRIO follows a "power-to-volume" scaling methodology, preserving the ratio of thermal power to fluid volume—i.e., power density—between the experimental facility and the prototype system. Additionally, key parameters such as operating pressure, component elevations, and relative heights are conserved, ensuring that natural circulation driving forces are accurately represented.

It should be noted that the entire design process of the SIRIO facility, was based on the ALFRED reactor design as defined in the LEADER configuration.

The scaling factor was derived from the ratio between the NGT volume foreseen for ALFRED and the volume of the available tank at SIET, which was originally employed as the Emergency Boration Tank (EBT) in the SPES-3 facility [74]. This approach ensures that the thermal-hydraulic behaviour observed in the scaled facility remains representative of the full-scale system. Therefore, the scaling factor results in:

$$SF = \frac{ALFRED\ NGT}{SIET\ EBT} = \frac{6\ m^3}{0.127\ m^3} = 47.244 \tag{11}$$

By maintaining the same height and radial geometry as in the reference design, the number of tubes in the SIRIO SG was calculated as follows:

$$N_{SIRIO\ SG\ tubes} = \frac{N_{ALFRED\ SG\ tubes}}{SF} = \frac{510}{47.244} = 10.795 \approx 11\ tubes \tag{12}$$

where the result of this ratio was then rounded to the nearest integer value to determine the final number of tubes. The evaluation of the power to be supplied to the SIRIO SG is based on the SG duty of ALFRED. Furthermore, since SIRIO is designed to be representative of the ALFRED SG operating in DHR mode, only 7% of the scaled power corresponding to an ALFRED SG tube is applied to the SIRIO tube.

$$\dot{Q}_{SIRIO} = \frac{\dot{Q}_{ALFRED}}{N_{ALFRED\ SGs} \cdot SF} \cdot 7\% = \frac{300}{8 \cdot 47.244} \cdot 7\% \approx 55\ kW \tag{13}$$

For the evaluation of IC number of tubes, following the same considerations of Equation 12):

$$N_{SIRIO\ IC\ tubes} = \frac{N_{ALFRED\ IC\ tubes}}{SF} = \frac{16}{47.244} = 0.339\ tubes \tag{14}$$

Equation 14) indicates that the required number of tubes is less than one. Consequently, a single tube was selected, but with a reduced length compared to the full-scale configuration by scaling the heat transfer area:

$$L^*_{SIRIO\ IC\ tube} = L_{ALFRED\ IC\ tube} \cdot N_{SIRIO\ IC\ tubes} = 2\ m \cdot\ 0.339\ tubes = 0.678\ m \tag{15}$$

In order to compute the total heat transfer area of the full-scale system also the collectors have to be considered (for the geometry details see Table 7). The collector is a sphere with an internal heat transfer area of:

$$S_{ALFRED\ IC\ coll} = 4 \cdot \pi \cdot \left(\frac{ID_{ALFRED\ IC\ coll}}{2}\right)^2 = 4 \cdot \pi \cdot \left(\frac{0.44}{2}\right)^2 = 0.608\ m^2 \tag{16}$$

Given that the tubes have an inner diameter of 29.46 mm, the equivalent length of the collectors can be calculated as:

$$L_{ALFRED\ IC\ coll\ eq} = 2 \cdot \frac{S_{ALFRED\ IC\ coll}}{\pi\ ID_{ALFRED\ IC\ tube}} = 2 \cdot \frac{0.608\ m^2}{\pi\ 0.02946\ m} = 13.138\ m \tag{17}$$

The total equivalent length of SIRIO IC is:

$$L_{SIRIO\ IC\ eq} = L^{*}_{SIRIO\ IC\ tube} + \frac{L_{ALFRED\ IC\ coll\ eq}}{SF} = 0.678\ m + \frac{13.138\ m}{47.244} = 0.956\ m \quad 18)$$

Although the scaling was originally based on the ALFRED design developed within the LEADER project, and subsequent updates have introduced modifications to the most recent FALCON configuration, the resulting scaling remains representative of the ALFRED system. Table 14 presents a comparison of the main features of the original ALFRED design, the updated STAGE 2 configuration, and the SIRIO facility.

***Table 14 Comparison between ALFRED (LEADER), ALFRED (FALCON STAGE 2) and SIRIO***

| **Parameter** | **ALFRED (LEADER)** | **ALFRED (STAGE 2)** | **SIRIO** |
|---|---|---|---|
| **Total Power** | 300 MW | 200 MW | 55 kW |
| **Number of Steam Generators** | 8 | 3 | 1 |
| **Number of tubes (x1 SG)** | 510 | 880 | 11 |
| **SG tube type** | double wall bayonet | single wall bayonet | single wall bayonet |
| **Number of coaxial tubes** | 4 | 3 | 3 |
| **Tube length [m]** | 6 | 6 | 6 |
| **SG Heat source** | Nuclear | Nuclear | Electrical |
| **IC tubes** | 16 x 2 m | 16 x 2 m | 1 x 0.68 m |
| **IC collectors' inner diameter [m]** | 0.44 | 0.44 | - |

Table 15 presents the deviations introduced by the scaling procedure on key operational parameters, with particular focus on thermal flux and power density. Due to practical constraints—such as the use of commercially available piping—some components could not fully comply with the ideal theoretical scaling. The discrepancy (Δ) between theoretical and adopted scaling was calculated as follows:

$$\Delta = \frac{X_{theoretical} - X_{SIRIO}}{X_{theoretical}} \quad 19)$$

Where $X$ representing the parameter being scaled. The resulting distortions include approximately -1.0% for thermal flux and decay power. Additional deviations were observed in volume parameters, including +13.0% for water volume, -1.8% for gas volume, and +1.63% for the combined water and gas volume.

These variations lead to a distortion of about +11.5% in power density, when based on the total stored water volume. When comparing the SIRIO facility to the ALFRED design in its original configuration, distortions of -2.86% for thermal flux and -12.4% for power density are observed.

Comparisons with the updated ALFRED STAGE 2 configuration indicate a deviation of -5.7% for thermal flux and +13.1% for power density. Despite these discrepancies, the SIRIO facility remains representative of both ALFRED design versions, as the deviations are within an acceptable range and do not significantly affect the preservation of key physical phenomena.

***Table 15 Deformation of SIRIO with respect to the theoretical scaling and variation to ALFRED***

| Parameter | Unit | Deformation Scaled Facility – SIRIO | Variation to ALFRED (LEADER) | Variation to ALFRED (STAGE 2) |
|---|---|---|---|---|
| **Decay Power** | kW | -1% | -- | -- |
| **Power/tube** | kW | -1% | -2.9% | -5.7% |
| **Thermal flux** | $kW/m^2$ | -1% | -2.9% | -5.7% |
| **Water volume** | L | 13.0% | -- | -- |
| **Gas volume** | L | -1.8% | -- | -- |
| **Total volume** | L | 1.6% | -- | -- |
| **Power density** | kW/Lwater | 11.5% | -12.4% | 13.1% |

A simple scheme of the SIRIO facility is shown in Figure 26 while a 3D-drawings is provided in Figure 27. Finally, the main components constituting the experimental plant are:

- SG (see Figure 28), comprising 11 BTs, each of them being immersed in a pipe filled with molten salts to replicate the lead thermal inertia. These tubes are enveloped in an electrical heating cable to feed the power input while molten salts prevent burnout due to oscillations in the two-phase mixture level. The inner-most tube of each BT is 3 meters long (half the total bayonet length), and the annular space between the first and second tubes is filled with stagnant water to thermally insulate the downcomer from the riser.
- IC housed within a water pool as depicted in Figure 29, constituted by a single tube, an upper and a lower header. The latter is connected to the gas line.
- By-pass Heat eXchanger (HX) located to the bypass line, comprising 2 tubes within a water pool, in order to remove the steady-state thermal power. A 3D representation of the HX, along with the IC, is shown in Figure 30.
- NGT connected to the lower header of the IC, storing NG (air).
- Two independent cooling pools for the HX and the IC acting as final heat sinks.

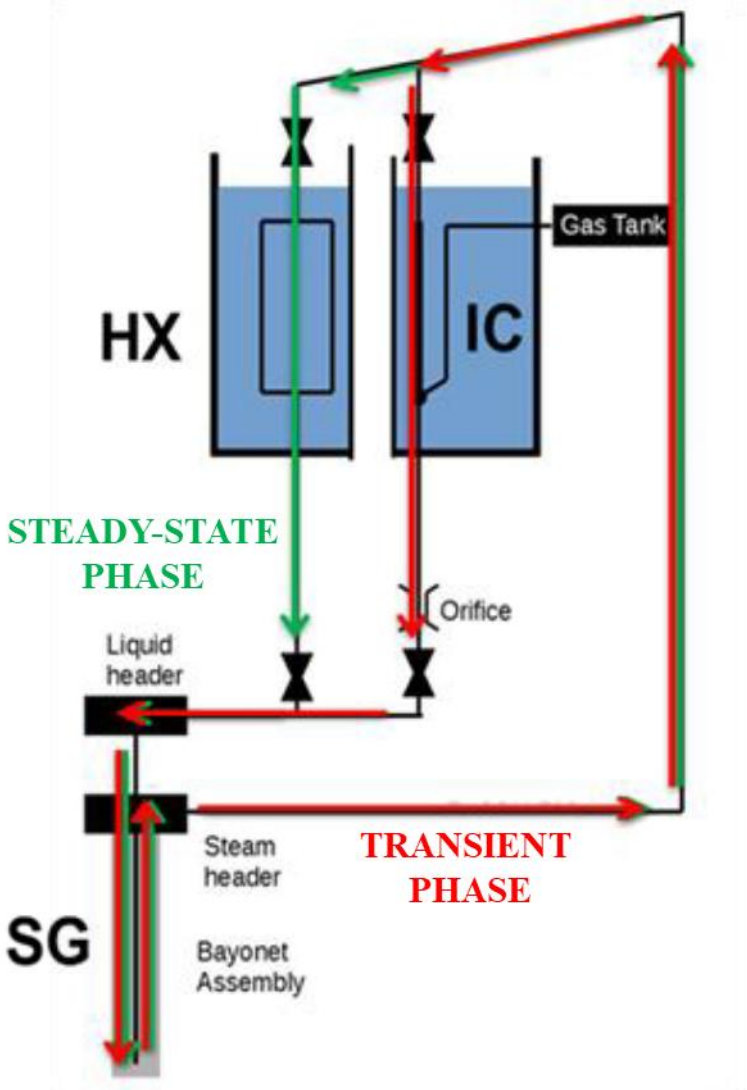


*Figure 26 Conceptual scheme of SIRIO*

*Figure 27 SIRIO general arrangement*

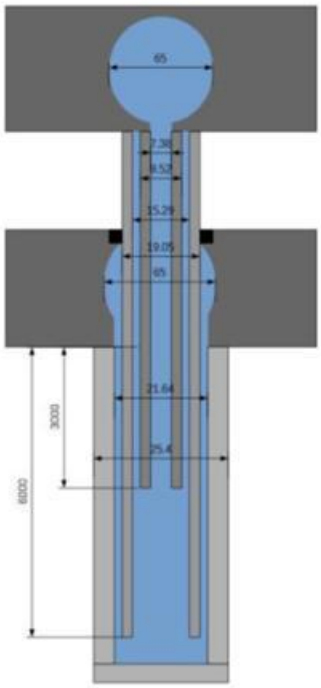

*(a)*

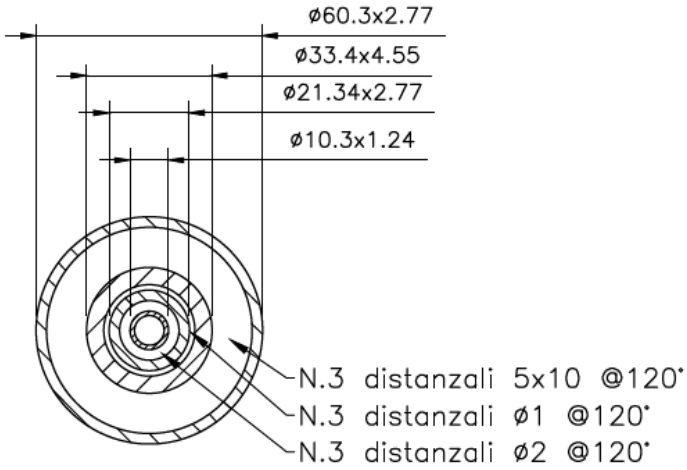


*(b)*

*(c)*


*(d)*

***Figure 28 SIRIO SG: bayonet tube geometry (a), tubes cross section view (b), bayonet tube picture (c) and head picture (d)***

***Figure 29 SIRIO IC picture***

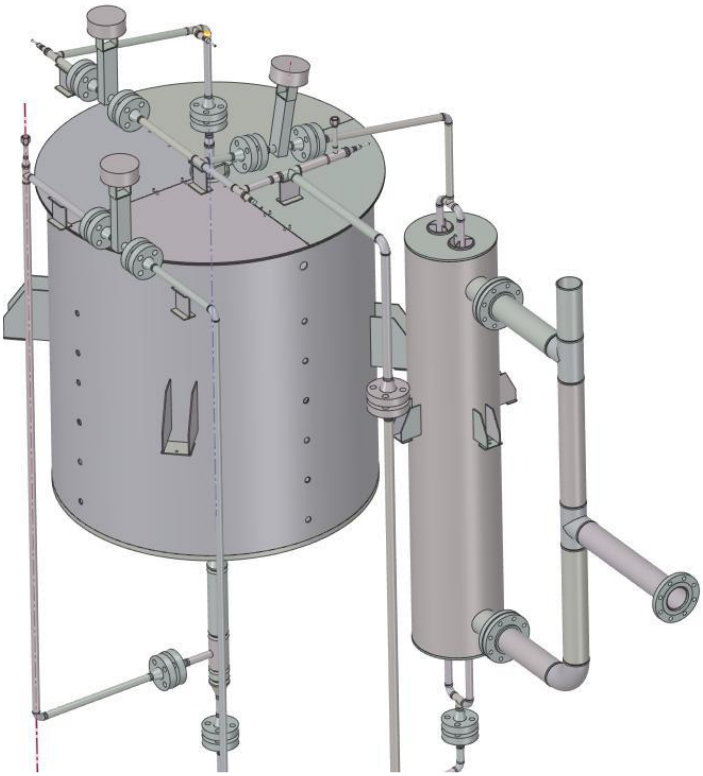

***Figure 30 SIRIO IC and HX 3D-drawing***

### 3.4.2. Experiment description

The experimental test analysed in this work was conducted as part of Work Package 3 of the PIACE project [75]. The corresponding post-test analyses were performed under Work Package 4.1, which focused on system prototype design and behavioural system analysis [76].

The SIRIO facility is designed to operate in two distinct modes: “Steady-State” and “Transient” phase. During the Steady-State phase, the fluid flows through the loop formed by the SG and the HX (green arrows, see Figure 26). In this configuration, the valves located upstream and downstream of the IC are closed, while those connected to the HX are fully open. Natural circulation drives the loop: the working fluid enters the SG, absorbs thermal power—set to a constant 55 kW provided by electrical heaters—and exits the SG. The fluid then flows into the HX, where it releases heat to the surrounding water pool completing the loop. The steady state is achieved by adjusting the water level in the HX pool until the power balance is achieved.

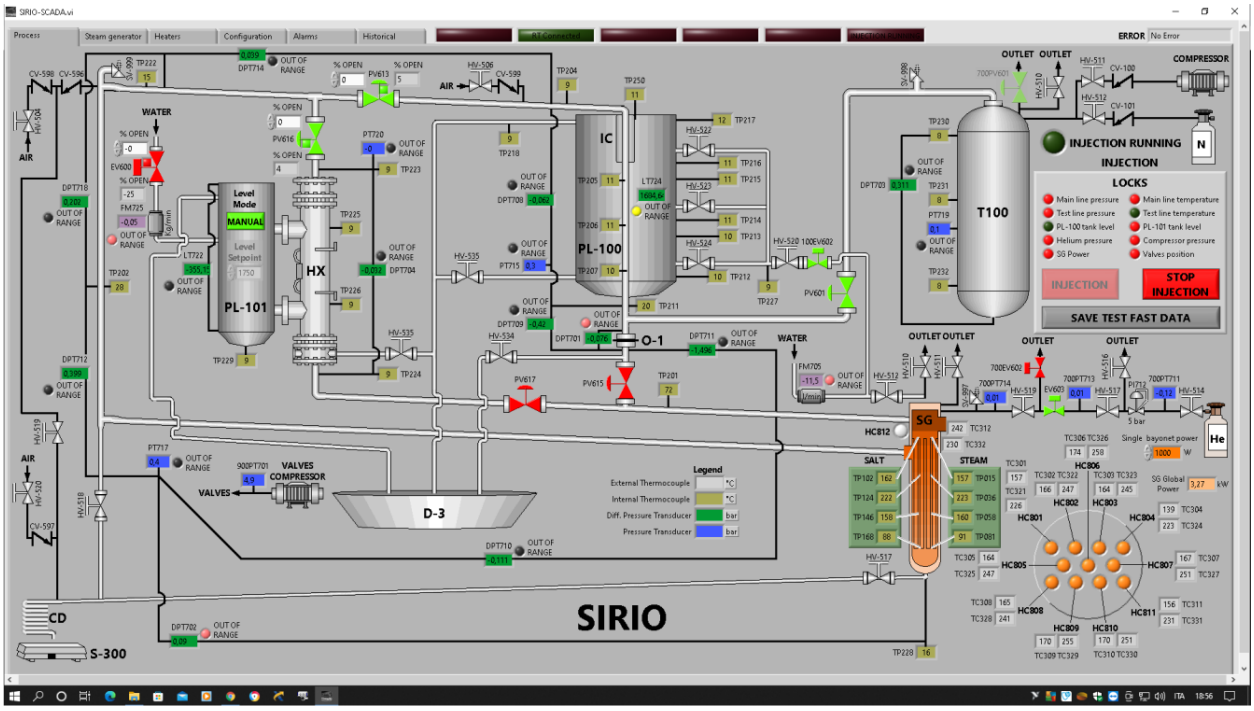


*Figure 31 SIRIO synoptic*

Once the target initial conditions are established, the facility transitions to the Transient phase, designed to simulate a Protected Loss of Offsite Power (PLOOP) event. At the Start of Transient (SoT), the valves upstream and downstream of the HX are closed, thereby interrupting the heat releasing path. The fluid, now unable to transfer the thermal power from the SG to the HX, begins to accumulate energy, resulting in a pressure increase. When the pressure reaches the threshold of 190 bar, the valve upstream of the IC opens, allowing steam to enter the IC where it transfers heat to the surrounding pool and condenses. The valve downstream of the IC opens 60 seconds after the upstream one, establishing a natural circulation loop between the SG and the IC.

During this phase, the power supplied by the SG shifts from a constant 55 kW to a decay power profile (see Figure 32). Initially, the decay curve maintains the power at 55 kW for 2000 seconds to represent the thermal inertia of the full-scale primary system.

After this period, the power follows a predefined decay trend, with an additional 5 kW included to compensate for partial heat losses in the system. Minor oscillations observed in the curve are attributed to the control system regulating the electrical power input to the bayonet heaters.

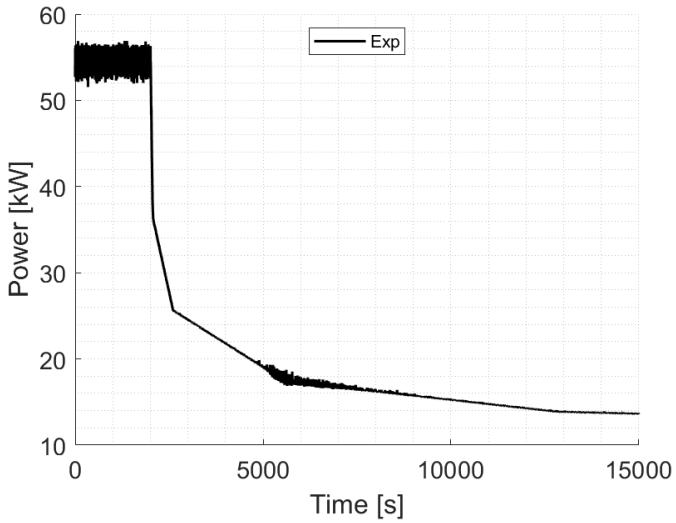


***Figure 32 SG thermal power in Transient phase***

The experimental boundary conditions are summarized in Table 16. The reported water mass inventory refers to the total amount used during the experiment. Any water confined between the HX isolation valves remains excluded from the Transient phase. During the transient, due to the pressure differential between the loop and the NGT, a portion of the fluid inevitably migrates into the NGT. This quantity is subsequently drained and weighed separately to quantify the fluid transfer. The total mass discharged from the loop at the end of the experiment corresponds to the water that actively participated in the transient phase. As a final step, any residual water trapped in the HX is also discharged and measured. Finally, the orifice installed at the bottom of the IC downcomer has a diameter of 5 mm; however, a dedicated experimental sensitivity analysis is planned for future campaigns to evaluate its influence on natural circulation performance during transient operation.

***Table 16 SIRIO experimental boundary conditions***

| **Parameter** | **Unit** | **Value** |
|---|---|---|
| **Water inventory** | kg | 75 |
| **Water pressure** | bar | 180 |
| **Gas pressure** | bar | 110 |
| **Thermal power supplied during the steady state** | kW | 55 |
| **Valve PV-613 set point** | bar | 190 |
| **Valve PV-615 delay** | s | 60 |
| **Orifice diameter** | mm | 5 |

### *3.4.3. Numerical model*

The numerical model of SIRIO facility has been realized through the system thermal-hydraulic code RELAP5/Mod3.3. The model has been realized through PIPE and SINGLE JUNCTION and VALVE components, modelling the regions occupied by the fluid, and HEAT STRUCTUREs that model the structural part of the facility. As shown in Figure 33, the model is divided into three systems: the first represents the primary loop of SIRIO, and the other two are the ultimate heat sinks on the pool side of the HX and IC.

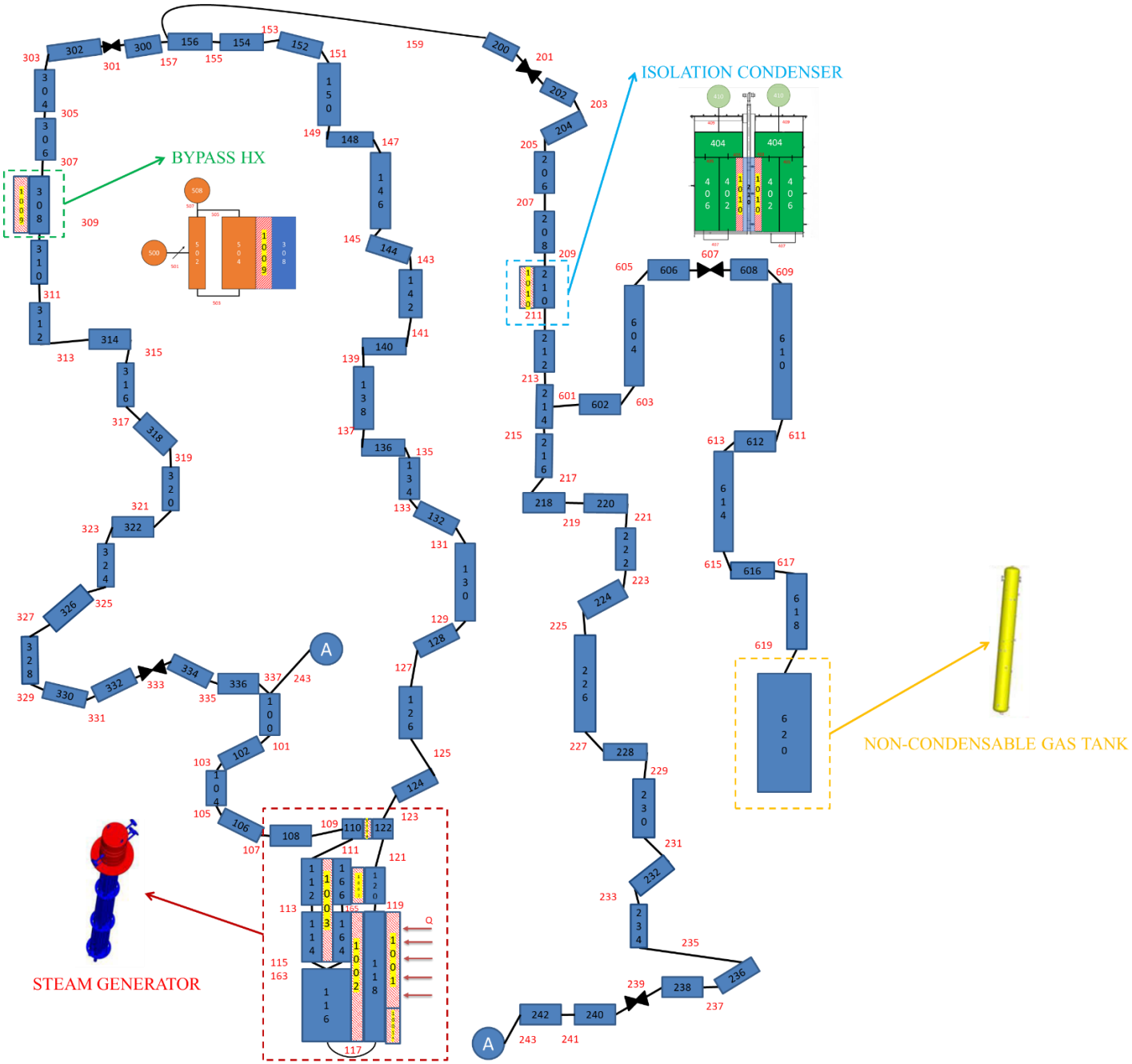


*Figure 33 R5 nodalization scheme of SIRIO*

The first digit of the hydrodynamic components number identifies a specific system as follows:

- "1XX" for the SG and the branch involved in both Steady-State and Transient phase
- "2XX" for the IC tube side and the branch involved in the Transient phase
- "3XX" for the HX tube side and the branch involved in the Steady-State phase
- "4XX" for the IC pool side
- "5XX" for the HX pool side
- "6XX" for the NGT and the NG line

Particular attention is paid on the modelling of molten salts since the thermodynamic properties of the fluid are not implemented in RELAP5/Mod3.3, and the expected heat transfer mechanism are natural convection and axial conduction within the molten salts, which cannot be modelled by the code.

A HS is implemented as a heat source simulating the heating cables, with thermophysical properties of those of the Dynalene MS-2 molten salts [77]. The whole loop is insulated with 5 cm rockwool modelled through several passive HSs (not shown in the figure), the room temperature is assumed to be 15 °C, and the HTC with the environment is equal to 8 W/m$^2$K. To ensure thermal balance, a proportional control system modulated the water level in the HX pool to offset the net power delivered to the fluid—that is, the input power from SG (55 kW) minus the system's intrinsic heat losses.

$$\Delta\Gamma = K_P\, e(t) \tag{20}$$

where:

- $\Delta\Gamma$ is the mass flow rate variation injected in the HX pool side
- $K_P$ is the proportional constant
- $e(t)$ is the error based on a setpoint (fixed level setpoint)

The calibration of the orifice pressure drop was performed during the commissioning phase through preliminary characterization tests using liquid water at ambient pressure and temperature. Based on the measured pressure drop, the mass flow rate during the experiments can be estimated using an established correlation, as shown in Figure 34. Absolute pressure and temperature measurements were used to determine key fluid properties such as density and viscosity. For the evaluation of the orifice pressure loss coefficient, only the frictional pressure drop was considered, excluding the gravitational contribution. The latter was subtracted using the following relation:

$$K = \frac{2 \cdot (\Delta p + \rho \cdot g \cdot H) \cdot \rho \cdot A^2}{\Gamma^2} \tag{21}$$

where:

- $K$ is the pressure loss coefficient.
- $\Delta p$ is the experimentally measured pressure drop across the orifice.
- $\rho$ is the fluid density.
- $H$ is the vertical distance between the pressure measurement points located upstream and downstream of the orifice.
- $A$ is the flow area
- $\Gamma$ is the mass flow rate

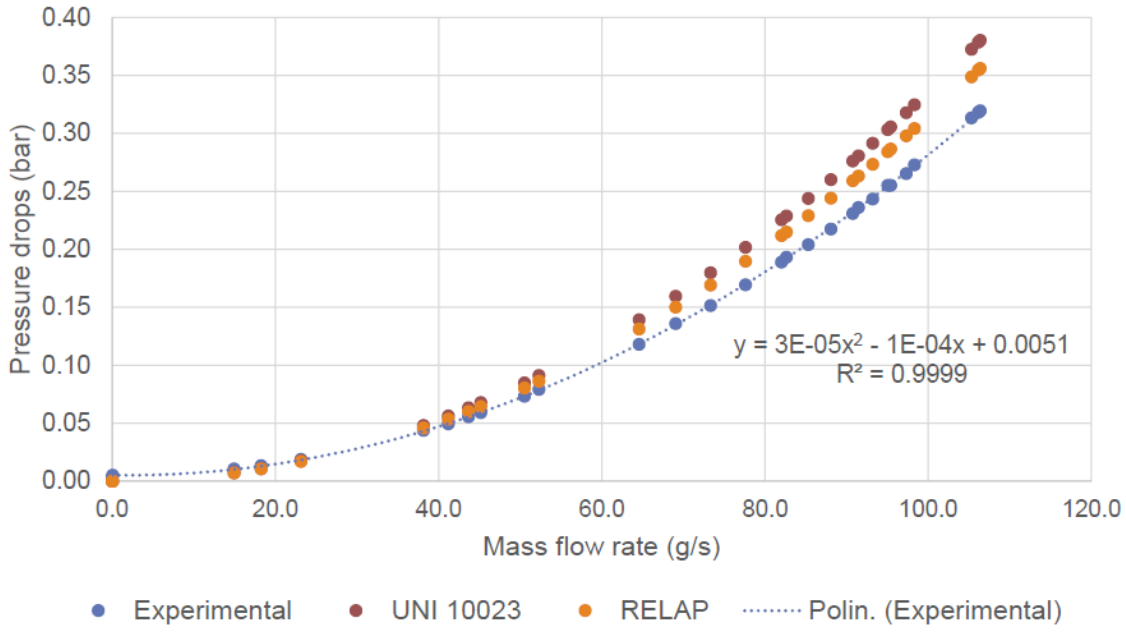


***Figure 34 Hydraulic characterization of the orifice***

Finally, based on the experimental points shown in Figure 35, a Reynolds-dependent pressure loss coefficient has been evaluated and implemented in the JUNCTION component representing the orifice:

$$K_{R5\ orifice} = 500 + 2 \cdot 10^{6} \cdot Re^{-1} \qquad 22)$$

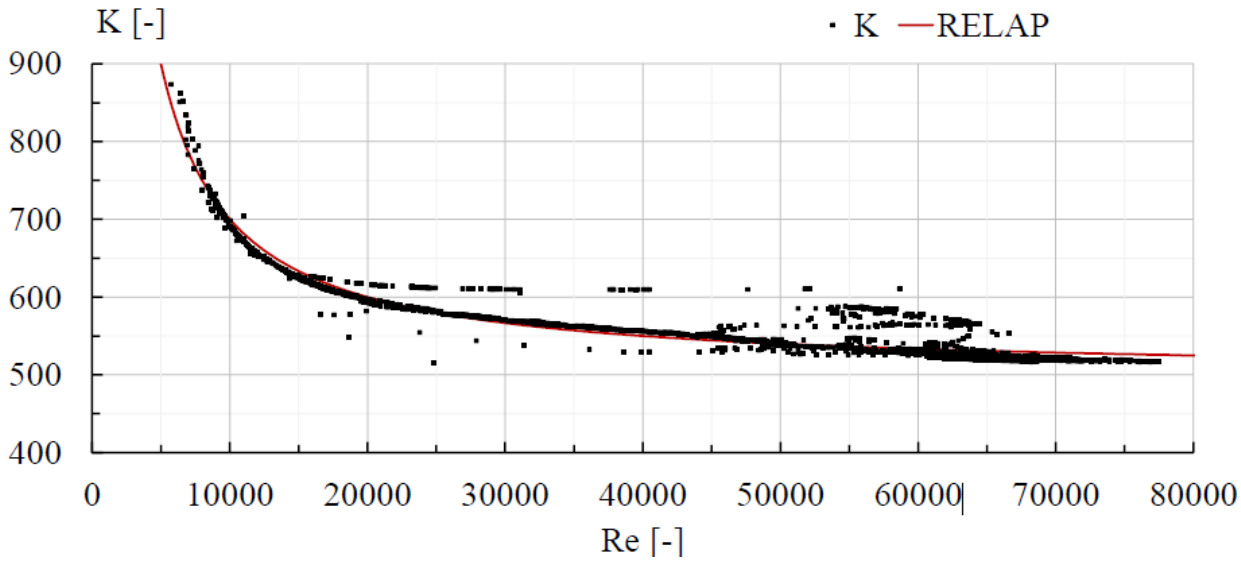


***Figure 35 Calibration of the orifice pressure loss coefficient***

Finally, although the numerical model reproduces the geometry of SIRIO, several code-related limitations are recognized and were explicitly examined within the PIACE framework. One concern involves heat transfer across the closed annular cavity separating the riser and downcomer SG BTs. This region can contribute to regenerative heat exchange within the SG; however, it could not be directly characterized experimentally because instrumentation was not available inside the BT downcomer. For the present analysis, the cavity was therefore modelled as a bounded fluid volume with no through-flow, providing a conservative but simplified representation.

A second limitation arises from the inherent difficulty of modelling pool thermal-hydraulics (stratification, mixing, natural convection) using 1D system code components. To partially mitigate this, a refined nodalization strategy was adopted: the IC pool was represented by two parallel 1D PIPE components—conceptually corresponding to inner and outer pool regions—interconnected by cross junctions to promote limited inter-region mixing. Post-test comparisons between measured pool temperature distributions and RELAP5 predictions showed that this segmented representation improved the code's ability to reproduce observed stratification and mixing trends, though full multi-dimensional fidelity remains beyond the scope of a 1D system analysis.

Sapienza University of Rome (UNIROMA1) introduced several modifications to the default version of RELAP5 to better capture the specific phenomena expected in the analysed configurations.

In particular, special attention was given to the simulation of pool boiling on the pool side of the IC, where nucleate pool boiling is expected. Since the standard RELAP5 version does not include a dedicated correlation for nucleate pool boiling, the Chen correlation [78]—originally developed for flow boiling—was adopted.

Instead, in the version used in this work, UNIROMA1 selected the Cooper correlation [79] to model pool boiling:

$$h = 55(p_r^{0.12-0.2\log\varepsilon})(-\log p_r)^{-0.55}\, M^{-0.5} q''^{0.67} \quad (23)$$

In which:

- $h$ is the heat transfer coefficient
- $\varepsilon$ is the surface rugosity
- $p_r$ is the reduced pressure
- $M$ is the fluid molecular weight
- $q''$ is the heat flux

Extensive validation campaign conducted by UNIROMA1 [80][81] to test this correlation against experimental data coming from PERSEO facility [82].

Finally, a comprehensive investigation of condensation phenomena—both in pure steam and in the presence of NG—was carried out as part of this work. Significant modifications were implemented in the RELAP5/Mod3.3 source code to improve its predictive capabilities in modelling these processes, particularly under low-pressure and low-flow-rate conditions relevant to passive systems. An extensive validation campaign was also conducted to assess the accuracy of the implemented correlations and ensure their applicability to experimental data. All these developments, including the theoretical background, implementation strategy, and validation results, are thoroughly discussed in Section 3.4.4.

### *3.4.4. Investigation on pure condensation and condensation with non-condensable gas*

Based on the post-test analysis performed in the framework of PIACE project [76], the need for a detailed investigation of condensation heat transfer mechanisms emerged, with a specific focus on both pure steam condensation and condensation in the presence of NG. This analysis was essential to improve the predictive accuracy of RELAP5/Mod3.3 in scenarios relevant to passive safety systems.

PURE STEAM CONDENSATION REVIEW

Condensation can be broadly categorized into two main regimes: gravity-controlled and shear-controlled.

Gravity-controlled condensation occurs when the gas phase is nearly stagnant, meaning the gas velocity is much lower than the liquid velocity. In this regime, heat transfer primarily occurs through conduction across the liquid film, as described by classical laminar film theory (Nusselt theory), although convective contributions may arise if the film becomes turbulent. Within the gravity-controlled regime, three sub-regimes are typically identified: laminar regime, laminar-wavy regime, and turbulent regime.

Laminar regime is described by the Nusselt theory [83], heat transfer occurs solely by conduction across the liquid film. The corresponding heat transfer coefficient correlation, also implemented in RELAP5, is:

$$h_{Nu} = \frac{k_l}{\delta_z} = k_l \left(\frac{\nu_l^2}{g}\right)^{-\frac{1}{3}} 1.1\ (Re_l')^{-\frac{1}{3}} \tag{24}$$

Laminar-wavy regime occurs when the film Reynolds number exceeds a critical transition value (typically around 30), surface waviness enhances heat transfer by promoting internal mixing within the film. To account for this effect, the Kutateladze correlation [84] was implemented in RELAP5 by UNIROMA1 in 2020.

$$h_{Kut} = k_l \left(\frac{\nu_l^2}{g}\right)^{-\frac{1}{3}} 0.756\ (Re_l')^{-0.22} \tag{25}$$

Turbulent regime occurs at higher film Reynolds numbers, the condensate film develops both a laminar sublayer and a turbulent region, where convective heat transfer becomes dominant. Although the Blangetti-Schlunder correlation [85] accurately describes this regime, it is not natively included in RELAP5. This correlation predicts a rising heat transfer coefficient with increasing film turbulence.

$$h_{Bla} = k_l \left(\frac{\nu_l^2}{g}\right)^{-\frac{1}{3}} 0.00402\ (Re_l')^{0.4}\ Pr_l^{0.65} \tag{26}$$

In addition to these, the Labuntsov correlation [86] is another well-known empirical correlation available in the literature, which provides an alternative formulation for gravity-controlled condensation.

$$h_{Lab} = k_l \left(\frac{\nu_l^2}{g}\right)^{-\frac{1}{3}} 0.023\ (Re_l')^{0.25}\ Pr_l^{0.5} \tag{27}$$

On the other hand, shear-controlled condensation arises when the gas phase velocity significantly exceeds the liquid phase velocity. In such conditions, shear forces from the vapor flow act on the condensate film, inducing turbulence and potentially entraining droplets into the core flow (particularly under annular flow conditions). These effects reduce the film thickness and enhance heat transfer to the wall. Importantly, in shear-controlled regimes, the orientation of the condensation surface becomes less significant. The Shah correlation [87], which has already been implemented in RELAP5 is the following:

$$h_{Shah,1979} = h_{LS}\left(1 + \frac{3.8}{Z^{0.95}}\right) \quad 28)$$

$$h_{LS} = 0.023\, Re_{LS}^{0.8}\, Pr_{LS}^{0.4}\, \frac{k_l}{D} \quad 29)$$

$$Z = \left(\frac{1}{x} - 1\right)^{0.8} p_r^{0.4} \quad 30)$$

However, this correlation presents discrepancies at high pressure which Shah attributed to the viscosity ratio of both phases. The updated Shah correlation [88], shown in Equation 31) has been implemented to the RELAP5 source by UNIROMA1.

$$h_{Shah,2009} = h_{Shah,1979}\left(\frac{\mu_l}{14\mu_g}\right)^{(0.0058+0.557p_r)} \quad 31)$$

A schematic representation of gravity-controlled film condensation is provided in Figure 36, while Figure 37 illustrates the behaviour of the nondimensional heat transfer coefficient as a function of the condensate Reynolds number under gravity-dominated conditions.

It is important to note that even in cases where the condensation process initially occurs under shear-dominated conditions—due to high vapor velocities—the mechanism may gradually transition to a gravity-controlled regime toward the end of the condensation path. This occurs as the vapor progressively condenses along the tube, leading to a reduction in its velocity. As discussed by Papini and Cammi [89], this shift is particularly relevant at low vapor qualities, where the Shah correlation tends to underpredict the heat transfer coefficient because it does not adequately capture the gravity-dominated behaviour.

In passive safety systems, where typical mass fluxes are relatively low (below approximately 200 kg/m²·s), shear effects are generally negligible. In such cases, the application of more accurate correlations specifically developed for gravity-controlled condensation is essential to properly account for the waviness and turbulence within the condensate film.

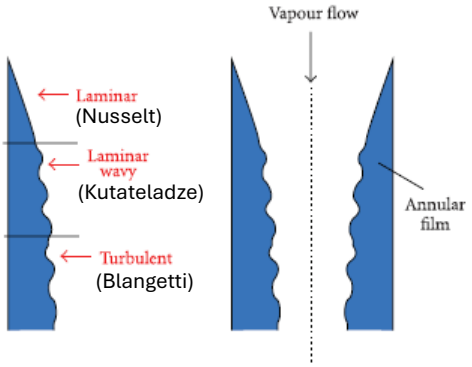


*Figure 36 Film condensation inside a vertical tube*

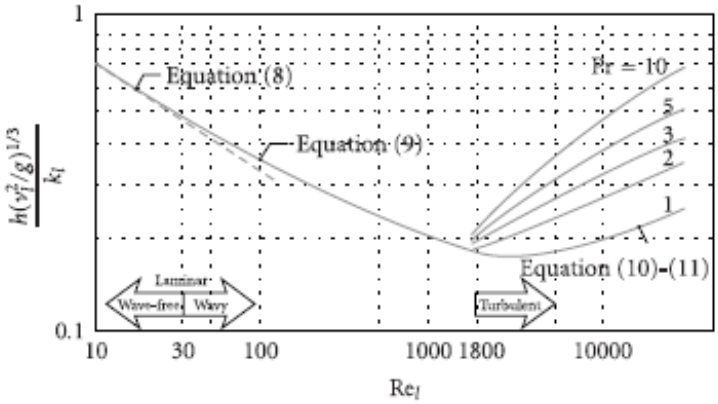


*Figure 37 Nondimensional heat transfer coefficient vs condensate Reynolds number in gravity-controlled film condensation*

CONDENSATION WITH NG REVIEW

NGs as they migrate from the bulk vapor towards the liquid–vapor interface, tend to accumulate at the interface since they do not undergo condensation like steam. This accumulation leads to an increase in the local partial pressure of the non-condensable gases and a corresponding decrease in the steam partial pressure at the interface. As a result, the temperature difference between the steam at the interface and the wall is reduced, ultimately leading to a lower condensation rate as the NCG concentration increases.

Consequently, the common assumption that the bulk gas temperature is equal to the interface saturation temperature (i.e., $T_{bulk} = T_{gas} = T_{spp} \approx T_{interface}$) is no longer valid. Instead, due to the reduced steam partial pressure at the interface, the following condition holds: $T_{bulk} = T_{gas} = T_{spp} > T_{interface}$

Despite this, system codes like RELAP5 maintain this simplified assumption when modelling condensation in the presence of non-condensable gases, effectively neglecting the contribution of sensible heat transfer. Additionally, RELAP5 assumes the validity of the Heat and Mass Transfer Analogy (HMTA), by which the mass transfer coefficient is derived. Under this framework, with the Colburn and Hougen diffusion approach [90], the total heat transferred to the wall—driven by the temperature gradient between the interface and the wall—is assumed to be entirely due to latent heat associated with steam condensation at the interface. The steam partial pressure (and thus the interface temperature) is then calculated iteratively by solving an energy balance equation at the interface.

$$q"_t = q"_l = q"_v \rightarrow h_{cond}\left(T_{gi} - T_w\right) = h_m\, h_{fgb}\, \rho_{vb}\, ln\left(\frac{1-\frac{p_{gi}}{p}}{1-\frac{p_{vb}}{p}}\right) \quad 32)$$

In which:

- $h_{cond}$ is the condensation HTC
- $T_{gi}$ is the water-gas interface temperature
- $T_w$ is the wall temperature

- $h_m$ represents the mass transfer coefficient. It is derived using the HMTA by adapting heat transfer correlations for turbulent, laminar, and natural convection regimes. Specifically, the Nusselt number is replaced by the Sherwood number, and the Prandtl number is replaced by the Schmidt number to obtain the corresponding mass transfer parameters.
- $\rho_{vb}$ is the saturation vapor density, evaluated at the steam partial pressure in the bulk vapor phase ($p_{vb}$). In the default version of RELAP5 it results that $\rho_{vb} = (1 - x_n)\rho_{mb}$ where $x_n$ is the NG mass quality and $\rho_{mb}$ is the combined vapor and gas density in the bulk at the bulk vapor/gas temperature. However, according to Ref. [91], it is recommended to use $\rho_{mb}$ instead of $\rho_{vb}$
- $p_{gi}$ denotes the steam partial pressure at the gas–liquid interface.
- $p$ is the total pressure
- $h_{fgb}$ is the latent heat of vaporization, initially evaluated at the bulk steam partial pressure ($p_{vb}$). However, since condensation physically occurs at the interface, the latent heat should be calculated at the interface pressure ($p_{gi}$). This consideration has been integrated into the RELAP5 source code modifications carried out in the present work. As a result, in the final implementation, $h_{fgb}$ is replaced by $h_{fgi}$, the latent heat of vaporization evaluated at the interface.

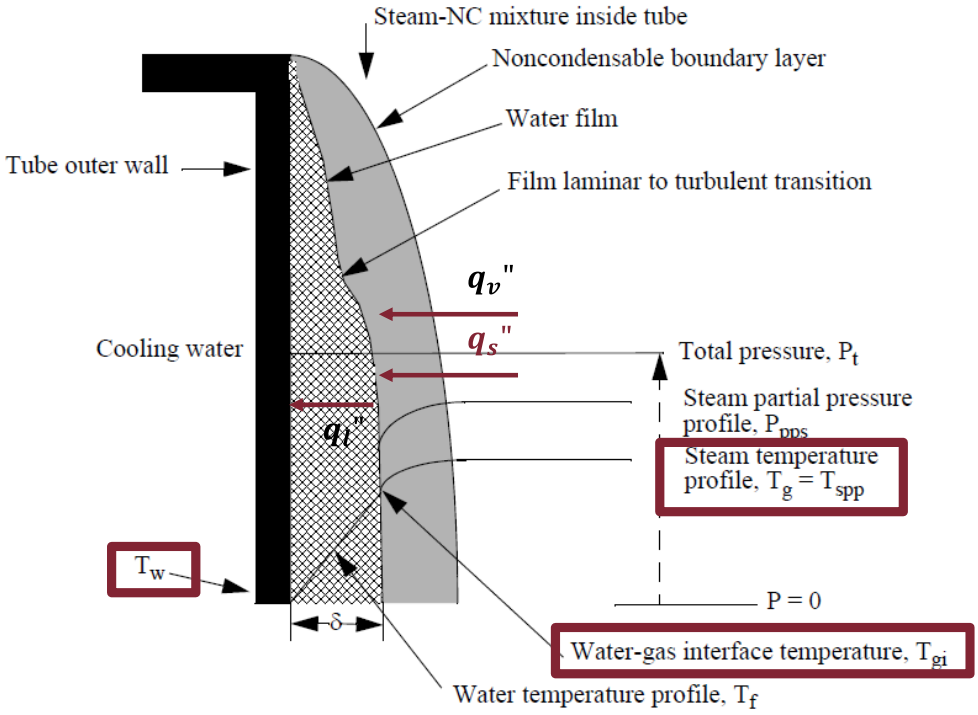


***Figure 38 Scheme of film condensation with NG***

However, it has been recognized that the bulk gas temperature—corresponding to the saturation temperature at the steam partial pressure in the bulk—is higher than the temperature at the gas–liquid interface. This temperature gradient acts as a driving force for sensible heat transfer from the bulk vapor to the interface. Therefore, the traditional energy balance must be revised to include this additional heat contribution crossing the interface. The quantities highlighted in red in Equation 33) are those modified by UNIROMA1.

$$q"_t = q"_l = q"_v + q"_s \rightarrow h_{cond}\left(T_{gi} - T_w\right) = h_m\, h_{fgi}\, \rho_{mb}\, ln\left(\frac{1-\frac{p_{gi}}{p}}{1-\frac{p_{vb}}{p}}\right) + h_s\left(T_b - T_{gi}\right) \qquad 33)$$

## VALIDATION CAMPAIGN

To assess the reliability and accuracy of the modifications introduced into the RELAP5 source code for modelling condensation phenomena—both in pure steam and in the presence of non-condensable gases—a dedicated validation campaign was carried out. This campaign involved comparisons between simulation results and experimental data from reference facilities, aiming to verify the improved predictive capabilities of the updated model under relevant thermal-hydraulic conditions.

Throughout this section, the percentage deviation between the experimental results and the numerical predictions—obtained using both the default version of RELAP5 and the version modified by UNIROMA1—is calculated using the following expression:

$$\Delta_{G,exp} = \frac{G_{R5} - G_{exp}}{G_{exp}} \cdot 100\% \quad (34)$$

$$\Delta_{G,R5} = \frac{G_{NEW\ R5} - G_{OLD\ R5}}{G_{OLD\ R5}} \cdot 100\% \quad (35)$$

where $\Delta_{G,exp}$ represents the deviation (in percentage) of a specific quantity $G$, with $G_{exp}$ being the experimental value and $G_{R5}$ the value predicted by the RELAP5 simulation, while $\Delta_{G,R5}$ is the variation of a specific quantity $G$ evaluated by both version of RELAP5.

The first dataset is derived from the experimental campaign conducted by Caruso et al. (Ref. [92]). Out of the 160 tests performed, 38 were selected—23 involving pure steam condensation and 15 involving condensation in the presence of non-condensable gases. The selected tests are those that best approximate the operating conditions of the SIRIO IC.

Table 17 presents the results of the 23 pure steam condensation tests, comparing the predictions from the default and modified versions of RELAP5. The table reports the percentage deviations in thermal power and condensation length relative to experimental data. It can be observed that the predicted heat transfer power remains largely consistent between the two RELAP5 versions, with deviations from experimental values ranging from -1% to 8%. In terms of condensation length, several tests indicate that the modifications introduced by UNIROMA1 result in improved agreement with experimental measurements compared to the default version. As regards the tests with NG, the comparison results of the thermal power are reported in Table 18. Significant improvements are observed with the modified version of RELAP5, which enhances the accuracy of numerical predictions. While the default version shows deviations from experimental data ranging from –39% to –1%, the modified version reduces these discrepancies to a range between –14% and 1%.

The second dataset comes from the experimental campaign performed by Siddique (Ref. [93]). Among the 74 tests carried out, 24 were selected of which 13 tests with air and 11 tests with helium.

In this case as well, the modified version of RELAP5 demonstrates significant improvements in predicting heat exchange power. For both air and helium cases, the implemented changes enhance the numerical accuracy by reducing the deviation from experimental results. In the air cases, deviations observed with the default version of RELAP5 range from –27% to –13%, whereas with the modified version, they are reduced to a range between –9% and 3%. Similarly, for helium cases, the deviations improve from a range of –11% to 7% (default version) to –7% to 9% with the modified version.

***Table 17 Pure steam experiments vs RELAP5 default and UNIROMA1 versions [92]***

| | THERMAL POWER | | | CONDENSATION LENGTH | | |
|---|---|---|---|---|---|---|
| **TEST** | **OLD R5** | **NEW R5** | **Δ OLD-NEW R5** | **OLD R5** | **NEW R5** | **Δ OLD-NEW R5** |
| **66** | 4% | 4% | 0% | 7% | 7% | 0% |
| **67** | 6% | 6% | 0% | 1% | 1% | 0% |
| **68** | 2% | 2% | 0% | 11% | 11% | 0% |
| **69** | 1% | 1% | 0% | 5% | 5% | 0% |
| **70** | 0% | 0% | 0% | 11% | 11% | 0% |
| **71** | 0% | 0% | 0% | 11% | 11% | 0% |
| **72** | 1% | 1% | 0% | 37% | 9% | -20% |
| **73** | -1% | -1% | 0% | 42% | 13% | -20% |
| **74** | 2% | 2% | 0% | 25% | 25% | 0% |
| **75** | 1% | 1% | 0% | 32% | 10% | -17% |
| **76** | 0% | 1% | 0% | 24% | 13% | -8% |
| **77** | 1% | 1% | 0% | 20% | 20% | 0% |
| **78** | 0% | 0% | 0% | 30% | 17% | -10% |
| **79** | 1% | 1% | 0% | 37% | 22% | -11% |
| **80** | 6% | 6% | 0% | 9% | 9% | 0% |
| **81** | 8% | 8% | 0% | 12% | 12% | 0% |
| **82** | 7% | 7% | 0% | 6% | 6% | 0% |
| **83** | 6% | 6% | 0% | -3% | -3% | 0% |
| **84** | 2% | 2% | 0% | 6% | 6% | 0% |
| **85** | 2% | 2% | 0% | 6% | 6% | 0% |
| **86** | 4% | 4% | 0% | -4% | -20% | -17% |
| **87** | 3% | 3% | 0% | 29% | 29% | 0% |
| **88** | 2% | 2% | 0% | 13% | 13% | 0% |

***Table 18 NG experiments vs RELAP5 default and UNIROMA1 versions [92]***

| | THERMAL POWER | | |
|---|---|---|---|
| **TEST** | **OLD R5** | **NEW R5** | **Δ OLD-NEW R5** |
| **144** | -1% | 1% | 2% |
| **145** | -5% | -3% | 2% |
| **146** | -6% | -2% | 4% |
| **147** | -12% | -1% | 12% |
| **148** | -16% | -2% | 16% |
| **149** | -18% | -3% | 19% |
| **150** | -23% | -4% | 26% |
| **151** | -39% | -14% | 40% |
| **152** | -3% | 1% | 5% |
| **153** | -7% | -2% | 5% |
| **154** | -12% | -6% | 7% |
| **155** | -16% | -5% | 13% |
| **156** | -20% | -9% | 13% |
| **157** | -15% | -1% | 16% |
| **158** | -21% | -8% | 16% |

***Table 19 Air experiments vs RELAP5 default and UNIROMA1 versions [93]***

| | THERMAL POWER | | |
|---|---|---|---|
| **TEST** | **OLD R5** | **NEW R5** | **Δ OLD-NEW R5** |
| **40** | -15% | 3% | 22% |
| **41** | -13% | -6% | 8% |
| **42** | -15% | -6% | 11% |
| **43** | -17% | -6% | 14% |
| **44** | -18% | -3% | 18% |
| **45** | -20% | -1% | 23% |
| **46** | -23% | -2% | 27% |
| **47** | -17% | -8% | 11% |
| **48** | -21% | -9% | 15% |
| **49** | -21% | -7% | 18% |
| **50** | -24% | -7% | 22% |
| **51** | -27% | -7% | 26% |
| **52** | -26% | -2% | 33% |

***Table 20 Helium experiments vs RELAP5 default and UNIROMA1 versions [93]***

| | THERMAL POWER | | |
|---|---|---|---|
| **TEST** | **OLD R5** | **NEW R5** | **Δ OLD-NEW R5** |
| **12** | -3% | -2% | 1% |
| **13** | -9% | -6% | 3% |
| **14** | -10% | -7% | 4% |
| **15** | -11% | -7% | 4% |
| **16** | 7% | 9% | 2% |
| **17** | -3% | 1% | 5% |
| **18** | -7% | -1% | 6% |
| **19** | -8% | 0% | 9% |
| **20** | -3% | 0% | 3% |
| **21** | -5% | -1% | 4% |
| **22** | -8% | -3% | 6% |

### *3.4.5. Simulation results*

A steady-state condition was numerically established using a 15000-second "null transient" simulation, which allowed the system to reach thermal equilibrium without introducing additional perturbations. The initial setup was configured to replicate the experimental water inventory within the primary loop, approximately 75 kg, as detailed in Table 16.

As shown in Table 21, RELAP5 tends to underestimate the temperature distribution throughout the primary loop by roughly 5°C. It is also important to highlight that during steady-state conditions, the bypass loop remained filled with liquid water, a result of an overestimated filling ratio. Consequently, all measured temperatures in the loop were below the saturation temperature at 180 bar, which is approximately 355°C. The internal water flow rate was estimated at 171 g/s; however, this value could not be validated against experimental data due to the absence of a flowmeter in the system.

***Table 21 Experimental vs RELAP5 initial conditions***

| **Parameter** | **Unit** | **SIRIO** | **RELAP5** | **Error** |
|---|---|---|---|---|
| **Water Inventory** | kg | 74.6 | 73.0 | -2.1% |
| **Water loop pressure** | bar | 178.1 | 180.0 | 1.1% |
| **Gas pressure (BC)** | bar | 110.7 | 110.0 | / |
| **Thermal power supplied during the steady state (BC)** | kW | 55* | 55 | / |
| **SG fluid inlet temperature** | °C | 307.4 | 301.7 | -5.7°C |
| **SG fluid outlet temperature** | °C | 348.1 | 343.7 | -4.4°C |
| **HX fluid inlet temperature** | °C | 343.6 | 340.1 | -3.5°C |
| **HX fluid outlet temperature** | °C | 310.2 | 303.4 | -6.8°C |
| **Gas Tank temperature (BC)** | °C | 23.4 | 20.0 | / |
| **Water mass flow rate** | g/s | - | 171 | / |
| **HX pool side water level** | mm | - | 630 | / |
| * oscillations around the average value due to the control system | | | | |

The transient begins with the isolation of the HX through the closure of its upstream and downstream valves. This removal of the heat sink causes the system pressure to rise rapidly, reaching the setpoint of 190 bar within 35 seconds. At this threshold, the inlet valve of the IC opens, allowing the fluid to expand into the IC branch, initially filled with NCGs. As steam enters, part of it condenses within the IC, accumulating upstream of the outlet valve, while the remaining flows toward the NGT. At the end of the test, approximately 15 liters of condensed water were collected in the NGT. After a 60-second delay, the IC outlet valve opens, initiating natural circulation within the loop. For the first 2000 seconds of the DHR phase, the thermal power is held constant at 55 kW, then decreases according to a predefined decay curve (see Figure 32).

The pressure evolution following the IC activation is shown in Figure 39. After an initial drop from 190 bar to an intermediate value around 150 bar, the pressure experiences a slight increase within the first 150 seconds, reflecting the delay in establishing stable natural circulation. The improved version of RELAP5, due to the implementation of enhanced turbulent film condensation model (specifically the Blangetti-Schlunder correlation), demonstrates a marked improvement over the default version. As shown in Figure 40 while the original RELAP5 version predicted a continued pressure rise—indicative of underestimated condensation heat transfer—the modified version achieves a quasi-steady state consistent with experimental observations, albeit with a small delay.

In the longer term, from 2000 to 3600 seconds, as the thermal power decreases, the pressure falls from 110 to 100 bar. The simulation accurately tracks the experimental trend, with a slight overprediction in the depressurization rate. The final equilibrium pressure in the simulation settles at around 100 bar, showing that the updated code more effectively captures the degrading condensation performance caused by NG (see Figure 45)

The differential pressure across the orifice provides an indirect indication of both the natural circulation flow rate and the water level above the orifice. As illustrated in Figure 46, the simulation successfully reproduces the experimental differential pressure peaks and the transient rising and falling phases. Over the long term, the simulation closely matches the experimental behaviour, with both converging toward near-zero differential pressure, indicating the cessation of natural circulation.

Figure 41 and Figure 43 present the IC inlet and outlet temperatures, respectively. In the initial phase of the transient, both are slightly overpredicted by the simulation. The IC inlet temperature closely follows the pressure trend, as it is dominated by saturated steam. The outlet temperature is lower than saturation due to the local steam partial pressure. Numerical oscillations and initial transient mismatches contribute to a 15°C discrepancy in the average temperature after 2000 seconds. In the full-power phase the numerical model underestimate the inlet temperature (see Figure 42) and overestimates the outlet temperature during the quasi-steady state, with a deviation reaching 30°C (see Figure 44).

As NGs diffuse into the IC, they degrade the heat transfer efficiency and increase pressure losses, reducing the mass flow rate and enhancing the temperature drop across the IC. However, RELAP5 underestimates NG accumulation in the IC. This is evident from the fact that the simulated temperatures remain at or near saturation, whereas the experimental data show inlet temperatures falling below saturation and more pronounced oscillations at the outlet—indicative of steam displacement by NGs, particularly at the bottom of the IC.

The SG inlet and outlet temperatures show trends closely linked to those of the IC. The SG inlet temperature is primarily governed by the IC outlet, while the SG outlet temperature follows the saturation temperature at the system pressure. Figure 47 and Figure 48 show the impact of the improved RELAP5 version, which successfully captures the qualitative behaviour of both inlet and outlet SG temperatures over the long term. The SG inlet temperature drops faster in the experiment than in the simulation, indicating more efficient heat transfer in the experimental IC. However, the SG outlet temperature aligns closely with the experimental data, thanks to the accurate pressure prediction in the loop.

The impact of the improvement of RELAP5 code is glaring to the IC pool side temperatures (shown in Figure 51 and Figure 52). Pool temperatures, measured by thermocouples at different elevations, show a good overall match in terms of trend. In the experiment, clear thermal stratification is observed, while the simulation of both versions predicts a nearly uniform pool temperature. This limitation is expected, given the one-dimensional nature of RELAP5/Mod3.3 and its difficulty in resolving three-dimensional flow and thermal gradients in large volumes, particularly with coarse nodalization. Nonetheless, in the long-term, the simulation captures the qualitative stratification trend, and the change in the temperature gradient matches the experimental behaviour. Additionally, the improved RELAP5 version provides a more pronounced stratification effect compared to the original, along with better agreement in absolute temperature values. This improvement translates into a more accurate prediction of the thermal power removed by the IC pool.

Table 22 summarizes the post-test water inventory in the loop. The total mass is conserved in the simulation. The volume of water remaining in the bypass HX section is accurately estimated at around 5.5 kg. However, the simulation overestimates the amount collected in the NGT—23 kg versus 15 kg experimentally—likely due to continued water migration in the simulation, while in the experiment, most migration occurred early in the transient due to initial pressure differences. Consequently, the simulated water inventory remaining in the loop at the end of the test is lower (44 kg) compared to the experimental result (54 kg), which may partially explain the slightly higher loop temperatures predicted during the DHR phase.

This simulation campaign, conducted as part of the PIACE project, demonstrates the improved predictive capabilities of the modified RELAP5/Mod3.3 in representing condensation in the presence of non-condensable gases under high-pressure conditions. While further refinements are needed to better capture complex multiphase interactions and stratification phenomena, the updated code version provides a significantly better match with experimental data compared to the default RELAP5. Given the complexity of the physical phenomena involved, the availability of detailed experimental benchmarks, and the improved simulation performance, this preliminary validation can be considered satisfactory for the scope of the present work.

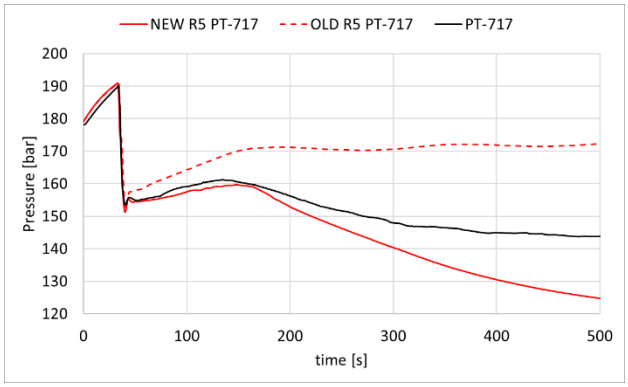


*Figure 39 Experimental vs RELAP5 pressure trend in the short term*

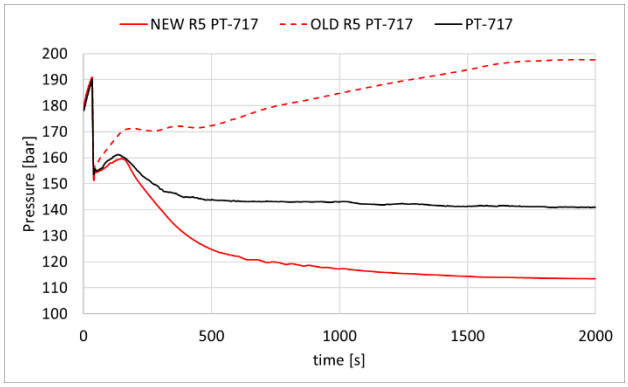


*Figure 40 Experimental vs RELAP5 pressure trend in the transient full power phase*

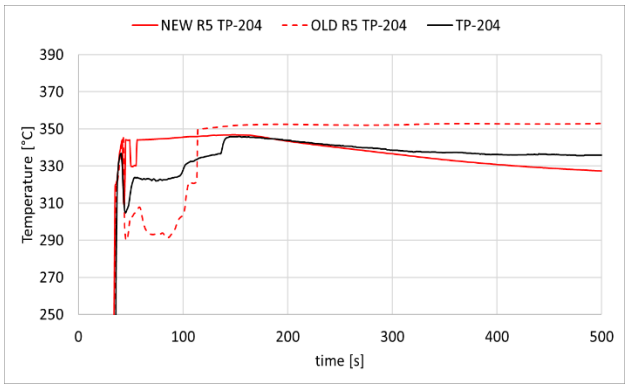


*Figure 41 Experimental vs RELAP5 IC inlet temperature in the short term*

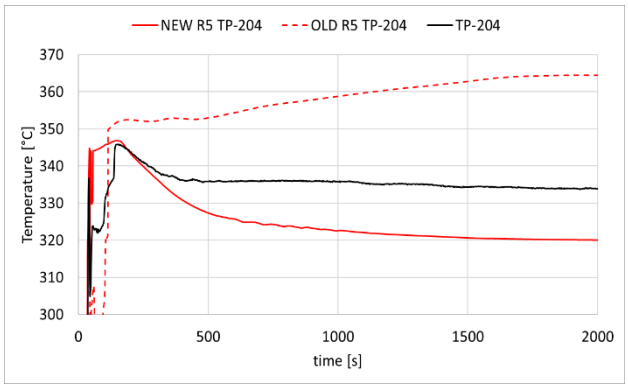


*Figure 42 Experimental vs RELAP5 IC inlet temperature in the transient full power phase*

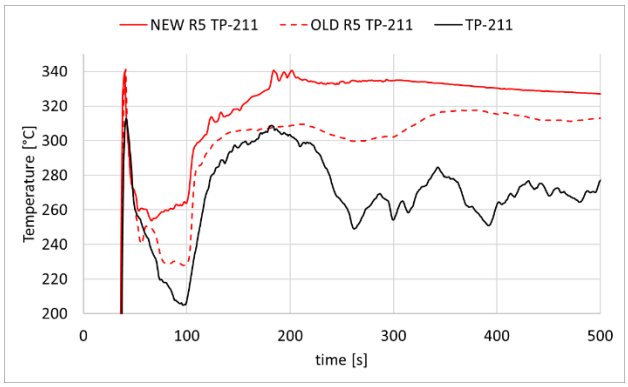


*Figure 43 Experimental vs RELAP5 IC outlet temperature in the short term*

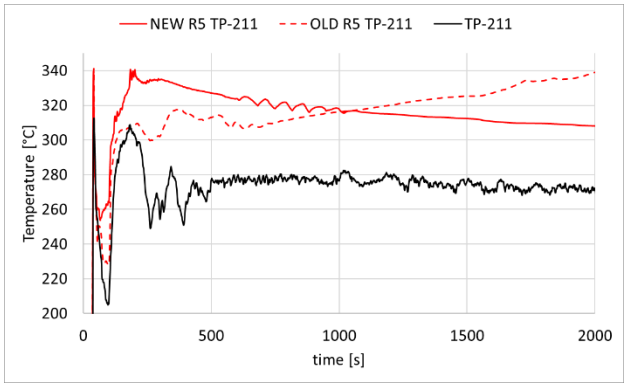


*Figure 44 Experimental vs RELAP5 IC outlet temperature in the transient full power phase*


*Figure 45 Experimental vs RELAP5 pressure in the long term*

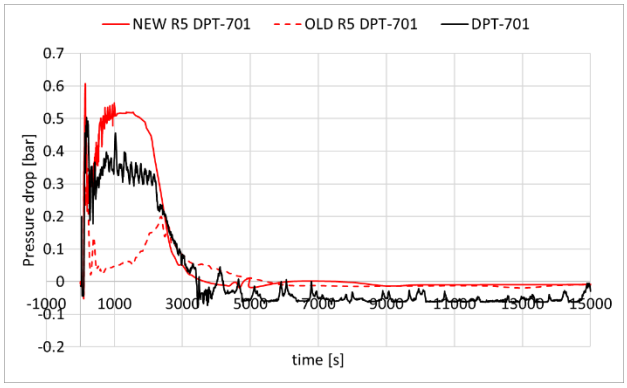


*Figure 46 Experimental vs RELAP5 orifice pressure drops in the long term*

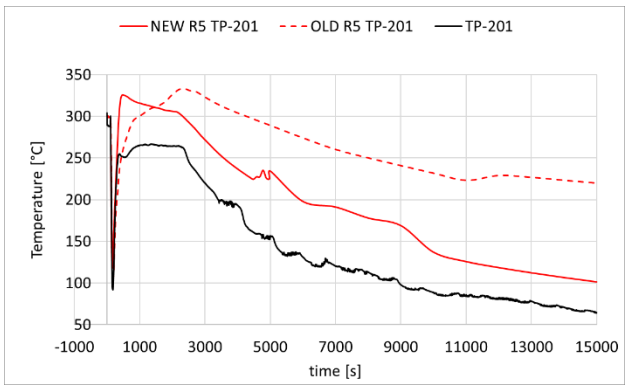


*Figure 47 Experimental vs RELAP5 SG inlet temperature in the long term*

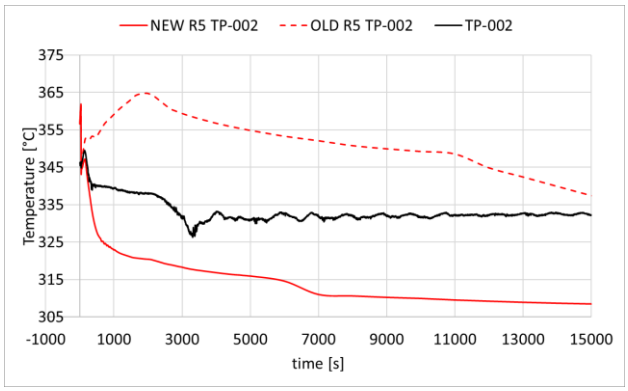


*Figure 48 Experimental vs RELAP5 SG outlet temperature in the long term*

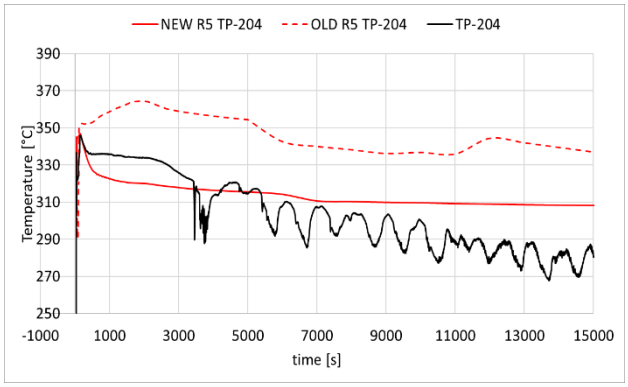


*Figure 49 Experimental vs RELAP5 IC inlet temperature in the long term*

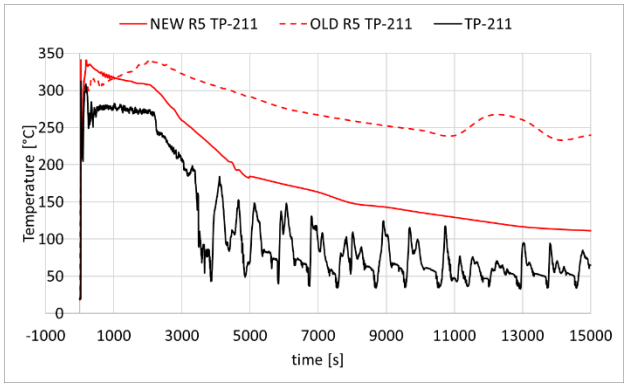


*Figure 50 Experimental vs RELAP5 IC outlet temperature in the long term*

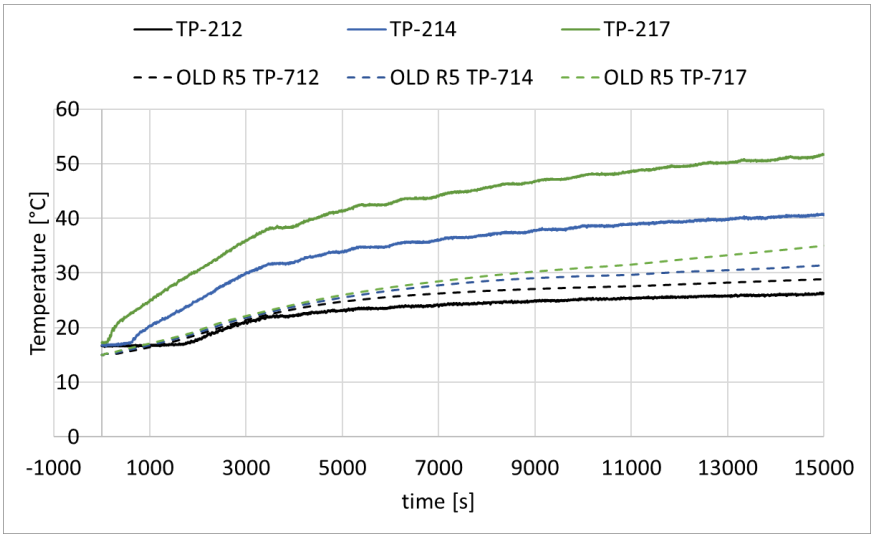


*Figure 51 Experimental vs OLD RELAP5 IC pool side temperature*

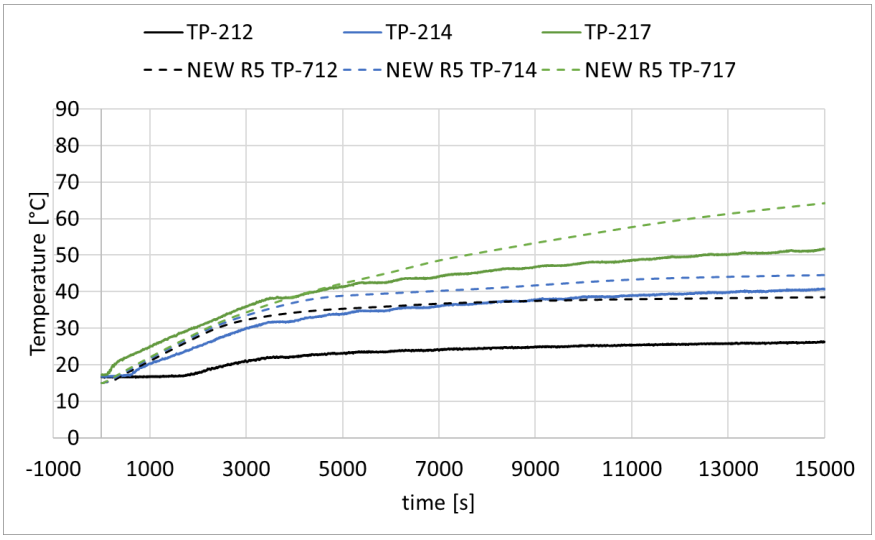


*Figure 52 Experimental vs NEW RELAP5 IC pool side temperature*

*Table 22 Experimental vs RELAP5 inventory distribution*

| Region | Unit | SIRIO | OLD RELAP5 | Error | NEW RELAP5 | Error |
|---|---|---|---|---|---|---|
| **HX line** | kg | 5.5 | 5.4 | -1.8% | 5.4 | -1.8% |
| **IC line** | kg | 54.4 | 54.3 | -0.2% | 46.2 | -15.1% |
| **NGT** | kg | 14.7 | 13.3 | -9.5% | 21.4 | 45.6% |
| **SIRIO** | kg | 74.6 | 73 | -2.1% | 73 | -2.1% |

### *3.4.6. Re-scaling and pre-test analysis*

As mentioned in Section 3.4.1, the SIRIO facility was originally designed to represent the ALFRED reactor based on the LEADER configuration. A re-scaling analysis, following the 'power-to-volume' approach, was subsequently conducted to align SIRIO with the revised ALFRED design developed by the FALCON consortium, starting from the STAGE 2 configuration [94].

A different approach was adopted to correlate the existing SIRIO facility with the revised ALFRED design. Specifically, the number of tubes in the SG was used as the reference parameter to calculate a new scaling factor. This assumption stems from the need to adapt the facility to the updated ALFRED configuration without requiring significant modifications to the existing SIRIO layout and main components. Following the methodology outlined in Section 3.4.1, the key parameters of the re-scaled system and their comparison with the full-scale reference are summarized in Table 23. It should be noted that the theoretical thermal power required from the heating cables during the steady-state phase exceeds the maximum available power (see the "Actual Thermal Power" entry in Table 23).

***Table 23 Comparison of the SG of ALFRED (FALCON) and SIRIO***

| Parameter | Unit | ALFRED (FALCON) | SIRIO |
|---|---|---|---|
| **Scaling factor** | - | - | 80 |
| **SG Duty** | kW | 66 666 | 833 |
| **Actual thermal power** | kW | - | 110 |
| **Number of tubes per SG** | - | 880 | 11 |
| **SG tube length** | m | 6 | 6 |

Additionally, for the scaling of the IC and the NGT, the parameters of which are described in Table 24.

***Table 24 Comparison of the IC and NGT of ALFRED (FALCON) and SIRIO***

| Parameter | Unit | ALFRED (FALCON) | SIRIO |
|---|---|---|---|
| **Volume NG tank** | $m^3$ | 16 | 0.2 |
| **Theoretical IC tubes number** | - | 16 | 0.2 |
| **Real IC tubes number** | - | 16 | 1 |
| **IC active length** | m | 2 | 0.564 |

Moreover, Table 25 presents the thermodynamic conditions used to estimate the required mass flow rate to replicate the representative conditions of ALFRED STAGE 2.

*Table 25 Thermodynamic conditions of ALFRED (FALCON) and SIRIO*

| Parameter | Unit | ALFRED (FALCON) | SIRIO |
|---|---|---|---|
| **Secondary-loop mass flow rate** | kg/s | 44.3 | 0.0728 |
| **Pressure** | bar | 175 | 175 |
| **SG inlet temperature** | °C | 335 | 335 |
| **SG outlet temperature** | °C | 435 | 435 |

For the sake of clarity, the designs of both versions of the SIRIO facility are reported and compared with their respective full-scale ALFRED systems—namely, the LEADER and FALCON configurations—in Table 26.

*Table 26 Scaling results of LEADER and FALCON configurations*

| Parameter | Unit | ALFRED (LEADER) | SIRIO (LEADER) | ALFRED (FALCON) | SIRIO (FALCON) |
|---|---|---|---|---|---|
| **Scaling factor** | - | - | 47.24 | - | 80.00 |
| **SG duty** | kW | 37500 | 55 | 66666 | 110 |
| **SG number of tubes** | - | 510 | 11 | 880 | 11 |
| **NGT volume** | $m^3$ | 6 | 0.127 | 16 | 0.2 |
| **IC active length** | mm | 2000 | 956 | 2000 | 564 |

Following the re-scaling, a pre-test analysis and comparison with full-scale ALFRED DHR simulations were carried out to verify the predicted consistency and ensure the fidelity of the scaling approach [94]. The selected accidental transient investigated corresponds to a PLOOP scenario. Following the onset of this event, the system transitions from steady-state full power operation to a decay power regime, according to a predefined decay heat curve. As part of the passive response mechanism, the SG becomes isolated, and the upstream valve of IC opens once the system pressure reaches the setpoint of 190 bar. The downstream IC valve subsequently opens with a programmed delay of 60 seconds. Numerical simulation results obtained from this analysis are compared against full-scale reference data available in the literature, specifically from the study by ref. [95].

The accidental transient starts from a steady-state numerical simulation representative of SIRIO steady-state phase. Therefore, the heating cables generates a thermal power which is removed by a flow rate of fluid of about 65.5 g/s (lower than the reference value in order to get the correct temperature having implemented heat losses in the SG). Since the flow rate is driven by natural circulation, the desired value is achieved through the regulation of the upstream control valve of the HX (VALVE 301, see Figure 33). The coolant enters the SG at a temperature of 335 °C and exits at 435 °C. Subsequently, the power is released to the HX. This power is removed from the water pool whose level is kept constant. The pressure loop is 175 bar imposed as a boundary condition.

*Table 27 R5 steady-state results*

| Parameter | Unit | Reference | Value |
|---|---|---|---|
| **Secondary-loop mass flow rate** | g/s | 72.8 | 65.5 |
| **Thermal power of heating cables (BC)** | kW | 110.0 | 110.0 |
| **SG inlet temperature** | °C | 335 | 336 |
| **SG outlet temperature** | °C | 435 | 433 |
| **Secondary loop pressure (BC)** | bar | 175 | 175 |
| **HX pool side level** | mm | - | 1123 |
| **HX upstream valve norm. flow area** | % | - | 60.9 |
| **Heat losses** | kW | - | 17.9 |

Starting from the full power steady-state conditions, PLOOP transient simulation is performed. The transient lasts 72 hours which is the grace time ensured by any nuclear safety system. The decay curve implemented in this transient is based on the following criteria: the starting point is the decay curve of the full-scale ALFRED (LEADER) evaluated by the typical neutron kinetic computer code and used to perform some numerical activities in the framework of LEADER project [42]. Subsequently, according to the single failure criterion, since ALFRED DHR is designed as 3 x 50%, the power of SIRIO is that of ALFRED scaled and distributed among 2 out of 3 loops. Finally, both decay curves are reported in Table 28.

*Table 28 Decay curves of ALFRED and SIRIO*

| Time (s) | ALFRED decay curve (MW) | SIRIO decay curve (kW) |
|---|---|---|
| 1 | 13.40 | 83.75 |
| 60 | 7.92 | 49.50 |
| 600 | 5.20 | 32.50 |
| 3600 | 3.12 | 19.50 |
| 10800 | 2.24 | 14.00 |
| 36000 | 1.52 | 9.50 |
| 86400 | 1.22 | 7.62 |

It is necessary to note that the decay curve implemented in the RELAP5 model differs from the theoretical one since it is good practice to impose a thermal power that includes a part that compensates for heat losses. An initial assessment shows that the heat losses of the whole plant are 9 kW. Therefore, each point of the decay curve has been increased by the heat losses scaled difference (practically all). Figure 53 shows the trend of the water loop pressure in the short term, in the first 500 seconds, and in the long term (72 hours). It can be seen that from the opening of the valve, the pressure reaches an intermediate value (of about 136 bar) between 190 bar that of the loop and 110 bar that of the gas line. Then, an increase in pressure occurs due to the flashing of water up to 192 bar. When the valve downstream of the IC is opened, natural circulation is established. Consequently, the mass flow rate increases, as well as the condensation rate, leading to a decrease in pressure. Finally, it can be seen that after 72 hours, the circuit pressure settles at 147 bar.

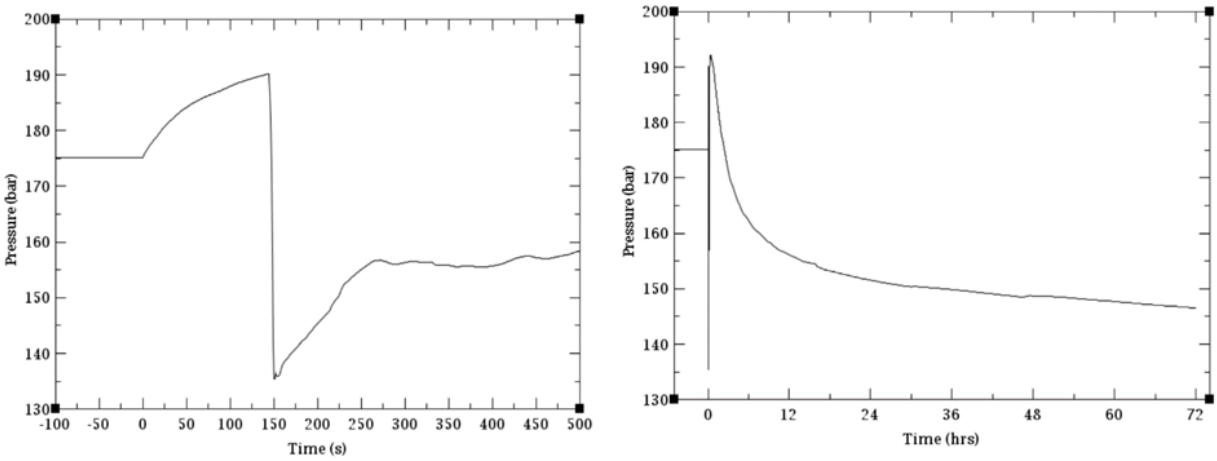


***Figure 53 Loop pressure trend in the short- and long- term phase***

It can be seen that the qualitative trend of the pressure returns with that of full scale in accordance with [95] in which the minimum pressure is 150 bar (vs 136 bar of SIRIO), the pressure in the first 250 s is 180 bar (vs 150 bar of SIRIO) and the pressure in the long term-phase is 185 bar (vs 147 bar of SIRIO). The trend of the SG inlet and outlet temperatures are shown in Figure 54. SG inlet temperature settles at 230 °C equals to the saturation temperature at the steam partial pressure. On the other hand, the SG outlet temperature settles at about 340 °C which is the saturation temperature of the total pressure (since the NG concentration at the SG outlet is null). According to [95], the qualitative trend of both curves is the same and the final temperatures of the full-scale system are 290 °C at the inlet and 357 °C at the outlet.

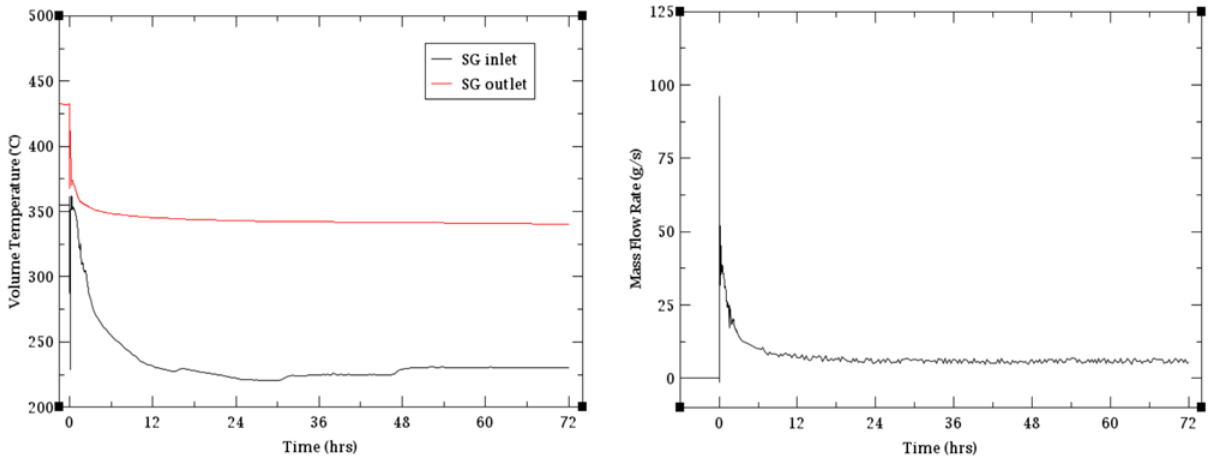


***Figure 54 SG inlet and outlet temperature (on left) and mass flow rate (on right)***

In addition, Figure 54 shows the mass flow rate in the loop during the transient. The plot shows that it has a monotonic decreasing trend equal to that of the decay curve. Finally, it is noted that the flow rate value in the long-term phase is about 5.5 g/s, which represents the scaled value of the long-term flow rate obtained in [95] (0.5 kg/s which scaled is 6.25 g/s).

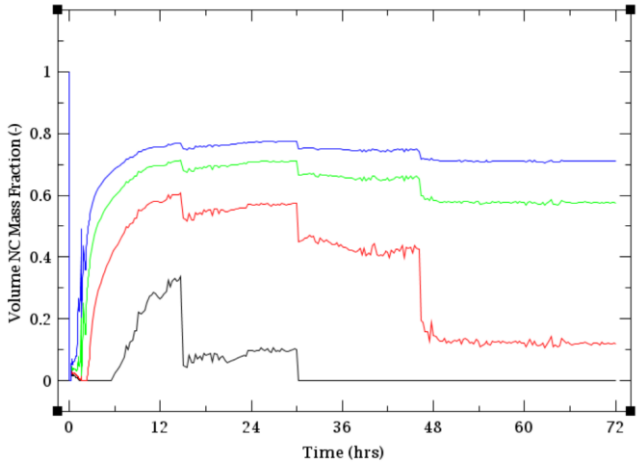


***Figure 55 NG mass fraction in IC tube side***

Moreover, Figure 55 shows the NG mass fraction distribution along the IC tube. It can be seen that the rate of variation of the concentration of non-condensable gases is equal to and opposite to that of the pressure i.e., the NG mass fraction increases if the pressure is decreasing and vice versa.

According to [95], the distribution of non-condensable gas obtained in full scale is similar to that of the experimental plant with a minimum of 0% to a maximum of 85% (compared to 71% obtained in SIRIO). Finally, Figure 56 shows the correct operation of passive removal of thermal power. From the moment the valve is opened, it takes about 350 seconds for the power removed from the IC to align with that generated by the heating cables located in the SG.

Subsequently, it is noted that, regardless of the nominal power of the heat sink, the power removed from the IC has the same trend as that generated by the SG. Moreover, it should be noticed that the difference between the power removed by the IC and that generated by the SG is due to the heat losses of the system which settle at around 8.5 kW in accordance with the evaluation mentioned above.

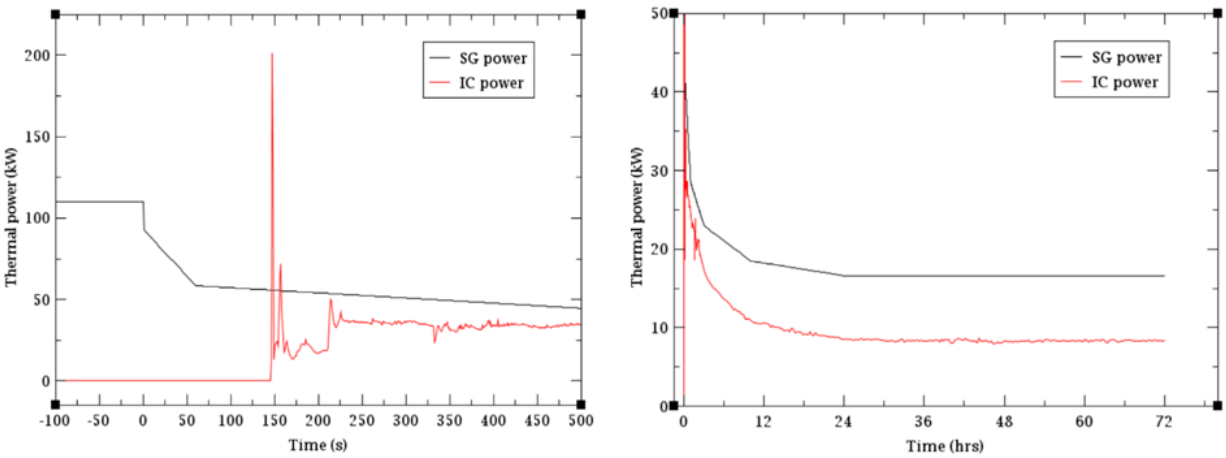


***Figure 56 Thermal powers trend***

# 4. ANALYSES TO SUPPORT THE DEVELOPMENT OF THE WESTINGHOUSE-LFR

Among the various LFR concepts developed through the years, Westinghouse Electric Company (WEC) made significant progress in designing an advanced pool-type reactor aimed at economic competitiveness even in the most challenging global markets. The Westinghouse Lead Fast Reactor (WEC-LFR) is a 450 $MW_e$-class system with a thermal power of 950 $MW_{th}$. It features a fast neutron spectrum, uses lead as coolant, and incorporates fully passive safety systems. As R&D activities continue to support the maturation of LFR technology, particular emphasis is placed on optimizing the reactor design, establishing robust experimental facilities, and validating numerical tools to ensure the safe and reliable performance of these next-generation nuclear systems.

## 4.1. Reactor design overview

The WEC-LFR [96], illustrated in Figure 57, represents a significant innovation with respect to traditional nuclear reactor technology. As part of the Generation IV reactor systems [7], the WEC-LFR is designed to leverage the benefits of lead when used as reactor coolant, positioning itself as a leading candidate for the next generation of nuclear power plants. This reactor concept aims to simultaneously achieve excellent performance in regard to economics, safety, and sustainability of nuclear energy, with the latter fully accomplished when suitable fuel reprocessing facilities become available.

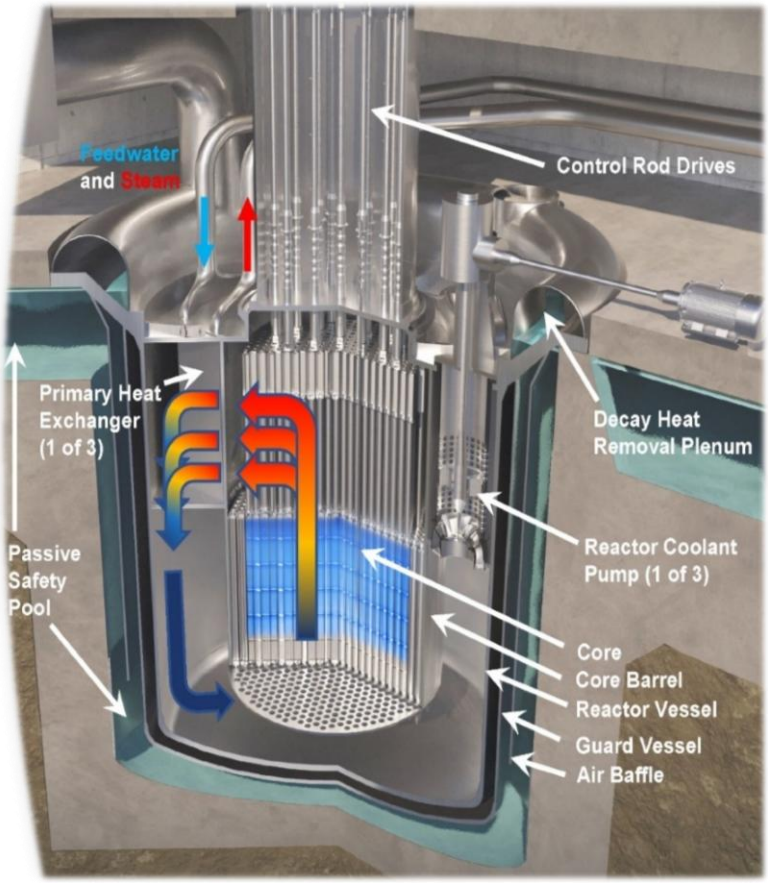


***Figure 57 Westinghouse-LFR Reactor Coolant System [96]***

The WEC-LFR is a compact pool-type reactor with a core thermal power of 950 $MW_{th}$ and a net electrical output of 450 $MW_e$, achieved using a supercritical water (sH2O) power conversion system, an air-cooled condenser, and an integrated energy storage system. The Westinghouse LFR was envisioned to adopt a staged approach to development, commencing with lower duty conditions (core-average outlet temperature ≤530°C and fuel burnup below 100 MWD/kg) to permit near-term demonstration using sufficiently tested materials. These conditions planned to be subsequently increased to enhance economic performance further, by leveraging experimental results on materials confirmed throughout development. Table 29 summarizes the main features of the WEC LFR for both phases [96].

***Table 29 WEC-LFR high-level characteristics [96]***

| **Parameter** | **Unit** | **Value** |
|---|---|---|
| **Rated power (thermal / Net electric)** | MW | 950 / 450 |
| **Primary coolant** | - | Liquid Lead |
| **Secondary coolant** | - | Supercritical Water |
| **Reactor coolant system configuration** | - | Pool-type |
| **Number of heat exchanger** | - | 3 |
| **Number of Reactor Coolant Pumps and location** | - | 3, in the cold leg |
| **Reactor vessel outer diameter / height** | m | 6.7 / 9 |
| **Fuel type** | - | $UO_2$ or MOX (Phase I) / UN (Phase II) |
| **Fuel cycle length** | yr | 2-8 (depending on fuel and fuel management scheme) |
| **Operating pressure (primary / secondary)** | bar | 1 / 340 |
| **Lead coolant min / max bulk temperature** | °C | 390 / up to 530 (Phase I)<br>390 / up to 650 (Phase II) |
| **Ultimate heat sink** | - | atmosphere |

The core design of the WEC-LFR (see Figure 58) emphasizes not only performance but also adaptability in terms of fuel and fuel cycle strategies. To support early deployment, the initial phase (Phase I) utilizes high-maturity uranium dioxide ($UO_2$) fuel. A future evolution (Phase II) considers transitioning to uranium nitride (UN) fuel, which offers superior thermal conductivity and higher heavy metal density. Additionally, a mixed oxide (MOX) fuel option is proposed, suitable for countries with reprocessing capabilities and policies that support plutonium reuse. All core configurations—$UO_2$, UN, and MOX—are designed to fit within the same core barrel and share common structural components, including the core support plate and control/shutdown assemblies. This standardized layout avoids the need for significant hardware modifications during fuel transitions. Despite differences in fuel rod characteristics such as pellet geometry, pitch, and cladding materials, the overall core configuration remains consistent, with fuel assemblies arranged in three enrichment zones and supplemented by reactivity control assemblies, as qualitatively shown in Figure 58. The number of assemblies (247), their enrichment distribution and other core features have been optimized as reported in [97].

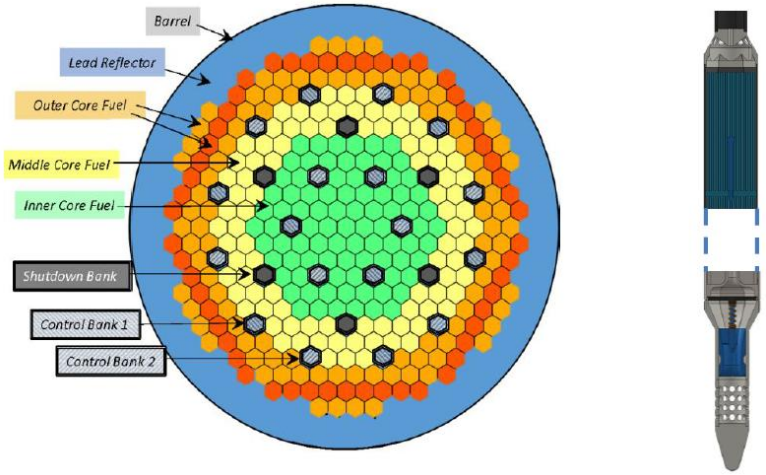


***Figure 58 Radial configuration of the Westinghouse-LFR core (left) and fuel assembly axial view (right) [96]***

The cladding materials are selected according to deployment phase requirements. For early phases, titanium-modified austenitic steels with corrosion-resistant coatings are favoured due to their compatibility with lead coolant and irradiation resistance. These coatings, such as $Al_2O_3$ applied by Pulsed Laser Deposition (PLD), offer enhanced corrosion protection and gas impermeability, making them suitable for containing tritium which would otherwise permeate through bare steel cladding.

The WEC-LFR core features cycle lengths ranging from 2–8 years depending on the fuel and fuel management scheme adopted, i.e., single or multi-batch. The envisioned refuelling strategy consists of moving used fuel assemblies, upon lapsing of a certain waiting time from shutdown to allow decay heat to decrease sufficiently, directly from the core into dry casks. Although the economic viability of this refuelling strategy requires confirmation, on a design-specific base, that accounts for the impact of the waiting time on fuel cycle cost and lost energy due to the plant's unavailability, its adoption would allow eliminating the need for traditional spent fuel pools, thus resulting in significant capital cost savings. Although an open fuel cycle is the reference configuration due to global constraints on reprocessing (i.e., local energy policies and general unavailability of fuel reprocessing facilities), the reactor's design remains flexible enough to accommodate semi-open or closed fuel cycle strategies should policy or resource considerations evolve.

The WEC-LFR core is equipped with two banks of control assemblies, each consisting of nine units (9+9), and a separate bank of six safety assemblies. Each bank is independently capable of initiating a reactor shutdown, with the safety assemblies designed for passive actuation. These assemblies occupy positions that would otherwise be filled with fuel elements and adopt the same hexagonal geometry as the displaced fuel, ensuring structural and hydraulic compatibility within the core. Each assembly includes a metal duct forming a hexagonal cavity, into which a neutron-absorbing rod can be inserted axially via control rod drive mechanisms mounted on the reactor vessel head.

A distinctive feature of this design is the capability for insertion of control and safety elements from both the top and bottom of the core, without the need for penetrations of the reactor vessel bottom head. The bottom-inserted elements operate through buoyancy-driven mechanisms, offering additional system redundancy and contributing to the flexibility in managing fuel burn-up and axial power distribution. As the metal ducts housing the absorber elements are permanently integrated into the core structure, they enable design opportunities that extend beyond those of conventional control rod configurations.

Notably, to enhance shutdown reliability under conditions involving severe core deformation, a novel passive, non-control-rod-based shutdown mechanism has been devised. This system involves the passive injection of neutron-absorbing material into axial cavities located within the duct walls of the control and safety assemblies. The mechanism exploits the inherent thermophysical behaviour of lead to respond autonomously to either an over pressurization of the reactor cover gas—such as might occur due to a failure in the primary heat exchanger—or an overtemperature condition in the reactor core. In either scenario, lead activates the passive system to release neutron-absorbing material into the core region, driving it into a subcritical state. Importantly, the system is designed for reversibility through use of existing reactor infrastructure developed for conventional operational needs.

The RCS of the WEC-LFR is housed within a compact Reactor Vessel (RV) surrounded by a Guard Vessel (GV). As schematically illustrated in Figure 57, the RV and the GV are integrated into a single structural assembly, supported by a shared cantilevered flange located at the top. Beyond serving their primary structural and confinement functions, both the RV and GV contribute actively to the passive decay heat removal process, forming key components of the Passive Heat Removal System (PHRS).

Radiative heat transfer between the RV and GV follows a fourth-power temperature dependency, which ensures that thermal losses during normal operation—when the RV temperature is approximately 390 °C—remain minimal and acceptable from an efficiency standpoint. However, in accident conditions, as the vessel temperatures rise significantly, the radiative heat transfer rate increases rapidly, significantly enhancing the system's heat removal capability.

The design of the RV and GV, including their sizing and wall thickness, was developed through an iterative optimization process that accounted for the complex interactions among vessel diameter, lead coolant temperature, the required thermal gradient across vessel walls, allowable creep stress limits, and the efficiency of radiation heat transfer. This optimization enabled a reduction in both vessel size (relative to other LFRs and accounting for plant's power output) and wall thickness, while preserving the necessary heat removal capacity. These refinements also helped to minimize the peak lead temperatures during transients and mitigate secondary stresses caused by thermal gradients. Additionally, design enhancements such as a reshaped lower vessel head and the use of advanced fabrication techniques enabled Westinghouse's logistics team to design a vessel compact enough for transport as a single unit to most potential deployment sites worldwide. Similar efforts were undertaken for the GV, which—due to its distinct operational and structural requirements—was engineered to be even thinner than the RV, further improving its performance in terms of passive heat removal.

A novel component belonging to the RCS of the WEC-LFR is the Primary Heat Exchanger (PHE). As shown in Figure 59, this hybrid-microchannel heat exchanger comprises stacked plates, some featuring ~4mm x 4mm finned channels for horizontal lead flow and others incorporating smaller channels —chemically etched or otherwise formed—for supercritical $H_2O$. These plates are stacked and diffusion-bonded to create a solid metal structure with numerous small internal channels. Among the latter, those dedicated to supercritical water are connected to larger headers however located outside the reactor vessel in order to limit PHE failures inside the RCS to very small channels only. This design offers several advantages, including exceptional compactness compared to traditional tube-and-shell designs, adaptability to specific spatial constraints, and high robustness, as no cross-pressure-boundary failures have been observed even under testing designed to induce them. In the unlikely event of a failure, the small channel size limits break flows to minimal volume and mass flow rates, significantly smaller than conventional designs [98].

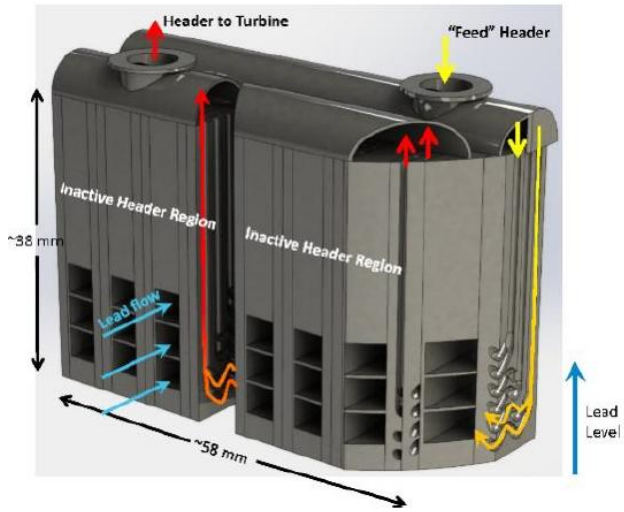


***Figure 59 PHE close-up view illustration of the upper portion [98]***

The LFR design targets a hot leg temperature ($T_{hot}$) of 650 °C and a cold leg temperature ($T_{cold}$) of 390 °C. These values are particularly significant for several reasons. The selection of the Thot value reflects a cost-informed design approach, grounded in a detailed and continuously updated model that considers both capital cost and plant's thermal efficiency, with the former accounting for estimated costs of both the primary and secondary systems. This model includes comprehensive simulations of the Power Conversion System (PCS), enabling optimization of performance and cost.

Unlike other advanced reactor concepts that propose outlet temperatures exceeding 800 °C to maximize thermal efficiency—often using Brayton cycles and necessitating expensive secondary side tubing materials —the WEC-LFR couples with a supercritical water PCS, which can achieve high efficiency while utilizing proven PCS technology. The chosen $T_{hot}$ of 650 °C aligns well with the capabilities of the most advanced steam turbine technologies currently available, minimizes the Levelized Cost Of Electricity (LCOE), and remains within operational limits of structural materials and nuclear fuels that are deemed achievable through a staged development approach as previously discussed in Table 29.

The choice of $T_{cold}$ at 390 °C is equally deliberate. While lower inlet temperatures might appear advantageous for increasing the core temperature differential and thermal efficiency, practical limitations must be addressed. Lead, the chosen primary coolant, presents challenges in terms of corrosion and erosion, particularly at high flow velocities. Therefore, reducing the flow rate through the core is desirable, which in turn requires a wider temperature difference between the inlet and outlet to sustain adequate heat removal.

Achieving a $T_{cold}$ of 390 °C, however, involves substantial design and analytical effort. This includes thermodynamic analysis of the secondary cycle, optimization of the PHE design to ensure effective heat transfer between feedwater and the incoming lead, core neutronics assessments to ensure adequate fuel performance throughout the active region, and evaluation of transient scenarios that might reduce lead temperature closer to its freezing point of 327 °C. The selected $T_{cold}$ provides an effective balance between thermal efficiency, system safety, and material integrity, ensuring the reliability and robustness of the WEC-LFR design. To maximize siting opportunities for the plant while addressing long-term concerns related to water sustainability, the PCS has been designed to rely on air-cooling as the ultimate heat sink.

This approach minimizes the dependency on large water bodies, allowing for more flexible plant siting—such as inland or remote locations—using either city water connections or on-site wells for auxiliary needs. As a result, siting becomes less complex, environmental impacts are reduced, and installation costs—particularly those related to land and water access—are significantly lowered.

In response to evolving energy market dynamics, including the increasing presence of non-dispatchable renewable sources, the WEC-LFR has been conceived from the outset with integrated thermal energy storage. This feature enhances the plant's ability to load-follow without altering the reactor's thermal output, thereby maximizing capacity factor and enabling output flexibility beyond nominal limits. The thermal storage system is based on a modular configuration using concrete and thermal oil, operating at atmospheric pressure and capable of storing heat at temperatures up to approximately 330°C.

When paired with a steam turbine system designed for oversizing, this storage allows for dynamic adjustment of steam flow, modulating electricity generation without affecting reactor conditions. This capability enables the plant to vary electrical output between approximately 65% and 125% of nominal power while maintaining steady-state reactor operation. The actual capacity of the thermal storage system will be tailored to local conditions, accounting for regional demand profiles, seasonal and climatic variability, and regulatory or market-based policies.

In some high-variability markets, storage capacities of 1 GWh-electric or more are envisioned. However, as the marginal value of increased storage capacity diminishes, system sizing will be optimized for cost-effectiveness rather than full redundancy. During periods when the storage is either fully charged or depleted, the plant can revert to a conventional load-following mode, adjusting reactor power through control rod movement, reactivity feedback mechanisms, and modulation of pump speed within the allowable operating envelope.

The WEC-LFR features a notably low core flow rate and minimal pressure loss, primarily achieved through the design of the PHE and the spacious fuel lattice enabled by the use of lead as a coolant. These characteristics allow for an exceptionally low pump power requirement—approximately 250 kW per pump [98]—with a total of three pumps, one for each PHE.

As illustrated in Figure 57, each reactor coolant pump is equipped with a 90-degree, speed-reducing gearbox and bearing assembly that drives a mixed-flow impeller. The impeller is comparable in size and design to those used in pressurized water reactor (PWR) systems. However, in contrast to PWR pumps, the LFR pumps operate at significantly lower rotational speeds (≤ 300 RPM) in order to minimize the relative velocity of the lead coolant, thereby reducing erosion of internal components.

The PHEs exhibit such low pressure drop on the lead side that, when combined with lead's high density and the corresponding hydrostatic pressure at shallow submergence, cavitation risks are effectively eliminated. This allows the impellers to be positioned directly at the PHE outlet without compromising performance or safety. Moreover, the relatively moderate lead temperature (below 400 °C) further mitigates concerns related to corrosion and erosion, enabling the use of a more conventional pump impeller materials. The radial loads on the pump shaft are supported by in-lead radial bearings located near the impeller, while axial loads are managed within the gearbox itself.

The gearbox exemplifies the application of proven, reliable technology to advanced reactor systems. Variants of this gearbox have been in industrial use for nearly a century, demonstrating excellent performance and durability under harsh conditions, often with minimal maintenance. This configuration permits the use of standard 1200 RPM horizontal electric motors, which are widely available on the commercial market. Additionally, locating the motors away from the reactor head—thus distancing them from heat and radiation—offers significant advantages in terms of maintainability and accessibility. In certain conditions, this arrangement could even allow for inspection or limited maintenance during reactor operation.

Finally, the decay heat removal after reactor shutdown is one of the most important safety functions in any nuclear power plant. The degree of diversity and reliability in fulfilling this function decisively affects the safety level of the nuclear power plant as a whole. For diversity and redundancy, the WEC-LFR decay heat removal function is performed by two different systems, normal decay heat removal system and the emergency decay heat removal system. The normal decay heat removal system is a non-safety grade system that removes the decay heat in the reactor core during outages, and could be used following an accident if available. The heat removal function of normal decay heat removal system is provided by the PHEs and condensers.

For the emergency decay heat removal, WEC-LFR aims at passively removing the decay heat generated in the reactor core in design basis accident conditions without the need for any operator intervention, external power, or signal input of “intelligence” or moving mechanical part, which is consistent with the passive safety category B, as defined in [49]. The innovative decay heat removal system is the PHRS. The PHRS is a safety grade system with high simplicity and reliability, capable of extended long term heat removal, and low risk of lead freezing.

Firstly, the overarching design philosophy principle adopted by Westinghouse towards design simplicity, together with the requirement of not using signal input of “intelligence” or moving mechanical parts, resulted in the selection of removing heat through the RV instead of utilizing auxiliary heat exchangers inside the reactor vessel, which complicate the design and necessarily requires extensive coolant piping and flow control devices. With a GV existing outside the LFR reactor vessel to mitigate the reactor vessel failure event, the cooling through the guard vessel via the gap between the reactor vessel and guard vessel was deemed highly preferable.

A rationale for the PHRS design is that water, which is well known for its heat removal capability, is introduced to provide sufficient heat removal in the early stage of accidents where the decay heat of the reactor core is relativity high. The LFR technology enables the utilization of water as the cooling medium in the design compared to other Generation IV reactor technologies due to the lack of exothermic reactions between lead and water. Furthermore, the state of knowledge of water cooling is high and extensive experience of water-cooling system design helps to accelerate the PHRS design and validation.

There is extensive cooling water supply on site, but there is still a risk of the water inventory being depleted in the extended phase of an accident. Thus, an extended cooling phase that relies on ambient air to provide cooling after the water is depleted was proposed. The ambient air has unlimited supply, which makes it the suitable choice as the ultimate heat sink and the air cooling was explored in the LFR design before [100].

However, because air is not an ideal coolant due to its low density and poor thermal conductivity, it is not suitable for the scenario with high decay heat. By combining an early water-cooling phase with a subsequent air-cooling phase, the PHRS concept was developed and satisfies the original design goals. Figure 60 illustrates the two cooling phases in PHRS.

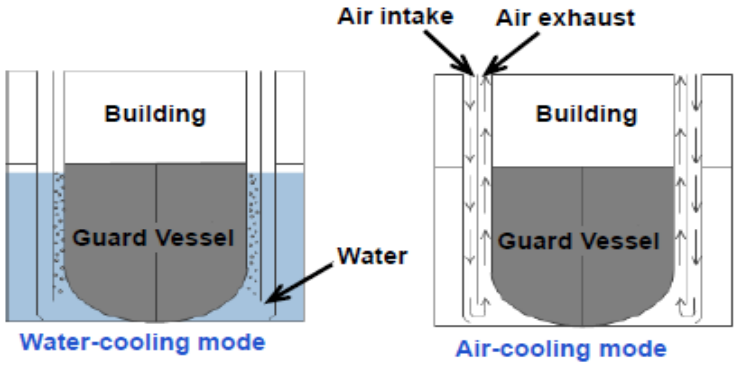


*Figure 60 PHRS working principle [100]*

The PHRS, as depicted in Figure 61 together with the reactor of the LFR, is a simple and reliable design that passively removes decay heat in an accident. It consists of a water pool system surrounding the guard vessel, which is called safety pool, filled with enough water to remove decay heat for seven days. The water in the safety pool is monitored and actively cooled during normal operation. In an accident, the lead coolant temperature in the reactor vessel will rise, resulting in increased heat transfer through the RV wall, through the gap between the RV and GV, through the GV and into the cooling water. With lack of any active cooling the water in the pool will increase in temperature and boiling heat transfer will occur between the GV and the water.

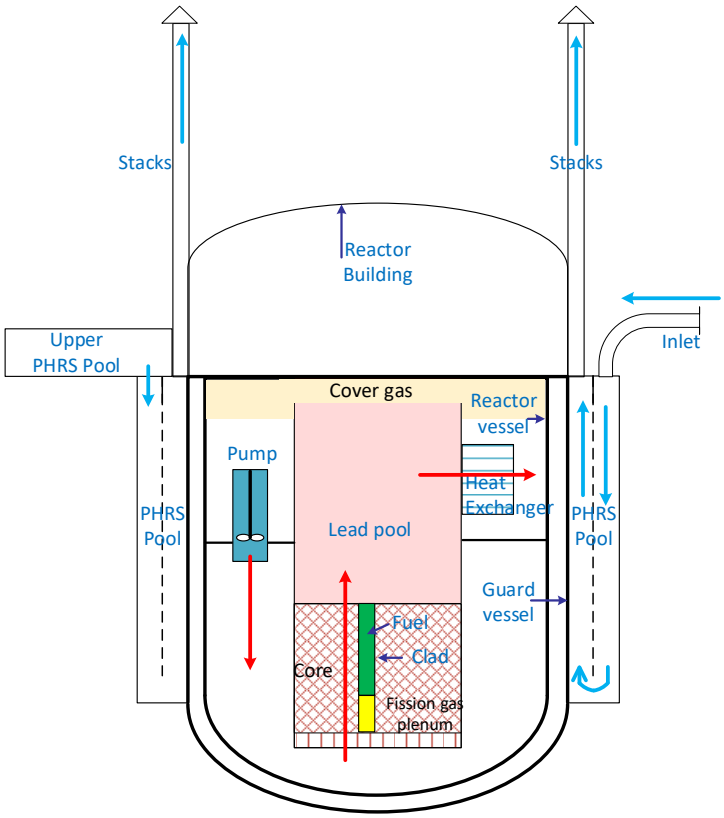


*Figure 61 Illustration of the PHRS and the flow path of coolants [100]*

The main heat transfer path from the core to the water pool (see Figure 62) comprises the following heat transfer phenomena:

- Transfer heat from the core to RV with natural circulation of lead,
- Conductive heat transfer through the RV wall,
- Radiation and convection heat transfer from the RV wall to the GV wall through the gas gap,
- Conductive heat transfer through the GV wall,
- Natural convection and boiling heat transfer from the GV wall to the water in the safety pool, which transitions to natural circulation of air upon water depletion

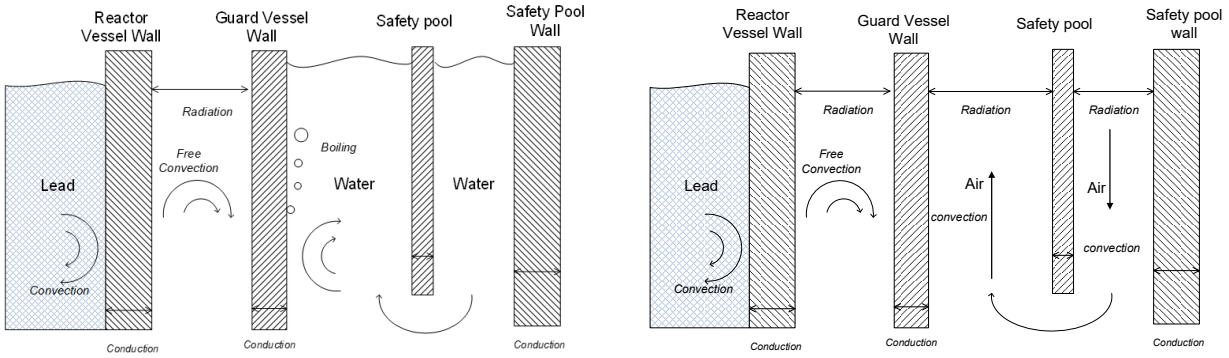


***Figure 62 Heat transfer phenomena in PHRS: water cooling (left) and air cooling (right) [100]***

The water volume in the safety pool is designed to last for at least 7 days. After seven days, the water in the safety pool is eventually depleted, and the cooling mode in PHRS is then transitioned to air cooling. The ambient air comes from several inlets and is discharged to outlet stacks by natural circulation (see Figure 61). The air cooling in PHRS could operate indefinitely if there is no intervention by the operator.

The PHRS is highly reliable [101] due to its simplicity and robustness. It does not require external power for operation in accidents. Without relying on signals of intelligence, the failure mechanisms from the sensors and instrumentation and control system, as well as operator error, are eliminated, and without an actuation mechanism, the failure modes associated with an actuation system are eliminated. The PHRS is able to provide cooling indefinitely and removes the necessity of operator intervention or a separate cooling system for the continuous cooling in long term.

The PHRS does not require any actuation signal since it is always on, even during normal reactor operation and shutdown, however limiting the associated thermal losses during these non-safety operating modes through the physics inherent in its design. In these operational modes, in fact, the temperature of the RV is not sufficiently high to promote significant radiative heat transfer from the RV to the GV, thus limiting this thermal loss to a low value. When the lead pool temperature increases in an accident, the PHRS removes significantly more heat due to the radiation heat transfer, which is related to the $4^{th}$ order of temperature, thus increasing its effectiveness when needed. The PHRS design also reduces the risk of the lead freezing inside RV in long term cooling as the radiation heat transfer is less effective at low temperatures.

## 4.2. PHRF

The WEC-LFR testing program is designed to address technological gaps in critical materials, components, and systems of the LFRs. Its objective is to enhance the technology readiness levels of these elements through a structured series of experimental campaigns. These campaigns leverage both existing facilities and newly developed ones—such as the eight test facilities recently established under the United Kingdom's Advanced Modular Reactor (AMR) program [102]. The overall aim is to provide engineering demonstrations that reduce design uncertainties and to generate high-quality experimental data for the verification and validation of the Modelling and Simulation (M&S) tools used in both engineering and safety analyses of the WEC-LFR.

The performance of the PHRS (described in Section 4.1) is being assessed through both numerical analyses and dedicated experimental campaigns. In this context, the UK's AMR program created a valuable opportunity to design, construct, and operate the PHRF. Within the framework of the AMR program, Work Package 7 (WP-7) was specifically focused on experimentally evaluating the PHRS performance. The activities under WP-7 included the development of a scaled PHRF facility, execution of a comprehensive test matrix, and complementary modelling and simulation tasks to support data interpretation and system validation.

WP-7 was carried out through a collaborative effort involving ANSALDO NUCLEARE, FRAZER-NASH CONSULTANCY, and Westinghouse Electric Company, along with contributions from other supporting organizations. ANSALDO NUCLEARE led the design, construction, and execution of testing at the PHRF. FRAZER-NASH CONSULTANCY contributed by developing high-resolution models of both the PHRS and the PHRF to assist in the facility's design process. Westinghouse, serving as the overall lead of the AMR program, provided the design specifications of the PHRS and conducted system-level analyses of the LFR to support both the PHRF design and the development of the experimental test matrix.

### *4.2.1. Description of the facility*

The PHRF (Passive Heat Removal Facility) [103] was developed based on the full-scale system with the primary objective of generating experimental data to validate modelling and simulation tools used for design and performance assessments. To ensure an accurate representation of the relevant physical phenomena, the system was hydrodynamically scaled using the "power-to-volume" approach. This method maintains the same working fluids and operating conditions as the reference system, while preserving the total height and the relative positions of the thermal centres of gravity.

As a result, the hydraulic behaviour, flow regimes, and time scales are appropriately replicated. Likewise, heat flux similarity is maintained to ensure that the dominant heat transfer mechanisms are accurately reproduced. A schematic overview of the scaling process is illustrated in Figure 63. Starting from the full-scale configuration—depicted in top view with the primary system, vessels, and water pool—a representative slice was extracted, then linearized and enclosed within a simplified external boundary. To achieve a practical facility size within site constraints, an overall geometric scaling ratio of approximately 1:10 was adopted.

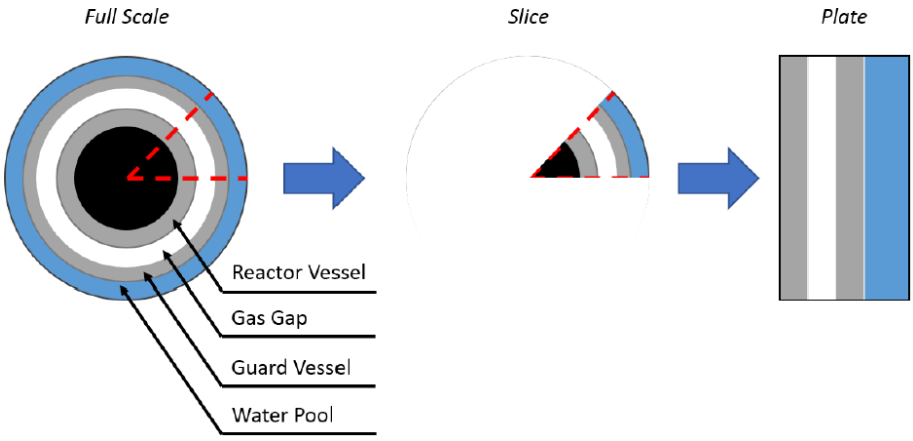


***Figure 63 Representation of the scaling process [103]***

Table 30 provides a systematic comparison between the full-scale system and the experimental facility. While the overall dimensions of the two vessels are preserved, the heat transfer surface area has been scaled proportionally to the geometric scaling factor. The baffle, which divides the water pool into two regions to promote natural air circulation, was specifically designed for the experimental setup according to project requirements. The air chimneys were scaled based on both the number and the total flow area, in order to replicate the expected flow velocities of the reference system.

The adopted scaling methodology ensures compliance with the main fluid dynamic similarity criteria. However, certain simplifications were necessary. The vessels, represented by linearized plates enclosed laterally, introduce edge effects that can slightly distort velocity profiles and cause some thermal losses—though these are minimized by the use of thermal insulation. Additionally, unlike the full-scale system, which is supported from the top, the experimental facility rests on a lower base. This structural difference introduces further heat losses through the bottom plate of the PHRF.

***Table 30 Comparison between PHRS and PHRF [103]***

| **Prototype (PHRS)** | **Model (PHRF)** | **Notes** |
|---|---|---|
| Full power | Scaled power | 1:10 power ratio |
| Reactor Vessel | Reactor Plate | Same height, thickness, material, 1/10 area ratio |
| Guard Vessel | Guard plate | Same height, thickness, material, 1/10 area ratio |
| Baffle | Baffle | Engineered from specification, 1/10 area ratio |
| 4x in/out chimneys | 1x in/out chimney | Scaled flow area, height, thickness, material |

A schematic picture of the PHRF is shown in Figure 64.

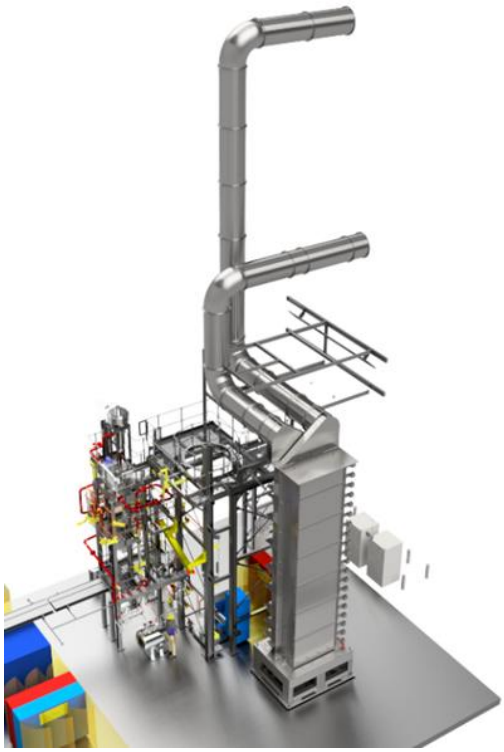

***Figure 64 3D Rendering of the PHRF [103]***

The purpose of the PHRF is to assess the TH performance of the PHRS and provide TH data for the V&V tools to model PHRS. In the WEC-LFR PIRT, three important phenomena associated with PHRS were identified as being relatively low state-of-knowledge:

- Transition from water cooling to air cooling in PHRS
- Natural convection heat transfer of air in PHRS
- PHRS stack performance during air-only cooling

Figure 65 illustrates the main body of the PHRF, representing the internal structures located within the reactor cavity. The assembly is mounted on a square steel base weighing approximately 9 tons and extends vertically to a height of about 8 meters. Its footprint measures roughly 2 meters by 2 meters. Internally, the structure houses several key components: a heating wall that simulates the core, plates representing the reactor and guard vessels, a baffle to guide natural circulation, and the surrounding water cavity. At the top, a vent diverter connects the structure to the external ducting. The main body itself weighs around 12 tons, increasing to approximately 25 tons when the water cavity is fully filled. The facility is extensively instrumented, with nearly 250 thermocouples installed to monitor temperatures across all relevant heat exchange surfaces and within the fluid domains.

It is important to note that the adopted scaling introduces geometric and physical distortions, particularly due to the presence of lateral walls. These walls, unlike the open annular geometry of the full-scale system, create edge effects that influence flow fields and require careful consideration when extrapolating experimental data to the real system. One notable consequence is the development of altered velocity profiles, which differ from those expected in the axisymmetric configuration of the actual reactor cavity.

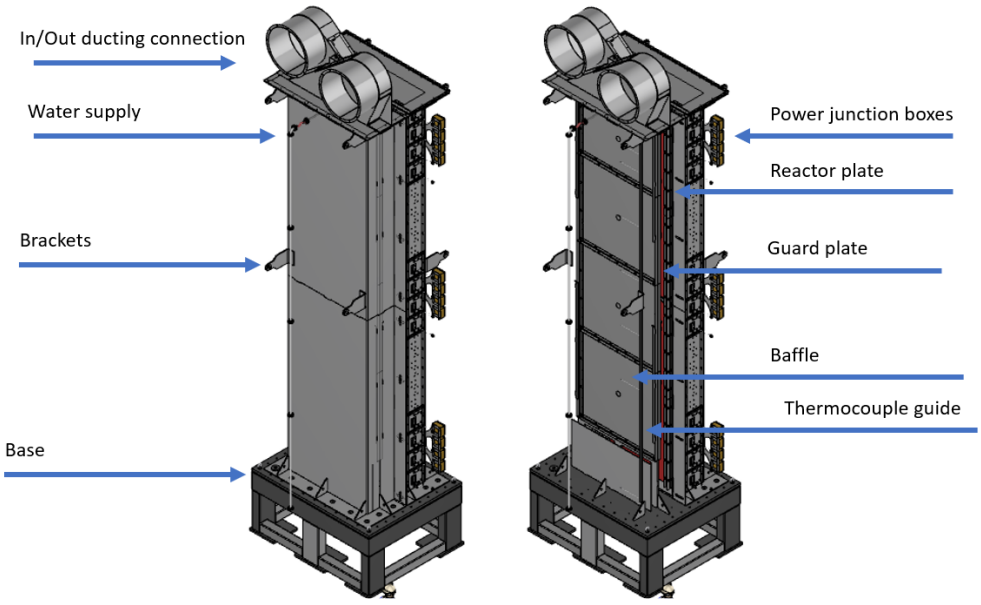


***Figure 65 PHRF main body [103]***

Figure 66 presents a photograph of the upper section of the PHRF main body, shown without its connection to the ducting system. Visible in the image is part of the internal heating structure, composed of 60 radiant plates distributed across 20 height levels. These Heating Plates (HPs) are mounted on a supporting frame anchored to the mechanically softer areas of the adjacent vessel-simulating plates. Each heating level is independently controlled by a dedicated control system, allowing the user to define either a temperature setpoint or power input along the vertical axis of the structure.


***Figure 66 PHRF main body top view [103]***

The Reactor Plate (RP) was scaled, maintaining the same height (around 7 m) and thickness (around 45 mm) of the real heat exchange surface within the PHRF, which spans approximately 2 meters in width. Based on an estimated maximum heat flux from the full-scale system of about 24 kW/m², the facility was designed to accommodate a total thermal power output of approximately 400 kW, ensuring adequate margin and aligning with the available site power capacity. A reference scaling factor of roughly 1:10 was adopted, balancing experimental relevance with practical constraints, and consequently defining the size of the PHRF sector.

A similar scaling logic was applied to the Guard Plate (GP), which shares the same height and thickness (approximately 15 mm) and width as the RP. Both plates are positioned at a separation distance of about 250 mm, consistent with the full-scale RV-GV spacing.

Regarding the water pool, distinct considerations were made for the lower and upper regions. The lower pool, located within the reactor cavity, was scaled to preserve both the power density and geometric height of the original system. This resulted in a thickness of approximately 650 mm and a width of about 2 meters—identical to the reference geometry. Conversely, the upper pool was not reproduced in the experimental setup. This choice was justified by the fact that the upper pool primarily serves as mass inventory and its contribution to the hydrostatic head is negligible in terms of thermal-hydraulic effects. Furthermore, the conceptual maturity of the upper pool design does not yet support detailed implementation in the PHRF.

The baffle structure inside the PHRF, in the absence of finalized design details, was engineered to satisfy key functional requirements. These include promoting effective natural circulation of air and water for adequate thermal coupling with the guard plate and minimizing bypass flow between the cold and hot zones—particularly near the component's lower region. The resulting component consists of a multilayer assembly with two 2-mm-thick stainless-steel plates separated by a 3-mm air gap. Edge reinforcements ensure mechanical integrity against deflection, given the component’s considerable height. Importantly, the baffle is fully removable, enabling the facility to support testing of alternative design configurations.

The air ducting system (see Figure 67) comprises two large-diameter ducts (900 mm each) — one for air intake and one for exhaust — extending to a total height of approximately 20 meters. These ducts are supported by existing structural frameworks, reinforced with scaffolding and dedicated supports to accommodate thermal expansion up to temperatures of 700°C. Instrumentation along the ducts enables precise measurement of temperature profiles and pressure drops. Flexible high-temperature couplings are employed at the interface between the main body and the ducting to compensate for thermal deformation and mechanical decoupling. Additionally, the air inlet duct can be equipped with a fan to maintain a constant flow rate, facilitating hydraulic characterization of the system.

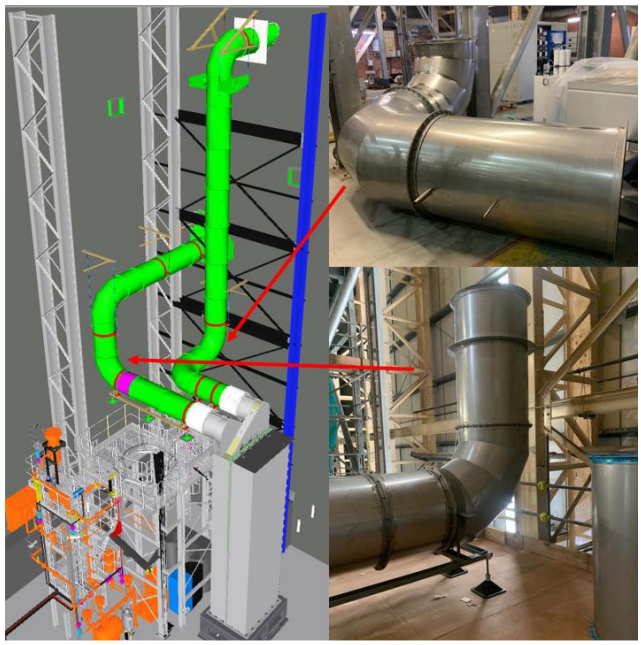

***Figure 67 PHRF ducting [103]***

### *4.2.2. Experiment description*

The PHRF was commissioned in March 2023, marking the start of its first experimental campaign [104]. This initial phase consisted of 14 tests, covering both air cooling and water-to-air transition scenarios. Table 31 presents the test matrix for this campaign. Tests Tst-1 through Tst-12 investigated air cooling without any water in the PHRF box, while Tst-13 and Tst-14 examined the transition from water cooling to air cooling. The main results of these tests are summarised below.

***Table 31 PHRF test matrix [104]***

| Test no. | Heater temperature [°C] | Blower rpm [%] | Initial Water Level [m] |
|---|---|---|---|
| **TST-1** | 400 | 0% | 0 |
| **TST-2** | 400 | 30% | 0 |
| **TST-3** | 400 | 60% | 0 |
| **TST-4** | 400 | 100% | 0 |
| **TST-5** | 550 | 0% | 0 |
| **TST-6** | 550 | 30% | 0 |
| **TST-7** | 550 | 60% | 0 |
| **TST-8** | 550 | 100% | 0 |
| **TST-9** | 650 | 0% | 0 |
| **TST-10** | 650 | 30% | 0 |
| **TST-11** | 650 | 60% | 0 |
| **TST-12** | 650 | 100% | 0 |
| **TST-13** | 700 | 0% | 3 |
| **TST-14** | 550 | 0% | 3 |

The air-cooling tests aimed to evaluate the PHRF's capability to remove heat through natural air circulation and to characterise flow patterns within the system. These steady-state experiments were performed under well-controlled conditions, with heater setpoints of 400 °C, 550 °C, and 650 °C—covering the range of temperatures expected in the PHRS of the WEC-LFR during a postulated accident. To study both natural and forced convection regimes, a blower installed in the inlet duct was operated at different speeds in certain tests.

Once steady state was reached, measured wall temperatures decreased progressively from the heating plates to the reactor plate and guard plate, while the air temperature increased along the flow path from the inlet, downcomer, and riser to the outlet. In some cases, certain thermocouples recorded temperatures exceeding the outlet air temperature, suggesting the presence of local recirculation within the PHRF. Overall, these tests successfully demonstrated the feasibility of the air-cooling phase in the PHRS and provided a robust dataset for TH model validation.


***Figure 68 PHRF synoptic***

The water–air transition tests aimed to evaluate the cooling performance of the PHRF during water cooling and to investigate the transient behaviour during the switch from water cooling to air cooling. These tests also supplied benchmark data for modelling this transition. Both Tst-13 and Tst-14 began with an initial water level of 3 m, corresponding to approximately one-third of the cavity height. In Tst-13, the heating plates were set to a temperature of 700 °C. Due to thermal radiation, the reactor plate maintained a relatively uniform temperature of about 600 °C. On the guard plate, two distinct thermal regimes were observed: above the water level, temperatures were around 450–500 °C, while below the water level they remained slightly above 100 °C, consistent with saturated boiling.

As the water boiled off, the falling level exposed successive thermocouples to air cooling. This sudden reduction in heat removal capacity caused a rapid temperature to increase on the guard plate. The water level decreased steadily until, at around 160 000 s, it dropped below the bottom edge of the baffle plate, breaking the water seal in the lower cavity. This event halted further temperature increases on the guard plate. Natural air circulation was subsequently established at approximately 180 000 s, providing stable air cooling and lowering the guard plate temperatures to a new steady state. Throughout the transition period, the PHRF maintained a relatively constant heat removal rate, comparable to that achieved in the later air-cooling phase. This confirmed the system's ability to shift from water cooling to air cooling without a significant loss of performance. Test Tst-14 repeated the transition under identical conditions, except with the heating plate set to 550 °C. The lower heat input extended the transient duration but produced similar thermal–hydraulic behaviour, confirming the reproducibility of the observed phenomena.

### *4.2.3. Numerical model*

The STH code RELAP5/Mod3.3 was used to develop the numerical model of the PHRF which is shown in Figure 69. The nodalization includes PIPE, SNGLJUN, TMDPVOL components to model the fluid volumes. Conversely the solid volumes are represented through HSs.

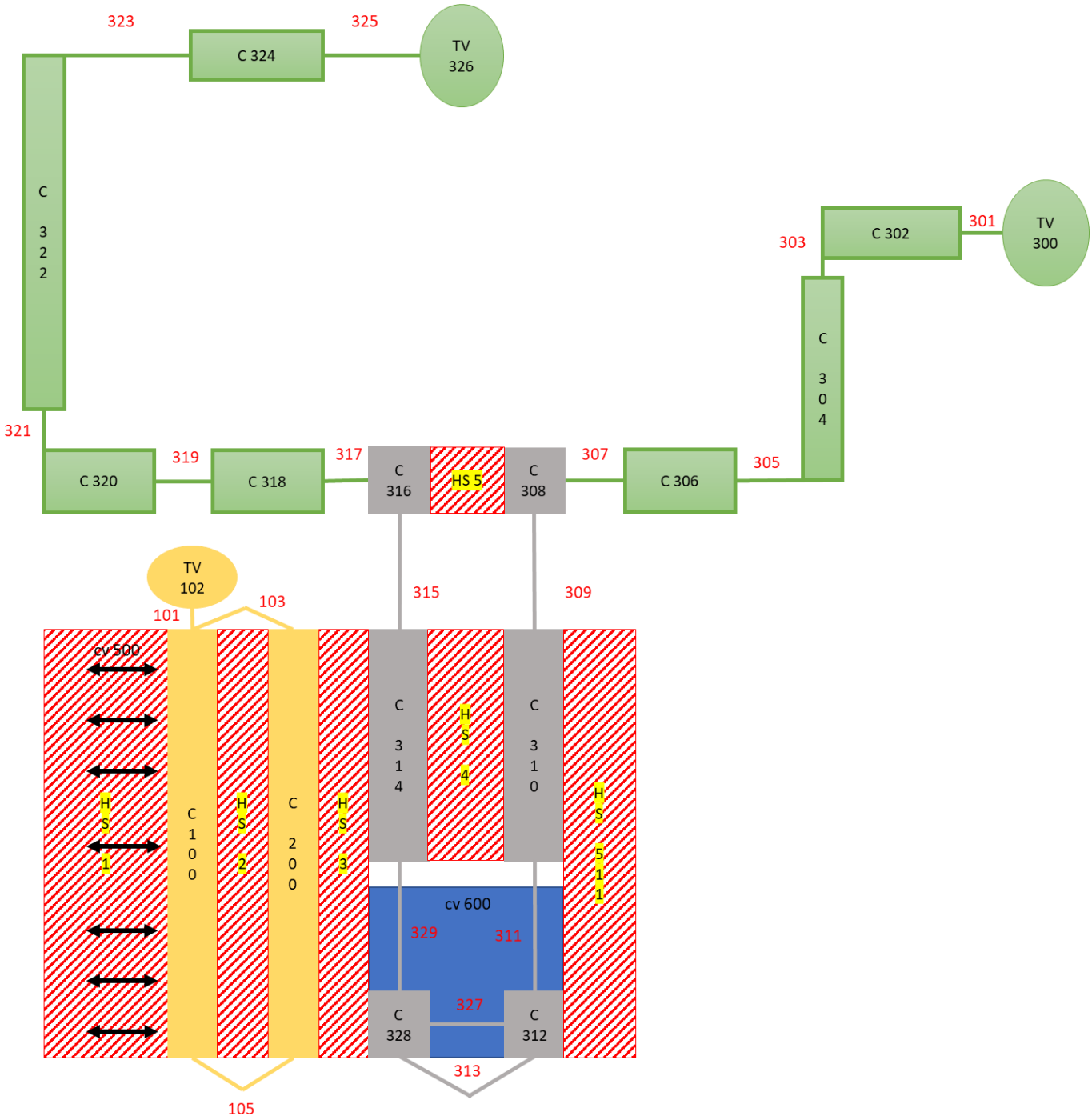


***Figure 69 R5 nodalization scheme of PHRF***

The control volumes shown in green represent the inlet and outlet ducting of the PHRF, while the grey volumes model the cavity regions within the main body. The orange volumes correspond to the regions inside the main body located between the HP and the RP, and between the RP and the GP.

Air can enter the system from outside the building via TMDPVOL 300. Once inside, it flows through the inlet channels—specifically through components C302 and C306—into the inlet manifold (C308), which distributes the air into the cold chamber of the lower pool, represented by pipe C310, consisting of 18 volumes. The flow continues to the bottom of the cavity (C312, with 2 volumes), then rises through the hot chamber of the lower pool (C314, also 18 volumes) and exits via the outlet manifold (C316). From there, the air flows through the outlet chimney ducts, modelled as a series of PIPEs from C318 to C324.

Inside the cavity, C100 and C200 represent the air regions located between the HP and RP, and between the RP and GP, respectively. The solid structures of the facility are modelled using dedicated HS. The passive HSs are modelled as follows: the chimney pipes include their own HSs, consisting of a 50 mm thick steel duct with 150 mm of thermal insulation. The hot side of the facility is represented by HS1 (20 nodes), which includes 200 mm of external insulation, 5 mm of steel, 98 mm of internal insulation, and a 2 mm thick layer representing the electric heaters. HS2 (20 nodes) corresponds to the RP, modelled as a solid 45 mm steel structure, while HS3 (20 nodes) represents the GP, a 15 mm thick steel plate. The baffle is modelled by HS4 (18 nodes), which simulates a multilayer structure composed of two 2 mm steel layers separated by a 3 mm stagnant air gap. The lateral surfaces of the PHRF are modelled with heat structures consisting of 5 mm of steel and 200 mm of thermal insulation.

The primary mode of heat transfer in the PHRF is thermal radiation, occurring mainly within four identified enclosures in the main body (see Figure 70). Enclosure (a) comprises the region between the HP, RP, and the lateral, roof, and bottom sidewalls (modelled by HS1, HS2, HS512, HS513, HS520, and HS524). Enclosure (b) encompasses the space between the RP, GP, and the corresponding surrounding structures (HS2, HS3, HS514, HS515, HS521, and HS525). Enclosure (c) includes the area between the GP, baffle, and surrounding walls (HS3, HS4, HS516, HS517, HS522, and HS526). Lastly, enclosure (d) represents the region between the baffle and the lateral surfaces (HS4, HS511, HS518, HS519, HS523, and HS527).

These radiation zones are simulated in RELAP5 using the radiation enclosure module, which calculates radiative heat exchange among all surfaces within a given enclosure. The view factors are determined analytically, as illustrated in Figure 71 and Figure 72. The emissivity of the heating plates is set to 0.9, while all other surfaces are assigned an emissivity of 0.7. Heat is supplied to the heating plates through volumetric heat generation in HS01, controlled by a feedback system that maintains a target set-point temperature. Each of the 60 heating plates is capable of delivering up to 7 kW of thermal power.

Additionally, the K-loss coefficients related to localized (concentrated) head losses mainly due to the ducting bends and abrupt area change in the inlet and outlet of the PHRF main body were computed using the empirical formulas provided in the Idelchik Hydraulic Handbook [64].

Lastly, the external environment was modelled by imposing a fixed ambient temperature of 15 °C, along with a convective HTC of 20 $W/m^2K$.

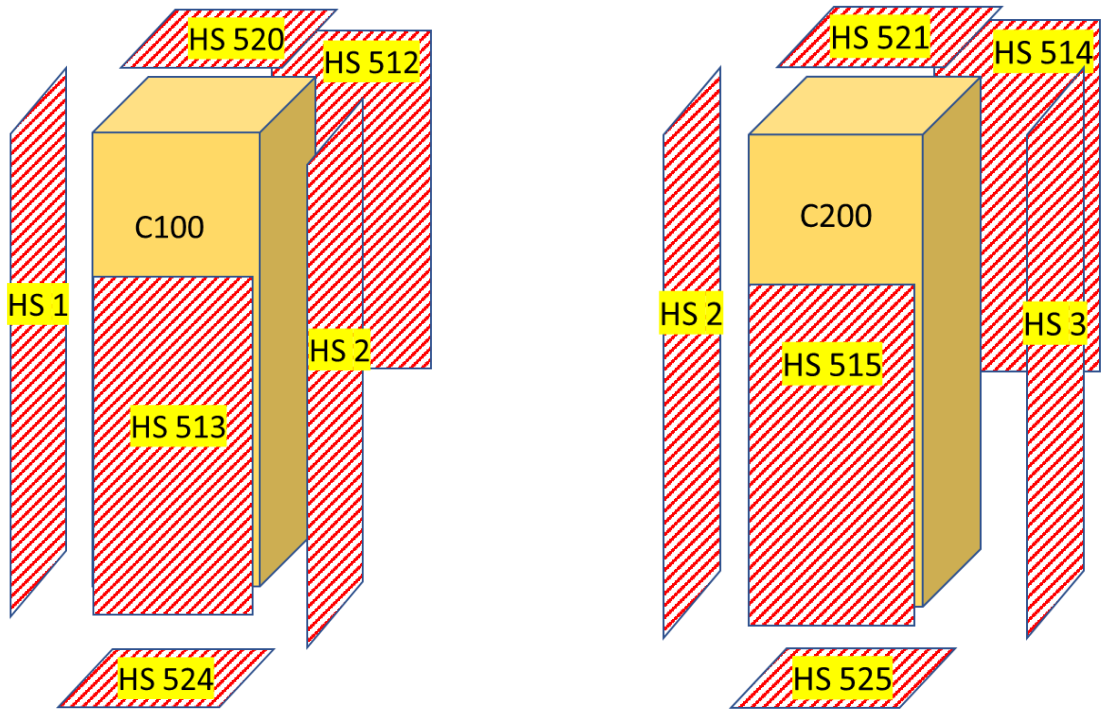


**(a)** **(b)**

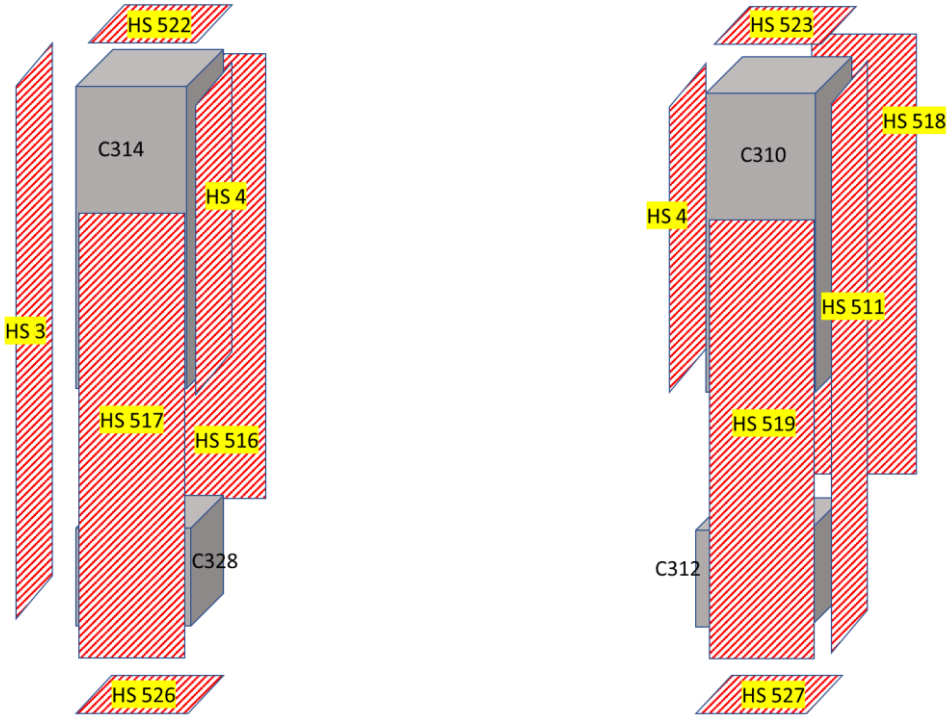


**(c)** **(d)**

***Figure 70 Enclosures and radiant surfaces: HP and RP zone (a), RP and GP zone (b), cavity riser (c) and cavity downcomer (d)***

**Rectangle to rectangle**

| Case | View factor |
|---|---|
| From rectangle $A_1$ at 90° to rectangle $A_2$ (mind it is singular if $x_1$=$\xi_1$=0). 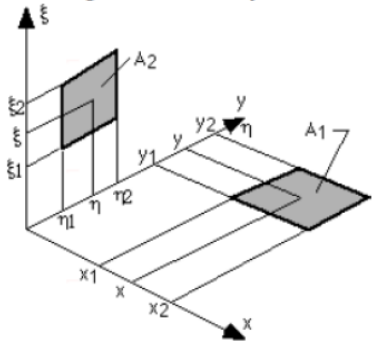 | $$F_{12}=\frac{1}{2\pi A_1}\sum_{l=1}^{2}\sum_{k=1}^{2}\sum_{j=1}^{2}\sum_{i=1}^{2}\left[(-1)^{(i+j+k+l)}\,B\left(x_i,y_j,\eta_k,\xi_l\right)\right]$$ with $A_1=(x_2-x_1)(y_2-y_1)$ $$B=(y-\eta)C\arctan(D)-\frac{C^2}{4}(1-D^2)\ln\left[C^2\left(1+D^2\right)\right]$$ $$C=\sqrt{x^2+\xi^2}\,,\quad D=\frac{(y-\eta)}{C}$$ (e.g. for squares touching: $x_1$=$\xi_1$=$10^{-6}$, $x_2$=$\xi_2$=1, $y_1$=$\eta_1$=0, $y_2$=$\eta_2$=1, $F_{12}$=0.20004) |

***Figure 71 View factor formula for orthogonal surfaces***

**Rectangle to rectangle**

| Case | View factor |
|---|---|
| From rectangle $A_1$ in parallel plane to rectangle $A_2$. 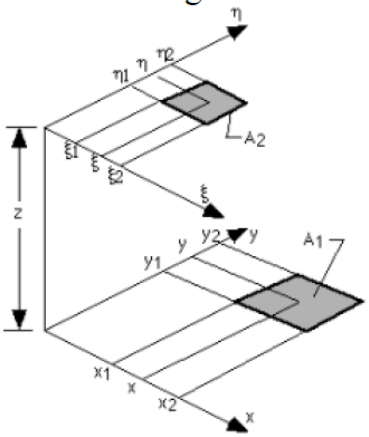 | $$F_{12}=\frac{1}{2\pi A_1}\sum_{l=1}^{2}\sum_{k=1}^{2}\sum_{j=1}^{2}\sum_{i=1}^{2}\left[(-1)^{(i+j+k+l)}\,B\left(x_i,y_j,\eta_k,\xi_l\right)\right]$$ with $A_1=(x_2-x_1)(y_2-y_1)$ $$B=vp\arctan\left(\frac{v}{p}\right)+uq\arctan\left(\frac{u}{q}\right)-\frac{z^2}{2}\ln\left(u^2+v^2+z^2\right)$$ $$u=x-\xi\,,\ v=y-\eta\,,\ p=\sqrt{u^2+z^2}\,,\ q=\sqrt{v^2+z^2}$$ (e.g. for frontal squares in a cube: $x_1$=$\xi_1$=0, $x_2$=$\xi_2$=1, $y_1$=$\eta_1$=0, $y_2$=$\eta_2$=1, z=1, $F_{12}$=0.1998) |

***Figure 72 View factor formula for parallel surfaces***

### 4.2.4. Simulation results

To verify the correct representation of the PHRF in terms of both its hydraulic behaviour (pressure losses) and thermal characteristics (heat capacities), as well as to ensure that the implemented heat transfer mechanisms between the different facility zones are accurately captured—particularly the emissivity values assigned in the numerical model—the PHRF shutdown test was simulated. Although this test was not formally part of the experimental campaign, it provided a valuable benchmark for assessing the overall accuracy of the PHRF numerical representation.

The boundary conditions implemented in the numerical model include the thermal power supplied by the HPs (see Figure 73), the air inlet temperature in the ducting (TP-702, see Figure 78), and the initial conditions manually specified throughout the PHRF model.

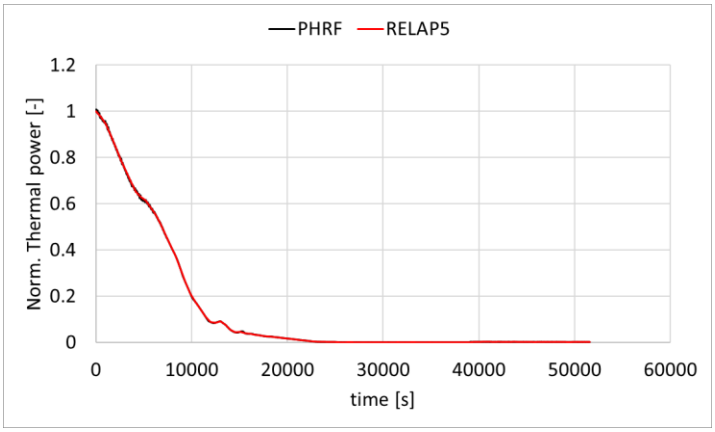


***Figure 73 Experimental vs RELAP5 thermal power of the PHRF***

Regarding the HP temperature, Figure 74 compares the experimental and numerical results. Except for the initial phase (approximately the first 500 s), both curves show excellent agreement, with an absolute deviation of about 5 °C in the long-term phase. The sudden rise in the RELAP5-predicted HP temperature is not supported by any identifiable physical phenomenon and is likely attributable to numerical artefacts. For the RP temperature, shown in Figure 75, the cooling rate is well reproduced in the short-term phase; in the long-term, the numerical prediction deviates from the experimental value by approximately 17 °C.

Figure 76 presents the temperature evolution on both sides of the GP. The model accurately captures the qualitative behaviour, with an initial temperature rise due to the missing of heat removal, followed by cooling driven by natural air convection. The timing of the peak temperature is correctly predicted, and the long-term deviation between the numerical and experimental results is approximately 10 °C. A notable discrepancy is observed in the temperature difference across the GP: the experimental value is significantly higher than those predicted, despite the GP being constructed from stainless steel. This difference is likely due to additional thermal resistance introduced by the thermocouples installed in the facility.

Figure 77 shows the baffle temperature evolution on both sides. Again, the model reproduces the qualitative trend accurately, with both the temperature gradient and long-term values closely matching the experimental results. Finally, Figure 78 reports the air inlet and outlet temperatures of the system. The outlet temperature trend is qualitatively well predicted by RELAP5, with the only major discrepancy being a delay in the peak temperature compared to the experiment. The long-term deviation between numerical and experimental outlet temperature is about 2 °C.

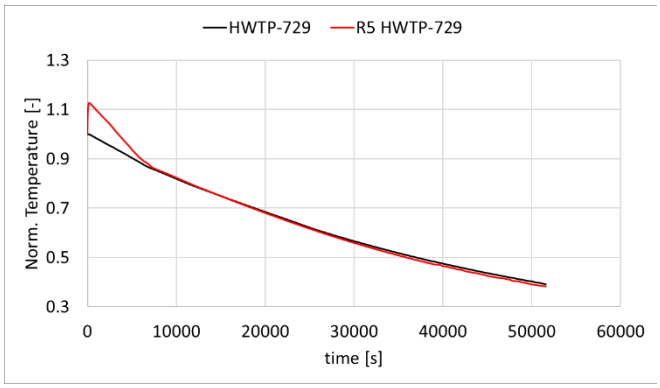


*Figure 74 Experimental vs RELAP5 HP temperature*

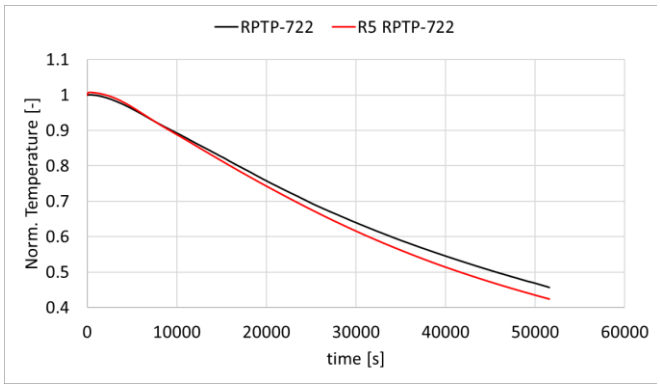


*Figure 75 Experimental vs RELAP5 RP temperature*

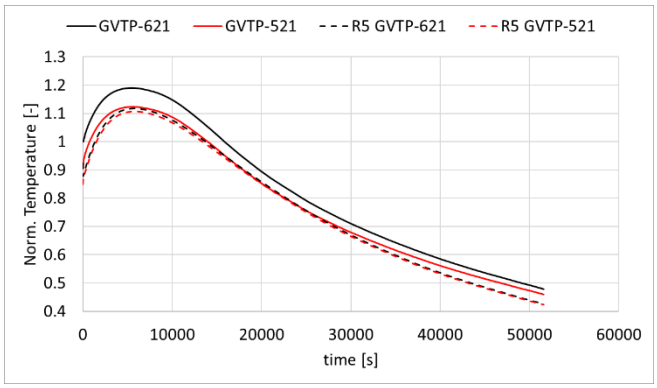


*Figure 76 Experimental vs RELAP5 GP temperatures*

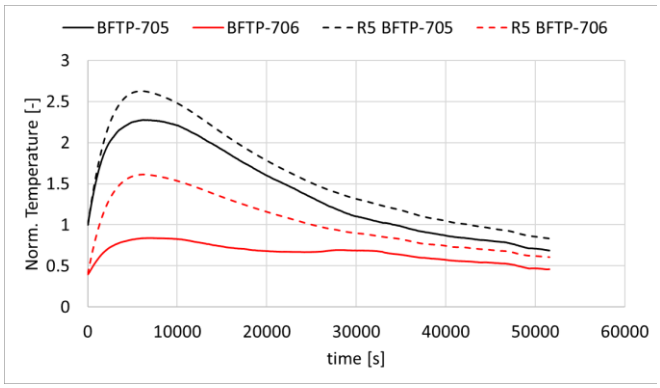


*Figure 77 Experimental vs RELAP5 baffle temperatures*

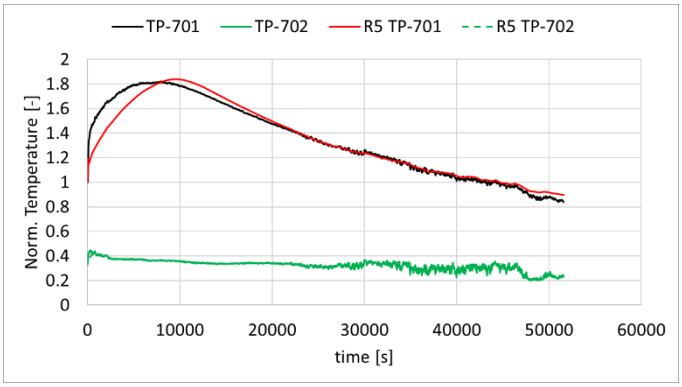


*Figure 78 Experimental vs RELAP5 ducting inlet and outlet air temperatures*

Based on these results, the PHRF numerical model can be considered reliable. This model was subsequently used to perform a numerical campaign aimed at reproducing the experimental tests listed in Table 31. However, due to limited available information and the absence of the blower in the model, only the natural circulation tests (TST-1, TST-5, and TST-9) could be simulated.

The PHRF thermal power, differentiate at each of the 20 height levels for every experimental test is shown in Figure 79 and implemented as boundary conditions.

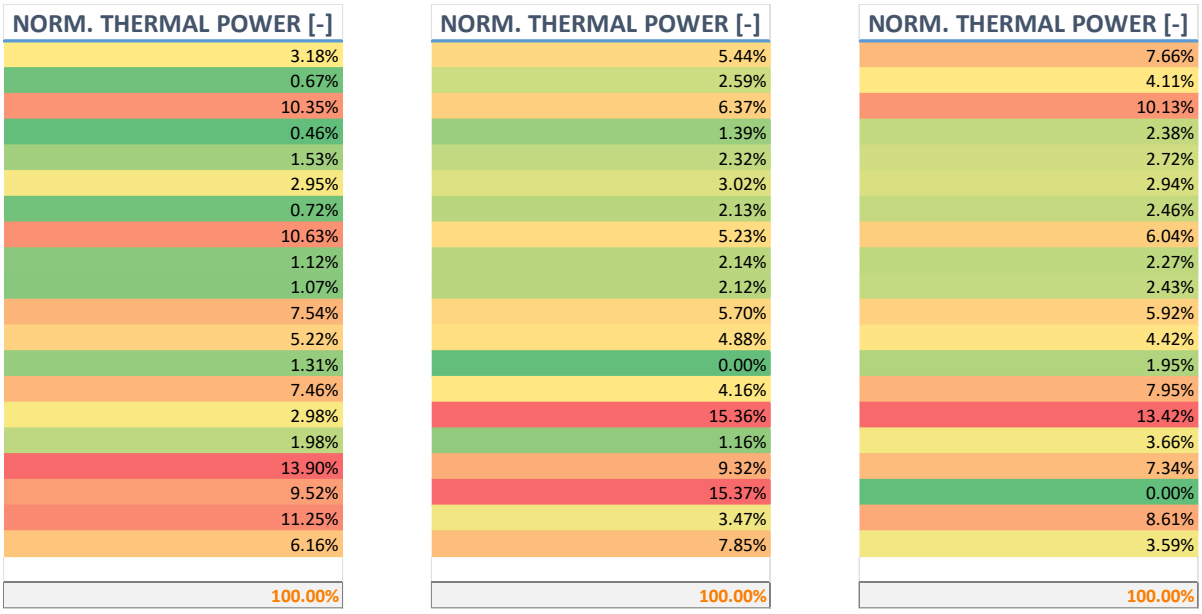


**(a)** **(b)** **(c)**

***Figure 79 PHRF thermal power: TST-1 (a), TST-5 (b) and TST-9 (c)***

The main outcome of these simulations is the thermal field predicted by RELAP5 across all zones of the PHRF, compared against the corresponding experimental measurements. The comparison focuses on the surface temperatures of the HP, RP, and GP, as well as the air temperature at the ducting inlet and outlet. The steady-state temperature distributions of all the plates obtained from the experimental measurements (left) and from the RELAP5 numerical simulation (right) are compared. In both cases, the plates exhibit a generally consistent temperature pattern, with higher values concentrated in specific regions and lower temperatures near the periphery or in localized areas.

The experimental data show some degree of spatial variability, with several plates exceeding and occasional hotspots, particularly in the upper section. The RELAP5 results reproduce the overall distribution trend, capturing the location of the main high-temperature zones and the cooler areas. However, certain discrepancies are evident: the simulation tends to slightly overpredict peak temperatures in some regions, while underestimating them in others, resulting in a smoother distribution compared to the experimental field. These deviations may stem from model limitations, such as the simplified representation of localized cooling effects or the inability to capture complex three-dimensional convective cells that cannot be resolved in the numerical model. Overall, the comparison confirms that the model can replicate the qualitative thermal pattern of the plates, while the quantitative differences suggest the need for further refinement to improve local accuracy. Finally, in all the considered cases, the ducting air outlet temperature predicted by RELAP5 is in good agreement with the experimental measurements, indicating a consistent representation of the overall thermal balance of the system.

| NORM. HP TEMPERATURE [-] | | | | R5 NORM. HP TEMPERATURE [-] |
|---|---|---|---|---|
| 1.015 | 1.000 | 1.037 | | 1.052 |
| 1.056 | 1.003 | 1.058 | | 1.168 |
| 1.086 | 1.004 | 1.143 | | 1.012 |
| 1.001 | 1.003 | 0.968 | | 1.403 |
| 0.991 | 1.003 | 0.911 | | 0.959 |
| 1.079 | 1.003 | 0.933 | | 0.938 |
| 0.995 | 1.003 | 0.962 | | 0.963 |
| 1.125 | 1.001 | 1.102 | | 0.972 |
| 0.980 | 1.003 | 0.862 | | 0.883 |
| 0.967 | 1.003 | 0.953 | | 0.875 |
| 1.203 | 0.954 | 0.904 | | 1.073 |
| 1.149 | 0.999 | 0.913 | | 0.959 |
| 0.913 | 1.003 | 0.934 | | 0.822 |
| 0.901 | 0.910 | 1.203 | | 1.005 |
| 0.944 | 0.948 | 0.877 | | 1.092 |
| 0.723 | 0.991 | 0.893 | | 0.849 |
| 0.959 | 0.817 | 0.812 | | 0.847 |
| 0.849 | 0.860 | 0.972 | | 1.074 |
| 1.081 | 0.628 | 1.177 | | 0.947 |
| 0.606 | 0.621 | 0.340 | | 0.671 |

**(a)**

| NORM. RP TEMPERATURE [-] | | | | R5 NORM. RP TEMPERATURE [-] |
|---|---|---|---|---|
| 0.914 | 0.922 | | | 0.918 |
| 0.979 | 0.987 | | | 0.983 |
| 0.959 | 0.776 | 0.964 | | 0.958 |
| 1.315 | 0.745 | | | 1.097 |
| 0.852 | 0.864 | | | 0.914 |
| 0.861 | 0.867 | 0.857 | | 0.862 |
| 0.837 | 0.880 | | | 0.860 |
| 0.799 | 0.901 | | | 0.853 |
| 0.814 | 0.824 | 0.799 | | 0.814 |
| 0.810 | 0.819 | | | 0.816 |
| 0.884 | 0.891 | | | 0.888 |
| 0.835 | 0.853 | 0.829 | | 0.840 |
| 0.774 | 0.796 | | | 0.786 |
| 0.841 | 0.868 | | | 0.856 |
| 0.886 | 0.886 | 0.884 | | 0.887 |
| 0.768 | 0.798 | | | 0.786 |
| 0.761 | 0.788 | | | 0.777 |
| 0.852 | 0.852 | 0.858 | | 0.856 |
| 0.777 | 0.789 | | | 0.784 |
| 0.535 | 0.546 | | | 0.642 |

**(b)**

| NORM. GP TEMPERATURE [-] | | | | | | R5 NORM. GP TEMPERATURE [-] | |
|---|---|---|---|---|---|---|---|
| | 0.565 | 0.555 | 0.537 | 0.177 | | 0.619 | 0.615 |
| | 0.554 | 0.544 | 0.525 | 0.513 | | 0.650 | 0.645 |
| 0.555 | 0.548 | 0.550 | 0.528 | 0.524 | 0.522 | 0.662 | 0.657 |
| | 0.516 | 0.532 | 0.490 | 0.506 | | 0.681 | 0.675 |
| | 0.509 | 0.516 | 0.489 | 0.493 | | 0.635 | 0.630 |
| 0.517 | 0.508 | 0.507 | 0.496 | 0.478 | 0.482 | 0.599 | 0.595 |
| | 0.499 | 0.498 | 0.473 | 0.474 | | 0.583 | 0.579 |
| | 0.487 | 0.490 | 0.460 | 0.460 | | 0.570 | 0.566 |
| 0.489 | 0.478 | 0.480 | 0.465 | 0.448 | 0.446 | 0.555 | 0.551 |
| | 0.466 | 0.466 | 0.448 | 0.446 | | 0.551 | 0.547 |
| | 0.466 | 0.459 | 0.443 | 0.440 | | 0.559 | 0.554 |
| 0.465 | 0.452 | 0.452 | 0.438 | 2288 | 0.424 | 0.545 | 0.541 |
| | 0.434 | 0.430 | 0.406 | 0.404 | | 0.530 | 0.527 |
| | 0.428 | 0.426 | 0.403 | 0.401 | | 0.538 | 0.534 |
| 0.422 | 0.422 | 0.415 | 0.400 | 0.393 | 0.389 | 0.538 | 0.534 |
| | 0.381 | 0.373 | 0.357 | 0.349 | | 0.512 | 0.508 |
| | 0.352 | 0.337 | 0.325 | 0.312 | | 0.500 | 0.496 |
| 0.320 | 0.334 | 0.320 | 0.288 | 0.424 | 0.282 | 0.502 | 0.498 |
| | 0.269 | 0.282 | 0.247 | 0.252 | | 0.450 | 0.446 |
| | 2289 | 0.255 | 0.198 | 0.226 | | 0.404 | 0.400 |

**(c)**

| NORM. AIR OUTLET TEMPERATURE [-] | NORM. AIR INLET TEMPERATURE [-] | | R5 NORM. AIR OUTLET TEMPERATURE [-] | R5 NORM. AIR INLET TEMPERATURE [-] |
|---|---|---|---|---|
| 0.129 | 0.033 | | 0.122 | 0.033 |

**(d)**

***Figure 80 TST-1: Experimental vs RELAP5 thermal field***

| NORM. HP TEMPERATURE [-] | | | | R5 NORM. HP TEMPERATURE [-] |
|---|---|---|---|---|
| 1.406 | 1.380 | 1.449 | | 1.459 |
| 1.459 | 1.390 | 1.395 | | 1.433 |
| 1.421 | 1.354 | 1.478 | | 1.416 |
| 1.363 | 1.379 | 1.334 | | 1.910 |
| 1.341 | 1.379 | 1.242 | | 1.390 |
| 1.410 | 1.379 | 1.261 | | 1.290 |
| 1.318 | 1.379 | 1.319 | | 1.368 |
| 1.483 | 1.316 | 1.374 | | 1.874 |
| 1.348 | 1.379 | 1.240 | | 1.332 |
| 1.297 | 1.379 | 1.327 | | 1.214 |
| 1.481 | 1.308 | 1.278 | | 1.371 |
| 1.484 | 1.380 | 1.311 | | 1.316 |
| 1.166 | 1.243 | 1.242 | | 1.156 |
| 1.319 | 1.287 | 1.483 | | 1.272 |
| 1.205 | 1.213 | 1.172 | | 1.665 |
| 1.088 | 1.379 | 1.292 | | 1.267 |
| 1.437 | 1.202 | 1.138 | | 1.231 |
| 1.168 | 1.183 | 1.271 | | 1.503 |
| 1.106 | 0.761 | 1.182 | | 1.167 |
| 0.995 | 1.009 | 0.623 | | 0.932 |

**(a)**

| NORM. RP TEMPERATURE [-] | | | | R5 NORM. RP TEMPERATURE [-] |
|---|---|---|---|---|
| 1.279 | 1.280 | | | 1.279 |
| 1.301 | 1.297 | | | 1.299 |
| 1.266 | 1.196 | 1.260 | | 1.343 |
| 1.785 | 1.159 | | | 1.538 |
| 1.175 | 1.192 | | | 1.325 |
| 1.179 | 1.191 | 1.172 | | 1.246 |
| 1.374 | 1.182 | | | 1.303 |
| 1.476 | 1.521 | | | 1.499 |
| 1.126 | 1.147 | 1.118 | | 1.269 |
| 1.132 | 1.150 | | | 1.170 |
| 1.197 | 1.214 | | | 1.205 |
| 1.163 | 1.190 | 1.166 | | 1.173 |
| 1.082 | 1.112 | | | 1.111 |
| 1.163 | 1.197 | | | 1.180 |
| 1.334 | 1.334 | 1.349 | | 1.339 |
| 1.152 | 1.199 | | | 1.176 |
| 1.121 | 1.154 | | | 1.138 |
| 1.219 | 1.219 | 1.218 | | 1.219 |
| 1.038 | 1.061 | | | 1.050 |
| 0.759 | 0.769 | | | 0.898 |

**(b)**

| NORM. GP TEMPERATURE [-] | | | | | | R5 NORM. GP TEMPERATURE [-] | |
|---|---|---|---|---|---|---|---|
| | 0.825 | 0.805 | 0.777 | 0.270 | | 0.938 | 0.930 |
| | 0.810 | 0.797 | 0.759 | 0.746 | | 0.975 | 0.967 |
| 0.808 | 0.803 | 0.804 | 0.766 | 0.764 | 0.759 | 1.015 | 1.006 |
| | 0.761 | 0.778 | 0.719 | 0.735 | | 1.059 | 1.049 |
| | 0.754 | 0.756 | 0.720 | 0.719 | | 1.006 | 0.997 |
| 0.761 | 0.756 | 0.746 | 0.724 | 0.707 | 0.705 | 0.966 | 0.958 |
| | 0.739 | 0.730 | 0.695 | 0.693 | | 0.982 | 0.973 |
| | 0.720 | 0.719 | 0.676 | 0.671 | | 1.014 | 1.004 |
| 0.728 | 0.720 | 0.717 | 0.689 | 0.672 | 0.662 | 0.946 | 0.938 |
| | 0.711 | 0.706 | 0.679 | 0.671 | | 0.887 | 0.880 |
| | 0.714 | 0.702 | 0.673 | 0.668 | | 0.867 | 0.860 |
| 0.718 | 0.703 | 0.705 | 0.672 | 2288 | 0.654 | 0.845 | 0.838 |
| | 0.687 | 0.681 | 0.636 | 0.636 | | 0.827 | 0.820 |
| | 0.694 | 0.692 | 0.648 | 0.647 | | 0.847 | 0.839 |
| 0.714 | 0.721 | 0.710 | 0.672 | 0.664 | 0.655 | 0.877 | 0.869 |
| | 0.650 | 0.639 | 0.602 | 0.591 | | 0.835 | 0.827 |
| | 0.597 | 0.571 | 0.547 | 0.523 | | 0.803 | 0.796 |
| 0.543 | 0.564 | 0.538 | 0.480 | 0.655 | 0.466 | 0.789 | 0.782 |
| | 0.433 | 0.453 | 0.388 | 0.400 | | 0.684 | 0.677 |
| | 2289 | 0.388 | 0.307 | 0.339 | | 0.612 | 0.607 |

**(c)**

| NORM. AIR OUTLET TEMPERATURE [-] | NORM. AIR INLET TEMPERATURE [-] | | R5 NORM. AIR OUTLET TEMPERATURE [-] | R5 NORM. AIR INLET TEMPERATURE [-] |
|---|---|---|---|---|
| 0.176 | 0.041 | | 0.188 | 0.040 |

**(d)**

***Figure 81 TST-5: Experimental vs RELAP5 thermal field***

| NORM. HP TEMPERATURE [-] | | | | R5 NORM. HP TEMPERATURE [-] |
|---|---|---|---|---|
| 1.584 | 1.505 | 1.580 | | 1.681 |
| 1.610 | 1.463 | 1.491 | | 1.608 |
| 1.570 | 1.361 | 1.582 | | 1.300 |
| 1.513 | 1.504 | 1.483 | | 1.272 |
| 1.454 | 1.504 | 1.363 | | 1.501 |
| 1.511 | 1.503 | 1.372 | | 1.427 |
| 1.430 | 1.504 | 1.439 | | 1.443 |
| 1.601 | 1.437 | 1.528 | | 1.810 |
| 1.471 | 1.505 | 1.370 | | 1.366 |
| 1.373 | 1.504 | 1.458 | | 1.371 |
| 1.602 | 1.412 | 1.379 | | 1.544 |
| 1.557 | 1.504 | 1.428 | | 1.456 |
| 1.450 | 1.504 | 1.424 | | 1.330 |
| 1.496 | 1.400 | 1.592 | | 1.614 |
| 1.344 | 1.353 | 1.298 | | 1.747 |
| 1.159 | 1.505 | 1.418 | | 1.440 |
| 1.369 | 1.005 | 0.983 | | 1.291 |
| 1.315 | 1.318 | 1.306 | | 1.033 |
| 1.299 | 0.839 | 1.423 | | 1.072 |
| 0.789 | 0.814 | 0.489 | | 0.872 |

**(a)**

| NORM. RP TEMPERATURE [-] | | | | R5 NORM. RP TEMPERATURE [-] |
|---|---|---|---|---|
| 1.427 | 1.415 | | | 1.421 |
| 1.424 | 1.350 | | | 1.388 |
| 1.399 | 0.792 | 1.382 | | 1.248 |
| 0.959 | 0.787 | | | 1.225 |
| 1.308 | 1.320 | | | 1.314 |
| 1.297 | 1.312 | 1.302 | | 1.304 |
| 1.367 | 1.310 | | | 1.339 |
| 1.453 | 1.505 | | | 1.480 |
| 1.258 | 1.284 | 1.259 | | 1.302 |
| 1.263 | 1.287 | | | 1.275 |
| 1.323 | 1.348 | | | 1.336 |
| 1.289 | 1.316 | 1.294 | | 1.300 |
| 1.251 | 1.277 | | | 1.264 |
| 1.368 | 1.403 | | | 1.386 |
| 1.427 | 1.427 | 1.457 | | 1.437 |
| 1.259 | 1.299 | | | 1.279 |
| 1.132 | 1.165 | | | 1.149 |
| 0.953 | 0.953 | 0.954 | | 0.999 |
| 0.942 | 0.960 | | | 0.951 |
| 0.824 | 0.835 | | | 0.845 |

**(b)**

| NORM. GP TEMPERATURE [-] | | | | | | R5 NORM. GP TEMPERATURE [-] | |
|---|---|---|---|---|---|---|---|
| | 0.961 | 0.952 | 0.903 | 0.329 | | 1.004 | 0.995 |
| | 0.930 | 0.943 | 0.871 | 0.879 | | 1.006 | 0.998 |
| 0.937 | 0.922 | 0.944 | 0.885 | 0.876 | 0.889 | 0.964 | 0.957 |
| | 0.884 | 0.907 | 0.834 | 0.855 | | 0.950 | 0.942 |
| | 0.877 | 0.879 | 0.837 | 0.835 | | 0.967 | 0.959 |
| 0.884 | 0.882 | 0.870 | 0.839 | 0.824 | 0.822 | 0.976 | 0.968 |
| | 0.867 | 0.858 | 0.815 | 0.812 | | 0.998 | 0.990 |
| | 0.852 | 0.850 | 0.799 | 0.792 | | 1.025 | 1.015 |
| 0.854 | 0.851 | 0.847 | 0.806 | 0.796 | 0.783 | 0.980 | 0.971 |
| | 0.841 | 0.834 | 0.803 | 0.792 | | 0.954 | 0.946 |
| | 0.846 | 0.832 | 0.797 | 0.793 | | 0.956 | 0.948 |
| 0.851 | 0.836 | 0.838 | 0.795 | 2288 | 0.777 | 0.944 | 0.936 |
| | 0.826 | 0.817 | 0.765 | 0.762 | | 0.939 | 0.931 |
| | 0.858 | 0.851 | 0.800 | 0.793 | | 0.968 | 0.959 |
| 0.871 | 0.897 | 0.874 | 0.817 | 0.825 | 0.805 | 0.969 | 0.960 |
| | 0.746 | 0.737 | 0.693 | 0.683 | | 0.900 | 0.891 |
| | 0.623 | 0.597 | 0.571 | 0.549 | | 0.813 | 0.806 |
| 0.493 | 0.520 | 0.494 | 0.443 | 0.780 | 0.435 | 0.729 | 0.723 |
| | 0.398 | 0.415 | 0.361 | 0.371 | | 0.636 | 0.630 |
| | 2289 | 0.385 | 0.301 | 0.342 | | 0.580 | 0.575 |

**(c)**

| NORM. AIR OUTLET TEMPERATURE [-] | NORM. AIR INLET TEMPERATURE [-] | | R5 NORM. AIR OUTLET TEMPERATURE [-] | R5 NORM. AIR INLET TEMPERATURE [-] |
|---|---|---|---|---|
| 0.213 | 0.042 | | 0.196 | 0.043 |

**(d)**

***Figure 82 TST-9: Experimental vs RELAP5 thermal field***

### 4.2.5. Pre-test analysis

Once the RELAP5 numerical model of the PHRF was successfully validated under both steady-state and transient conditions, it was applied to the simulation of a water test. Unlike the corresponding experimental test, the initial water level in the simulation was set to the nominal value, i.e., approximately 7 m. Following the same approach adopted in the experimental campaign, the thermal power supplied by the HP was controlled to maintain a surface temperature setpoint of 700 °C. This setup replicates the high thermal inertia associated with liquid lead, which significantly limits the cooling rate. The boundary conditions adopted for this simulation are summarised in Table 32.

***Table 32 PHRF boundary conditions***

| Quantity | Value | Unit of measure |
|---|---|---|
| HP temperature setpoint | 700 | °C |
| Air inlet temperature | 15 | °C |
| PHRF initial temperature | 30 | °C |
| PHRF initial water level | 7000 | mm |

The thermal power supplied by the HPs is presented in Figure 83. During the initial phase, lasting approximately 1.5 hours, the HPs operate at their maximum allowable power of 420 kW. This corresponds to the period in which the water is heated to reach saturation conditions. Once boiling begins, the total power progressively decreases, following the same trend as the water level (see Figure 84). This behaviour is driven by the change in heat transfer mechanism from highly efficient pool boiling to less efficient steam convection. To maintain the HP surface temperature at the prescribed setpoint, the control system reduces the supplied power accordingly. At around 50 hours, a sudden increase in thermal power is observed. This is caused by the entry of cold air into the system, triggered when the water level drops below the height of the baffle, enabling air ingress. This phenomenon also affects the water level evolution, reducing the depletion rate at the same instant. This marks the onset of the water-to-air cooling transition. The entire water inventory is depleted after approximately 75 hours. In the long-term natural air convection phase, the thermal power stabilises.

Figure 85 and Figure 86 show the RP and GP surface temperatures at various height levels. Both components exhibit the same qualitative trend, with a horizontal thermal gradient resulting from the combined effects of radiation and conduction. While submerged, the GP temperatures remain fixed at water saturation conditions. Once boiling ceases at a given location, a sudden temperature increase occurs due to dryout, with higher measurement points showing this rise earlier than lower ones. The RP displays the same pattern, albeit with a slight delay at equivalent elevations. In the natural air convection phase, the RP and GP temperatures stabilise. The air mass flow rate and temperature profiles (Figure 87 and Figure 88) clearly show all phases of the transient. Initially, during the pool boiling phase, temperatures remain constant at water saturation temperature, followed by a steam convection phase marked by a gradual temperature increase due to superheated steam. At around 50 hours, the water-to-air transition occurs, with a sudden rise in mass flow rate and a sharp drop in temperature. In the long-term natural air convection regime, the system stabilises with a constant mass flow rate and constant outlet temperature, ensuring a stable thermal balance.

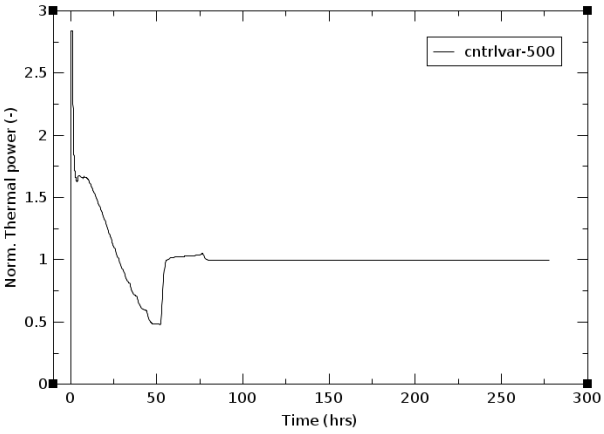


*Figure 83 PHRF thermal power*

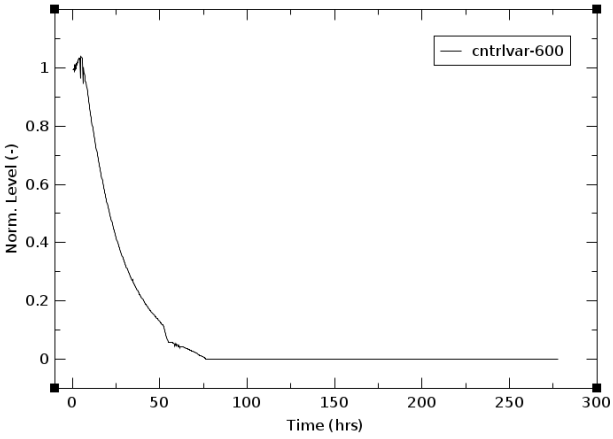


*Figure 84 Water level*

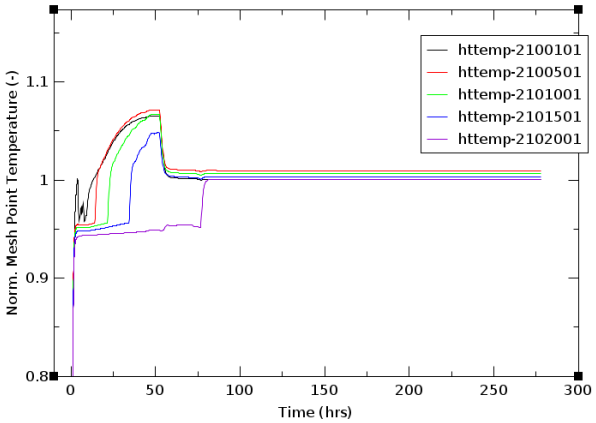


*Figure 85 RP temperatures*

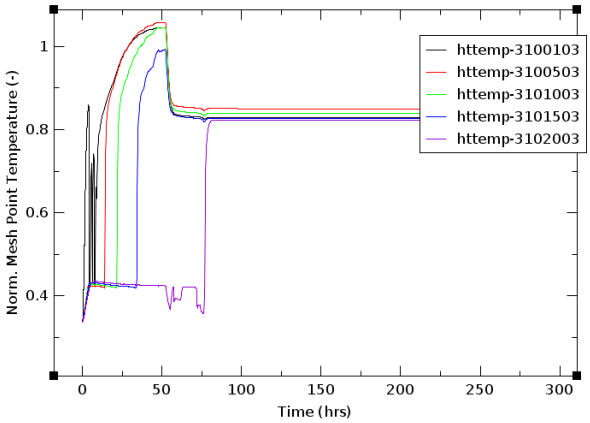


*Figure 86 GP temperatures*

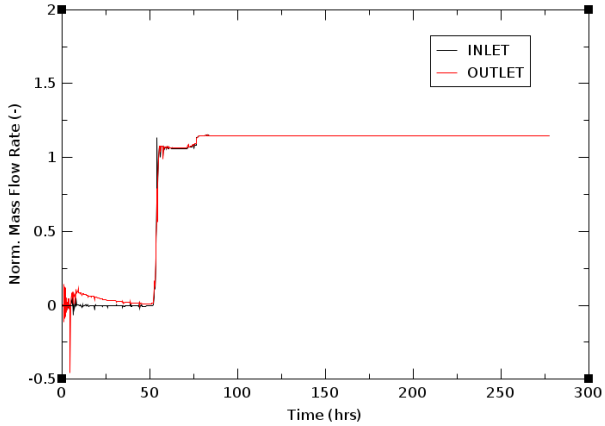


*Figure 87 Ducting air mass flow rate*

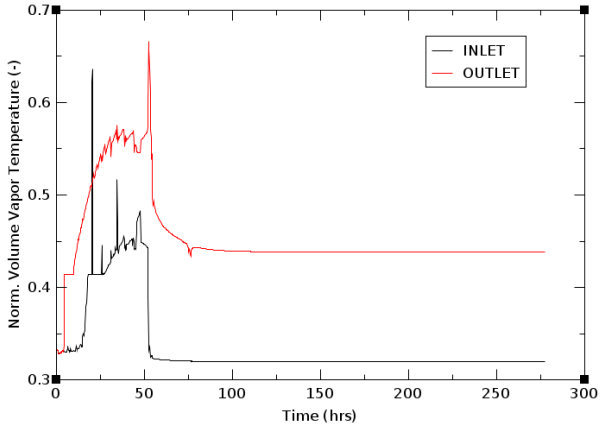


*Figure 88 Ducting air temperature*

## 4.3. VLF

Within the framework to support the development of the WEC-LFR, the UK Department for Business, Energy & Industrial Strategy (BEIS) initiated a competition focused on the development of advanced modular reactor technologies, structured in two phases [102]. The team led by Westinghouse Electric Company LLC, in collaboration with key partners ANSALDO NUCLEARE and ENEA, and several key UK labs and universities proposed the WEC-LFR for development.

In the first phase, the focus was on conceptual and feasibility engineering, identifying high-priority R&D needs, and determining the experimental test facilities required to address key knowledge gaps in the technology. The second phase was dedicated to the experimental test facilities for their detailed design, construction, and initial operation.

Among these facilities is the VLF, a test rig designed to demonstrate the operation and thermal-hydraulic performance of the fuel bundle and the PHE of the WEC-LFR. The VLF is highly adaptable, allowing for loop reconfigurations to meet additional needs. Although the VLF is conceived as a component test facility and is not scaled from the WEC-LFR for system-level analysis, its key components, such as the electrically heated rod bundle and the heat exchanger, are scaled versions of the actual components.

These scaled components maintain similarity in thermal-hydraulic behaviour. The VLF distinguishes itself as a new experimental facility capable of achieving high-temperature conditions (up to 650°C), facilitated by its main components, which are surface-treated with an alumina coating.

### *4.3.1. Description of the facility*

The VLF (Versatile Loop Facility) is an experimental facility designed for the thermal-hydraulic characterization of key components of the WEC-LFR, including the PHE (liquid lead/supercritical water) and the fuel bundle [105]. The experimental data gathered will help in characterizing the hydraulics of these components, assess their heat transfer performance, guide optimization strategies, and validate computational codes for analysing in-lead components with complex geometries.

The facility comprises three main systems: the primary loop, the secondary loop, and the lead preparation, conditioning, and pressure control system. The VLF includes a lead loop made by AISI 321H that can operate at temperatures up to 650°C, containing a 500-kW electric fuel bundle simulator representing the Westinghouse LFR bundle. It also features a hybrid micro channel-type diffusion-bonded heat exchanger, representing the PHE of the WEC-LFR design. Heat removal is performed by a supercritical water-cooling loop designed for pressures up to 330 bar and maximum operating temperatures of 620°C. Table 33 shows the reference nominal operating conditions that have been thoroughly analysed in this work.

*Table 33 VLF nominal conditions [105]*

| Parameter | Unit | Value |
|---|---|---|
| **FPBS thermal power** | kW | 500 |
| **Prim. Lead cold leg temperature** | °C | 390 |
| **Prim. Lead hot leg temperature** | °C | 530 |
| **Prim. Lead mass flow rate** | kg/s | 24.5 |
| **Sec. Water inlet temperature** | °C | 20 |
| **Sec. Water maximum temperature** | °C | 520 |
| **Sec. Water mass flow rate** | kg/s | 0.474 |

As shown in Figure 89, the primary lead loop is constituted by the following components: the Fuel Pin Bundle Simulator (FPBS) which is the heat source, the PHE which is the heat sink, and the primary pump which ensures the forced circulation of lead in the loop.

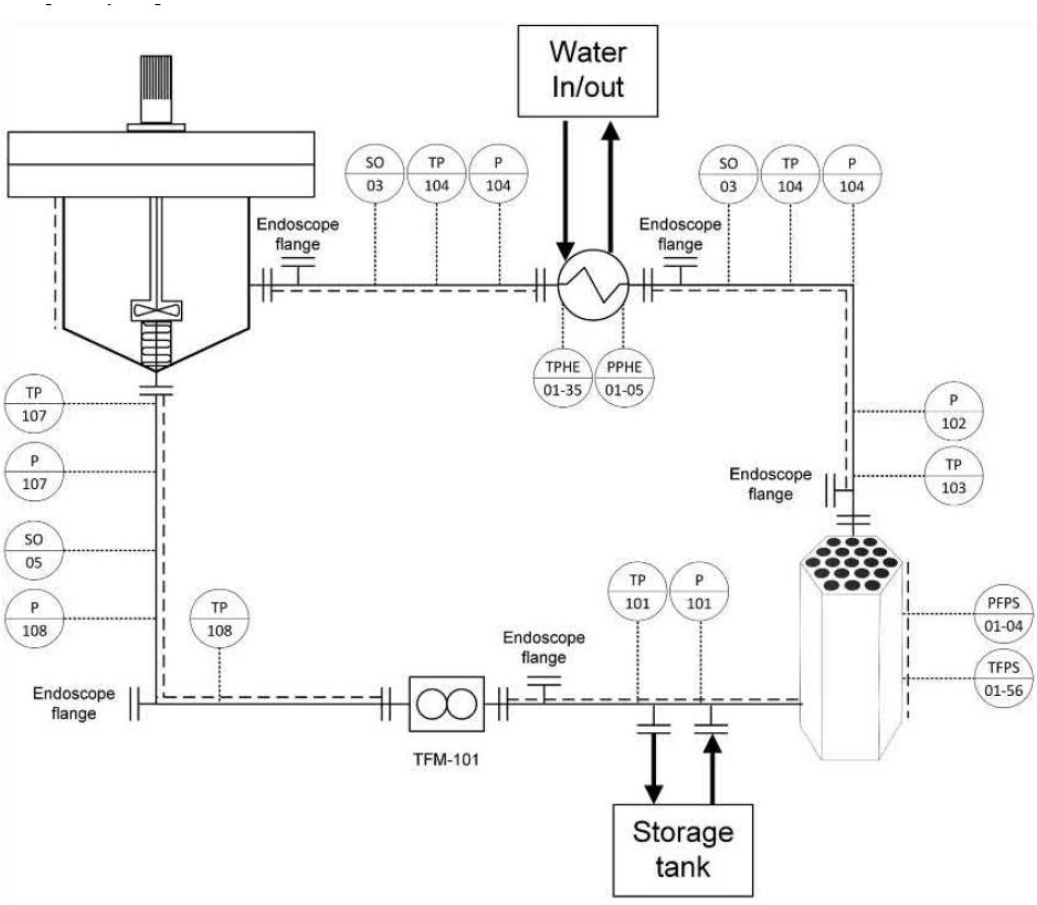


*Figure 89 Simplified diagram of the VLF primary loop [105]*

The power source is the FPBS, an electrical simulator representing the WEC-LFR fuel bundle on a reduced scale, connected to the main piping via standard 3" flanges. The fuel pins of FPBS are indirectly heated. The FPS is highly instrumented (around 50 thermocouples and 4 pressure sensors) in order to better characterize the thermal hydraulics features of this component. Thermocouples (3-mm k-type) are mounted in the bulk of the subchannels and in the outer walls of the fuel pins.

The loop is highly instrumented, with measurement points chosen to characterize circuit temperatures (by means of 3-mm k-type thermocouples, eight points, see Figure 89), pressures (absolute pressure measures, eight points, see Figure 89), flow rate (thermal flowmeter, see Figure 89), and oxygen concentration (ENEA custom sensor [106], five points, see Figure 89).

The FPBS delivers up to 500 kW of power through 19 pins that simulate the fuel cladding tubes. These pins are supported by spacer grids and powered by a dedicated direct current rectifier. To simulate off-normal power conditions, the FPBS can be operated using a reduced number of fuel pins while maintaining full power, thereby increasing the heat flux per pin to approximately 130% of the nominal value. As the liquid lead circulates through the FPBS, it heats up from an inlet temperature of 390 °C to a nominal temperature of 530 °C. The main parameters of the FPBS are reported in Table 34 [105].

***Table 34 FPBS main data [105]***

| **Parameter** | **Unit** | **Value** |
|---|---|---|
| **Total thermal power** | kW | 500 |
| **Maximum power per pin** | kW | 33 |
| **Number of pins** | - | 19 |
| **Axial heating profile** | - | Uniform |
| **Pin outer diameter** | mm | 10.7 |
| **Active length** | mm | 1312 |
| **Clad material** | - | SS316 |
| **Grid spacers** | - | Yes |

The PHE is the heat sink of the primary loop, transferring heat to the secondary loop. This component is a hybrid microchannel heat exchanger, manufactured through a diffusion bonding process using high temperature and pressure to fuse a set of stacked plates into a single metallic block. These plates are etched, extruded, or processed to form channels, which are then encapsulated during bonding. The resulting product is akin to a mono-block core, where fluid channels are created without welding. These heat exchangers offer a high heat transfer area-to-volume ratio, leading to extreme compactness, which directly benefits the design of the primary reactor pool by minimizing its volume. Additionally, the strength of this component and the small size of the secondary channels reduce the likelihood and potential consequences of PHE channel rupture, making this design particularly advantageous for the Westinghouse LFR. The main technical data of the PHE are reported in Table 35 [105].

*Table 35 PHE main data [105]*

| Parameter | Unit | Value |
|---|---|---|
| **Nominal Size** | kW | 500 |
| **Lead channel size (L x L)** | mm | 4x4 |
| **Number of lead channels** | - | 707 |
| **Water channel size (L x L)** | mm | < 1 hyd. diameter |
| **Number of water channels** | - | > 2500 |
| **Lead mass flow rate** | kg/s | 24.5 |
| **Lead in/out temperatures** | °C | 530/390 |
| **Water mass flow rate** | kg/s | 0.32 |
| **Water in/out temperatures** | °C | 350/520 |
| **Water pressure** | bar | 300 |
| **Material** | - | SS316 |

Lead circulation is ensured by a vertical primary pump, which is installed in a tank (S-301, see Figure 89) located downstream of the PHE. This tank also works as an expansion vessel and pressure control for the circuit, maintained by an argon gas cover set at approximately 20 kPa. The pump is connected to the tank via an upper flange and an elastic joint at the bottom, directing the high-pressure lead (around 2 bar at nominal flow rate) towards the cold leg of the VLF. The pump is controlled by an inverter, allowing for flow rate variations between 15 and 40 kg/s. The main technical specifications of the primary pump are detailed in Table 36 [105].

*Table 36 Primary pump main data [105]*

| Parameter | Unit | Value |
|---|---|---|
| **Flow rate range** | kg/s | 15-40 |
| **Head range** | m | 0.7-4.2 |
| **Shaft length** | mm | 1200 |
| **Maximum motor power** | kW | 12 |
| **Nominal speed** | rpm | 1480 |

The secondary loop is made by AISI 321H and its purpose is to absorb the power generated by the FPBS and release it to the external environment (500 $kW_{th}$). A key design requirement is to maintain acceptable thermal gradients at the interface (PHE) while ensuring flexibility to simulate all operating conditions of the full-scale system. Figure 90 presents a simplified diagram of the secondary loop, highlighting its main components and monitoring instrumentation. Regarding the pressure measurements, a Cerabar PMP51 is installed suitable for the operating conditions of the secondary loop with a relative uncertainty of 0.1%.

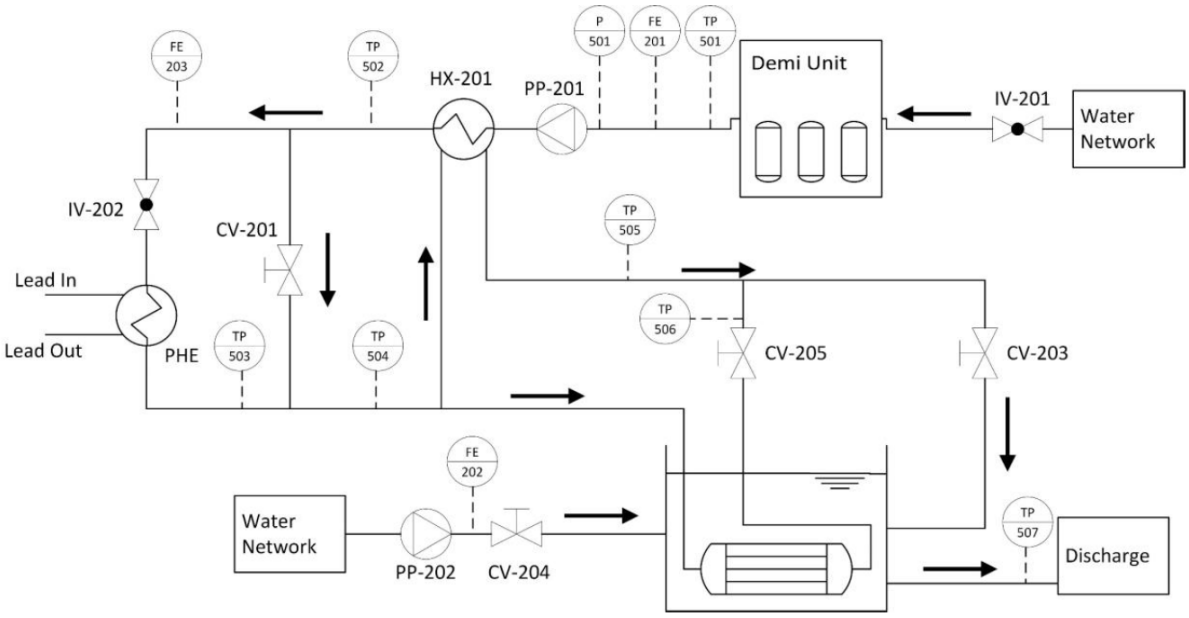


***Figure 90 Secondary loop overview [105]***

The main flow consists of approximately 30 l/min of water, coming from the water network, which passes through a reverse osmosis demineralization station and is then pressurized to 300 bar by a triplex piston pump (PP-201). The water then enters a regenerative heat exchanger (HX-201) where, it reaches a temperature of up to 350°C. The heat exchanger, similar to the PHE, is a diffusion-bonded type. A control valve (CV-201) directs part of the flow to the PHE, with the remaining flow bypassing the PHE. This configuration allows for flexibility in the thermal cycle, enabling the testing of different operating conditions.

The temperature downstream of the PHE can reach up to 620°C. After the bypass, the water temperature stabilizes around 430°C under normal operating conditions. The flow is then split into two branches: one returns to the HX-201 regenerative heat exchanger to preheat the feedwater, while the other flows to a coil immersed in an ambient pressure pool. The CV-205 control valve regulates the division between these two paths. The streams recombine at a nominal temperature of 90.5 °C before passing through the CV-203 depressurization valve, which reduces the pressure to atmospheric, allowing the flow to enter the cooling pool. The CV-203 valve is manually operated with a variation of the relative flow area of 1% per step which causes an expected pressure drop variation of 6 bar.

Since the design pressure of the secondary loop is 330 bar, the nominal behaviour of this valve is contained within the safety margins. To maintain the thermal balance in the condenser, an auxiliary flow of about 150 l/min is introduced into the pool, ensuring the discharge temperature limits (below 60°C).

### 4.3.2. Numerical model

The version of RELAP5/Mod3.3 used to develop the numerical model of the VLF [107] has been modified incorporating the state-of-the-art thermophysical properties of liquid lead [34], as well as the corresponding heat transfer correlations [35]. This modified code version has been employed in post-test analyses and numerical benchmark exercises [38], demonstrating its reliability in simulating the key phenomena observed during experiments involving liquid lead and providing satisfactory predictions of the main operating parameter trends. The average nodalization size of the model is 0.3 m with a maximum 25% length difference between two adjacent nodes. The first digit of the hydrodynamic components number identifies a specific system as follows:

- "1XX" for the piping of the primary loop and the PHE lead side
- "2XX" for the PHE supercritical water side
- "3XX" for the piping of the secondary loop
- "4XX" for the cold side of the HX-201
- "5XX" for the hot side of the HX-201
- "6XX" for the tube side of the condenser
- "7XX" for the S-101 and the primary pump
- "8XX" for the pool side of the condenser
- "9XX" for the subchannels within the FPBS

The nodalization scheme of the primary loop is shown in Figure 91. The main components which constitute the primary loop are highlighted in the figure. The S-101 tank was modelled with TMDPVOL 700 and the PIPEs 702 and 704 components. The TMDPVOL simulates argon atmosphere and sets the pressure of the entire loop. The primary pump was simulated by a TMDPJUN 703 that imposes the mass flow rate of lead circulating in the loop.

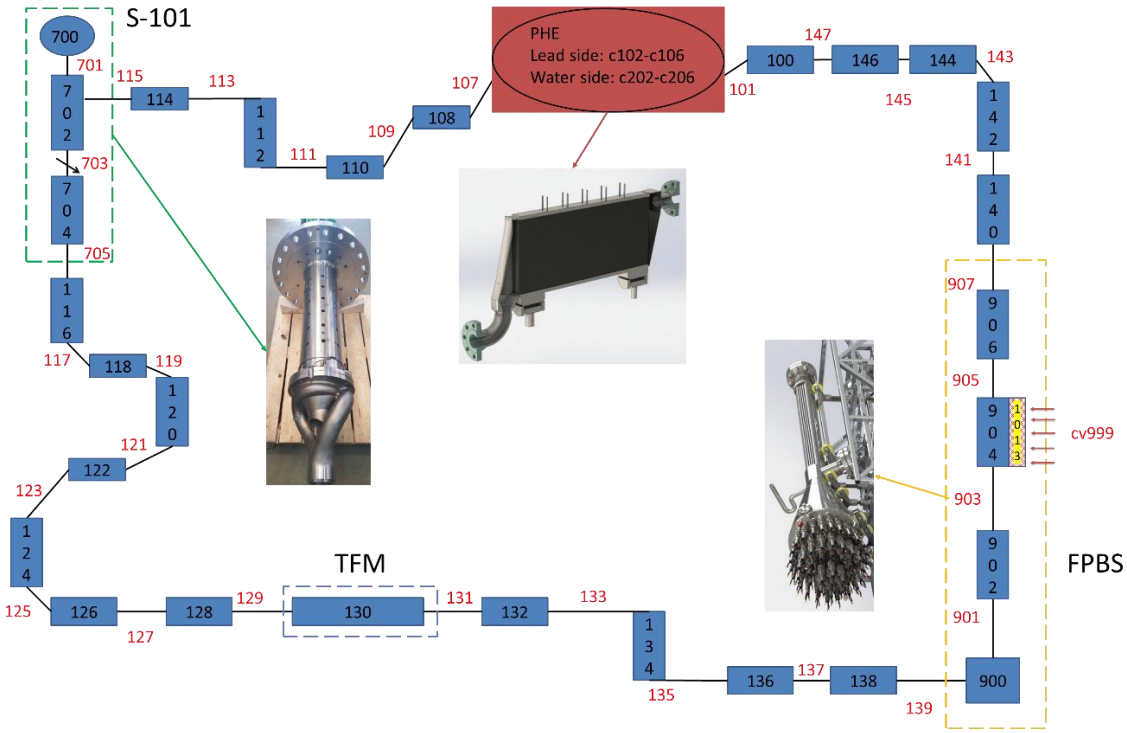


*Figure 91 VLF primary loop nodalization scheme*

The FPBS is simulated with all subchannels collapsed in a single channel and was divided axially by differentiating the active height (PIPE 904) from the non-active zones. Power generation is modelled through a heat structure (HS-1013) that includes the geometry and materials that make up the heating rods of the FPBS. As far as the PHE is concerned, not all the information necessary to faithfully simulate this component (geometry, materials, heat transfer coefficients) are known, therefore the PHE was modelled with two pure counter-current pipes thermally coupled by HS-1001 (see Figure 92) and the model was suitably tuned to obtain the desired nominal conditions.

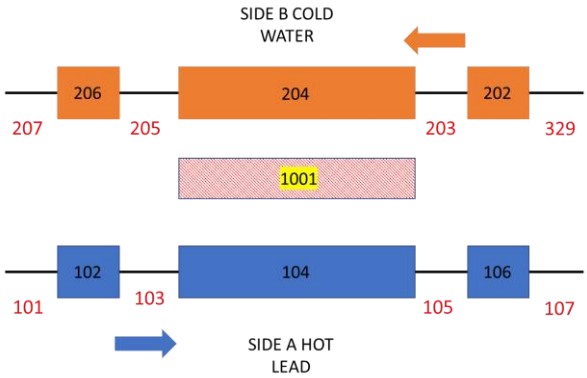


***Figure 92 PHE nodalization scheme***

On the other hand, the nodalization of the VLF secondary loop is shown in Figure 93.

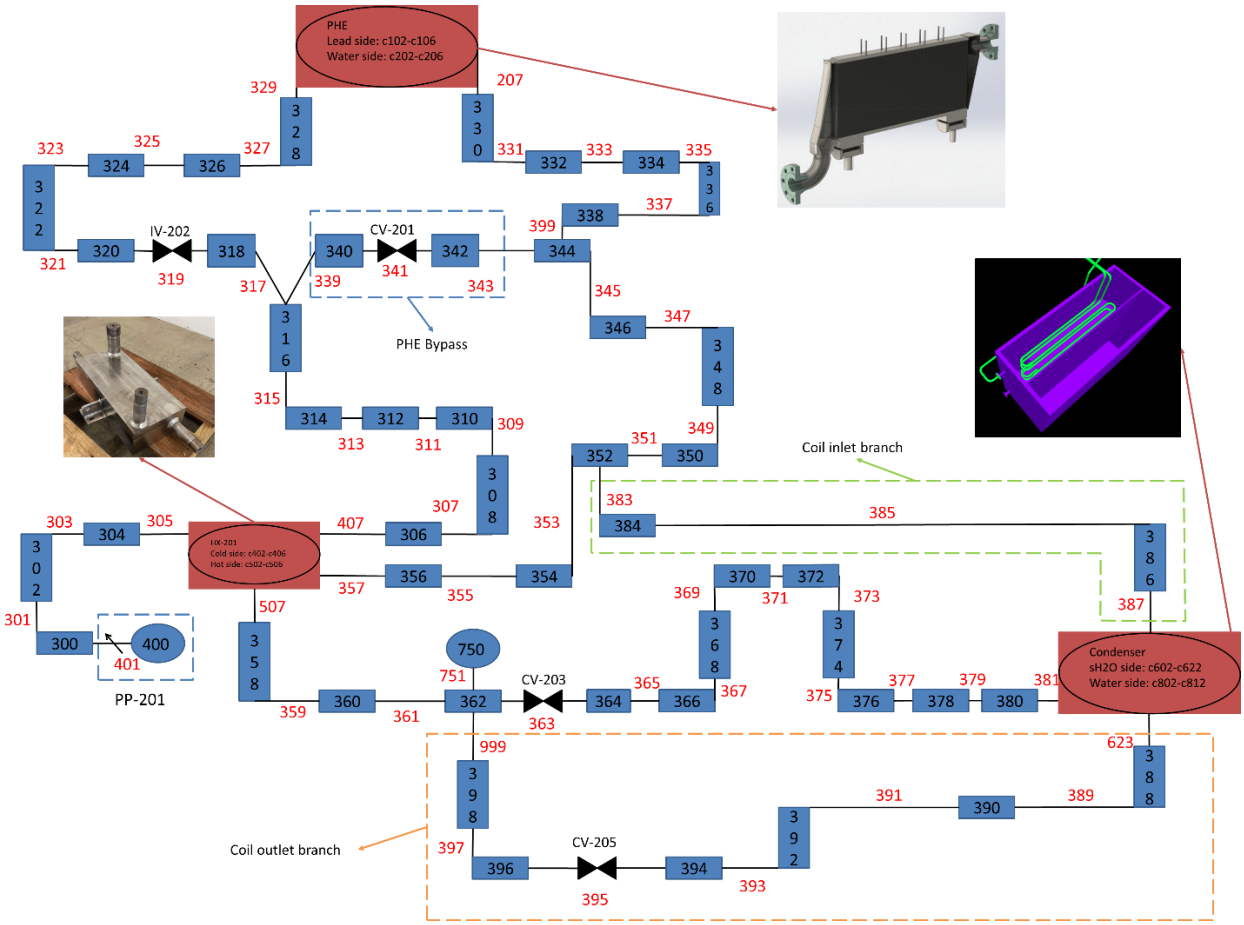


***Figure 93 VLF secondary loop nodalization scheme***

PP-201 secondary pump is modelled by the TMDPVOL 400, which imposes the pressure of 300 bar in the water loop and an ambient temperature of 20 °C, and by the TMDPJUN 401, which imposes the mass flow circulating in the loop. As far as the HX-201 is concerned, the same modelling issues arisen when considering the PHE are still valid. For this, also in this case two pure counter-current tubes are used, thermally coupled by means of the heat structure HS-1002 (see Figure 94). The entire numerical model was suitably calibrated to obtain the desired nominal conditions.

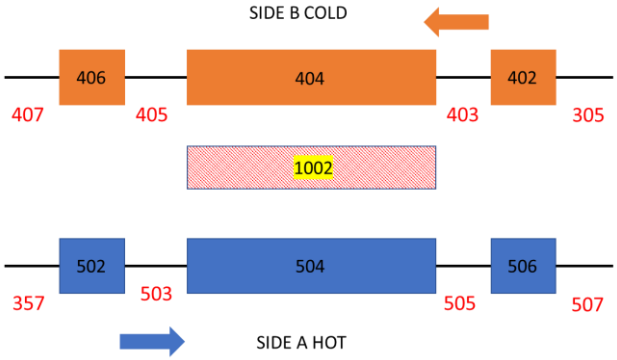


***Figure 94 HX-201 nodalization scheme***

The main heat sink of the experimental plant is the condenser which has been modelled as shown in Figure 95. On the tube side a series of "PIPE" components are adopted, labelled “6XX”. They reproduce the coil geometrical profile by means of “PIPEs” vertical orientation (alternating horizontal and vertical segments) and localized pressure drop coefficients (to account for the coil curves). The pool side of the condenser is continuously filled by the fluid coming from the loop portion downstream of the CV-203 depressurization valve (connected to the condenser via the SNGLJUN 381) and by water from the water network. The latter, which is delivered by the PP-202, is simulated by means of the TMDPVOL 800 which imposes the conditions of ambient pressure and temperature and by the TMDPJUN 801 which imposes the mass flow rate circulating on the pool side of the condenser. Finally, the SNGLJUN 815 connects the condenser pool side to the TMDPVOL 816. The latter simulates the atmosphere above the pool. For this, it has been implemented filled with air at atmospheric pressure and room temperature.

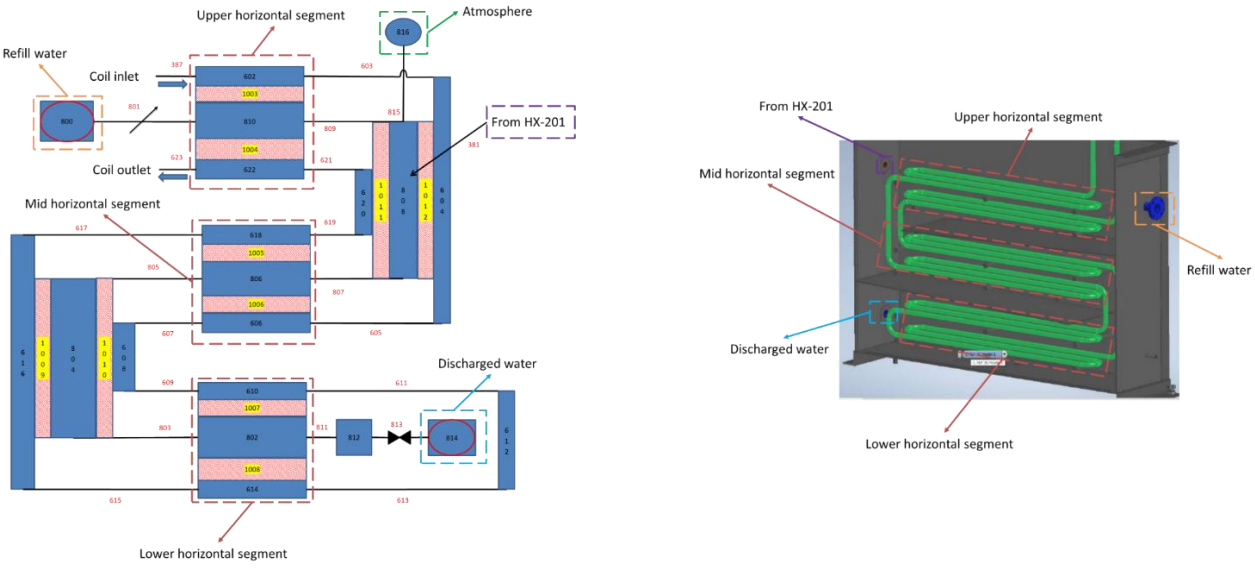


***Figure 95 VLF condenser nodalization scheme***

TMDPVOL 750 and SNGLJUN 751 have been implemented, which fix the pressure in the volume upstream of the depressurization valve, since the pressure drop across CV-203 cannot be managed numerically (300 bar upstream vs 1 bar downstream). These components are used to facilitate the simulation of reaching a steady state at the desired conditions. When performing the steady state and transient analysis, to ensure consistency with physics, a numerical restart of the simulation was performed by removing these components, increasing the simulation time to verify that the steady state is actually reached. All the control valves are modelled with "VALVE" components taking into account the Cv curves specified by the manufacturer. Moreover, the "VALVE" components are provided with an integral control given by the following relationship:

$$\Delta s = K_I \int_0^t e(\tau)\, d\tau \qquad 36)$$

In which:

- $\Delta s$ is the stem variation
- $K_I$ is the integral constant
- $e(\tau)$ is the error based on a setpoint

The setpoints with which the errors for the valve control were calculated are the following:

- CV-201 setpoint is the PHE outlet water temperature, fixed at 520 °C
- CV-203 setpoint is the pressure downstream PP-201, fixed at 300 bar
- CV-205 setpoint is the HX-201 cold side outlet temperature, fixed at 350 °C

Passive heat structures were used to simulate the pipeline insulation for both primary and secondary loops. Imposed boundary conditions, i.e., ambient temperature of 20 °C and a heat transfer coefficient of 8 W/m$^2$K, were adopted to simulate the external air. The whole experimental facility is insulated with 10 cm of PAROC.

To develop a numerical model that accurately reflects the characteristics of the experimental plant, the adopted strategy involves separately investigating the main components of the system. These models are then calibrated by aligning key thermal-hydraulic parameters—such as pressure drops, heat transfer rates, and inlet and outlet temperatures—with the known data provided by the manufacturer. The first component for which the characterization is performed is the PHE whose RELAP5 nodalization scheme is illustrated in Figure 92.

On the lead side represented by the "1XX" components, the pressure and temperature boundary conditions are imposed by a TMDPVOL, numbered 100, and the mass flow rate by TMDPJUN 101. On the water side represented by the "2XX" components, on the other hand, the boundary conditions of pressure and temperature are imposed by TMDPVOL 200 and TMDPJUN 201 imposes the flow rate value. These four components are part of the PHE stand-alone model and not shown in Figure 92 (referring to the version included in the overall VLF nodalization scheme where they are not needed).

As said above, the PHE is a compact, diffusion-bonded heat exchanger. It is composed by several stacked plates, each one provided with channels for the fluid passage. The internal geometric configuration of this exchanger is unknown. However, to perform the transient analysis objective of the current work, what was needed was only a realistic layout of these components, above all in terms of heat transfer surface, material inventories and pressure drops (they are the parameters mostly influencing the component TH behaviour during transient scenarios). To obtain it, some assumptions on the heat exchanger geometry were made to fill the gaps in the design data. For both primary and secondary sides, the heat exchangers channels were modelled with an equivalent pipe characterized by lumped parameters.

They are characterized by the length and the hydraulic diameter of a single channel, but the total flow area and mass flow. This allows to keep the actual inventory and to properly model the component pressure drops. The latter are simulated by means of concentrated k-loss coefficients. In addition, RELAP5 heat structure components were used to model the thermal transfer taking place inside the heat exchangers, as well as to account for the steel inventory (i.e., thermal inertia). In the input deck, the heat transfer coefficient correlations adopted for supercritical water and molten lead were Dittus-Boelter [108], and Seban-Shimazaki [36], respectively. The results of the simulation are shown in Table 37 together with the component nominal data. In Table 37, as well as in the following tables throughout the rest of the Section, the parameters indicated with (**BC**) are the ones set as boundary conditions.

***Table 37 TH characterization of the PHE***

| Parameter | Unit | Nominal data | RELAP5 | Error |
|---|---|---|---|---|
| **Heat load** | kW | 500 | 500.8 | 0.15% |
| **Lead inlet temperature (BC)** | °C | 530 | 530 | / |
| **Lead outlet temperature** | °C | 390 | 388.9 | -1.1 °C |
| **Lead mass flow rate (BC)** | kg/s | 24.5 | 24.5 | / |
| **Lead pressure drops** | kPa | 8.3 | 8.3 | 0.12% |
| **Water inlet temperature (BC)** | °C | 350 | 350.0 | / |
| **Water outlet temperature** | °C | 520 | 519.7 | -0.28 °C |
| **Water mass flow rate (BC)** | kg/s | 0.32 | 0.32 | / |
| **Water pressure drops** | kPa | 109.6 | 108.6 | -0.88% |

Table 37 shows that the error is less than 0.3 % showing the good representativeness of the numerical model. Once the desired conditions are reached, the TMDPVOLs and TMDPJUNs are removed and the PHE tuned model is included in the overall VLF nodalization scheme. The same procedure described above was repeated for the HX-201 regenerative heat exchanger, affected by the same data unavailability of the PHE. Its numerical model is shown in Figure 94. Also, in this case a simulation with RELAP5 modified by ENEA has been performed. All the results are collected in Table 38 together with the component nominal data.

***Table 38 TH characterization of the HX-201***

| Parameter | Unit | Nominal data | RELAP5 | Error |
|---|---|---|---|---|
| **Heat load** | kW | 710 | 710.5 | 0.07% |
| **Hot side inlet temperature (BC)** | °C | 430 | 430 | / |
| **Hot side outlet temperature** | °C | 90.5 | 91.0 | 1.02 °C |
| **Hot side mass flow rate (BC)** | kg/s | 0.314 | 0.314 | / |
| **Hot side pressure drops** | kPa | 139.5 | 139.5 | -0.01% |
| **Cold side inlet temperature (BC)** | °C | 20 | 20 | / |
| **Cold side outlet temperature** | °C | 350 | 350.2 | 0.24 °C |
| **Cold side mass flow rate (BC)** | kg/s | 0.474 | 0.474 | / |
| **Cold side pressure drops** | kPa | 148.9 | 148.4 | -0.35% |

In this case, Table 38 shows that a negligible error lower than 0.5% has been made, meaning that the behaviour of the numerical model is faithfully representative of the component under the nominal conditions in which it operates. Also, in this case, once the desired conditions are reached, the HX-201 numerical model is implemented in the overall VLF nodalization scheme. Another component belonging to the experimental plant for which the thermal-hydraulic characterization has been made is the condenser i.e., the main heat sink of the VLF. The nodalization scheme is illustrated in Figure 95.

The tube-side domain of the condenser is represented by the "6XX" components whose inlet pressure, temperature and flow conditions are imposed as boundary conditions. The shell-side domain of the condenser is represented by the "8XX" component set. The environmental conditions of water delivered from the network (i.e., 2.5 kg/s of water at 20 °C and atmospheric pressure) are imposed by TMDPVOL 800 and TMDPJUN 801. With respect to Figure 95, what is added are the TMDPVOL 700 and TMDPJUN 701, simulating the thermodynamic conditions, i.e., pressure, temperature and mass flow, of the water that comes from the hot side outlet of the HX-201. For the condenser, since the geometry and configuration are known, no tuning operation has been carried out, but the model has been implemented as built. The thermal-hydraulic characterization of the condenser in comparison with the nominal data are reported in Table 39.

***Table 39 TH characterization of the condenser***

| Parameter | Unit | Nominal data | RELAP5 |
|---|---|---|---|
| **Heat load** | kW | - | 345.9 |
| **Coil side inlet temperature (BC)** | °C | 430 | 430 |
| **Coil side outlet temperature** | °C | <90 | 114.2 |
| **Coil side mass flow rate (BC)** | kg/s | 0.16 | 0.16 |
| **Refill water inlet temperature (BC)** | °C | 20 | 20 |
| **Refill water mass flow rate (BC)** | kg/s | 2.5 | 2.5 |
| **Water from HX-201 inlet temperature (BC)** | °C | 90 | 90 |
| **Water from HX-201 inlet mass flow rate (BC)** | kg/s | 0.474 | 0.474 |
| **Discharged water temperature** | °C | <60 | 58.9 |
| **Discharged water mass flow rate** | kg/s | 2.974 | 2.974 |

The results of the simulation are in good agreement with respect to nominal data. For this, the component model was included in the overall VLF nodalization scheme. After having performed the thermal-hydraulic characterization of the main components that make up the experimental plant with various system codes and a sub-channel code (to have more detail of the FPBS) and having verified the correct behaviour of the components in nominal conditions, it was confirmed that the various numerical models are faithfully representative of these components. These stand-alone models are all implemented in the VLF overall nodalization scheme. With this input, a pre-test analysis was carried out to verify the behaviour of the whole plant both in nominal condition and in accidental transients

### *4.3.3. Transient analysis*

The transient analysis is based on a steady state numerical simulation which represents the normal operation of the WEC-LFR. In this configuration, the FPBS generates a power of 500 kW through the heating rods removed from a lead flow rate that enters at 390 °C and exits at a temperature of 530 °C. As far as the primary loop is concerned, the results of the steady state simulation are shown in Table 40.

***Table 40 Primary loop steady state conditions***

| Parameter | Unit | Nominal data | RELAP5 | Error |
|---|---|---|---|---|
| **FPBS thermal power (BC)** | kW | 500 | 500 | / |
| **FPBS inlet temperature** | °C | 390 | 388.6 | -1.4 °C |
| **FPBS outlet temperature** | °C | 530 | 529.3 | -0.7 °C |
| **Lead mass flow rate (BC)** | kg/s | 24.5 | 24.5 | / |
| **PHE power** | kW | 500 | 495.9 | -0.8% |
| **PHE lead side pressure drops** | kPa | 8.3 | 8.3 | 0.2% |
| **PHE inlet temperature** | °C | 530 | 528.9 | -1.1 °C |
| **PHE outlet temperature** | °C | 390 | 389.1 | -0.9 °C |
| **Prim. loop heat losses** | kW | - | 3.94 | / |

The thermal power generated by the FPBS is released to the secondary loop through the PHE, which in turn removes the thermal power by means of supercritical water flow (regulated by the CV-201) entering it at a temperature of 350 °C and exiting at a temperature of 520 °C Subsequently, a portion of the flow rate (regulated by the CV-205) heads towards the HX-201 to preheat the water coming from the network, which make the temperature difference from 20 °C to 350 °C. Meanwhile, the remaining goes to a coil immersed in an ambient pressure pool. The two streams re-join one last time before crossing the CV-203 depressurization valve which brings the flow back to ambient pressure, with a pressure drop of about 300 bar, entering the cooling pool. Finally, with a refill flow injected in the pool, the water is discharged at a temperature lower than 60 °C. Regarding the secondary loop, the results of the steady state simulation are summarized in Table 41.

*Table 41 Secondary loop steady state conditions*

| Parameter | Unit | Nominal data | RELAP5 | Error |
|---|---|---|---|---|
| **HX-201 power** | kW | 710 | 709.8 | -0.03% |
| **HX-201 cold side inlet temperature (BC)** | °C | 20 | 20 | / |
| **HX-201 cold side outlet temperature** | °C | 350 | 350.0 | 0 °C |
| **HX-201 cold side pressure drops** | kPa | 148.9 | 148.6 | -0.23% |
| **HX-201 cold side mass flow rate (BC)** | kg/s | 0.474 | 0.474 | / |
| **PHE water side inlet temperature** | °C | 350 | 349.6 | -0.41 °C |
| **PHE water side outlet temperature** | °C | 520 | 520.0 | 0 °C |
| **PHE water side pressure drops** | kPa | 109.6 | 109.5 | -0.12% |
| **PHE water side mass flow rate** | kg/s | 0.321 | 0.317 | -1.25% |
| **CV-201 valve opening** | % | 75.9 | 76.0 | 0.16% |
| **HX-201 hot side inlet temperature** | °C | 430 | 427.3 | -2.7 °C |
| **HX-201 hot side outlet temperature** | °C | 90.5 | 92.4 | 1.9 °C |
| **HX-201 hot side pressure drops** | kPa | 139.5 | 142.2 | 1.95% |
| **HX-201 hot side mass flow rate** | kg/s | 0.314 | 0.317 | 0.96% |
| **CV-203 valve opening** | % | 72.3 | 73.5 | 1.70% |
| **Condenser power** | kW | - | 338.4 | / |
| **Coil side inlet temperature** | °C | 430 | 426.8 | -3.2 °C |
| **Coil side outlet temperature** | °C | <90 | 111.3 | / |
| **Coil side mass flow rate** | kg/s | 0.16 | 0.157 | -1.88% |
| **Refill water inlet temperature (BC)** | °C | 20 | 20 | / |
| **Refill water mass flow rate (BC)** | kg/s | 2.5 | 2.5 | / |
| **Shell side inlet temperature** | °C | 90 | 96.7 | 6.7 °C |
| **Shell side mass flow rate** | kg/s | 0.474 | 0.474 | 0% |
| **CV-205 valve opening** | % | 76.1 | 73.7 | -3.23% |
| **Discharged water temperature** | °C | <60 | 59.5 | / |
| **Discharged water mass flow rate** | kg/s | 2.974 | 2.974 | 0% |
| **Sec. loop heat losses** | kW | - | 3.79 | / |

Starting from the VLF steady state conditions some operational and accidental scenarios were investigated with the aim of characterizing the VLF behaviour under transient conditions. The selected scenarios are:

- Secondary loop start-up procedure.
- Secondary loop shutdown procedure.
- Loss of heat sink.
- Loss of FPBS.

The simulations were conducted with different time steps, ranging from $10^{-4}$ s to $10^{-3}$ s, to verify the independence of the simulation outcomes from this parameter. No sensible differences were detected in the numerical results. The ones presented in the following sections are for $10^{-3}$ s. For the transient analysis, the initial state considered corresponds to the steady state conditions presented in Table 40 regarding the primary loop and Table 41 as far as the secondary loop is concerned.

START-UP PROCEDURE

The VLF secondary loop start-up operations have the main purpose to make the secondary loop available to extract heat from the primary, allowing its filling procedure to begin [105]. The secondary system must be heated up separately from the primary loop to avoid lead freezing. Once the circuit is warm, it can be coupled with the primary loop through the PHE. The start-up of the two loops is separately performed. For this, the procedure referred to the secondary system can be numerically investigated on its own, as done in the following. This sequence is arranged in three consecutive phases, featuring electric cables to heat the secondary coolant and achieve thermal equilibrium in the circuit and at the interface with the primary loop. The three phases were conducted as follows:

- Steady State: the secondary loop is initialized with water at 20 °C and atmospheric pressure, setting the PP-201 mass flow to its minimum (0.152 kg/s). The PHE and the condenser are isolated during this phase by their respective valves. The system mass flow circulates with no parallel branches (see Figure 90), reaching a pressure of 20 bar downstream PP-201 and upstream CV-203. The water level within TK-202 completely submerges the coil. Discharge mass flow matches the refill one. This simulation is used as a starting point for the following two phases.
- Pressurization: CV-203 is stepwise closed in 1% normalized area steps, to achieve 285 bar in the system. To allow the system pressure to stabilize at each step, a 40-seconds time window is foreseen between two following variations. The procedure lasts roughly 1.2 hours (Figure 96a), once the setpoint is reached downstream PP-201 (where the pressure probe is located).
- Heat-up: The last phase consists in rising the secondary loop temperature by using Heating Cables (HC) and the regenerative HX-201. The cables are installed in three sections (Table 42) and their nominal power has been evaluated thanks to a parametric study. The temperature setpoints to be achieved for the simulation to be successful are 350 °C at the HX-201 cold side outlet, and 400 °C in the isolated section encapsulated between IV-202 and PHE secondary side outlet. The maximum temperature increase rate has been set to 10 °C/min. Since the HC2 and HC3 relative sections are filled with stagnant fluid, their nominal power is considerably lower than HC1. In 3 hours, the temperature setpoint is reached at the HX-201 cold side outlet and after 30 minutes the other two setpoints are reached. During the simulation the temperature rise stays below the chosen maximum rate.

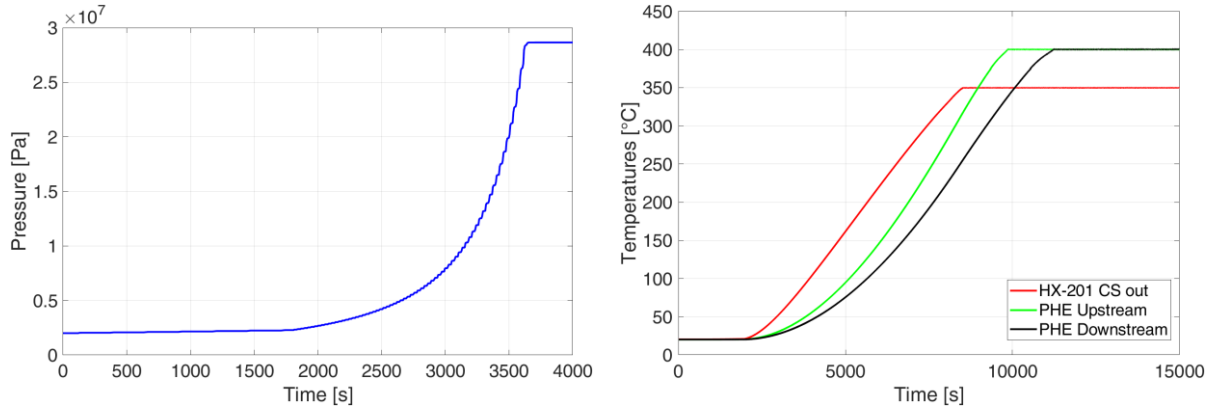


**(a)** **(b)**

***Figure 96: Start-up procedure: secondary loop pressurization phase (a) and following heating phase (b).***

***Table 42: Heating cables' location and power***

| Tag# | Cable's location | Nominal power (W) |
|---|---|---|
| **HC1** | Between HX-201 Cold Side outlet and IV-202 | 51000 |
| **HC2** | Between IV-202 and PHE water side inlet | 830 |
| **HC3** | Between PHE water side outlet and first branch | 1020 |

SHUTDOWN PROCEDURE

Bringing the secondary loop from steady state nominal condition to a cold and depressurized state is the aim of the VLF shutdown strategy. Every process was separated into Time Windows (TW) to help with the analysis of the transient dynamics. The IV-202 was intended to be an on/off valve with a 5-second closing time in the reference process. The first transient evolution has been conceptually divided in five TWs, highlighted in Table 43.

***Table 43: Reference shutdown procedure time windows***

| TW# | Time interval | Actions |
|---|---|---|
| **1** | From 0 s to 560 s | Linear decrease of FPBS power, primary and secondary mass flows |
| **2** | From 560 s to 750 s | Linear decrease of FPBS power, heating cables power turned ON and CV-201 opening |
| **3** | From 750 s to 1275 s | Linear decrease of FPBS power, primary mass flow coast down and IV-202 closing |
| **4** | From 1275 to 15000 s | Heating cable power shut down (system cooling) |
| **5** | From 15000 s onwards (not simulated) | PP-201 coast down (system depressurization) |

Together with the primary and secondary mass flows, the FPBS power decreases linearly in TW 1. The former ones were reduced to their pump's minimum allowed value (60% at 240 s for the primary flow and 33% at 400 s for the secondary one). The primary one is kept constant up to TW3, while the second up to TW5 (Figure 97a). On the other hand, the FPBS power keeps reducing until TW3 is over, having a lower slope in TW2. The reasoning behind this is to keep both systems' temperature fields as constant as possible until the PHE power is low enough to be replaced by heating cables. As soon as the change from a power source to another is actuated, the secondary system is decoupled from the primary, and can be cooled without freezing the primary coolant, avoiding an excessive temperature transient in any loop's section. TW2 starts when the HC1 are turned on. CV-201 is opened slightly after (Figure 97b). Both operations are gradually performed with a linear trend lasting 150 s. CV-201 opening lowers the mass flow in the PHE branch, reducing its exchanged power. At the end of TW2, HC1 power reaches its nominal value and CV-201 is completely open. During TW3 the FPBS power continues to decrease, and when it approaches zero (at 1200 s Figure 97a) the primary mass flow is decreased with a linear ramp lasting 50 s. Then, the IV-202 closes in 5 seconds, isolating the PHE and decoupling the systems. The valve sudden closure (it is an on/off valve) causes a temperature drop downstream CV-201. This negative effect cannot be avoided since the valve closure is mandatory to avoid lead freezing in the PHE (Figure 97c). This operation ends TW3, entering in TW4. Here, the secondary loop is gradually cooled down to ambient temperature thanks to a linear reduction of the HC1 power. The resulting temperature decrease rate is nearly 1°C /min. Finally, in TW5, the PP-201 is shutdown to depressurize the loop (not included in the simulations). Through this reference procedure the secondary loop successfully reaches a cold depressurized state.

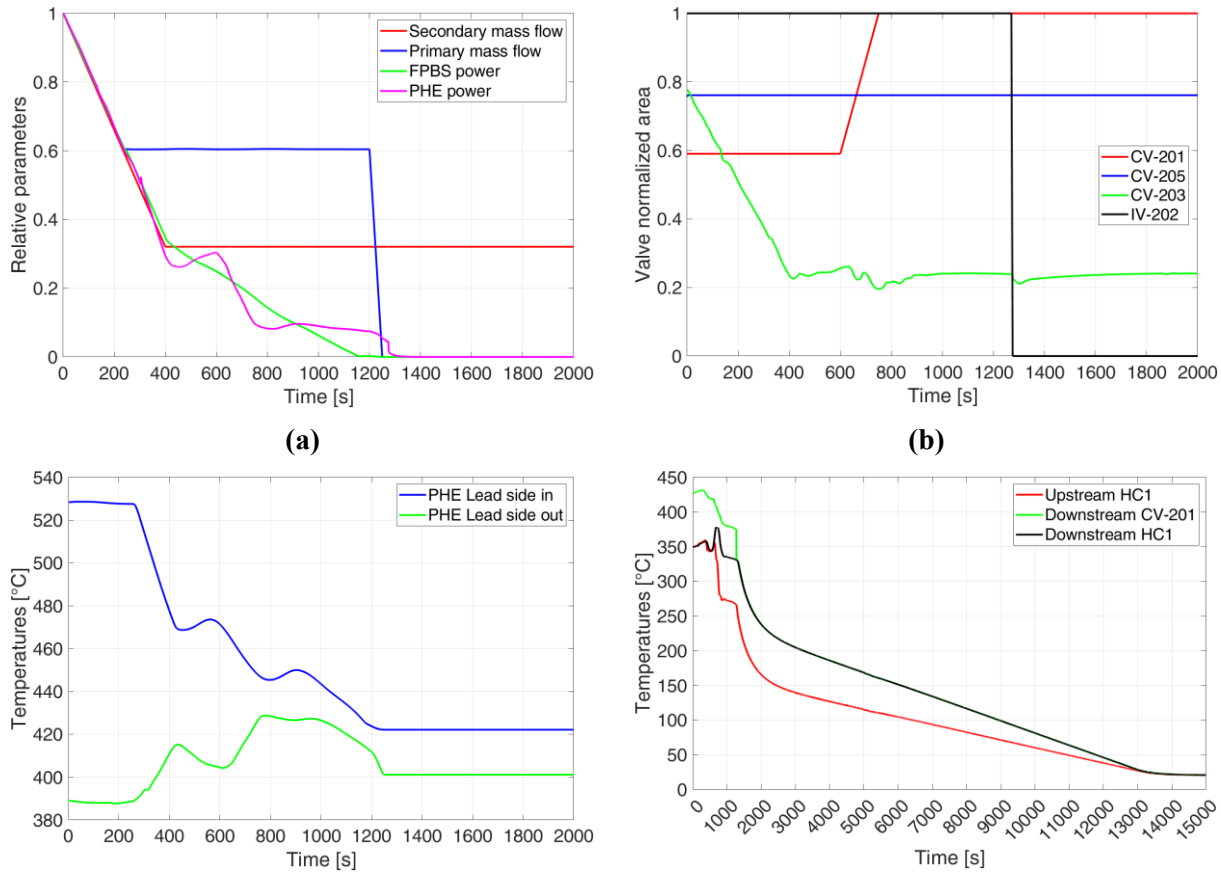


***Figure 97: Shutdown reference procedure: Powers and mass flows relative decrease (a), valves normalized area (b), PHE lead inlet/outlet temperatures (c), selected secondary system temperatures (d).***

LOSS OF HEAT SINK

The PIE associated with this accidental transient is the unintentional closure of the valve CV-204 caused by the operator. The closure of this valve is simulated by setting to zero the flow rate provided by the TMDPJUN 801 (see Figure 95) which represents the pump PP-202, dedicated to the continuous filling of the condenser shell side. The flow rate is reduced from the nominal value to 0 in 5 seconds. Primary loop conditions are unaltered with FPBS power and flow rate kept at their nominal values. Regarding the secondary loop, the valve control systems are kept in operation and the PP-201 continues to provide the nominal flow rate. The simulation lasts 5000 seconds. The first effect caused by the initiating event is the increase of the pool temperature (i.e., condenser shell side), which reaches the saturation point in about 18 minutes (black line in Figure 98). Once reached the saturated conditions, pool water starts to boil, decreasing the water inventory and degrading the heat transfer in the condenser. The coil side outlet temperature consequently increases up to 260 °C (blue line in Figure 98).

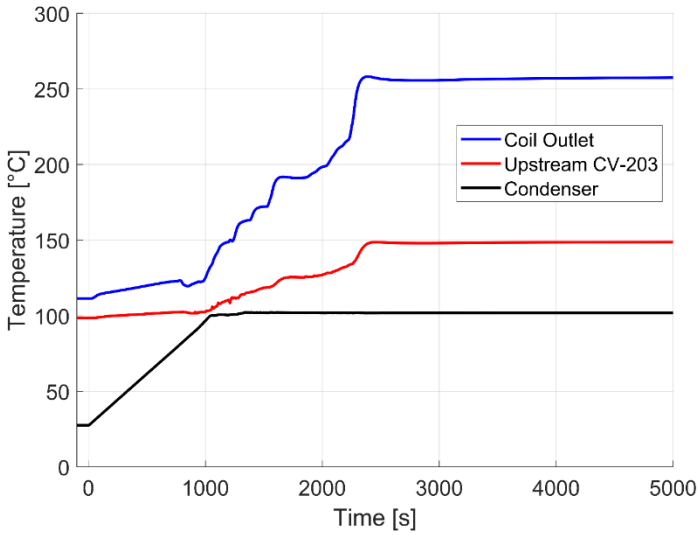


***Figure 98 Condenser temperatures trends***

The behaviour of the secondary loop valves is shown in Figure 99. As for the CV-201, its setpoint is the PHE outlet temperature. Since there are no changes in the conditions in both the PHE and the HX-201, the CV-201 stem position remains unchanged throughout the transient (blue line in Figure 99). Instead, upstream CV-203, the mixing temperature rises driven by the serpentine heating (red line in Figure 98). This also leads to increased pressure drops in the corresponding pipeline section. To keep the system pressure at the nominal value, CV-203 slightly opens, reducing the related valve pressure losses (red line in Figure 99). Instead, downstream the valve, the pressure increases from atmospheric value up to 3.5 bar. Thus, the water stream that is discharged into the condenser experiences a two-phase flow, with a void fraction of 38%. Since the setpoint of the HX-201 cold side outlet temperature remains unchanged, the distribution of the flow rates between the two branches in parallel must also be the same. Consequently, the pressure drops related to the HX-201 hot side branch keep the same, giving that the corresponding flow rate and temperature field are unaltered. Thus, also the total pressure drops associated with the other branch, the one hosting the coil, must remain unchanged. Since the contribution related to the coil distributed pressure drops increases (due to rising temperatures within the component), the concentrated ones due to the CV-205 (located downstream the coil outlet) must decrease. This leads to the CV-205 slightly opening visible in Figure 99 (black line). For this, the trend of the CV-205 stem position follows the one of the CV-203.

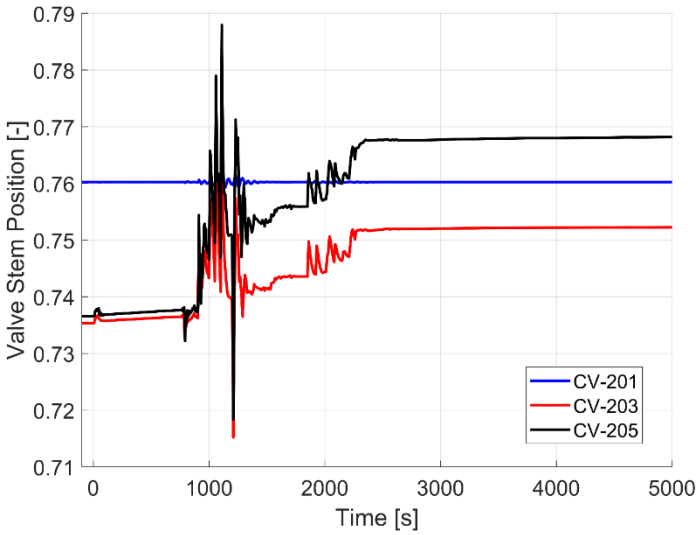


***Figure 99 Valves stem positions***

Finally, Figure 100 shows the thermal power exchanged in the heat exchangers belonging to the VLF. Since all the inlet/outlet thermodynamic conditions of the PHE and the HX-201 do not change or are kept constant by the control system, the power exchanged within these components is unaltered in this transient (blue and red lines in Figure 100). Instead, the condenser experiences a significant heat transfer degradation due to the water boiling in the shell side which partially uncovers the coil tubes. It can be seen from Figure 100 that the thermal power exchanged in the condenser decreases from 338 kW to 239 kW (black line).

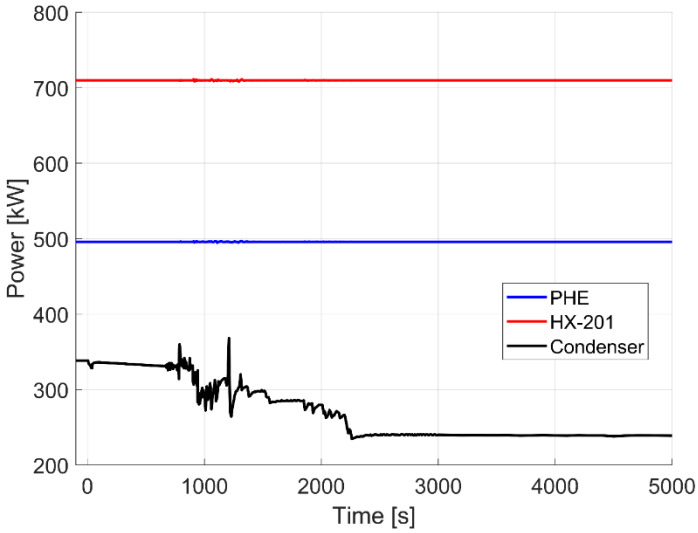


***Figure 100 Thermal powers trends***

Therefore, after the initial transient, the system settles into a new steady state configuration. In this state, the high-temperature section (comprising the PHE and HX-201) continues to operate unchanged compared to nominal conditions. However, the low-temperature section (including the serpentine and TK-202) undergoes a significant heating due to the absence of refill flow, which leads to a degradation of condenser heat transfer capability. As a result, the secondary coolant returns to the water network at saturation conditions instead of 59 °C. In conclusion, the simulation results show that the system can handle the effects of this accidental sequence, as it responds gradually to the initiating event, providing the operator or automatic control system with sufficient time to detect the issue and take corrective actions to prevent any potential risks to the loop.

LOSS OF FPBS POWER

This accidental transient is triggered by the FPBS loss of power. The power generated by the FPBS is reduced from the nominal value to 0 in 5 seconds. Instead, the mass flow rate of the primary loop is kept at its nominal value. Also, in the secondary loop the control system is kept in operation and the mass flow rate provided by PP-201 is maintained at the nominal value. The first effect that is noticed during this accidental transient is the fall of the temperatures of the primary circuit. From Figure 101 it is immediately estimated that lead freezing starts in 390 seconds (about 7 minutes). In addition, in the first 50 seconds, the PHE outlet temperature increases by 10 °C, reaching a peak of 400 °C and then cooling down to the freezing temperature.

This phenomenon can be explained by the following figures. Because of the control system of the valves of the secondary loop, the flow rate passing through the PHE water side decreases, causing the bypass of the heat sink of the primary loop (the PHE itself). As far as the secondary loop is concerned, it can be seen how the control system tries to maintain the nominal temperatures (the PHE outlet temperature remains at its nominal value for 10 seconds while the PHE inlet temperature is maintained for 20 seconds).Figure 102 shows the valves stem positions variation caused by the control system. The CV-201 valve is the component devoted to control the outlet temperature of the PHE on the water side. It can be seen that when the FPBS power is absent, the valve completely opens to maintain the nominal temperature of 520 °C. The CV-203 valve is devoted to the pressure control of the secondary loop where, since the main heat source is absent, the pressure tends to decrease. This decrease is counteracted in the first phase of the transient with the closure of the valve. After the initial movement, the component reaches a new equilibrium position by following the pressure setpoint. Finally, the CV-205 is dedicated to controlling the cold side outlet temperature of the HX-201. Also, in this case, since the main heat source is missing, the valve closes completely in order to deliver all the mass flow coming out of the PHE towards the HX-201 with the consequent insulation of the condenser.

The main effects of the behaviour of the valves can be seen on the temperatures of the HX-201 (see Figure 103) and on the various fractions of flow rates circulating in the loop (see Figure 104). It can be deduced from Figure 103 that the control system is able to maintain the nominal temperatures of the component up to 20 seconds of the transient and then cool down. Figure 104 shows the flow repartition through the main branches of the secondary loop. The mass flow supplied by the PP-201 pump keeps unchanged since set as a boundary condition. The flow rate through the IV-202 valve and the flow through the CV-201 valve respectively decreases and increases due to the fact that the CV-201 valve has opened completely. They are complementary trends since their sum is the system flow rate. The closure of the CV-205 valve isolates the condenser, while the flow through the CV-203 keeps unchanged since equals to the total system flow rate.

As far as the condenser is concerned, the inlet temperature on the shell side, and the one associated with the refill and discharged water are shown in Figure 105. It can be seen that, being the condenser isolated from the control system, the temperatures decrease.

Finally, the trends of the thermal power of the various heat exchangers belonging to the experimental plant are plotted in Figure 106. The graph shows that the power of the FPBS drops to 0 in 5 seconds as the postulated initiating event. On the other hand, for the other components, the power decreases after an initial phase of 20 seconds at the nominal power ensured by the control system. Summarizing, all the actions performed by the secondary loop control system are not enough to arrest the cool down. They can only delay the lead solidification that, according to the simulation outcomes, occurs nearly 7 minutes after the initiating event. Thus, any accident mitigation action should be performed in this time window.

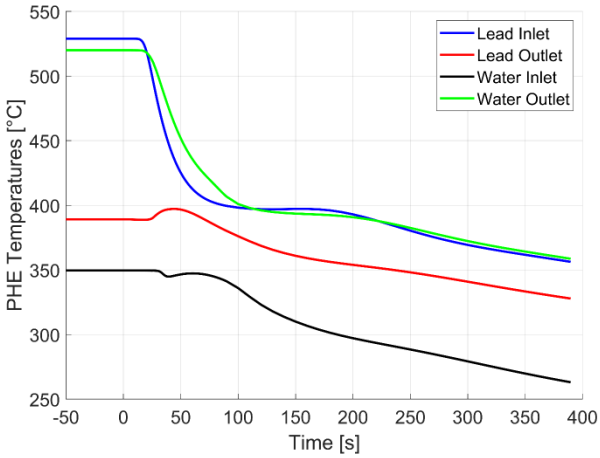


*Figure 101 PHE temperatures trends*

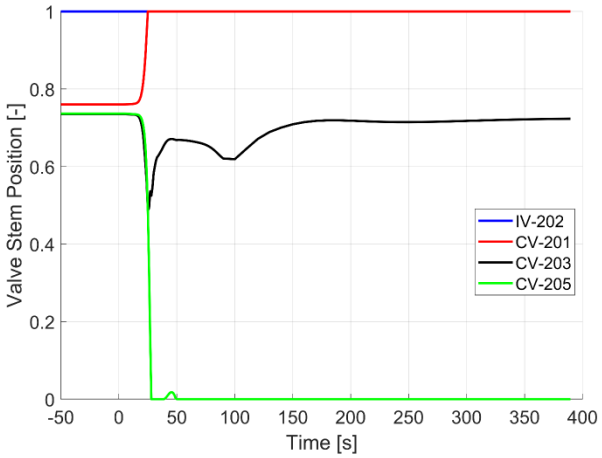


*Figure 102 Valves behaviours during the transient*

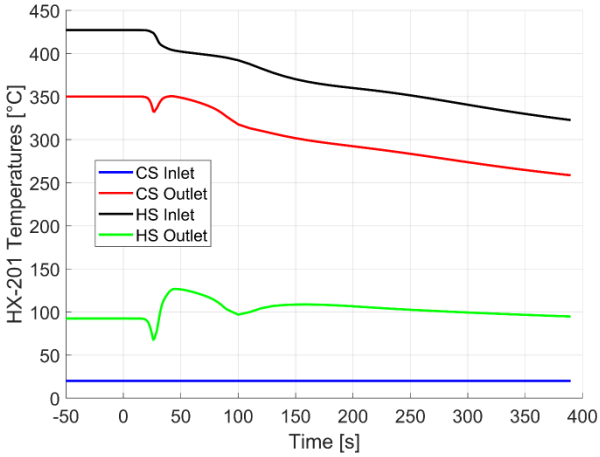


*Figure 103 HX-201 temperatures trends*

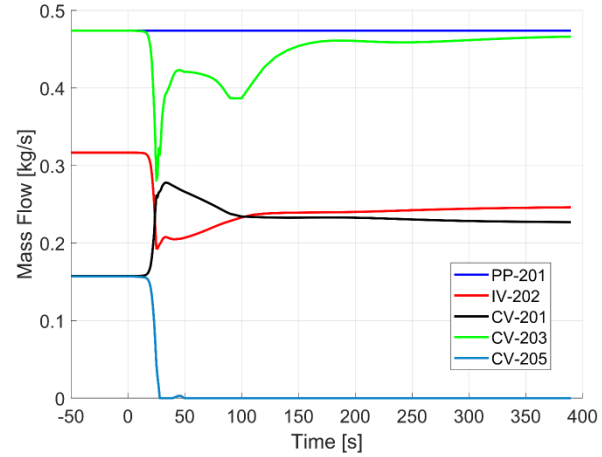


*Figure 104 Secondary loop mass flow rates*

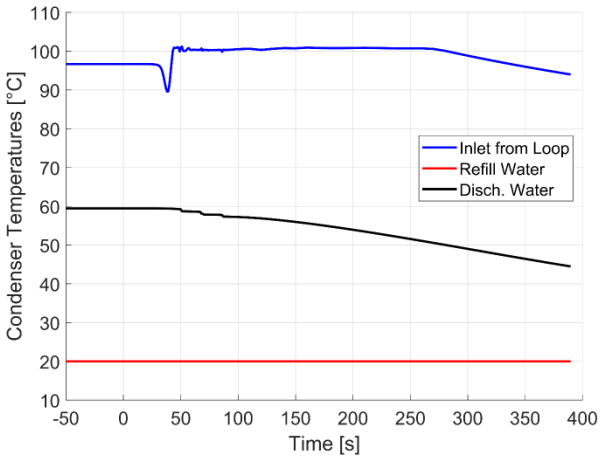


*Figure 105 Condenser temperatures trends*

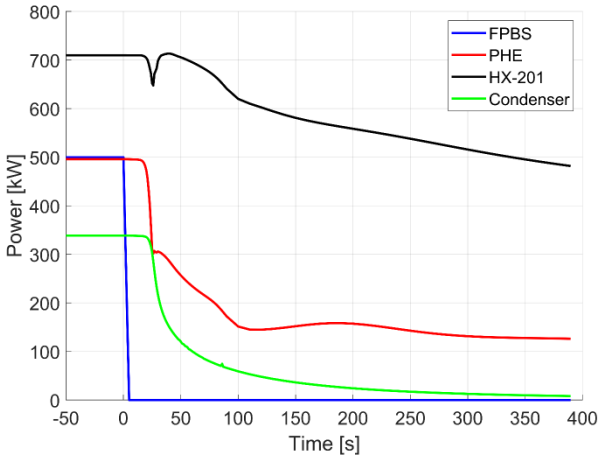


*Figure 106 Thermal powers trends*

### *4.3.4. Component-level analysis*

This section introduces the TH analysis performed at the component-level to complement the system-level evaluations. Due to the innovative design, structural complexity, and safety relevance of certain components, dedicated simulations using high-fidelity codes were required. These analyses provided deeper insights into localized phenomena, such as heat transfer performance, flow distribution, and thermal stratification, which are not adequately captured by 1D system codes. As such, component-level studies were essential to validate the design assumptions and support the overall safety assessment.

FPBS TH ANALYSIS

Particular attention was paid to the main heat source of the VLF, namely the FPBS. Firstly, the subchannel code DASSH, developed by Argonne National Laboratory [40] was used. Being the geometry known, no tuning operations have been performed. The FPBS data implemented in the DASSH input deck are derived from Table 34 (geometrical features) and Table 33 (inlet temperature and mass flow boundary conditions).

The lead temperature distribution in the subchannels is depicted in Figure 107 at the inlet (a), the middle (b) and the outlet (c) of the FPBS. The six internal sub-channels around the centre pin are those at maximum temperature in all axial positions. Given the low number of pins that make up the FPBS, the radial temperature gradient is low, varying from maximum to minimum temperature of 5 °C at both z = L/2 and z = L.

Then, the maximum internal clad temperature is plotted in Figure 108 showing the same radial temperature gradient of the coolant one.

Finally, Figure 109 shows the radial distribution of pin centreline temperature arranged in a hexagonal assembly at the inlet (a), the middle (b) and the outlet (c) of the FPBS. The central pin exhibits the highest temperatures for all the axial positions. Moreover, due to the small number of pins, the radial temperature gradient is small ranging from the maximum to the minimum temperature in 3 °C for both z = L/2 and z = L.

Then, a stand-alone numerical simulation was performed with RELAP5/Mod3.3, whose FPBS nodalization scheme is shown in Figure 91. As mentioned above, the FPBS was modelled by using lumped parameters, i.e., with a single pipe component representing all the subchannels collapsed. The comparison between the two simulations is illustrated in Figure 110 where the coolant temperature axial profile is reported. For DASSH, the value computed at each vertical quote is the weighted average of all the subchannel temperatures, weighted by using the corresponding mass flows. In this way, the outcomes of the subchannel code can be compared with the result of RELAP5/Mod3.3 lumped parameter model.

As expected, no sensible differences can be detected. Indeed, the coolant temperature is the result of the thermal balance. Once the thermophysical properties implemented for the liquid lead (particularly the specific heat) and the imposed boundary conditions (i.e., power source and inlet temperature and mass flow) are the same, also the resulting coolant temperature must be consistent between the two codes. The only aspect to be noted is that the vertical nodalization adopted in RELAP5/Mod3.3 is coarser with respect to DASSH (black/yellow star markers vs blue/green squared ones in Figure 110). This is due to the fact that the FPBS detail needed for the system-level analysis is lower.

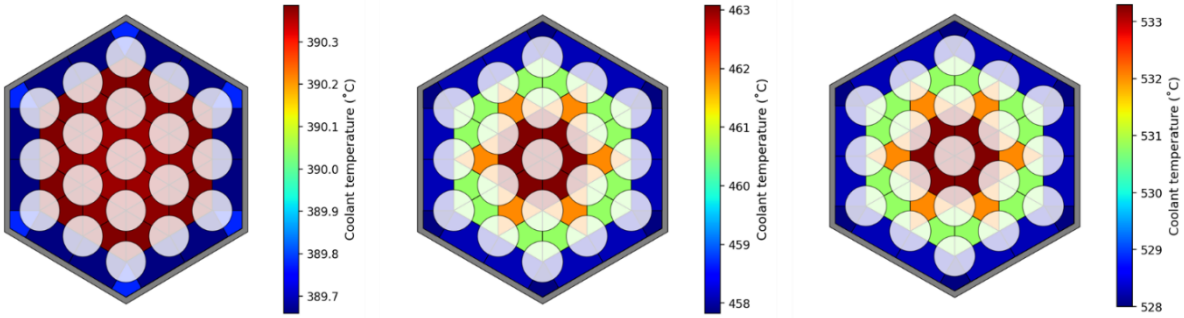


(a) (b) (c)

*Figure 107 Lead temperature at: z= 0 (a), z=L/2 (b), z=L (c)*

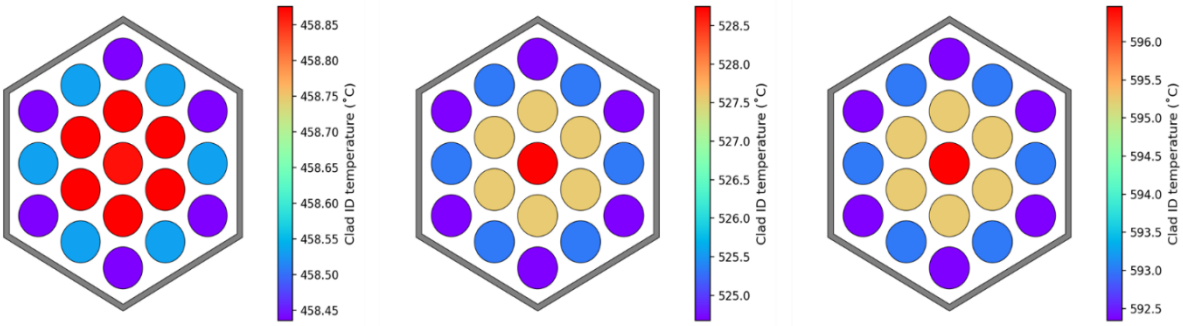


(a) (b) (c)

*Figure 108 Clad ID temperature at: z= 0 (a), z=L/2 (b), z=L (c)*

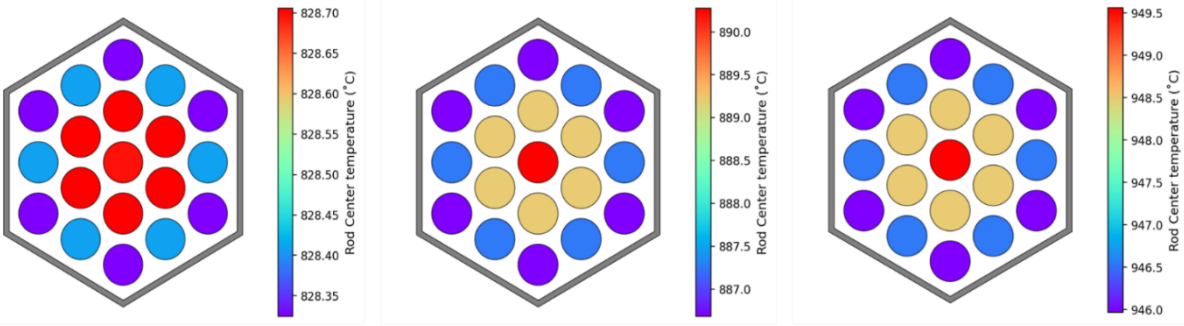


(a) (b) (c)

*Figure 109 Rod centre temperature at: z=0 (a), z=L/2 (b), z=L (c)*

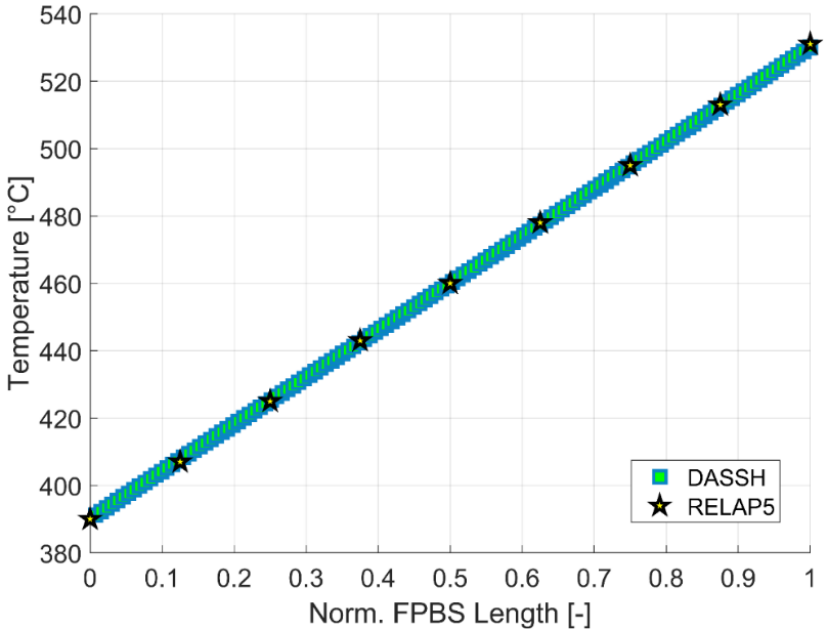


***Figure 110 RELAP5/Mod3.3 vs DASSH: coolant temperature axial profile.***

Another interesting comparison between the two codes is the one related to the pin radial thermal field. Referring to the outlet section, the main temperatures computed by RELAP5/Mod3.3 and DASSH are reported in Table 44. For the STH code, the adopted lumped parameter model relies on an equivalent component representing the average pin behaviour. Instead, DASSH is able to characterize the thermal field of each pin. Thus, the temperatures reported in Table 44 are the ones associated with the hottest pin. DASSH computes a higher temperature gradient between the clad external surface and the coolant (26 °C with respect to 15 °C). This is due to the different correlations adopted by the two codes to evaluate the wall-to-fluid heat transfer. While the STH code uses Seban-Shimazaki [36], DASSH relies on Lyon-Martinelli [109], resulting in a lower heat transfer coefficient. This discrepancy propagates throughout the overall pin radial profile up to the centreline fuel temperature.

***Table 44 RELAP5/Mod3.3 vs DASSH: pin radial temperature field.***

| **Parameter** | **Unit** | **RELAP5** | **DASSH** |
|---|---|---|---|
| **Coolant Temperature** | °C | 530 | 533[1] |
| **Clad Ext. Surf. Temperature** | °C | 545 | 559 |
| **Clad Int. Surf. Temperature** | °C | 583 | 596 |
| **Pin Simulator Ext. Surf. Temperature** | °C | 917 | 945 |
| **Pin Simulator Centreline Temperature** | °C | 922 | 950 |

[1]This is the temperature of the hottest channel, the one associated with the hottest pin.

PHE TH ANALYSIS

Microchannel Heat Exchangers (MCHEs) have gained significant attention in recent years due to their superior heat transfer performance, compact design, and potential applications in advanced nuclear energy systems [110]. Despite these advantages, several challenges remain in their widespread adoption, particularly concerning manufacturability, fouling resistance, and accurate TH modelling. A relevant example of this innovative component and subjected in this TH analysis is the PHE of the VLF.

To address these R&D gaps, a comparative analysis of MCHE using both a STH and a CFD code adopting as a case study the PHE of the VLF has been performed [111]. The objective is to assess the accuracy and applicability of each approach, highlight their limitations, and propose improvements for future modelling strategies.

The case study adopted in the present work is the PHE of the VLF (depicted in Figure 111) which represents a scaled version of the PHE of the WEC-LFR. The block dimensions are 950 mm x 107 mm x 500 mm [105].

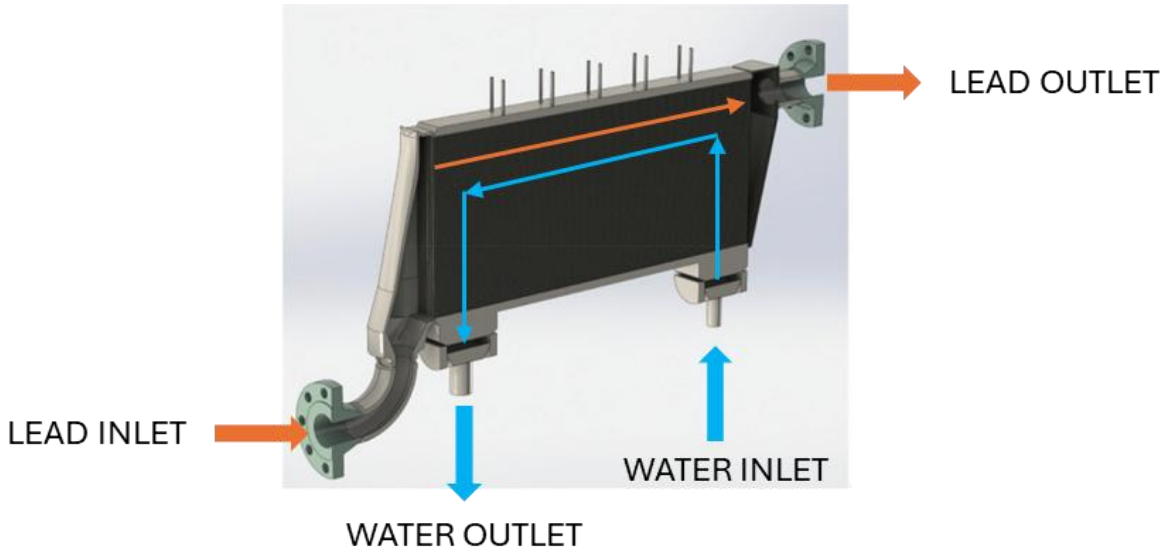


***Figure 111 PHE view [105]***

The methodology is based on the development of models with STH and CFD codes. Due to the lack of experimental data, the verification of the numerical models is conducted through the comparison of the numerical results with the nominal data provided by the supplier. Additionally, a benchmark between the two different codes is performed. The main parameters of the PHE of the VLF are summarized in Table 35 (see Section 4.3.1)

Due to the CFD high computational cost and long processing times, in this work a unit cell has been identified consisting of 4 water channels per lead channel. Moreover, it has been assumed that the configuration of the unit cell is pure counter-current flow neglecting the typical zig-zag path of the MCHEs. This simplification leads to an underestimation of the pressure drops, as it disregards the localized losses introduced by each bend forming the zig-zag path. Furthermore, it also underestimates the heat transfer performance by neglecting the enhancement caused by the increased turbulence induced by the flow redirection. Nevertheless, this is a preliminary analysis, and future work is planned to include the zig-zag configuration in order to provide a more accurate assessment.

Finally, the active length was assumed to be equal to the axial distance between the two inlet and outlet nozzles on the supercritical water side which results to be approximately 600 mm (see Figure 111). The key-parameters rescaled to the unit cell are reported in Table 45.

***Table 45 Key-parameters of the PHE unit cell***

| **Parameter** | **Unit** | **Value** |
|---|---|---|
| **Nominal Size** | W | 707.21 |
| **Number of lead channels** | - | 1 |
| **Lead mass flow rate** | g/s | 34.701 |
| **Number of water channels** | - | 4 |
| **Water mass flow rate** | g/s | 0.114 |

Figure 112 shows the numerical model developed with ANSYS-CFX [39].

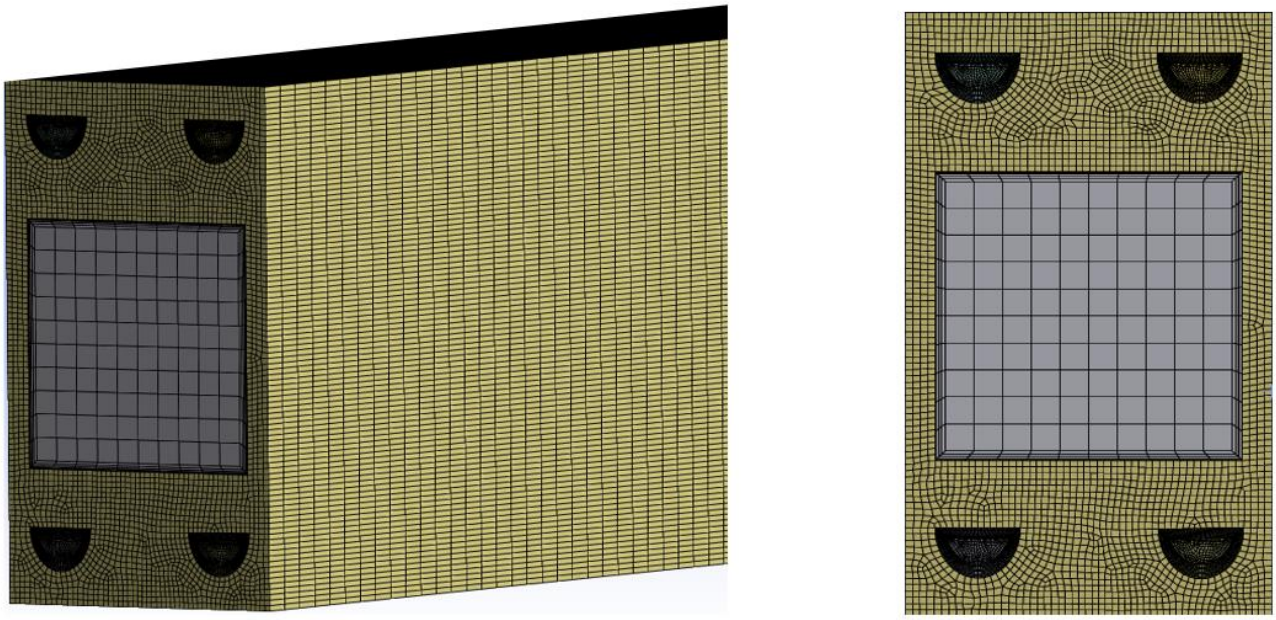

***Figure 112 Mesh of the PHE unit cell***

This model foresees three regions for solving the steady-state conjugate heat transfer problem: the lead domain in the square channel, the supercritical water domain in the D-shape channels and the solid domain. As shown in Figure 112, two different mesh have been adopted i.e., about 5 x $10^{-4}$ m body size in the lead domain and 5 x $10^{-5}$ m body size in the solid and water domains. It should be noticed that the liquid lead is not included in the ANSYS default fluids, so the thermophysical properties of lead (provided by Ref. [34]) had been implemented as look-up tables namely viscosity, density, specific heat and thermal conductivity vs temperature with variation of 0.1 °C. On the other hand, as far as supercritical water is concerned, although the water fluid is present by default in ANSYS, there are many references (e.g., Ref. [112]) reporting the high numerical

instability of water in the supercritical region. Therefore, the thermophysical properties provided by IAPWS-IF97 [113] have also been implemented for supercritical water as a look-up table with a temperature variation of 0.1 °C. With regard to the types of boundary conditions, in the fluid domains in the inlet faces a flow rate and temperature were set, in the outlet faces an average static pressure was set to zero. About the boundary conditions of the solid domain, the adiabaticity condition was set on the outer walls. Additionally, the SST k-ω turbulence model [114] was applied in both fluid domains, with the mesh constructed to maintain a near-wall resolution of approximately $y+ \approx 1$, ensuring accurate capture of boundary layer effects. Finally, wall rugosity was also added to the model with a value of $4.5 \times 10^{-5}$ m.

Conversely, the numerical model developed with RELAP5/Mod3.3 is shown in Figure 113.

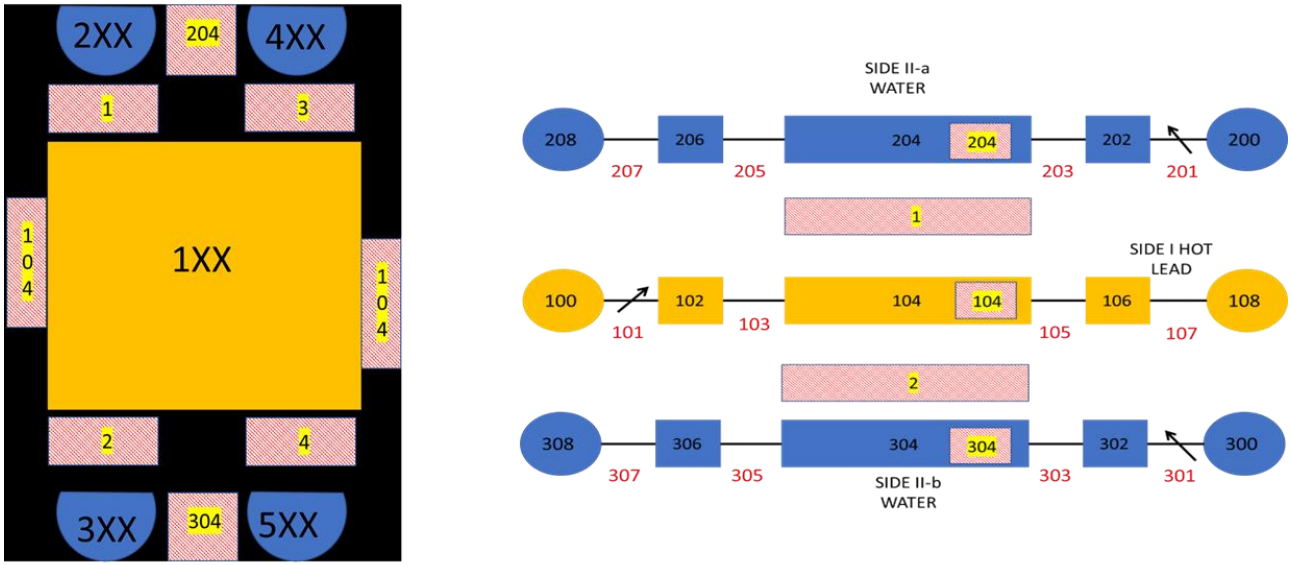


***Figure 113 R5 nodalization scheme of PHE unit cell***

An axial mesh size of approximately 4 cm has been adopted according to the indications provided in [115]. The first digit of the hydrodynamic components number identifies a specific system as follows: 1XX for the PHE lead side, 2XX and 4XX identify the PHE water side upper channels and 3XX and 5XX identify the PHE water side lower channels. No localized pressure losses are foreseen since this model represents only the straight section of the lead/water channels and the abrupt area changes between the inlet/outlet collectors and the channels have been neglected. Instead, a wall roughness was added to the model with a value of $4.5 \times 10^{-5}$ m.

The heat transfer which takes place in the unit cell is modelled by the heat structures 1, 2, 3 and 4 (see Figure 113) which thermally couple lead with supercritical water. Then, the heat structures 204 and 304 thermally couple respectively the upper and lower water channels. Finally, the heat structure 104 accounts for the remaining steel inventory located between adjacent lead channels. In the input deck, the heat transfer coefficient correlations adopted for supercritical water and liquid lead are respectively Dittus-Boelter [108] and Seban-Shimazaki [36], the default ones present in the code for the two fluids. It should be noted that these HTC correlations have not been experimentally derived for the geometrical and thermodynamic conditions characterizing this problem, but they have been kept since no ad-hoc correlations are available in literature for the MCHEs. This is another expected outcome of the experimental campaign referring to the VLF facility. Once available, these correlations will be implemented in the numerical tools to improve their modelling capabilities.

Since RELAP5 is a one-dimensional code but the problem presented in this work results in a 3-D temperature distribution, a preliminary simulation (labelled RUN_A) was carried out to verify the appropriateness of the conductive problem simulated with the STH code, in terms of heat transfer surfaces and steel thickness implemented in the input deck. The generic expression of the global heat transfer coefficient in rectangular geometry is given in Equation 37):

$$U = \frac{1}{\frac{1}{h_{Pb}} + \frac{s}{k} + \frac{1}{h_{H_2O}}} = \frac{\mathrm{k}}{\mathrm{s}} \qquad 37)$$

In which:

- $U$ is the overall heat transfer coefficient
- $h_{Pb}$ is the lead-side heat transfer coefficient
- $s$ is the thickness of the steel
- $k$ is the thermal conductivity of the steel
- $h_{H_2O}$ is the water-side heat transfer coefficient

In Equation 37), the second equality holds under the assumption of infinite heat transfer coefficients on both the lead and water sides, effectively isolating the conductive thermal resistance by the convective terms. In this simulation, fixed temperatures and heat transfer coefficients are imposed in both fluid domains, allowing the system to be governed purely by the conductive behaviour of the solid domain. The primary objective is to quantify the conductive component of the total thermal resistance—modelled in RELAP5 through a 1D heat conduction approach—and compare it with the CFD solution, which resolves conduction in two dimensions. The key result of this setup is the amount of power (indicated in Table 46 as "Thermal power") transferred between the two fluid domains through the solid wall under an imposed temperature difference, as summarized in Table 46. This thermal power serves as a direct measure of conductive heat transfer, enabling an effective comparison of the conduction modelling fidelity between the two approaches.

***Table 46 RUN_A comparison between CFD and R5***

| **Parameter** | **Unit** | **CFD** | **RELAP5** | **Δ%** |
|---|---|---|---|---|
| **Lead temperature (BC)** | K | 600 | 600 | / |
| **Lead HTC (BC)** | W/m$^2$K | $10^{10}$ | $10^{10}$ | / |
| **Water temperature (BC)** | K | 500 | 500 | / |
| **Water HTC (BC)** | W/m$^2$K | $10^{10}$ | $10^{10}$ | / |
| **Thermal power** | W | 9990.0 | 9922.6 | 0.67% |

It can be seen that the error committed is less than 1%, which confirms the good accordance between the conductive problems simulated with the STH and CFD codes. Furthermore, variations in the imposed temperatures within the fluid domains lead to a linear change in the thermal power exchanged between the two regions. However, the relative discrepancy between the two codes remains unaffected, as it stems solely from geometric factors—such as heat transfer surface area and wall thickness—and material properties, specifically thermal conductivity. These preliminary analyses were used to test the appropriateness of the 1D conduction approach available in the STH code with respect to this heat transfer problem. Due to its geometrical complexity, this was one of the major concerns. However, simulation outcomes demonstrated the suitability of R5 and of the discussed modelling approach. After that, the numerical simulation representative of the nominal behaviour of the PHE has been performed (labelled RUN_B). The boundary conditions implemented in RUN_B are reported in Table 47.

***Table 47 BCs of RUN_B***

| Parameter | Unit | Value |
|---|---|---|
| **Lead inlet temperature** | °C | 520 |
| **Lead mass flow rate** | g/s | 34.7 |
| **Water inlet temperature** | °C | 350 |
| **Water mass flow rate** | g/s | 0.114 |

To ensure the numerical accuracy and reliability of the CFD results, a grid independence study was performed. This analysis aimed to verify that the predicted thermal-hydraulic parameters were not significantly affected by further mesh refinement, thereby confirming the adequacy of the selected mesh resolution for capturing the relevant flow and heat transfer phenomena.

***Table 48 Grid independence study***

| Parameter | Mesh 1 | Mesh 2 | Mesh 3 |
|---|---|---|---|
| **N° of nodes [Millions]** | 0.49 | 0.74 | 0.93 |
| **Lead outlet temperature [°C]** | 391.15 | 391.11 | 391.11 |
| **Water outlet temperature [°C]** | 521.84 | 521.90 | 521.91 |
| **Thermal power [W]** | 697.73 | 697.90 | 697.91 |

As shown in Table 48, variations in the number of mesh nodes did not result in significant differences in the key parameters relevant to the present study. The values of thermal power and fluid outlet temperatures remained stable across the different mesh configurations, indicating that the numerical solution is not sensitive to further grid refinement. This confirms that the adopted mesh resolution is sufficient to accurately capture the thermal-hydraulic behaviour of the system and ensure the suitability of the CFD results as reference for subsequent analyses. The global numerical results of both models are summarised in Table 49, where also the deviations between the nominal data and CFD (labelled $\Delta_{CFD\text{-}Nom}$), between the nominal data and RELAP5 (labelled $\Delta_{R5\text{-}Nom}$) and finally between CFD and RELAP5 (labelled $\Delta_{CFD\text{-}R5}$) are shown.

***Table 49 Results and comparison of RUN_B***

| Parameter | Unit | Nominal data | CFD | $\Delta_{CFD\text{-}Nom}$ | RELAP5 | $\Delta_{R5\text{-}Nom}$ | $\Delta_{CFD\text{-}R5}$ |
|---|---|---|---|---|---|---|---|
| **Thermal power** | W | 707.2 | 697.9 | -1.32% | 693.7 | -1.92% | -0.60% |
| **Lead outlet temperature** | °C | 390 | 391.1 | 1.1 °C | 391.8 | 1.8 °C | 0.7 °C |
| **Lead pressure drops** | kPa | - | 0.94 | / | 0.92 | / | -2.13% |
| **Water outlet temperature** | °C | 520 | 521.9 | 1.9 °C | 511.8 | -8.2 °C | -10.1 °C |
| **Water pressure drops** | kPa | - | 1.70 | / | 1.41 | / | -17.06% |

As far as the CFD and STH results are concerned, a deviation with respect to nominal data lesser than 2% is present for both when considering the thermal power. The main deviation observed between the CFD and RELAP5 results compared to the nominal data lies in the exchanged thermal power. Both codes predict lower thermal power values than expected, which is consistent with the modelling assumptions adopted in this study.

Specifically, the zig-zag flow path—a key geometric feature known to enhance heat transfer by promoting flow turbulence and increasing the effective heat exchange surface—was not included in the simplified models used for both simulations. As a result, the reduced thermal interaction is a direct consequence of neglecting this enhancement mechanism, which highlights the importance of accurately representing complex geometrical features when evaluating heat exchanger performance. This aspect will be considered in the prosecution of this numerical activity. Regarding the CFD results, an inconsistency seems to be present in the outlet temperature, that is similar to the nominal one despite a lower predicted thermal power. It can be attributed to interpolation errors in the specific heat of supercritical water.

Given the strong temperature dependence of specific heat in the supercritical region, a dedicated refinement of the lookup table for specific heat as a function of temperature was performed, reaching a resolution of 0.1 °C as previously stated. This refinement aimed to minimize interpolation errors and ensure the most accurate representation possible of thermophysical properties.

Despite this effort, the outlet temperature deviation persists and can be solely attributed to the sensitivity of the energy balance to specific heat variations. This is evident in Table 49, where, despite matching the nominal thermal power between CFD and RELAP5 under fixed mass flow conditions, the simulations shows a deviation of 10 °C in outlet temperature—highlighting the critical influence of specific heat accuracy in supercritical flow simulations.

Regarding the comparison between the two numerical simulations, Table 49 shows a good agreement. The main deviation is related to the supercritical water-side pressure drops error of approximately 17%. As will be shown later on, this is due to the different temperature distributions obtained by the two codes.

On the local level, Figure 114 presents a comparison between RELAP5 and CFD temperature predictions along the normalized axial position of the PHE lead side. The left plot illustrates the axial temperature distribution, where the CFD results (blue markers) predict higher temperatures compared to RELAP5 (orange markers), particularly in the central region. Both models exhibit a similar decreasing trend along the axial coordinate, indicating qualitative agreement in temperature evolution. The right plot depicts the relative temperature deviation between RELAP5 and CFD, defined in Equation 38).

$$\Delta = T_{RELAP5} - T_{CFD} \quad 38)$$

On the lead side, the maximum temperature error is about 15 °C which occurs at the half of the PHE. The comparison of lead side pressure obtained from RELAP5 and CFD simulations along the normalized axial position of the system is plotted in Figure 115.

The left plot illustrates the axial pressure distribution, with both models exhibiting a nearly linear pressure decrease. The CFD results (blue markers) predict a slightly higher pressures compared to RELAP5 (orange markers), though the discrepancy remains minimal throughout the domain. The right plot depicts the deviation defined in the Equation 39).

$$\Delta = \frac{p_{RELAP5} - p_{CFD}}{p_{CFD}} 100\% \quad 39)$$

The deviation within -0.03%, indicates good agreement between the two models. As far as the lead velocity is concerned, the comparison between RELAP5 and CFD is depicted in Figure 116. The trends are consistent with the temperature trends where the lead velocity calculated by CFD is greater than that evaluated by RELAP5 since the thermal field predicted by CFD is higher and, at imposed flow rates, this leads to greater velocities. The right plot shows the deviation between the two models, as defined in Equation 40), with a maximum value of approximately 0.12%.

$$\Delta = \frac{v_{RELAP5} - v_{CFD}}{v_{CFD}} 100\% \quad 40)$$

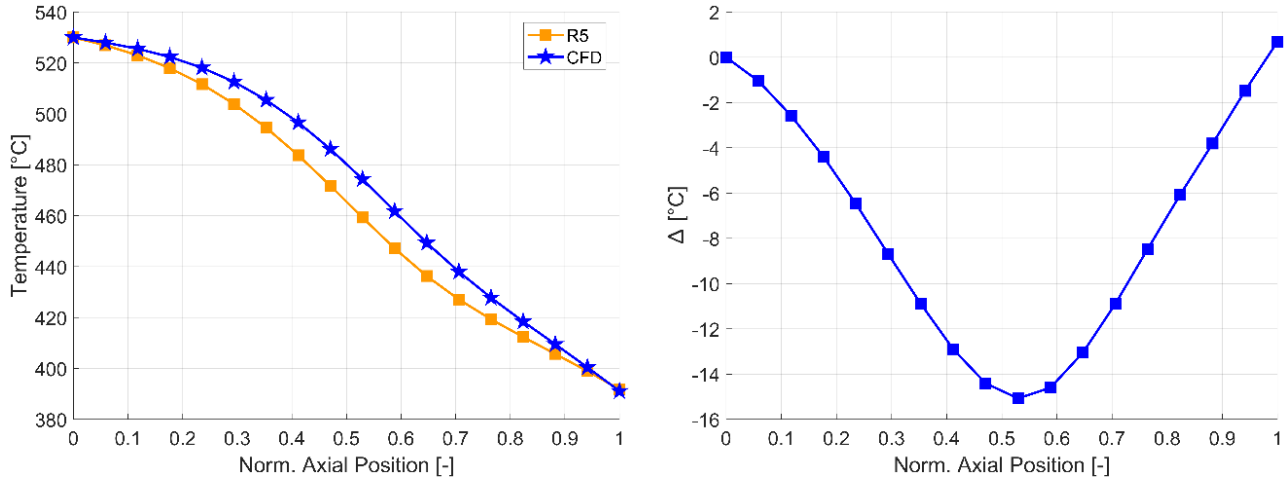


***Figure 114 Lead side temperature comparison between CFD and RELAP5***

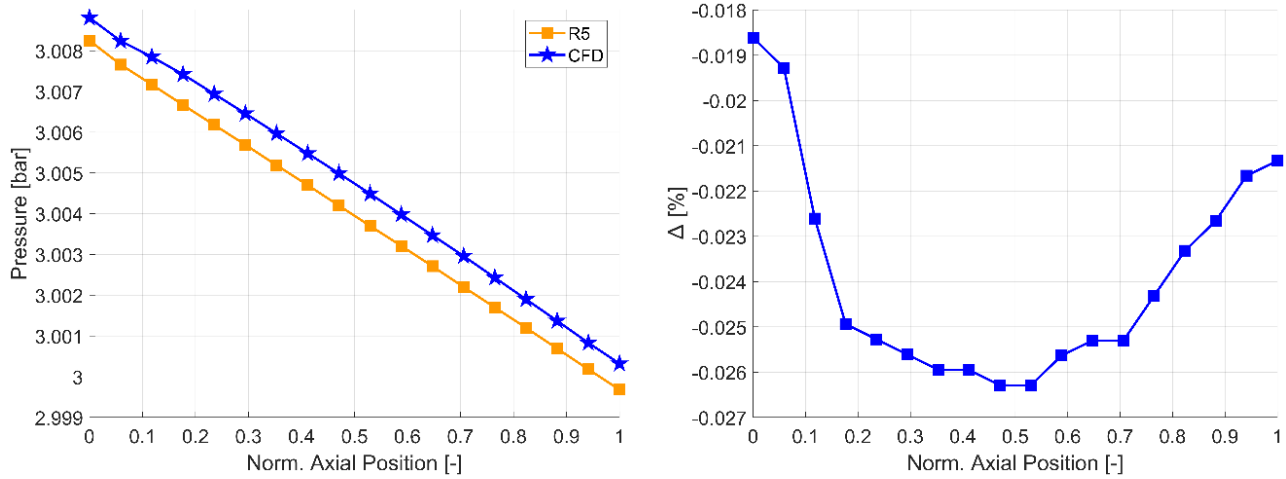


***Figure 115 Lead side pressure comparison between CFD and RELAP5***

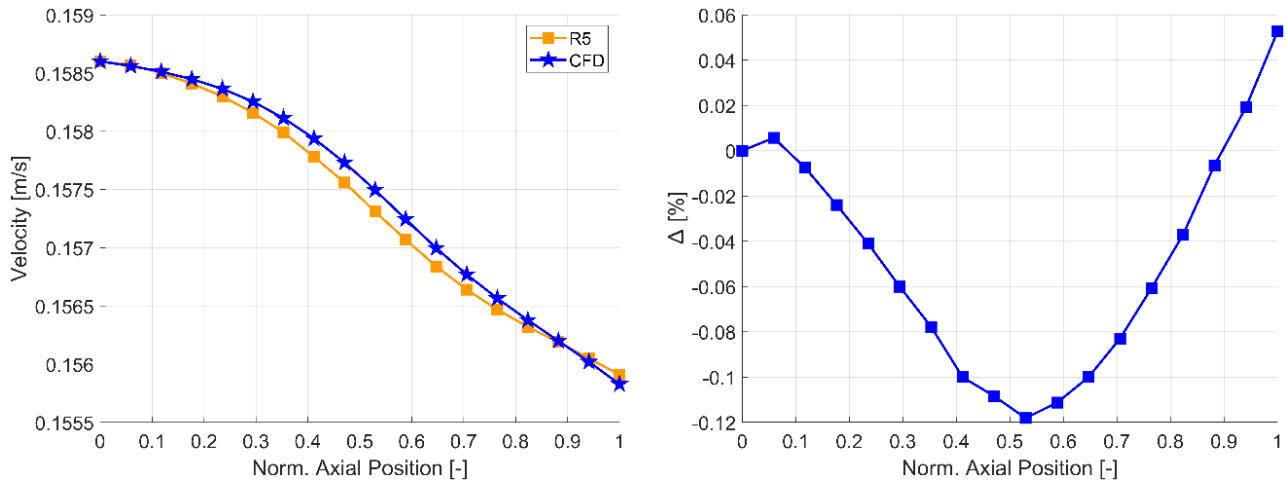


***Figure 116 Lead side velocity comparison between CFD and RELAP5***

Figure 117 presents the comparison of temperature predictions from RELAP5 and CFD simulations along the normalized axial position of PHE water side.

The left plot illustrates the axial temperature distribution. The CFD results (blue markers) consistently predict higher temperatures compared to RELAP5 (orange markers), with the discrepancy increasing along the axial coordinate. Both models exhibit a similar trend, with temperatures increasing along the flow direction, though RELAP5 underestimates the temperature throughout the domain. The right plot shows that the maximum temperature error is 27 °C which occur at the middle of the PHE.

Then, the water side pressure trend between CFD and RELAP5 and the relative error are depicted in Figure 118. No discrepancies are present with a pressure drop error close to zero throughout the PHE.

Finally, the water side velocity evaluated by both models is plotted in Figure 119. The left plot presents the velocity profiles along the relative axial position for both RELAP5 (represented by orange markers) and CFD (represented by blue markers). indicate that the CFD simulation predicts higher velocities compared to RELAP5 across most of the axial domain. In the initial section (up to approximately 0.2), both methods exhibit a similar trend with small discrepancies.

However, as the axial position increases, the difference between the two methods becomes more pronounced, with the CFD-predicted velocity being consistently higher. Toward the upper axial region, the two profiles appear to converge. The right plot quantifies the relative deviation between RELAP5 and CFD results, The deviation curve reveals a systematic underprediction of velocity by RELAP5. At the lower axial positions, the deviation is relatively small (within -5%). As the axial position increases, the discrepancy becomes more significant, reaching a maximum deviation of approximately -35% near the mid-section. In the upper axial region, the deviation reduces again, approaching zero, indicating better agreement between the two methods in that region.

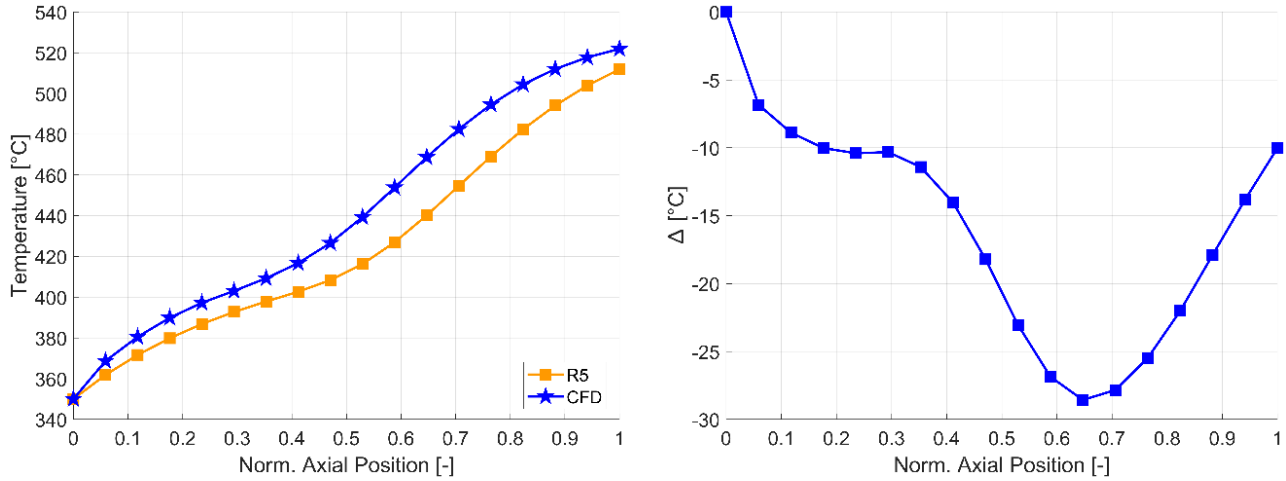


***Figure 117 Water side temperature comparison between CFD and RELAP5***

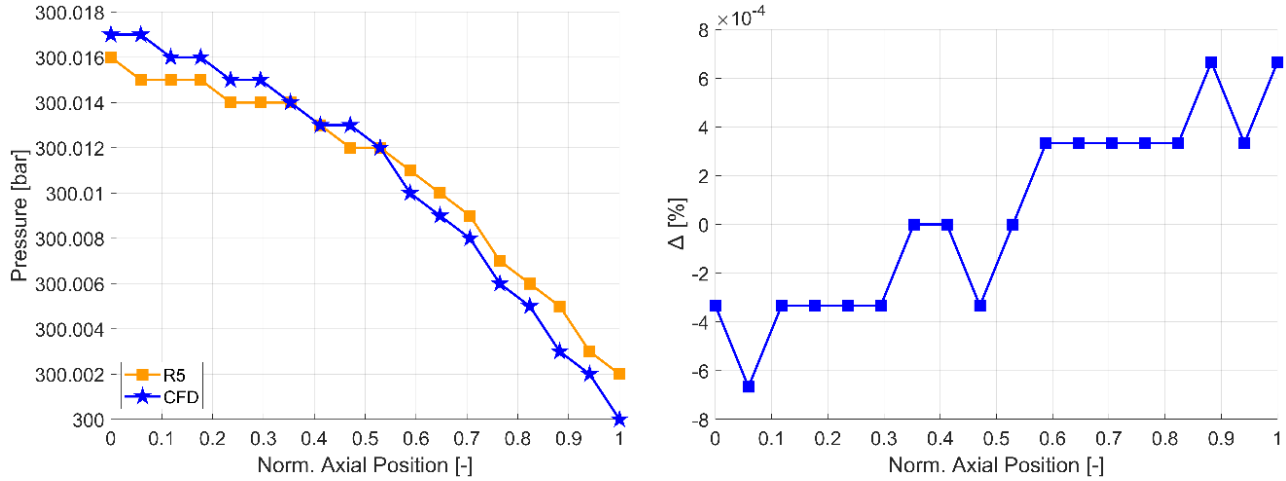


***Figure 118 Water side pressure comparison between CFD and RELAP5***

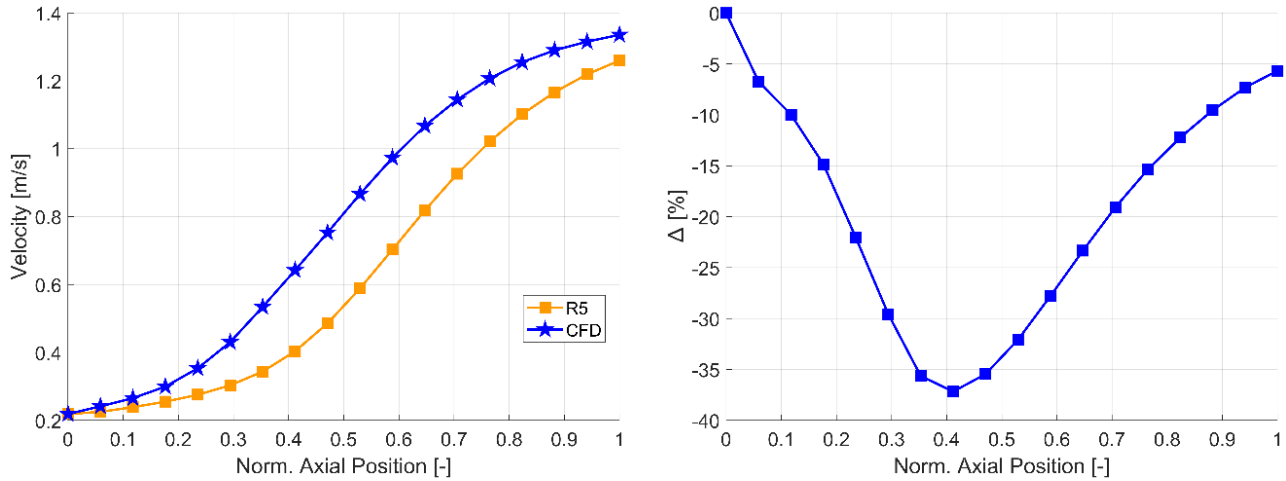


***Figure 119 Water side velocity comparison between CFD and RELAP5***

# 5. ANALYSES TO SUPPORT THE DEVELOPMENT OF MYRRHA

MYRRHA (Multi-purpose hYbrid Research Reactor for High-tech Applications) is an advanced nuclear research facility currently under development at the Belgian Nuclear Research Centre (SCK CEN) [116][117]. It is designed to support a broad spectrum of applications, including fuel and materials irradiation, the qualification of Generation IV reactor technologies, medical radioisotope production, and the transmutation of nuclear waste.

As a strategic component of the European roadmap for sustainable nuclear energy, MYRRHA plays a pivotal role in demonstrating technologies aimed at closing the nuclear fuel cycle. In particular, it supports the reduction of long-term radiotoxicity of spent nuclear fuel through partitioning and transmutation processes. Additionally, MYRRHA is envisioned as a unique international platform for cutting-edge research and development in nuclear science and technology.

The facility combines a high-power linear proton accelerator—delivering 600 MeV proton beams at a current of 2.5 mA—with a LBE spallation target. The spallation target is positioned at the core of a subcritical fast-spectrum reactor, which is also cooled by LBE. MYRRHA adopts a pool-type configuration, where the LBE used in the spallation target and that used in the reactor core flow in distinct but interconnected loops. An overview of MYRRHA's main design features is shown in Figure 120.

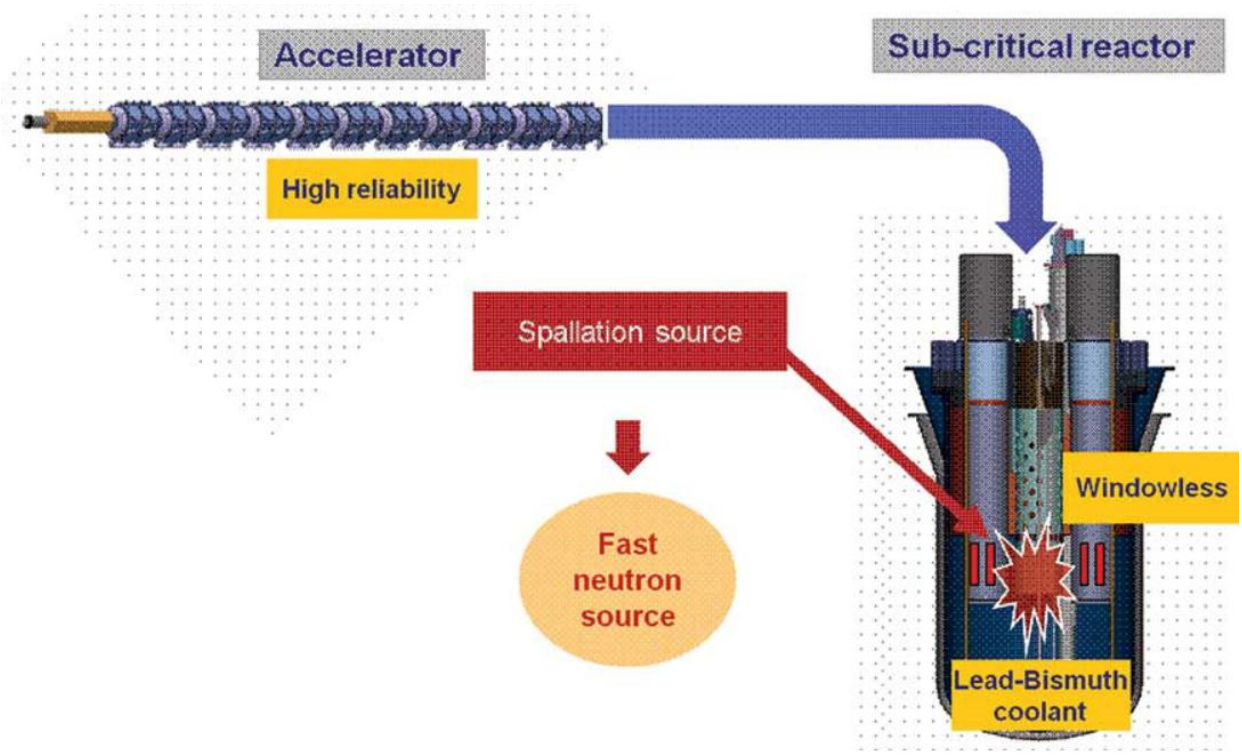


***Figure 120 Conceptual scheme of MYRHHA [116]***

## 5.1. Reactor design overview

MYRRHA reactor (shown in Figure 121) is a pool-type ADS capable of operating both in subcritical mode, with an external proton accelerator, and in critical mode.

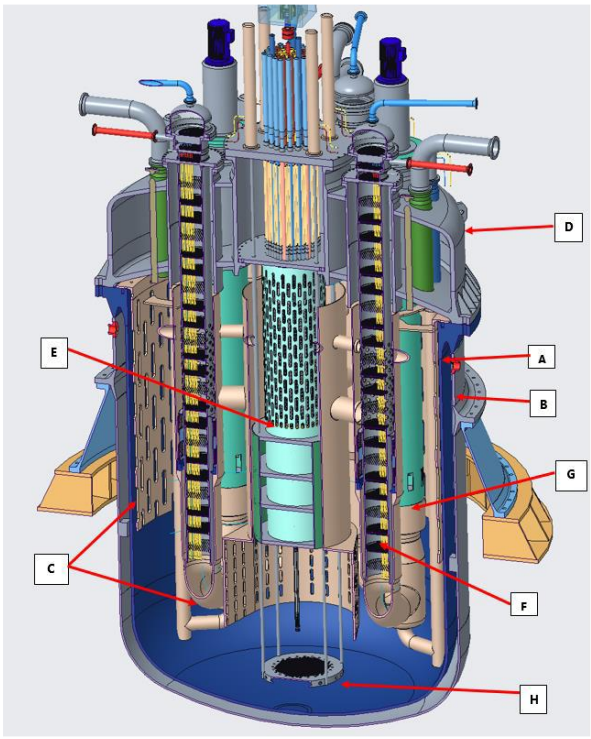


***Figure 121 MYRRHA reactor assembly isometric cross-sectional view [118]***

Referring to Figure 121, the main components constituting MYRRHA are the following: A: Primary reactor vessel (RV), B: Safety vessel (SV), C: Diaphragm (DIA), D: Reactor cover (RC), E: Core barrel (CB), F: Primary heat exchanger (PHX), G: Primary pump (PP), H: Core restraint system (CRS), I: In-vessel fuel handling machine (IVFHM)

Its core is fuelled with MOX and cooled by LBE. In the pool-type configuration, all primary system components are housed within a large reactor vessel and inserted from the top through the reactor cover. This vessel consists of a primary vessel, which is surrounded by a safety vessel acting as secondary containment in the event of a leak or structural failure. The reactor cover seals the system and supports all internal components.

The core, fully submerged in LBE, is centrally located within the vessel and enclosed by a core barrel and shielding jacket. It accommodates fuel assemblies, control and safety rods, a spallation target assembly, reflector assemblies, instrumentation, surveillance capsules, and in-pile test sections. The radial positioning of the core is fixed by a core restraint system, and fuel handling is performed by a permanently installed In-Vessel Fuel-Handling Machine (IVFHM).

Spent fuel is stored internally within the diaphragm structure, which also supports multiple reactor functions. The diaphragm is a large internal structural component that provides lateral support and flow guidance for primary system elements.

Constructed as a perforated circular steel basket mounted to the primary vessel flange, it contains vertical chimneys that house the Core Unit (CU), Primary Heat eXchangers (PHX), Primary Pumps (PP), IVFHM, the Fuel Transfer Channel (FTC), and the In-Vessel Fuel Storage (IVFS). Dedicated piping connects key components (e.g., the core to the PHX, and the PHX to the PP), ensuring the guided circulation of the LBE coolant.

During normal operation, LBE enters the core from below at a maximum inlet temperature of 220 °C, a value selected to ensure the Peak Cladding Temperature (PCT) remains below the safety threshold of 400 °C. This temperature also defines the cold plenum's thermal boundary and constrains the allowable oxygen concentration to mitigate corrosion.

After absorbing heat in the core, LBE exits the core unit—comprising the core and Above-Core Structure (ACS)—through the core chimney, reaching a maximum mixed outlet temperature of 270 °C at full power. The thermal head across the core results in the free surface of the hot plenum being located below that of the cold plenum.

Hot LBE is routed through horizontal diaphragm pipes into chimneys containing four primary heat exchangers, which operate in parallel and interface with the reactor's secondary and tertiary loops. These PHXs extract the core's thermal power and transfer it to the secondary system during steady-state operation. The main parameters of MYRRHA design are reported in Table 50.

***Table 50 MYRRHA general design parameters [118]***

| **Parameter** | **Value** | **Unit** |
|---|---|---|
| **Maximum core power** | 64 | $MW_{th}$ |
| **Maximum heat sink rated power** | 70 | $MW_{th}$ |
| **Maximum core inlet LBE temperature** | 220 | °C |
| **Maximum average hot plenum LBE temperature** | 270 | °C |
| **Overall primary coolant system pressure drop** | 2.63 | bar |

Three cooling loops are foreseen: the primary cooling system of the reactor is the RCS, which utilizes LBE as the primary coolant. This circuit is responsible for heat removal directly from the reactor core. Heat is then transferred to the secondary cooling system, which employs water as the working fluid. The secondary system, in turn, is connected to the tertiary cooling system, which uses air as the final heat sink. Both the secondary and tertiary systems operate in active mode during normal operating conditions, relying on pumps and forced convection, while switching to passive operation under accident conditions to ensure reliable decay heat removal through natural circulation. A three-dimensional schematic of the secondary and tertiary cooling systems, starting from their connection to the reactor vessel and extending upwards, is presented in Figure 122.

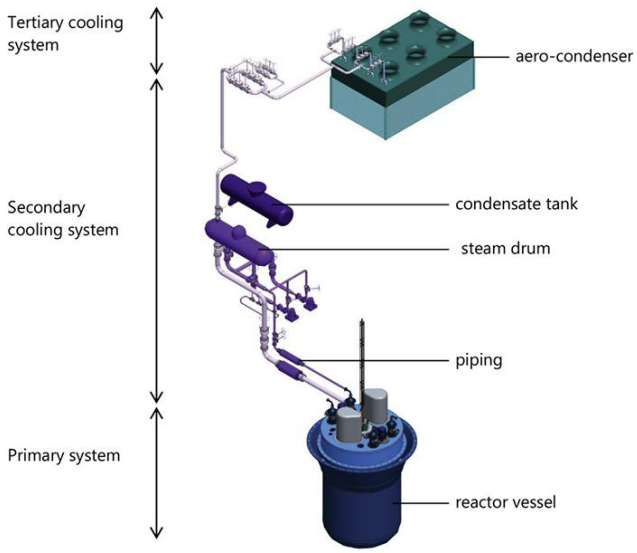


*Figure 122 MYRRHA cooling loops [117]*

The core layout consists of 163 hexagonal channels, arranged in seven concentric rings (crowns) according to design revision 1.8. The outermost ring functions as a reflector, enhancing neutron economy. These channels are enclosed by a stainless-steel jacket and further surrounded by the core barrel, forming the structural boundary of the core. The configurations for both the subcritical and critical core layouts are illustrated in Figure 123.

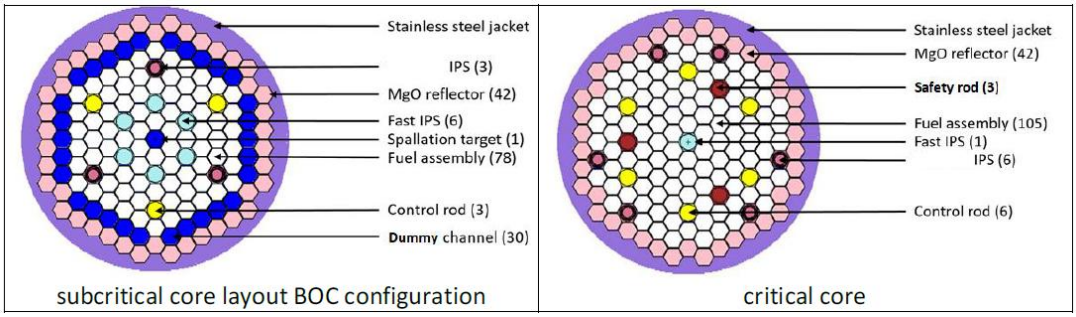


*Figure 123 MYRRHA core layout [118]*

The Fuel Assembly (FA) design follows a configuration commonly used in Sodium-cooled Fast Reactors (SFRs). Each assembly comprises a hexagonal bundle of 127 cylindrical fuel pins, housed within a hexagonal wrapper. The top and bottom of the wrapper are connected to inlet and outlet nozzles, which guide the LBE coolant through the fuel bundle. Inside each fuel pin, fuel pellets are accommodated, along with a gas plenum that serves to contain helium filling gas and fission gases released during operation. The fuel pins are maintained in position by helical wire-spacers wound around their outer surfaces. The MYRRHA fuel pin design closely resembles that of traditional SFR fuel pins. As depicted in Figure 124, each pin consists of a cylindrical cladding fabricated from 15-15Ti austenitic stainless steel, a material selected for its mechanical strength and corrosion resistance under fast reactor conditions.

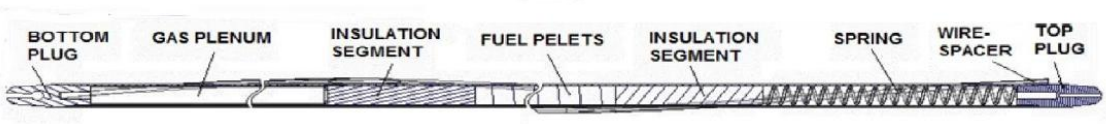


*Figure 124 Cross section of a fuel pin [118]*

The CU is a central, vertically extended structure within the reactor that houses and supports the entire reactor core, including the core assemblies and in-pile sections (IPS) (see Figure 125). It is anchored to the reactor cover and extends downward to connect with the flat plate of the diaphragm. The CU is designed to facilitate bottom-access core handling operations by the IVFHM, which can manipulate core components when the core restraint grid is lowered.

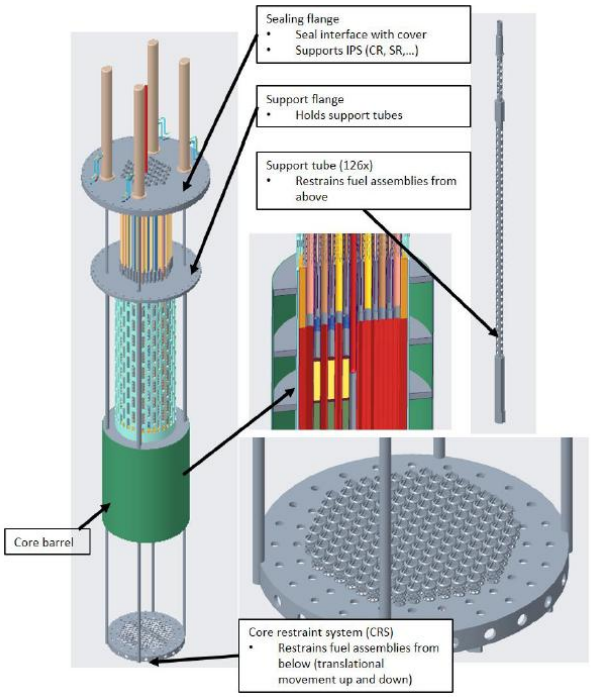


***Figure 125 CU assembly [118]***

The diaphragm serves as a structural and hydraulic interface within the MYRRHA reactor pool, separating the cold and hot LBE plena while providing a controlled flow path between them. The primary LBE coolant flows from the cold plenum, upward through the core, and into the hot plenum. From there, it is directed through a system of pipes to the PHXs, after which it flows toward the PPs, where it is recirculated back into the cold plenum. The walls enclosing the hot plenum, along with the pipework connecting the PHXs and PPs, are integral components of the diaphragm structure. In addition to its hydraulic functions, the diaphragm also provides mechanical support for in-vessel systems, including the IVFS.

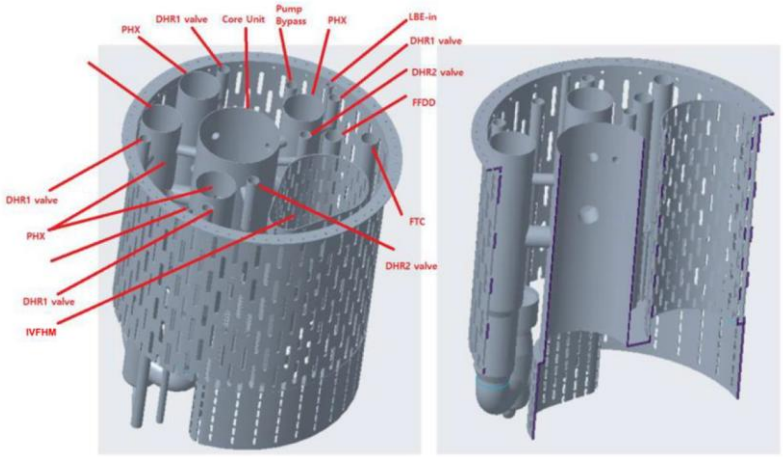


***Figure 126 Overview of the diaphragm and its components [118]***

The MYRRHA PHX (see Figure 127) features a shell-and-tube bundle design, where the primary LBE flows downward on the shell side, while the secondary water coolant flows upward through the tube side.

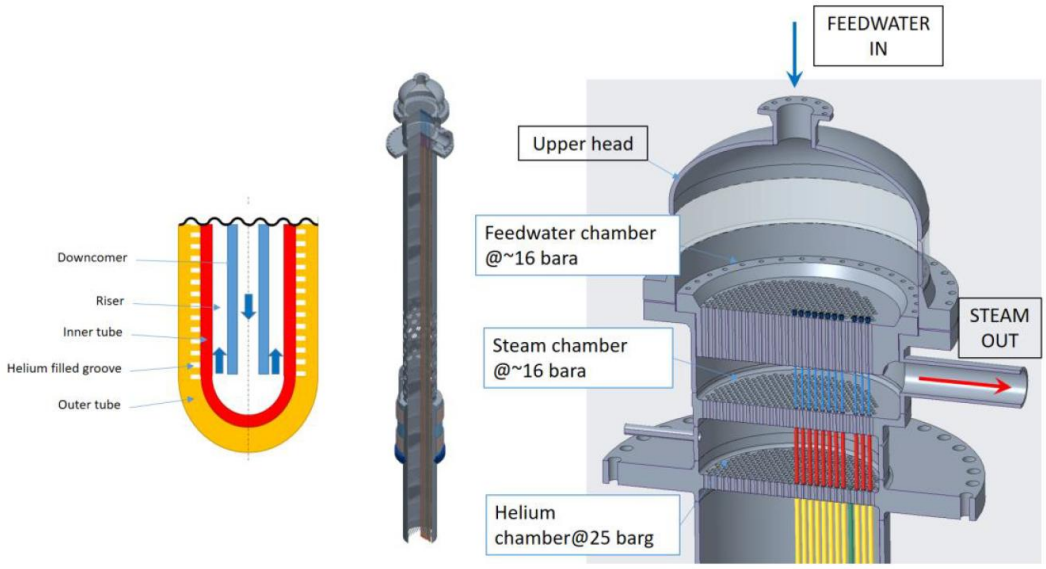


***Figure 127 Overview of the PHX: double wall bayonet tube schematic structure (left), overall 3D view (centre) and PHX head structure and flow path (right) [118]***

The tube bundle is housed within a cylindrical PHX shroud and is supported structurally by a series of spacer grids that maintain its position and alignment. Each PHX unit is installed by penetrating the RV through the RC, where it is flanged and sealed upon assembly. The diaphragm structure provides a dedicated chimney for each of the four PHX units, guiding the primary coolant flow. A flexible bellow system is incorporated into the design to accommodate thermal expansion while ensuring mechanical stability and minimising bypass flow around the component. The main features of the PHX are summarized in Table 51.

***Table 51 PHX main parameters [118]***

| **Parameter** | **Value** | **Unit** |
|---|---|---|
| **Type** | Shell-and-tube | - |
| **N° of PHXs** | 4 | - |
| **LBE inlet temperature** | 270 | °C |
| **LBE outlet temperature** | 220 | °C |
| **Secondary side coolant** | Water-steam mixture | - |

Next, two identical PPs (Figure 128) are installed in a vertical orientation and are fully submerged in the primary LBE coolant. These pumps generate an upward flow through the pump body and discharge the coolant into the cold LBE volume. The primary pumps are designed to ensure stable hydraulic performance for core cooling during normal operation, while also maintaining a flow path conducive to natural circulation in the event of a pump shutdown.

Additionally, the pumps contribute to primary gas confinement, preventing any release of reactor cover gas into the reactor hall. At the diaphragm interface, they function as a sealing boundary, effectively separating the cold and hot LBE volumes. From a safety perspective, the pumps are engineered to operate without compromising the overall safe performance of the reactor. Furthermore, their design incorporates radiological shielding, offering protection to maintenance personnel by minimising exposure during inspection or servicing activities.

***Figure 128 PP general view [118]***

Finally, since MYRRHA is a pool-type reactor, it relies on its RV to perform the essential safety function of containing the primary coolant. This containment function is redundantly supported by the SV, which acts as a secondary barrier. The RV assembly also includes structural components that connect both the RV and SV to the surrounding civil engineering infrastructure. To ensure containment of the cover gas plenum, the reactor flange is designed to provide a gastight seal with the RC. Additionally, the vessel assembly serves as the mechanical support for both the RC and the DIA, thereby supporting all components of the primary system. The SV is specifically engineered to retain any potential LBE leakage and to withstand a guillotine failure and subsequent drop of the RV. While such an event may cause significant deformation of the SV, its structural integrity is maintained to prevent LBE release. The RV is also responsible for containing the cover gas, ensuring a sealed environment under normal and off-normal conditions.

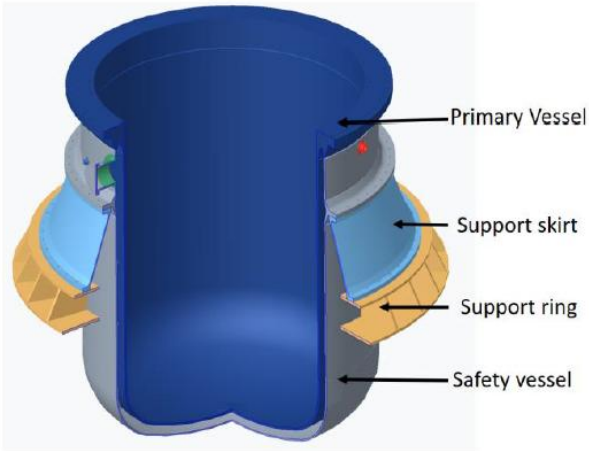


***Figure 129 Vessel assembly overview [118]***

In scenarios involving a loss of heat sink through Decay Heat Removal System 1 (DHR1)—which includes the PHX and associated loops—or during a severe core disruption, the inter-vessel space between the Primary and Safety Vessels is used as a cooling cavity by the Reactor Vessel Auxiliary Cooling System (RVACS), also referred to as DHR2. During RVACS activation, this space is filled with water, released from storage tanks located near the top of the reactor building, forming a passive decay heat removal path. However, the operation of RVACS is inhibited if LBE is present in the inter-vessel cavity, as it would compromise the system's cooling function. The RVACS operates on a passive safety principle that involves flooding the cavity between the RV and SV with subcooled water stored in tanks located above the Reactor Hall. When this water encounters the hot external surface of the RV, its temperature rises progressively until it reaches the saturation point, initiating boiling. The resulting steam is then vented out of the containment, facilitating passive heat removal. The RVACS is configured as four identical open loops, each functioning independently. A schematic representation of a single RVACS loop and its connection to the inter-vessel cavity is provided in Figure 130.

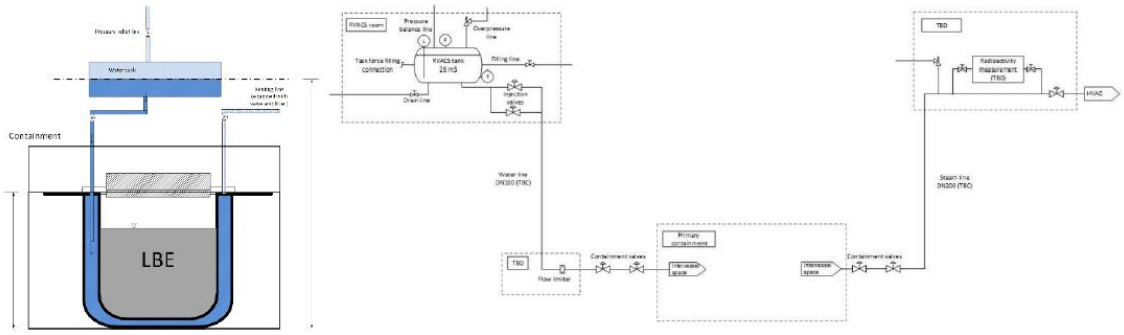


***Figure 130 RVACS overview sketch and schematic diagram [118]***

## 5.2. PIRT analysis

As part of the European ANSELMUS project [51], and specifically within Work Package 1, Task 1.1, a PIRT analysis was performed for the MYRRHA reactor. The analysis began with the definition of a reference configuration [118] based on a well-established design, serving as the foundation for the systematic decomposition of the reactor system into its principal components. This structured partitioning enables a focused assessment of safety-relevant physical phenomena across the reactor architecture. The components constituting MYRRHA partitioning are Core, FA, Pin, Fuel pellet, Clad, Primary Coolant (LBE), Above Core Structures, Barrel, Hot Plenum, Cold Plenum, Diaphragm, PHX, Primary Pumps, Connecting pipes top (CB & PHXs), Connecting pipes bottom (PHXs & PPs), IVFS, Instrumentation & Control and Potential energy.

Subsequently, a set of representative accidental scenarios was selected to reflect the most critical events capable of challenging the integrity and safety of the reactor system. In particular, three key transients were identified: Protected Loss Of Forced Flow (PLOFF), Protected CR Withdrawal (PCRW), and Protected Diaphragm Break (PDB). These scenarios were chosen based on engineering judgment to encompass a broad range of expected physical phenomena, thereby facilitating the identification of those phenomena associated with higher uncertainty or limited knowledge. Each scenario was systematically broken down into distinct temporal phases, and corresponding Figures of Merit (FoMs) were defined to support structured safety assessments and ranking efforts within the PIRT framework.

The PLOFF scenario is a design-basis accident in MYRRHA, triggered by the malfunction of the PPs. Such an event results in the loss of forced circulation in the primary circuit and, consequently, a reduction of coolant flow through the core. This induces a temperature rise in the fuel and cladding materials. To capture the worst-case behaviour, the selected envelope case assumes a complete failure of one primary pump's internal components, coupled with a non-locked rotor condition in the remaining operational pump. This approach covers the full spectrum of potential coast-down responses, independent of the specific mechanical failure mode. The LOFF transient progresses through an initial phase of flow reduction, followed by a transitional regime during which the system shifts from forced to natural circulation, often accompanied by flow oscillations. Eventually, the system reaches a long-term condition characterized by stable natural circulation. The key FoMs for this scenario include the avoidance of cladding failure and the preservation of the primary system pressure boundary integrity.

The PCRW scenario involves either a stepwise or linear extraction of control rods, resulting in a positive reactivity insertion and a corresponding increase in reactor power. As the control rods are withdrawn, the power output increases steadily, until the reactivity insertion is halted, after which the system transitions to a new equilibrium at a higher power level. This scenario is particularly important for assessing reactivity-induced accidents, where global power excursions are governed by delayed neutron feedback and thermal-hydraulic interactions. The transient can be described in three phases: the initial reactivity insertion, the transition phase after the rods stop moving, and the long-term equilibrium at the new power output. Safety-relevant FoMs in this context include the maximum centreline temperature in the most heavily loaded fuel pin and the differential thermal expansion between fuel and cladding, which could contribute to mechanical stress.

The PDB scenario investigates the consequences of hypothetical structural failures at different locations within the diaphragm. Five possible break locations were explored, including sections near the lower and upper horizontal pipes, pump chimney, and core unit chimneys. System code calculations suggest that depending on the break's location and size, severe hydraulic phenomena such as core flow reversal and prolonged oscillations of the free surfaces may occur. These dynamic behaviours typically stabilize around 20 seconds into the transient. Compared to the LOFF scenario without structural damage, DB events are generally more violent and disruptive. Once natural circulation is re-established, the overall flow rate becomes dependent on the pressure losses in the intact system and across the rupture site. For the purposes of the PIRT exercise, a large break in the core barrel was chosen as the bounding case. As with the LOFF scenario, the primary Figures of Merit are the maintenance of cladding integrity and the overall integrity of the primary system pressure boundary.

Following the identification of representative accident scenarios and their corresponding FoMs, a thorough mapping of the associated physical phenomena was conducted. This step was essential for integrating key safety-relevant processes into the methodology. The structured incorporation of these phenomena enabled a systematic prioritization of safety issues, thereby informing the planning of future experimental campaigns, model refinement activities, and validation efforts supporting the ongoing development of the MYRRHA design.

The PIRT process concluded with a consolidated consensus among the expert panel members regarding the significance of each identified phenomenon. This consensus emerged from a combination of iterative technical discussions, engineering judgement, and the outcomes of supporting numerical analyses. Each phenomenon was ranked in terms of its Importance (IMP) to system behaviour and the current State of Knowledge (SOK) available.

The final prioritization results, which reflect unanimous agreement across the panel, are comprehensively summarized in Table 52, Table 53 and Table 54 for the PLOFF, PCRW and PDB scenarios, respectively. These ranked listings offer a robust and transparent basis for steering future R&D activities, enhancing model fidelity, and focusing experimental validation on the most safety-critical aspects of MYRRHA's behaviour during abnormal operating conditions.

***Table 52 PLOFF PIRT results***

| Component | Phenomenon | IMP | | | SOK |
|---|---|---|---|---|---|
| | | I | II | III | |
| Core | Fission reaction | L | | | H |
| | Direct heating of internal structures (gamma heating) | L | L | L | H |
| | Radiation heating of the coolant due to polonium activation | L | L | L | M |
| | Decay heat | H | H | H | H |
| | Radial and axial power distribution | H | M | M | M |
| FA | Peaking factors | H | M | M | M |
| | Geometry pin tolerance | L | L | L | M |
| | Geometry wire tolerance | L | L | L | M |
| | Fuel thermal properties | M | M | L | M |
| | Stored energy in the pin (fuel heat capacity) - Heat capacity of core assemblies | M | M | L | M |
| | Clad conductivity | M | L | L | H |
| | Cladding heat capacity | L | L | L | H |
| | Gap conductance between fuel and cladding | M | M | L | M |
| | Distributed friction losses (Pressure losses) | H | H | H | H |
| | FA inlet pressure losses | M | M | M | H |
| | FA outlet pressure losses | M | M | M | H |
| | Core restrain system (Pressure losses) | M | M | L | M |
| | Convection heat transfer between the pin and the LBE in the bundle | H | M | M | M |
| | Convection radial heat transfer between FA (inter-assembly) | L | L | L | M |
| Pin | Clad oxidation | L | L | L | M |

| | | | | | |
|---|---|---|---|---|---|
| | Pin power | H | H | H | H |
| | Intra-assembly flow distribution | L | L | L | H |
| | Pin gas plenum pressurization | M | L | L | M |
| **Primary Coolant (LBE)** | Density | M | M | H | H |
| | Heat Capacity | M | M | H | H |
| | Thermal conductivity | H | M | M | H |
| | Viscosity | M | M | M | H |
| **Above Core Structures** | Structure material physical properties | L | L | M | H |
| | Geometry change due to temperature distribution | L | L | L | H |
| | Feedback reactivity | L | L | L | H |
| | Pressure losses | L | L | L | H |
| **Barrel** | Structure material physical properties | L | L | L | H |
| | Flow distribution | L | L | L | M |
| | Thermal stratification | L | L | M | M |
| | Pressure losses | M | M | M | H |
| **Hot Plenum** | 3D velocity field | L | L | L | M |
| | 3D temperature field and stratification | L | L | L | M |
| | Pressure losses | L | L | L | M |
| **Cold Plenum** | 3D velocity field | L | L | L | M |
| | 3D temperature field and stratification | L | L | L | M |
| | Pressure losses | L | L | L | M |
| **PHX** | Entrance pressure losses | M | M | L | M |
| | Bundle friction pressure losses | L | M | M | H |
| | Grid pressure losses | L | M | M | H |
| | Exit pressure losses | L | M | M | H |
| | Material physical properties of steel | L | L | L | H |

| | | | | | |
|---|---|---|---|---|---|
| | Heat transfer from LBE to PHX tubes | L | L | H | H |
| **Primary Pumps** | Head | H | | | H |
| | Inertia - Coast down | M | L | | H |
| | Mechanical failure | H | | | L |
| | Pressure losses | H | H | H | M |
| **Connecting pipes top (CB & PHXs)** | Distributed pressure losses | L | L | L | H |
| | Local pressure losses | L | L | L | H |
| **Connecting pipes bottom (PHXs & PPs)** | Thermosiphon effect | L | M | M | M |
| | Distributed pressure losses | L | L | L | H |
| | Local pressure losses | L | L | L | H |
| **IVFS** | Decay heat | L | L | M | H |
| **Instrumentation & Control** | Event detection | H | | | H |
| | Signal logic delay time | H | | | H |
| | CR/SR insertion time - Delay of reactivity insertion | H | | | H |
| | Rate of scram reactivity insertion | H | | | H |
| **Potential energy** | Stored potential energy (LBE free surface level) | H | M | | H |

***Table 53 PCRW PIRT results***

| **Component** | **Phenomenon** | **IMP** | | | **SOK** |
|---|---|---|---|---|---|
| | | **I** | **II** | **III** | |
| **Core** | Fission reaction | H | | | H |
| | Direct heating of internal structures (gamma heating) | L | L | L | H |
| | Radiation heating of the coolant due to polonium activation | L | L | L | M |
| | Decay heat | L | H | H | H |
| | Space-dependent (3D) neutronics behavior | M | L | | M |
| | Doppler reactivity feedback | H | L | | H |

| | | | | | |
|---|---|---|---|---|---|
| | Axial expansion reactivity feedback | H | L | | M |
| | Coolant density reactivity feedback | M | L | | H |
| | Reactivity feedback due to structural material thermal dilatation | M | L | | M |
| | Radial and axial power distribution | H | | | M |
| **FA** | Peaking factors | H | | | M |
| | Fuel thermal properties | H | H | H | M |
| | Stored energy in the pin (fuel heat capacity) - Heat capacity of core assemblies | H | H | M | M |
| | Clad conductivity | L | L | L | H |
| | Cladding heat capacity | L | L | L | H |
| | Gap conductance between fuel and cladding | H | M | L | M |
| | Distributed friction losses (Pressure losses) | L | H | H | H |
| | FA inlet pressure losses | L | M | M | H |
| | FA outlet pressure losses | L | M | M | H |
| | Core restrain system (Pressure losses) | L | M | M | M |
| | Convection heat transfer between the pin and the LBE in the bundle | M | M | M | M |
| | Convection radial heat transfer between FA (inter-assembly) | L | L | L | M |
| **Pin** | Clad oxidation | L | L | L | M |
| | Pin power | H | H | H | H |
| | Intra-assembly flow distribution | L | L | L | H |
| | Pin gas plenum pressurization | H | H | L | M |
| | PCMI (Pellet-Cladding Mechanical Interaction) | H | H | | M |
| **Fuel Pellet** | Radial thermal expansion | H | M | L | H |
| | Heat storage and conduction | H | H | H | M |
| | Radial relocation of fuel fragments | H | H | H | M |
| **Clad** | Clad radial thermal expansion | H | H | | M |
| | Expansion due to gas plenum pressurization | H | H | | M |

| | | | | | |
|---|---|---|---|---|---|
| **Primary Coolant (LBE)** | Density | L | M | H | H |
| | Heat Capacity | L | L | L | H |
| | Thermal conductivity | L | M | M | H |
| | Viscosity | L | M | M | H |
| **Above Core Structures** | Structure material physical properties | L | L | M | H |
| | Geometry change due to temperature distribution | L | L | L | H |
| | Feedback reactivity | L | L | L | H |
| | Pressure losses | L | L | L | H |
| **Barrel** | Structure material physical properties | L | L | L | H |
| | Flow distribution | L | L | L | M |
| **Primary Pumps** | Head | L | | | H |
| | Inertia - Coast down | | M | | H |
| | Pressure losses | L | H | H | M |
| **Instrumentation & Control** | Event detection | H | | | H |
| | Signal logic delay time | H | | | H |
| | CR/SR insertion time - Delay of reactivity insertion | H | | | H |
| | Rate of scram reactivity insertion | H | | | H |
| **Potential energy** | Stored potential energy (LBE free surface level) | | H | | H |

***Table 54 PDB PIRT results***

| **Component** | **Phenomenon** | **IMP** | | | **SOK** |
|---|---|---|---|---|---|
| | | **I** | **II** | **III** | |
| **Core** | Fission reaction | L | | | H |
| | Direct heating of internal structures (gamma heating) | L | L | L | H |
| | Radiation heating of the coolant due to polonium activation | L | L | L | M |
| | Decay heat | H | H | H | H |
| | Radial and axial power distribution | H | M | M | M |

| | | | | | |
|---|---|---|---|---|---|
| **FA** | Peaking factors | H | M | M | M |
| | Geometry pin tolerance | M | M | M | M |
| | Geometry wire tolerance | M | M | M | M |
| | Fuel thermal properties | M | M | L | M |
| | Stored energy in the pin (fuel heat capacity) - Heat capacity of core assemblies | M | M | L | M |
| | Clad conductivity | M | M | M | H |
| | Cladding heat capacity | L | L | L | H |
| | Gap conductance between fuel and cladding | M | M | L | M |
| | Distributed friction losses (Pressure losses) | H | H | H | H |
| | FA inlet pressure losses | M | M | M | H |
| | FA outlet pressure losses | M | M | M | H |
| | Core restrain system (Pressure losses) | H | H | M | M |
| | Convection heat transfer between the pin and the LBE in the bundle | H | M | M | M |
| | Convection radial heat transfer between FA (inter-assembly) | L | L | L | M |
| **Pin** | Clad oxidation | L | L | L | M |
| | Pin power | H | H | H | H |
| | Intra-assembly flow distribution | L | L | L | H |
| | Pin gas plenum pressurization | M | M | L | M |
| **Primary Coolant (LBE)** | Density | M | M | H | H |
| | Heat Capacity | M | M | H | H |
| | Thermal conductivity | H | M | M | H |
| | Viscosity | M | M | M | H |
| **Above Core Structures** | Structure material physical properties | L | L | M | H |
| | Geometry change due to temperature distribution | L | L | L | H |
| | Feedback reactivity | L | L | L | H |
| | Pressure losses | L | L | L | H |

| | | | | | |
|---|---|---|---|---|---|
| **Barrel** | Structure material physical properties | L | L | L | H |
| | Flow distribution | M | M | M | M |
| | Thermal stratification | M | M | M | M |
| | Pressure losses | H | M | M | H |
| **Hot Plenum** | 3D velocity field | H | M | M | M |
| | 3D temperature field and stratification | H | M | M | M |
| | Pressure losses | M | M | M | M |
| **Cold Plenum** | 3D velocity field | L | L | L | M |
| | 3D temperature field and stratification | L | L | L | M |
| | Pressure losses | M | M | M | M |
| **Diaphragm** | Break pressure loss | H | H | M | L |
| | Distributed pressure losses | H | H | M | H |
| **PHX** | Entrance pressure losses | M | M | L | M |
| | Bundle friction pressure losses | M | M | L | H |
| | Grid pressure losses | M | M | L | H |
| | Exit pressure losses | M | M | L | H |
| | Material physical properties of steel | L | L | L | H |
| | Heat transfer from LBE to PHX tubes | L | L | H | H |
| **Primary Pumps** | Head | M | | | H |
| | Inertia - Coast down | M | M | | H |
| | Pressure losses | M | M | M | M |
| **Connecting pipes top (CB & PHXs)** | Distributed pressure losses | L | L | L | H |
| | Local pressure losses | L | L | L | H |
| **Connecting pipes bottom (PHXs & PPs)** | Thermosiphon effect | L | M | M | M |
| | Distributed pressure losses | L | L | L | H |
| | Local pressure losses | L | L | L | H |

| | | | | | |
|---|---|---|---|---|---|
| **IVFS** | Decay heat | L | L | L | H |
| **Instrumentation & Control** | Event detection | H | | | H |
| | Signal logic delay time | H | | | H |
| | CR/SR insertion time - Delay of reactivity insertion | H | | | H |
| | Rate of scram reactivity insertion | H | | | H |
| **Potential energy** | Stored potential energy (LBE free surface level) | H | H | | H |

## 5.3.HEXACOM

In the MYRRHA project, the PHX forms the critical boundary between the nuclear core and the secondary water-steam circuit. It features a double-walled bayonet tube design with intermediate helium leak detection. Although this concept has been proposed for nuclear use since the 1960s and is well established in industrial applications, detailed performance data in nuclear conditions remain limited.

To fill this gap, SCK CEN developed an integrated test facility by coupling the existing COMPLOT (COMPonent LOop Testing) LBE loop with the newly constructed HEXACOM (Heat EXchAnger at COMplot) water/steam loop. This combined setup enables full-scale testing of a single-tube PHX prototype representative of MYRRHA's design. In this configuration, the HEXACOM circuit replicates the reactor's secondary system, while COMPLOT provides the LBE coolant for the primary side. The two circuits are connected via configurable double-wall bayonet tubes.

### *5.3.1. Description of the facility*

The HEXACOM facility [119] has the main goal to evaluate the thermal-hydraulic performance of different PHX layouts under representative operating conditions. It also supports the development and validation of heat transfer correlations specific to bayonet tubes in LBE environments. Additionally, the facility allows investigation of steam/water-side thermal-hydraulics at low pressure (<20 bar) and provides a testbed for analysing system stability, full-power behaviour, and decay heat removal (DHR). The general arrangement of HEXACOM is depicted in Figure 131.

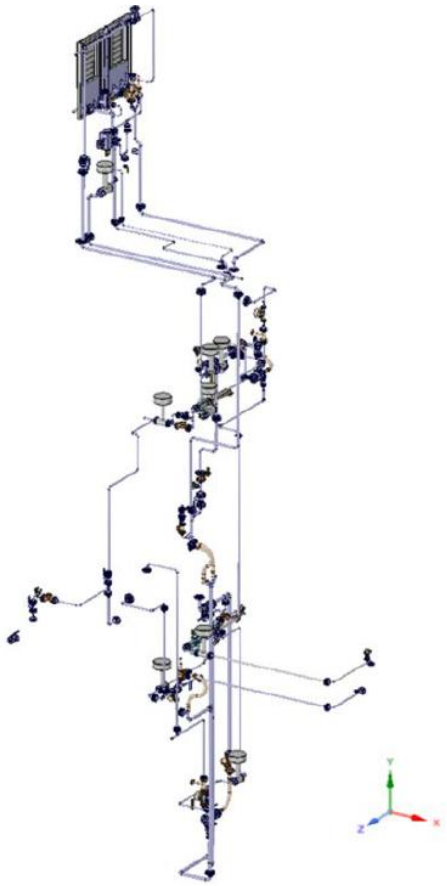

***Figure 131 HEXACOM general arrangement [119]***

A simplified P&ID of the open loop setup is shown in Figure 132.

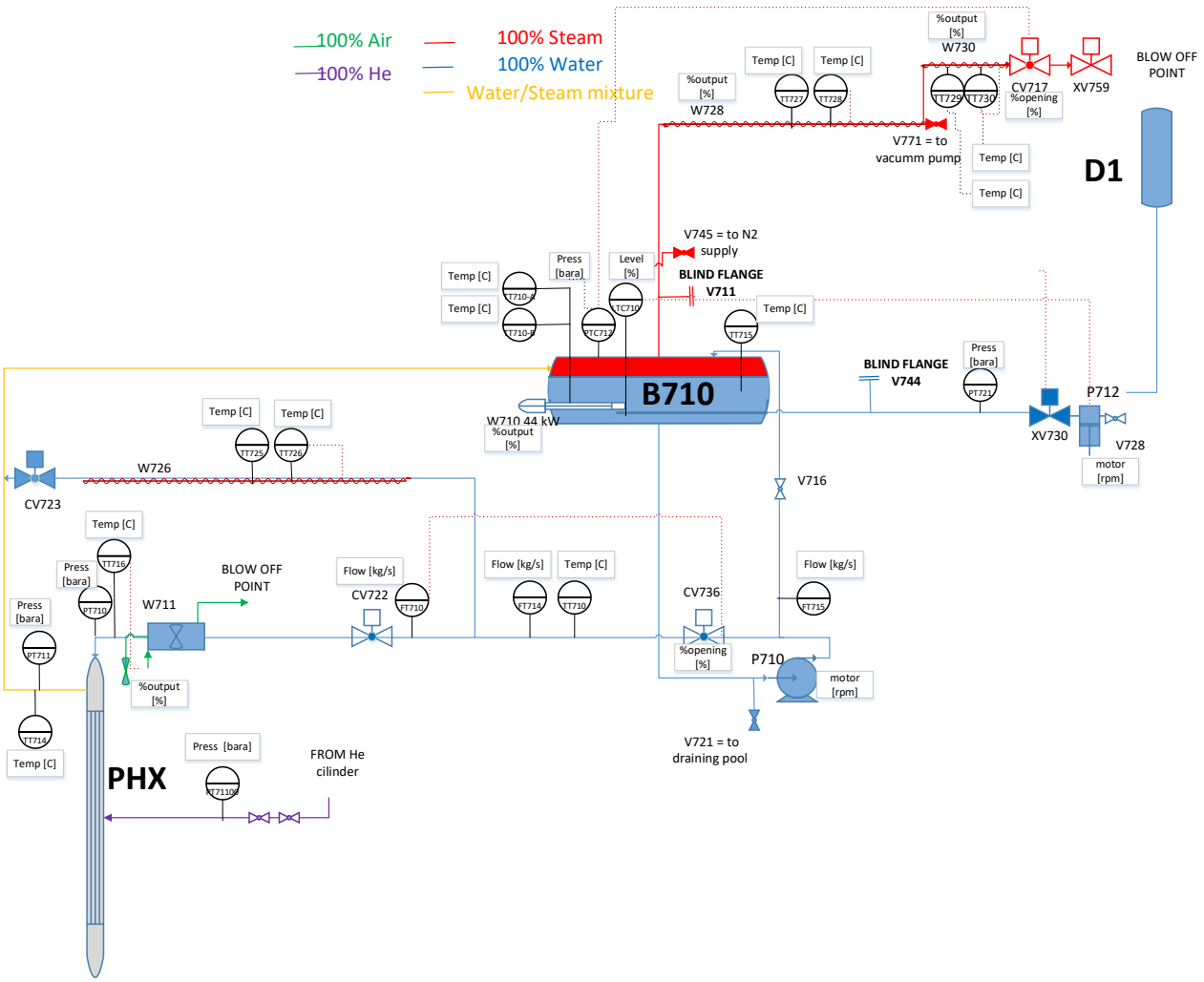


***Figure 132 Simplified diagram of the HEXACOM facility [119]***

The main loop includes:

- The PHX test section
- The Steam Drum Separator, SDS (B710)
- The Condensate Tank, CT (B712, not shown – used in closed loop mode)
- The electrical heaters located into B710 (W710)
- Two main pumps:
  - P710 recirculates the water into B710 and feeds the PHX
  - P711 recirculates the water into B712 and feeds B710 (not shown– used in closed loop mode)
  - P712 is charging pump to reintegrate water from demineralized water tank (D1) to B710
- The air cooler (W711)
- Control Valves (CV717, CV722, CV723 and CV736)
- The pipelines for connection
- Instrumentation (thermocouples, pressure transducers, level meters, and flow meters)
- Trace heating on few specific lines
- The demineralized water line and tank (D1)
- The main condensers (W712 A-B, not shown– used in closed loop mode)

As mentioned above, the main component and test section of HEXACOM is the PHX which is intended to support the design of MYRRHA PHX. The PHX of HEXACOM consists of a single double wall bayonet tube of which external walls are coupled with impingement and contains helical cavities with the height 1:1 with respect to the full scale of about 4.5 m. The PHX is shown in Figure 133.

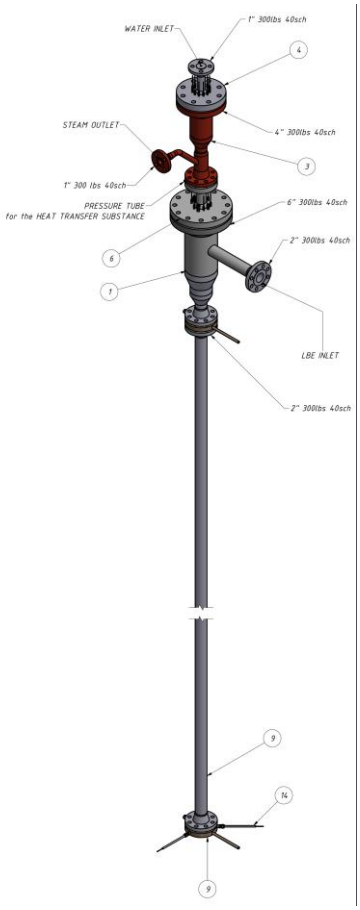


***Figure 133 PHX drawings***

The other key relevant HEXACOM component, namely the SDS (B710) (depicted in Figure 134) is essentially a horizontal vessel with central cylindrical body enclosed with two semi-elliptical lateral heads with a volume of about 650 l. Its design power, pressure and temperature are, respectively, 100 kW, 25 bar and 250°C. The main functions of the SDS include separating the steam and water mixture exiting the PHX, releasing single-phase steam to the environment or to the air coolers in closed-loop mode, and collecting water from the bypass-overflow line of pump P710. Additionally, the SDS delivers water to the feed pump P710 and regulates system pressure through a 44-kW horizontal heater (W710). It is also equipped with safety valves for pressure relief in the event of overpressure.

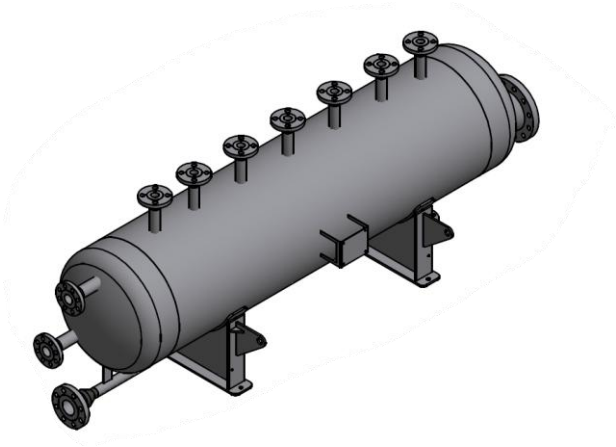

***Figure 134 SDS drawings***

The loop is designed to operate in the following ways:

- Stand-Alone Open Loop
- Open Loop with COMPLOT
- Stand-Alone Closed Loop
- Closed Loop with COMPLOT

This work focuses on the Stand-Alone open loop operation of the HEXACOM facility. In this configuration, the main circulation pump (P710) runs at nominal speed, delivering flow that is split between the PHX and a bypass line. The mass flow rate to the PHX is regulated by control valve CV736. As COMPLOT is inactive, no steam is produced in the PHX—water enters and exits in liquid phase, returning to the B710 tank. If needed, the PHX inlet temperature can be adjusted via the air cooler W711.

The primary heat source is the 44 kW electric heater (W710) inside the B710 tank. Steam generated here is separated: liquid recirculates via P710, while steam is vented through a steam line regulated by CV717, responding to pressure at the top of B710. Water losses are replenished by pump P712, drawing from reservoir D1.

For safety, the PHX bypass valve (CV723) remains normally closed but opens automatically during a station blackout, while CV722 closes, to prevent cold water from contacting LBE. Trace heating is applied on the bypass and steam lines to prevent condensation-induced and steam-drive water hammer. Finally, the main parameters of HEXACOM facility are summarized in Table 55.

*Table 55 HEXACOM loop operating conditions*

| **HEXACOM LOOP PERFORMANCES** | | |
|---|---|---|
| **Parameter** | **Value** | **Unit** |
| **Design pressure** | 25 | bar |
| **Design temperature** | 250 °C | °C |
| **SDS design power** | 100 | kW |
| **P710 maximum flow rate** | 12 | $m^3/h$ |
| **P711 maximum flow rate** | 18 | $m^3/h$ |
| **Operating pressure** | 16 | bar |
| **PHX inlet temperature** | 196.5 | °C |
| **PHX outlet quality** | 0.3 | - |
| **HEXACOM LOOP WITH PHX TEST SECTION** | | |
| **Parameter** | **Value** | **Unit** |
| **Thermal power** | 37 | kW |
| **Pressure at PHX inlet** | 16.0 | bar |
| **PHX inlet temperature** | 196.5 | °C |
| **PHX outlet temperature** | 200.0 | °C |
| **PHX outlet quality** | 0.3 | - |
| **PHX inlet mass flow rate** | 0.0619 | kg/s |
| **Pressure at SDS top** | 15.1 | bar |
| **Maximum mass flow at P710 outlet** | 2.700 | kg/s |
| **Minimum mass flow at P710 outlet** | 0.320 | kg/s |
| **LBE inlet mass flow** | 4.609 | kg/s |
| **LBE inlet temperature** | 275.0 | °C |
| **LBE outlet temperature** | 221.0 | °C |

### 5.3.2. Experiment description

To support the qualification of the RELAP5 numerical model and the performance evaluation of the MYRRHA PHX, an experimental campaign was carried out on HEXACOM facility in July 2024. This test campaign aimed to provide high-quality data under controlled conditions, representative of selected operating scenarios relevant to MYRRHA.

The experimental setup was designed to replicate the thermal-hydraulic behaviour of the PHX, with particular focus on the heat transfer mechanisms within the water/steam loop. The following section provides a detailed description of the test configuration, boundary conditions, instrumentation layout, and key measured parameters, serving as a benchmark for the validation of the numerical models developed in this study.

The main objectives achieved in this experiment and analysed deeply are the following: First (O1), the operational state known as "RUNNING mode" was successfully reached, meaning the system operated at full pressure (nominally 16 bar) while releasing steam from the plant. Second (O2), the loop was maintained in the "HOT STANDBY mode" for at least three hours, demonstrating operation at full pressure without steam release. Third (O3), the experiment confirmed the system's capability to perform refilling operations via pump P712. Finally (O4), a step ramp-up to the maximum power of heater W710 was successfully executed.

It should be noted that in this test, HEXACOM is not coupled with COMPLOT, therefore the facility has been operated as Stand-Alone Open Loop (for more details, see Section 5.3.1).

The start-up phase of the HEXACOM facility (O1) represents a critical operational sequence aimed at gradually bringing the system to its nominal "RUNNING mode" under controlled thermal and pressure conditions. This phase ensures the safe pressurization and thermal stabilization of the water/steam circuit, which is essential prior to initiating steady-state operation or executing transient scenarios.
The following describes the sequence in detail, along with the main operational constraints and outcomes. During the start-up, a double-phase control logic was implemented, resulting in a total duration of approximately 12.5 hours to achieve full operating pressure, as illustrated in Figure 135. Initially, the system was heated at constant power until reaching a temperature of 100 °C. Subsequently, a controlled ramp-up of 10 °C/h was applied to gradually increase the pressure at the PHX inlet (pressure transmitter PT710) to approximately 16.0 bar, corresponding to about 15.2 bara at the B710 tank (pressure transmitter PT712).

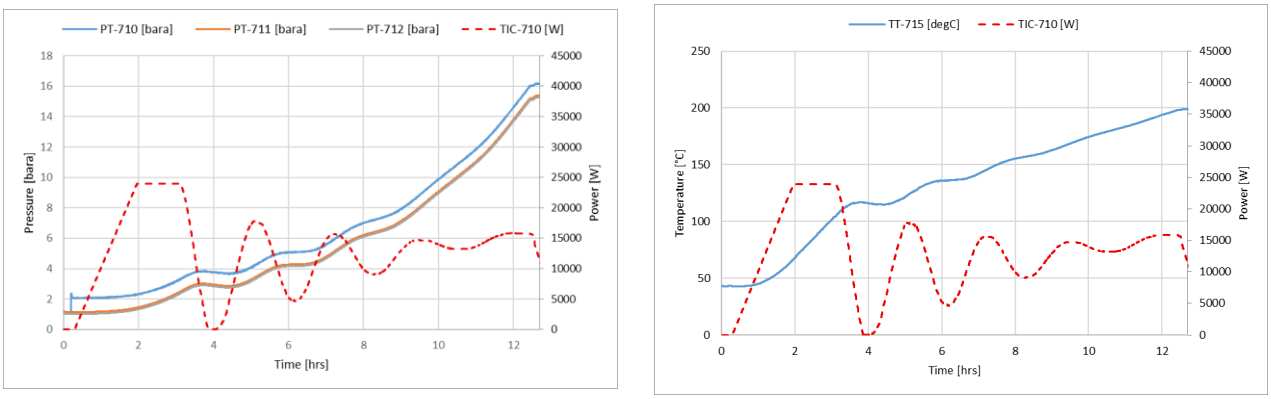


*Figure 135 Pressure vs W710 power (left) and Temperature vs W710 power (right) at start-up phase*

This pressure difference accounts for a measured pressure drop of approximately 0.8 bara across the PHX, primarily due to local instrumentation and flow resistance, as shown in Figure 136. To prevent exceeding the PHX inlet pressure limit of 16.0 bar, the pressure at B710 was intentionally fixed at 15.2 bara. The execution of the start-up sequence met all predefined operational targets, successfully establishing the "RUNNING" condition (release of steam) required for subsequent testing phases.

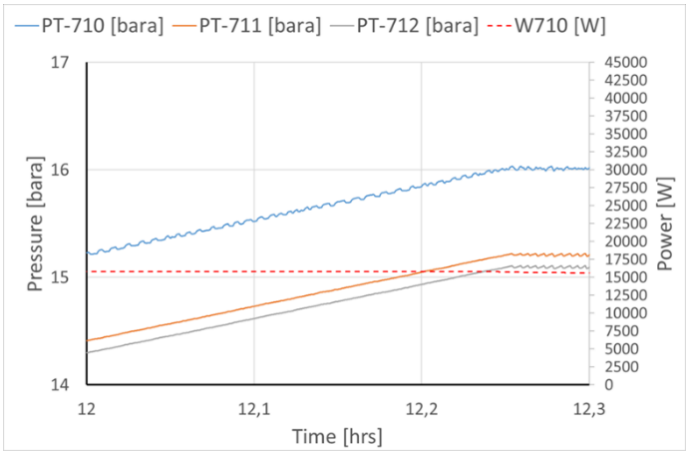


***Figure 136 PHX pressure drop during start-up phase***

The "HOT STANDBY" mode (O2) was maintained continuously for over seven hours, as shown in Figure 137, with the system temperature stably held at approximately 198.0 °C, exhibiting only minor fluctuations. Notably, this steady condition was achieved without any steam release from the facility, as confirmed by the zero opening of control valve CV717.

The successful execution of this operating mode demonstrates the fulfilment of Objective O2, which was specifically designed to assess the heat loss characteristics of the system by fine-tuning the power input required to maintain thermal equilibrium. In this configuration, the electric heater W710, regulated via the PID controller linked to temperature indicator TT715, served as the only active heat source, while the only heat sink was represented by ambient heat losses.

Since the system was not coupled to any additional cooling or secondary loops, achieving thermal steady-state in this mode confirms that the power supplied precisely compensates for heat losses of the facility. As a result, configuration is readily compatible with coupling to the COMPLOT loop in future integrated tests.

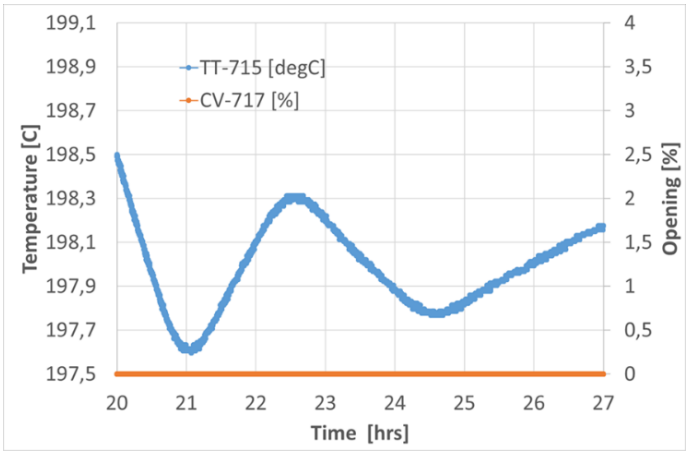


***Figure 137 Hot Standby mode of HEXACOM***

A series of three refill tests were conducted to evaluate the capability of maintaining system pressure and steam generation during water reintegration from reservoir D1 via pump P712, as part of the assessment of Objective O3. The first test (REFILL 1) was executed from HOT STANDBY conditions, as illustrated in Figure 138. In this case, the system's response was insufficient to prevent a pressure fluctuation —approximately a 1 bar reduction recovered in about 30 minutes—, due to the sudden thermal imbalance at low power levels. The second refill test (REFILL 2) was performed during a power ramp-up phase exceeding 22 kW. Under these conditions, it was possible to successfully refill the system while maintaining steam production, provided the P712 pump speed remained between 25–35%.

The third test (REFILL 3) was carried out at constant power (20 kW), again demonstrating that refilling and continuous steam generation are feasible with P712 operating at 25% speed. These results confirm the successful achievement of Objective O3. The key operational insight from these tests is that, to avoid system depressurization during refill operations, the system should operate at a minimum power level of 22 kW, with P712 pump speed not exceeding 35%. This ensures thermal balance and pressure stability while enabling effective water reintegration under realistic operating conditions.

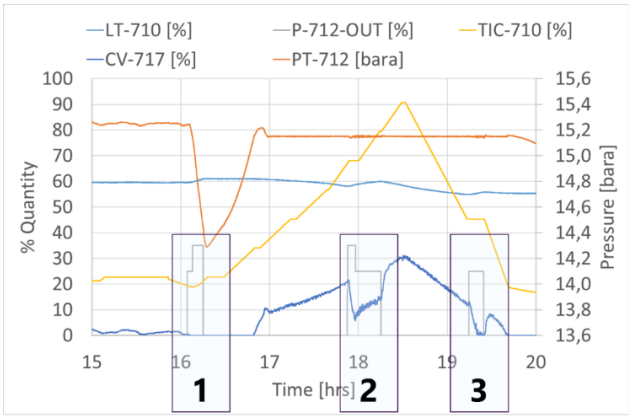


***Figure 138 HEXACOM refill operations***

The power ramp-up test was successfully completed, fulfilling the conditions defined for Objective O4. Throughout the entire ramp, including during simultaneous water refill operations, the pressure control remained remarkably stable, with fluctuations confined within ±0.01 bara (see Figure 139). This precise regulation demonstrates the robustness of the pressure control system, even under dynamic thermal and hydraulic conditions.

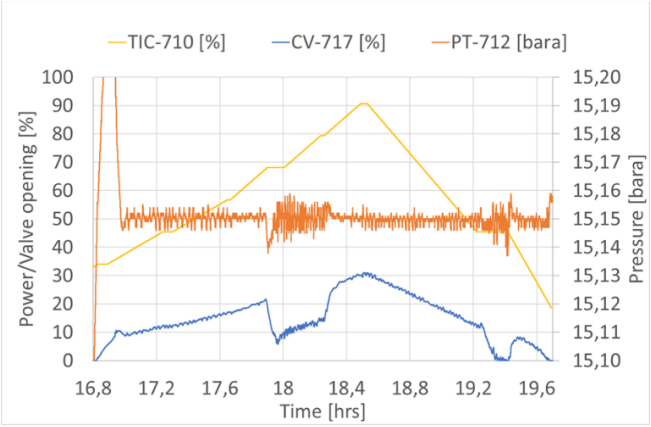


***Figure 139 HEXACOM power ramp up***

### *5.3.3. Numerical model*

The version of RELAP5/Mod3.3 employed in this numerical study has been specifically modified to incorporate the thermo-physical properties of LBE [34] and the corresponding heat transfer correlations [35]. This enhanced version has been successfully applied in post-test analyses and benchmarking exercises [38], demonstrating its capability to accurately reproduce key thermal-hydraulic phenomena observed in LBE experiments, as well as to predict the main trends of relevant operating parameters with a high degree of reliability.

Conversely the other numerical models developed in this research, the qualification procedure described in Section 2.2 was applied to the HEXACOM model [120] to ensure its reliability for steady-state and transient analyses.

The process consists of the following parts: the first presents the application of STEPS 1 to 12. The second covers the implementation of STEP 13, dedicated to the stand-alone qualification of specific components that require individual assessment due to their modelling complexity. Finally, Section 5.3.4 addresses the execution of STEPS 15 to 17, which include steady-state and transient test comparisons as well as the evaluation of heat loss representation within the model.

In the present work, regarding the local verification steps, only the maximum observed error and the corresponding region of the component where this error occurs are reported. Conversely the steps aimed at verifying global limits are presented and discussed. To highlight the importance of model qualification, two RELAP5 models are introduced: one fully qualified according to the described procedure, and one unqualified. The comparison between their simulation results clearly demonstrates the significant impact that proper model qualification has on the accuracy and credibility of the thermal-hydraulic predictions.

The resulting numerical model [120] implemented for this study is illustrated in Figure 140. The numerical model comprises three distinct subsystems, each represented by a different colour (see Figure 140). The purple-coloured control volumes correspond to the LBE-side region of the PHX, which is part of the COMPLOT loop. The green-coloured control volumes represent the air-side of the W711 air cooler, while the pink-coloured control volumes correspond to the water/steam domain of the HEXACOM loop. The average nodalization size of the model is 200 mm with a maximum of about 10% length difference between two adjacent nodes.

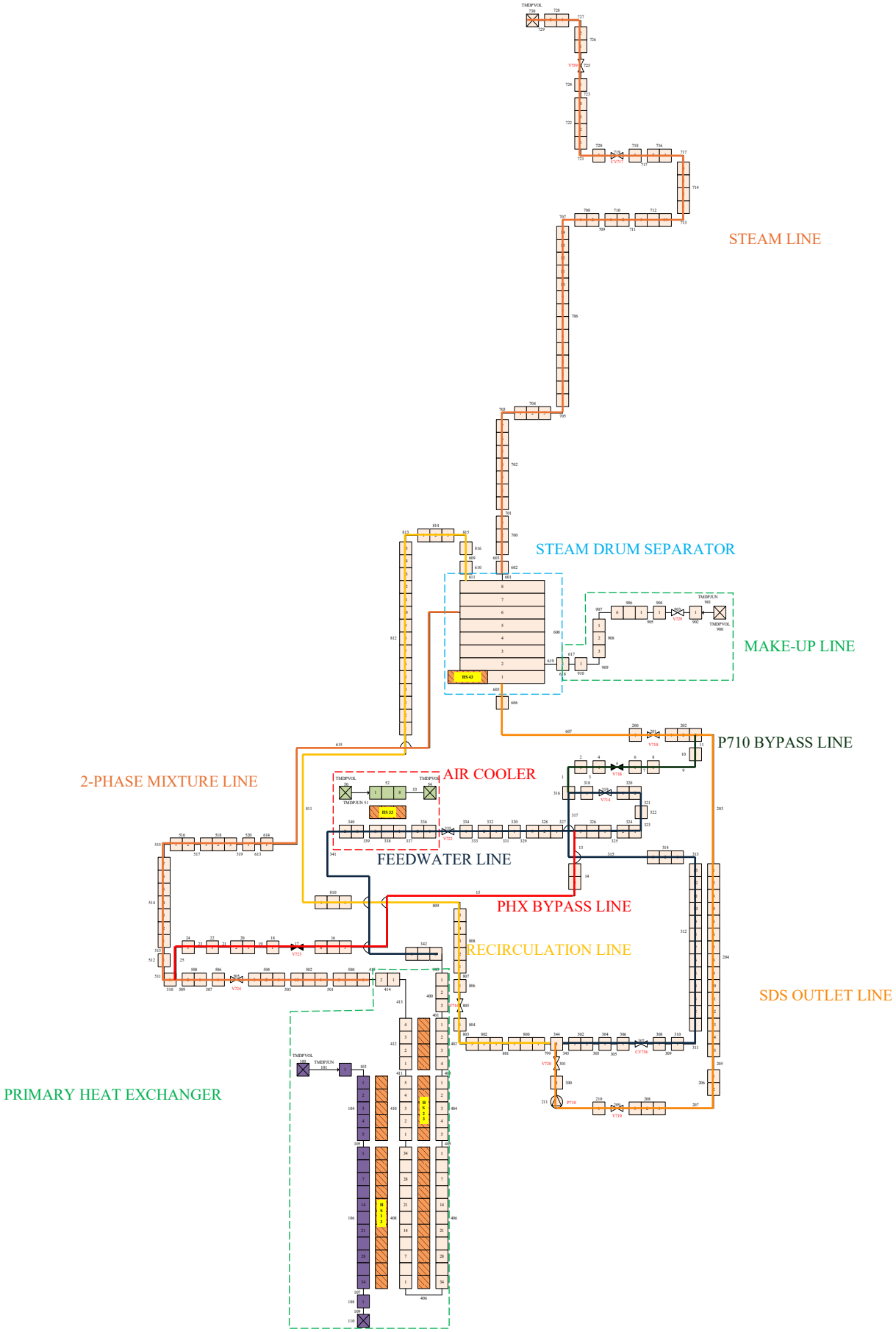


***Figure 140 R5 nodalization scheme of HEXACOM***

The first digit of the hydrodynamic components number identifies a specific system as follows:

- "0XX" for the W711 air side, PHX and P710 bypass line
- "1XX" for the PHX LBE side
- "2XX" for the pipeline between the B710 tank and upstream of P710 pump
- "3XX" for the feedwater line between downstream of P710 pump and PHX inlet
- "4XX" for the PHX water side
- "5XX" for the 2-phase mixture line between PHX outlet and the B710 tank
- "6XX" for the B710 tank and its nozzles
- "7XX" for the steam line between the B710 tank and the environment
- "8XX" for the overflow bypass line between the downstream of P710 pump and the B710 tank
- "9XX" for the make-up line including the D1 tank and P712 pump

The application of the qualification procedure to the RELAP5 model of the HEXACOM facility is supported by a series of comparative tables that quantitatively assess the deviations between the as-built design data, the unqualified numerical model, and the qualified model developed according to the procedure. With regard to the hydraulic domain, the application of the qualification procedure is illustrated in Table 56. Specifically, for STEPS 3 and 4, the elevation changes were identified as follows: the distance between the thermal centres of the PHX and the SDS was used for STEP 3, while for STEP 4, the elevation difference between the bottom of the PHX and the highest point of the HEXACOM loop, corresponding to the steam outlet elevation within the test room, was considered.

***Table 56 Hydraulic qualification***

| | **Region** | **Unqualified model** | **Qualified model** | **Acceptance** |
|---|---|---|---|---|
| **STEP 1** | Line between PHX outlet and the B710 tank | -11% | -11% | ±50% |
| **STEP 2** | All hydraulic components | 0° | 0° | max [±1°; ±3.5%] |
| **STEP 3** | PHX to B710 elevation change | +0.45% | +0.45% | ±0.5% |
| **STEP 4** | PHX to steam outlet elevation change | -0.68% | -0.68% | ±1.0% |
| **STEP 5** | Line between PHX outlet and the B710 tank | -1.49% | -1.49% | ±1.5% |
| **STEP 6** | All hydraulic components | 0% | 0% | ±1.5% |
| **STEP 7** | HEXACOM total volume | +0.002% | +0.002% | ±1.0% |

It is worth noting that no differences were observed between the qualified and unqualified models in this aspect, as the hydraulic section of the input deck did not involve specific modelling assumptions or simplifications that could introduce deviations relative to the as-built configuration. Additionally, the K-loss coefficients related to localized (concentrated) head losses are not predefined and must be explicitly provided by the user. For this purpose, the coefficients were evaluated based on the empirical formulas provided in the Idelchik Hydraulic Handbook [64].

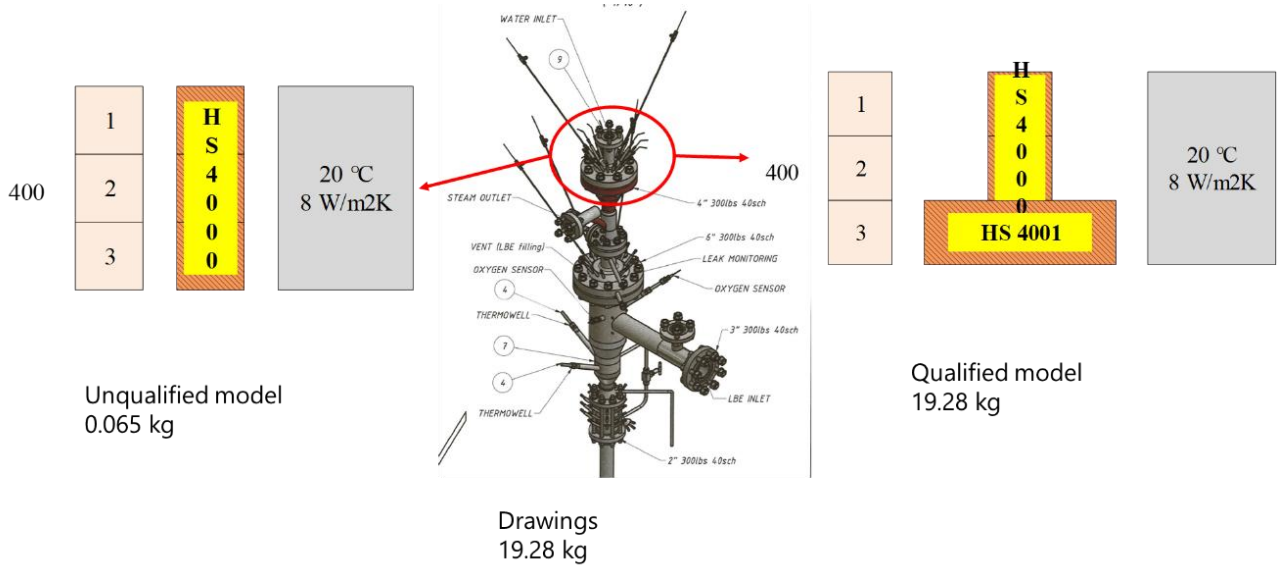


***Figure 141 Methodology of heat structure modelling***

The modelling of passive heat structures—solid parts in contact with the environment not shown in Figure 140—is essential for accurately capturing the system's heat loss behaviour. The standard approach couples each hydrodynamic component to the environment via a heat structure, assigning an ambient temperature and fixed HTC. This heat structure is discretized with axial nodes matching the hydrodynamic component's control volumes.

However, this method only considers heat conduction through the pipe wall and ignores additional thermal masses such as flanges, vessel heads, supports, and instrumentation housings outside the pipe geometry. This simplification causes a non-negligible error in estimating total thermal inertia compared to the as-built configuration. To overcome this, the qualified model uses an improved method where each hydrodynamic component is coupled with two heat structures: one reflecting the pipe wall's actual geometry, and a second with an artificially increased outer radius to represent external thermal masses.

This ensures the model's total thermal mass aligns with the physical system. Figure 141 illustrates the difference between the standard (left) and qualified (right) approaches, showing how the unqualified model underestimates thermal mass relative to as-built data, justifying the enhanced method. Table 57 presents the impact of this qualification, reporting relative deviations between as-built data, unqualified, and qualified models. Unlike hydraulics, a notable difference exists between the two thermal modelling approaches. The conventional model neglects external thermal masses, leading to a substantial underestimation of total solid mass compared to the real system.

Consequently, the unqualified model fails to meet the acceptance criteria in STEP 8 and STEP 10 of the qualification procedure, which demand thermal mass agreement within a margin. Only the qualified model satisfies these criteria by including the additional thermal structure with a fictitious radius to represent external masses.

***Table 57 Heat transfer qualification***

| | Region | Unqualified model | Qualified model | Acceptance |
|---|---|---|---|---|
| **STEP 8** | Line between PHX outlet and the B710 tank | -90.86% | -0.78% | ±2.5% |
| **STEP 9** | Line between PHX outlet and the B710 tank inner surface | -1.49% | -1.49% | ±1.5% |
| | Feedwater line between downstream of P710 pump and PHX inlet outer surface | -23.69% | -0.47% | ±5.0% |
| **STEP 10** | HEXACOM total mass | -46.517% | +0.002% | ±2.0% |
| **STEP 11** | HEXACOM total inner surface | +0.002% | +0.002% | ±1.0% |
| | HEXACOM total outer surface | -2.94% | -0.03% | ±4.0% |

The active heat structures refer to all solid components involved in heat transfer not directly interacting with the environment, such as the internal walls of heat exchangers or electrically heated elements. These structures play a fundamental role in modelling the heat transfer dynamics within the system and are schematically represented in Figure 140.

In particular, HS 13 and HS 23, together with their associated hydrodynamic components (1XX and 4XX), constitute the PHX. The HS 33 structure models the wall of the air cooler W711, which functions as a pure counter-current heat exchanger, coupling the forced air flow (PIPE 52) with the water flowing through PIPE 338. Lastly, HS 43 represents the electric heating rods W710, which are located within the SDS and are responsible for providing the primary thermal input during standalone operations. The HTC in the LBE side is evaluated by Seban-Shimazaki correlation [36] suitable for tube internal flow.

Moreover, in accordance with STEP 12 of the qualification procedure, the thermo-physical properties of the construction materials were referenced as follows: properties for AISI 316L and AISI 304L, which constitute the HEXACOM piping and PHX tubes, were taken from [62]; data for helium, used in the double-wall bayonet tube of the PHX, were sourced from [58]; and properties for Rockwool, employed as thermal insulation around the piping, were obtained from [121].

Finally, all valves within the loop are represented using VALVE components, with particular emphasis on the control valves CV736 and CV717. The pump P710 is modelled as a PUMP component. Conversely, the pump P712, located on the makeup line, is modelled as a TMDPJUN component (TMDPJUN 901, see Figure 140), where the mass flow rate profile is explicitly defined by the user. Finally, in both models, the environmental boundary conditions were defined by imposing a constant ambient temperature of 20 °C and a convective HTC of 8 W/m²K.

Next, the stand-alone qualification of specific components in accordance with STEP 13 of the adopted qualification procedure was performed. Certain elements within the RELAP5 model require individual treatment due to their intrinsic complexity or because their behaviour cannot be directly validated through global system metrics.

These components include, for example, control valves, pumps, and non-conventional heat exchangers, whose performance must be assessed separately by comparing simulation results against manufacturer data, empirical correlations, or dedicated experimental results, when available. The objective of this step is to demonstrate that the numerical model is capable of correctly representing the local behaviour of these components under the expected operating conditions of the facility.

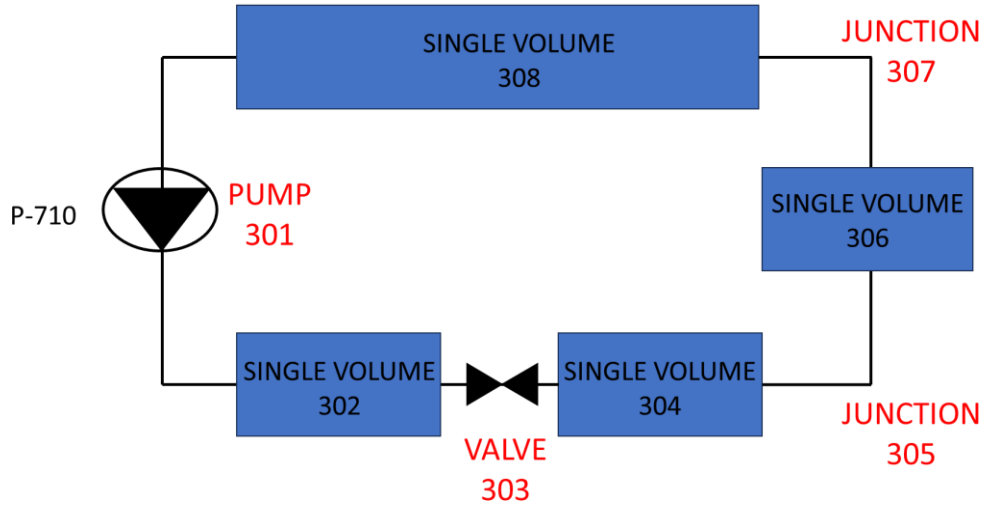


***Figure 142 P710 stand-alone model***

The first component subjected to the stand-alone qualification procedure is the P710 pump. The corresponding stand-alone numerical model is illustrated in Figure 142 and consists of a closed-loop system comprising the pump under investigation and a control valve.

The loop is initialized with the nominal operating conditions of HEXACOM, specifically with liquid water at 16 bar and 198 °C, and the valve initially set to a fully open position. During the transient simulation, the valve is gradually closed to induce a variation in flow rate across the pump. The main outcome of this simulation is the homologous head and torque versus flow rate curves, as computed by RELAP5.

These curves are then compared to the performance data provided by the pump manufacturer, as shown in Figure 143. Since the RELAP5-predicted curves fall entirely within the envelope defined by the supplier data, the numerical representation of the P710 pump is considered successfully qualified.

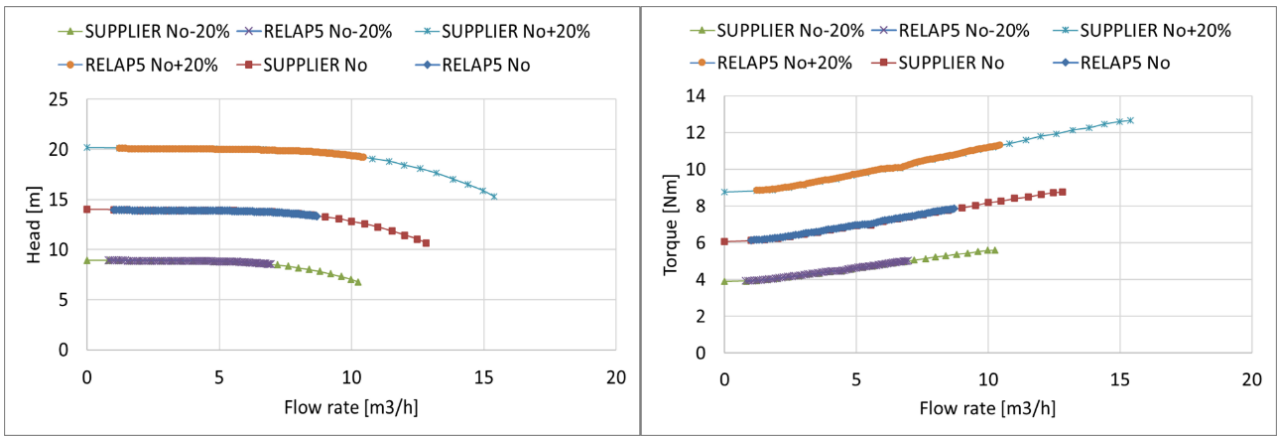


***Figure 143 P710 simulation results***

The next component subjected to stand-alone qualification is the CV736 control valve, which regulates the feed-water flow rate through the PHX. The dedicated stand-alone numerical model used for this purpose is shown in Figure 144. The model is initialized with liquid water at 16 bar and approximately 190 °C, consistent with HEXACOM's operating conditions. The objective of the simulation is to verify the flow rate across the valve as a function of its degree of opening, under a fixed pressure drop across the component.

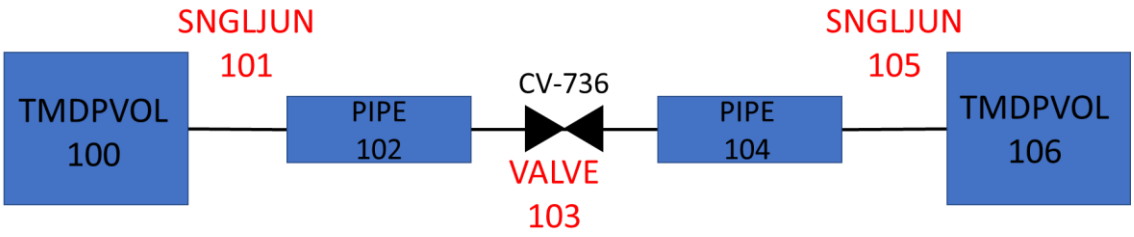


***Figure 144 CV736 stand-alone model***

As illustrated in Figure 145, a direct comparison with supplier-provided reference data revealed the need for model calibration. To accurately replicate the valve's behaviour, a correction factor of approximately 1.18 was applied to the Cv coefficient. This tuning step was necessary to align the numerical predictions with the known physical characteristics of the valve. It is important to note that the un-tuned version of the valve model is used in the unqualified HEXACOM configuration, while the corrected version is integrated into the qualified model.

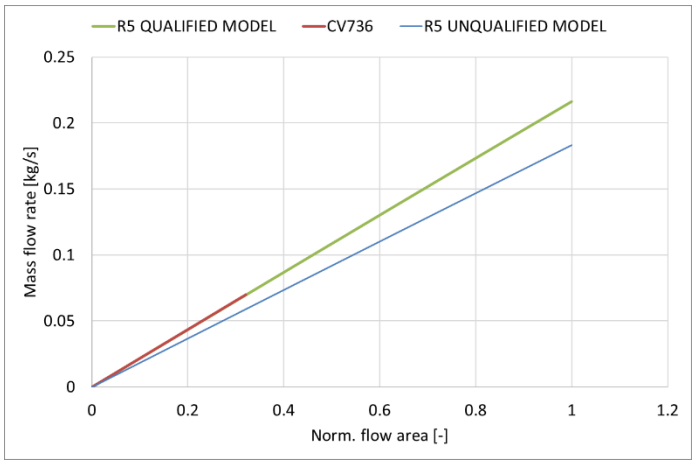


***Figure 145 CV736 simulation results***

The following component evaluated through stand-alone qualification is the CV717 control valve, which is responsible for regulating the pressure within the loop. The stand-alone numerical model of the valve is illustrated in Figure 146. In this configuration, the upstream control volumes are initialized with saturated steam at 16 bar, while the downstream volumes contain air at ambient pressure and temperature, replicating the boundary conditions representative of venting scenarios. As with the previously qualified CV736 valve, the same modelling approach and validation methodology were adopted.

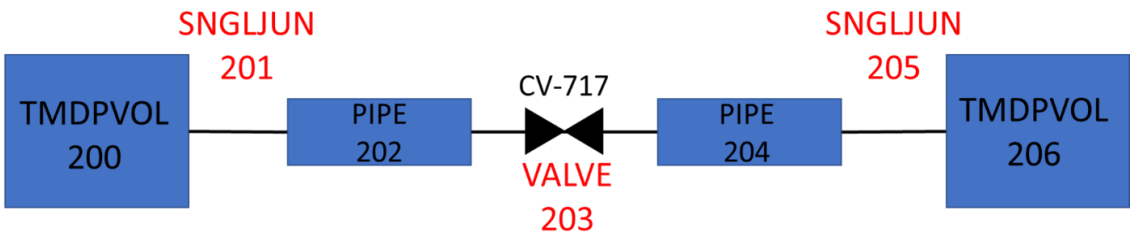


***Figure 146 CV717 stand-alone model***

The results of the simulation, shown in Figure 147, revealed a deviation between the valve's numerical behaviour and the performance data provided by the manufacturer. To correct this discrepancy, a Cv correction factor of approximately 0.67 was applied. This adjustment was necessary to align the simulated flow behaviour with the expected performance characteristics. As in the previous case, the un-tuned version of the valve is retained in the unqualified HEXACOM model, whereas the corrected version is integrated into the qualified model.

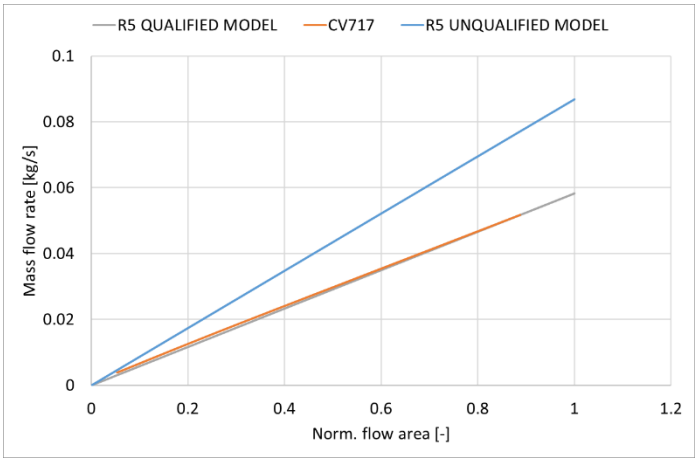


***Figure 147 CV717 simulation results***

The final component subjected to stand-alone qualification is the PHX of HEXACOM facility. The corresponding numerical model is shown in Figure 148, where the blue-coloured control volumes represent the water side, and the orange-coloured volumes correspond to the LBE side. The feed-water inlet is modelled using TMDPVOL 398, which imposes pressure and temperature boundary conditions, and TMDPJUN 399, which prescribes the mass flow rate. The water enters the PHX and exits as a two-phase mixture toward TMDPVOL 416. On the LBE side, the boundary conditions—temperature, pressure, and flow rate—are imposed through TMDPVOL 100 and TMDPJUN 101. The PHX riser, modelled by PIPE 408 and PIPE 410, is thermally coupled to the LBE channel via heat structure HS 1001, which includes a multilayer wall composed of stainless steel and helium, representing the double-wall bayonet tube. In addition, heat structure HS 1002 models the regenerative heat transfer between the down-comer and the riser.

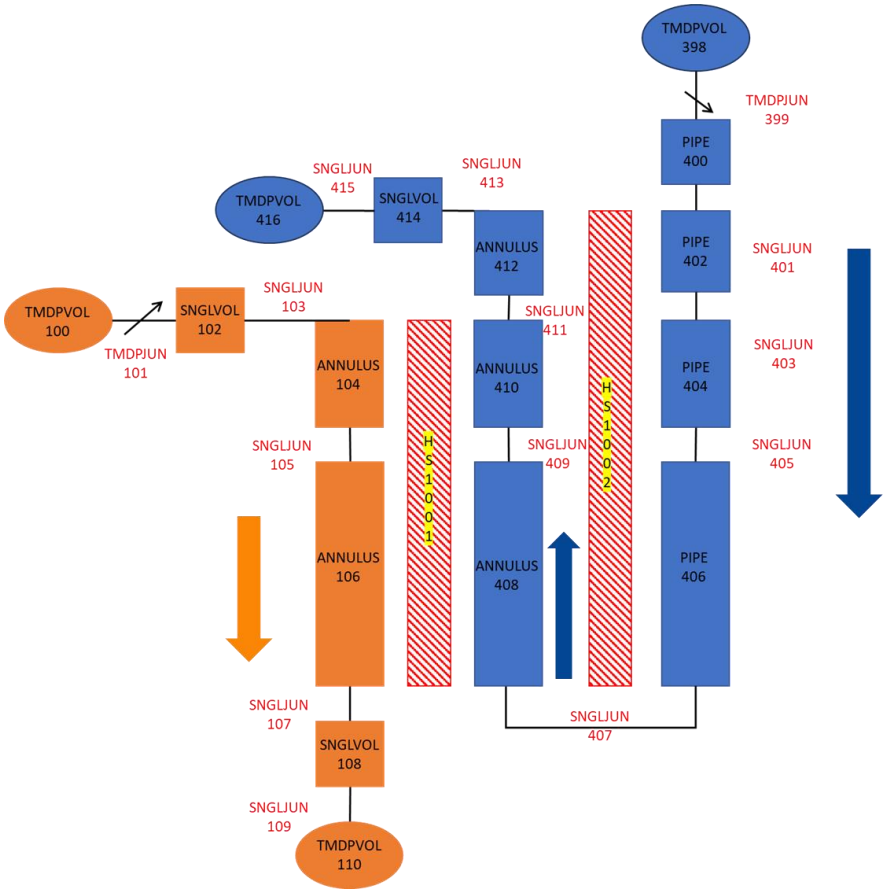


***Figure 148 PHX stand-alone model***

Finally, Table 58 presents the steady-state results of the stand-alone simulation of the PHX. The main outcomes include the outlet conditions of both working fluids and the thermal power transferred within the heat exchanger. The comparison reveals a negligible deviation between the predictions of the numerical model and the nominal design data of the PHX. Based on these results, the HEXACOM PHX numerical model is successfully qualified.

***Table 58 PHX simulation results***

| Parameter | Unit | Nominal data | RELAP5 | Error |
|---|---|---|---|---|
| **Thermal power** | kW | 37 | 36.99 | -0.03% |
| **LBE inlet temperature (BC)** | °C | 275 | 275 | / |
| **LBE mass flow rate (BC)** | kg/s | 4.609 | 4.609 | / |
| **LBE outlet temperature** | °C | 221 | 221.6 | 0.6 °C |
| **Water inlet temperature (BC)** | °C | 196.5 | 196.5 | / |
| **Water mass flow rate (BC)** | kg/s | 0.0619 | 0.0619 | / |
| **Steam outlet quality** | - | 0.3 | 0.297 | -1% |

### *5.3.4. Simulation results*

This section provides a comparative assessment of the qualified and unqualified RELAP5 models developed for the HEXACOM facility, with the objective of quantifying the impact of model qualification on the accuracy of numerical predictions. The analysis is organized according to the final phases of the qualification procedure, specifically STEP 16 (transient validation), STEP 15 (steady-state validation), and STEP 17 (heat loss assessment).

For each of these steps, a representative experimental test is selected to serve as a reference, chosen for its relevance to the operating conditions of the facility and its suitability in reproducing the thermal-hydraulic behaviour under investigation. In each case, a set of key parameters is identified and monitored, and the simulation results are systematically compared with the corresponding experimental measurements.

In addition, the code user is expected to define acceptance criteria tailored to each scenario, ensuring consistency with the experimental uncertainty, the relevance of the physical phenomena, and the objectives of the test. This structured and traceable methodology enables a robust evaluation of model performance and highlights the advantages introduced by the qualification process. With reference to STEP 16, the experimental case, the selected parameters, and the corresponding acceptance criteria are summarised in Table 59.

***Table 59 STEP 16 parameters***

| **Test** | **Key parameter** | **Acceptance** |
|---|---|---|
| **O1-phase (HEXACOM start-up)** | Time interval from cold to 16 bar | ± 10% |
| | Trend of the PHX pressure drop (difference between PT-710 and PT-711) | ± 5% |

Figure 149 compares the absolute pressure measured by sensor PT-712 in the SDS with predictions from the qualified and unqualified RELAP5 models during HEXACOM's start-up phase, corresponding to loop pressurization. All curves display similar qualitative behaviour, and in the early cold phase, both models align well with the experimental data.

The observed sinusoidal oscillations result from the periodic power variations of electrical heater W710, which directly affect the pressure rise rate. As the simulation advances, discrepancies emerge, with both models predicting a faster pressure increase than recorded experimentally. This deviation is mainly due to the absence of axial heat conduction modelling in the steam line above the SDS.

With valve CV717 closed during start-up, no flow occurs in that region, eliminating convective heat transfer. However, in the actual system, axial heat conduction in solids significantly contributes to heat losses—a mechanism not captured in standard RELAP5 modelling. This limitation leads the models to overpredict the heating rate. A notable difference arises between the qualified and unqualified models due to their differing thermal capacities, as outlined in Table 57. The qualified model shows an error of approximately 10% in the time to reach nominal pressure, whereas the unqualified model's error is about 23%, highlighting the importance of accurately modelling thermal structures in transient analyses.

Similar conclusions apply to the temperature measured by sensor TT-715 in the SDS, whose trend also aligns with the discussed differences in thermal modelling.

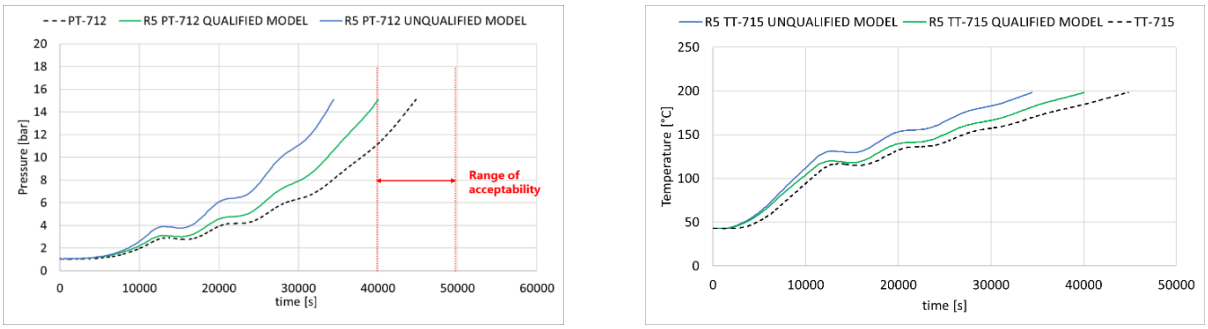


***Figure 149 Experimental vs RELAP5 pressure (left) and temperature trend (right)***

Finally, the pressure drop across the PHX between the experimental data and the numerical results obtained from both the qualified and the unqualified model are depicted in Figure 150. The left plot focuses on the short-term phase, while the right plot extends the analysis to the long-term phase. In the left plot, which refers to the short-term start-up phase, all experimental data points are displayed to capture the characteristic oscillatory behaviour observed during the initial pressurization. In contrast, the right plot, representing the long-term evolution, shows the experimental curve as a moving average, which effectively smooths out the oscillations and allows for a clearer comparison with the overall trend predicted by the numerical models.

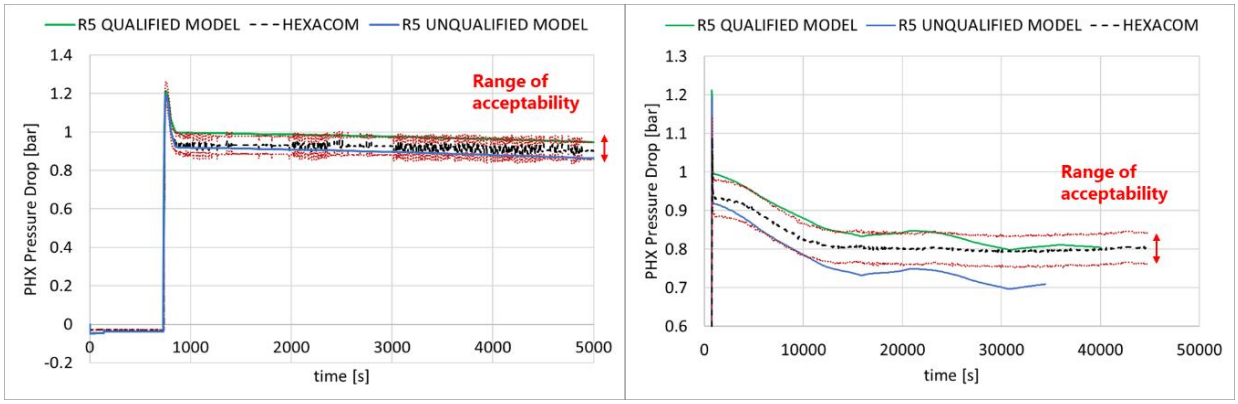


***Figure 150 PHX pressure drop***

In both cases, a range of acceptability is indicated in red. During the short-term phase, all models reproduce the initial pressure peak consistently, corresponding to the activation of the P710 pump. The qualified model remains well within the acceptable bounds, demonstrating strong agreement with the experimental measurements. In contrast, the unqualified model quickly under-predicts the pressure drop following the initial transient and falls outside the acceptable range. In the long-term evolution, the discrepancy between the two models becomes more pronounced. While the qualified model continues to follow the experimental trend within the defined limits, the unqualified model exhibits a systematic underestimation of the pressure drop. This deviation highlights the modelling limitations of the unqualified input, particularly related to the representation of CV736, which significantly influences the loop's hydraulic resistance under evolving thermal-hydraulic conditions.

Having assessed the performance of the qualified and unqualified models during transient conditions in accordance with STEP 16 of the qualification procedure, the analysis now shifts focus to the steady-state conditions, as required by STEP 15. This step is essential to verify the ability of the nodalization to accurately reproduce the thermal-hydraulic parameters characterizing the nominal operation of the facility. Also, for this case, Table 60 reports the relevant test, the monitored key parameters and their acceptance criteria to achieve STEP 15. For STEP 15 only the numerical results of the qualified model are shown.

***Table 60 STEP 15 parameters***

| **Test** | **Key parameter** | **Acceptance** |
|---|---|---|
| **HEXACOM steady-state** | Absolute pressure | ± 0.5% |
| | Pressure drops | ± 0.5% |
| | Temperature | ± 3 °C |
| | Mass flow rate | ± 5% |
| | CV736 norm. flow area | ± 5% |
| | CV717 norm. flow area | Qualitative trend |

For this purpose, an integral-type valve control system was implemented in the RELAP5 model to regulate the opening of CV736 and CV717 control valves following Equation 41)

$$\Delta s = K_I \int_0^t e(\tau)\, d\tau \qquad 41)$$

In which:

- $\Delta s$ is the stem variation (0% fully closed, 100% fully open)
- $K_I$ is the integral constant
- $e(\tau)$ is the error based on a set-point (process value - setpoint)

The reference set-points used to evaluate the variation of the stem position are the following:

- CV736 set-point is the mass flow rate crossing the valve itself, fixed at 0.07 kg/s
- CV717 set-point is the pressure at the top of the SDS, fixed at 15.25 bar (in the phase before REFILL 1) and at 15.15 bar (in the phase after REFILL 1)

While this approach allows the system to reach and maintain target conditions in a numerically stable manner, it is acknowledged that the adopted control logic may not accurately represent the actual control system implemented in the experimental facility.

Figure 151 presents the comparison between the experimental data and the RELAP5 simulation results for the pressure measured by sensor PT-712, located at the top of the SDS. Since this quantity is imposed as a boundary condition in the numerical model, the RELAP5 prediction perfectly aligns with the experimental curve throughout the steady-state phase.

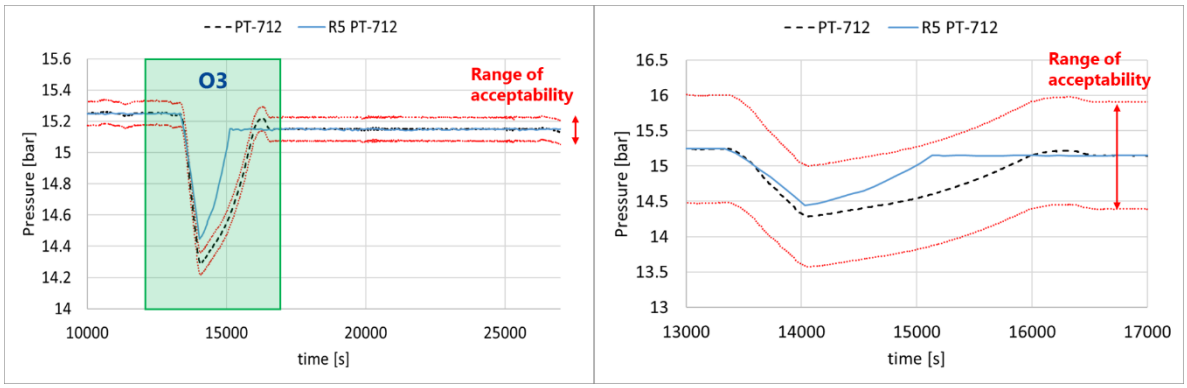


***Figure 151 Experimental vs RELAP5 pressure trend in the SDS***

The left plot shows the overall evolution of the pressure, while a specific portion corresponding to the REFILL 1 phase is highlighted with a green rectangle and further detailed in the right plot. During this phase, it can be observed that the result from the qualified model temporarily exceeds the predefined acceptance limit. This discrepancy, however, is not indicative of a modelling error but rather reflects the change in the applicable acceptance criteria. The initial threshold of ±0.5%, valid under steady-state conditions, no longer applies during the transient refill phase. In such conditions, the acceptable deviation is relaxed to ±5%, as shown in the right plot. When considering this adjusted criterion, the qualified model's result remains within acceptable bounds, confirming its validity under both steady-state and transient conditions.

The same considerations apply to the comparison of the temperature measured by sensor TT-715, also located within the SDS, as shown in Figure 152. In this case, however, the numerical prediction provided by the qualified RELAP5 model remains within the steady-state acceptance criteria throughout the entire simulation. This includes both the nominal steady-state phase, and the transient phase associated with REFILL 1, without requiring any relaxation of the predefined limits.

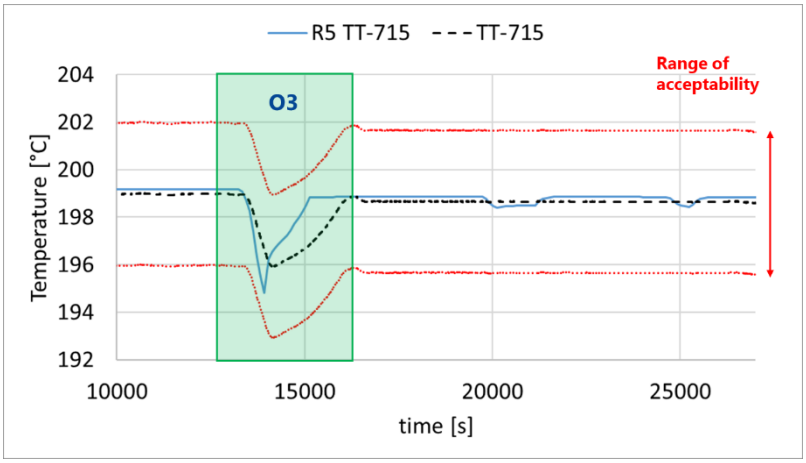


***Figure 152 Experimental vs RELAP5 temperature trend***

Figure 153 illustrates the pressure drop across the PHX, highlighting both a steady-state condition and a transient phase. In the steady-state portion of the simulation, the numerical results from RELAP5 remain well within the defined acceptance criteria, confirming the model's capability to reproduce the nominal hydraulic behaviour of the heat exchanger.

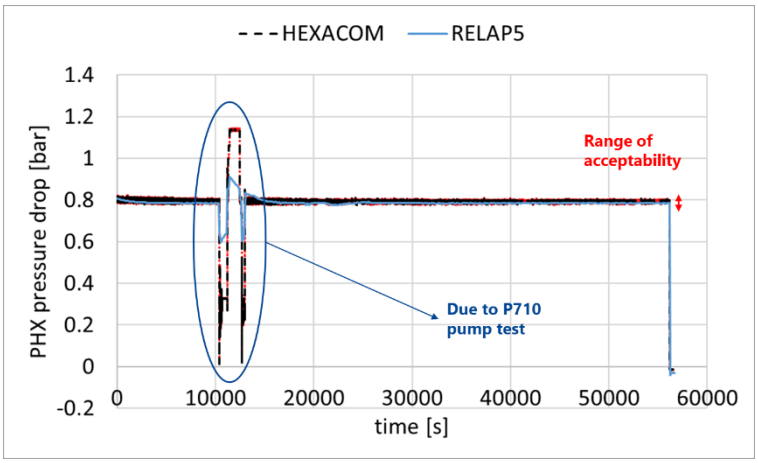


***Figure 153 PHX pressure drop tend***

The figure also captures a transient event induced by the operator during testing, in which the P710 pump speed was varied from its minimum to maximum allowable operating range. This pump ramp-up generates a dynamic response in the system that significantly affects the pressure drop across the PHX. However, this transient phase introduces a mismatch between the experimental data and the RELAP5 results, primarily due to differences in the control logic governing the CV736 valve. As will be shown later, this discrepancy affects the simulation's ability to fully capture this specific phase only in the portion of loops downstream CV736, although it does not compromise the model's overall validity under nominal conditions. The comparison of the absolute pressure upstream (left plot) and downstream (right plot) of the PHX are shown in Figure 154, as obtained from experimental measurements and RELAP5 simulations. During the steady-state phase, the numerical results—determined by the geometric and hydraulic characteristics defined in the model—fall within the established acceptance limits, confirming the adequacy of the nodalization under nominal conditions.

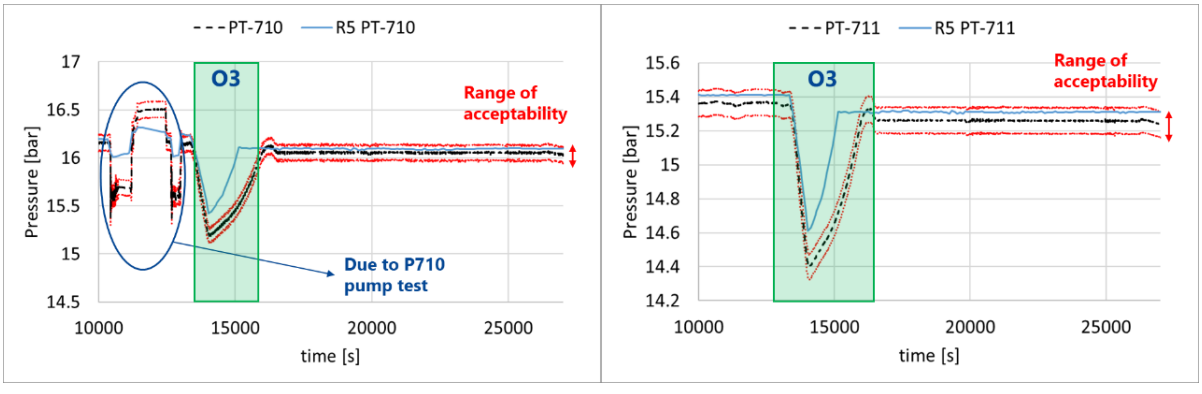


***Figure 154 PHX upstream (left) and downstream (right) absolute pressure***

The figure also captures two distinct transient events. The first corresponds to the P710 pump test, during which the pump speed was varied from minimum to maximum. In this case, the simulation results deviate from the experimental data, exceeding the predefined limits.

As previously discussed, this discrepancy is attributed to the differences in control logic for the CV736 valve between the physical system and the RELAP5 model. The second transient phase corresponds to REFILL 1. In this case, although deviations are observed, the numerical predictions remain within the broader acceptance limits defined for transient conditions, rather than the more stringent steady-state criteria, in line with the approach described earlier. Figure 155 shows the comparison between experimental and numerical results for the feed-water mass flow rate (left plot), measured by sensor FT-710, and the total mass flow rate delivered by the P710 pump (right plot), evaluated as the sum of the signals from FT-710 and FT-715.

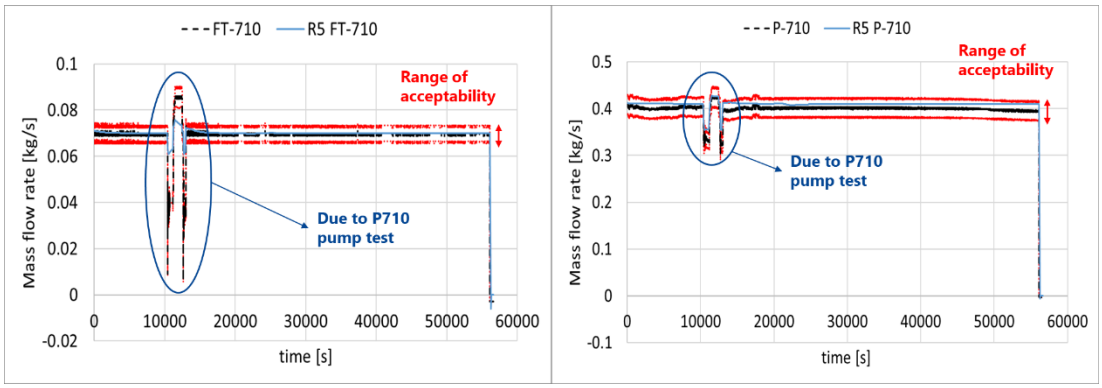


***Figure 155 Experimental vs RELAP5 mass flow rate in the feedwater line (left) and total (right)***

In steady-state conditions, the feed-water flow rate from the RELAP5 simulation perfectly matches the experimental data, as it is directly imposed by the CV736 valve control system implemented in the model. The total pump flow rate also falls within the defined acceptance range and is the result of the intersection between the pump homologous curve and the hydraulic characteristic of the HEXACOM loop. This outcome is particularly significant, as it validates both the hydraulic fidelity of the circuit—including distributed and concentrated losses in both parallel sub-loops and the overall system—and the performance curve of the pump, as modelled. In addition to the steady-state comparison, the figure also highlights the transient phase corresponding to the pump test, during which the P710 speed was varied. As previously discussed, the feed-water flow rate, during this transient, deviates from the experimental range, due to its position downstream of the CV736 and thus being influenced by differences in the implemented control logic. In contrast, the total pump flow rate, which is located upstream of CV736, remains within the acceptable bounds even during the transient, further supporting the accuracy of the pump modelling and the representation of the hydraulic behaviour of the system. Finally, Figure 156 presents the time evolution of the normalized flow area for the two control valves: CV736 (left plot) and CV717 (right plot).

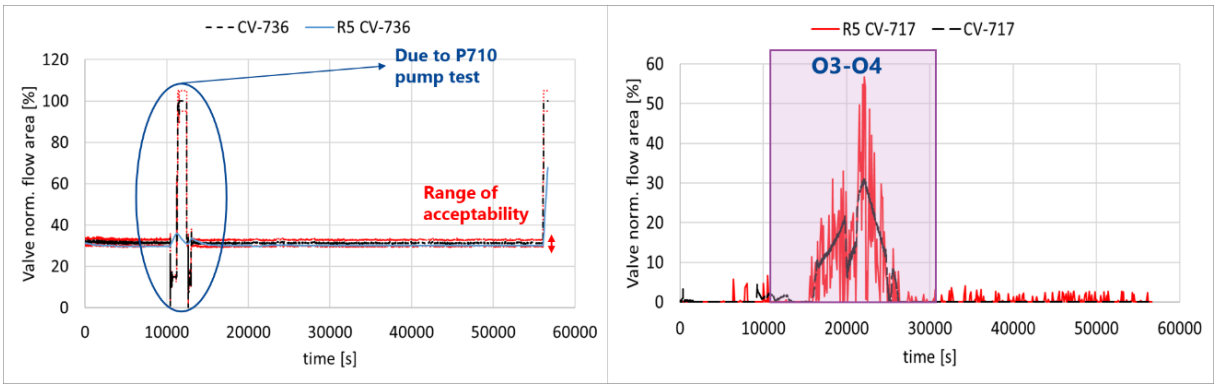


***Figure 156 CV736 (left) and CV717 (right) normalized flow area***

As indicated in Table 60, no quantitative acceptance criterion is defined for CV717, since it does not exhibit a steady-state behaviour at any point during the experimental campaign, and its response is significantly influenced by the difference in control logic between the physical system and the numerical model. Focusing on CV736, the results further support the findings discussed previously. During the steady-state phase, the valve opening predicted by the RELAP5 model falls within the defined acceptance limits. This means that, in order to achieve the same feed-water flow rate set-point as in the experiment, the model requires a valve opening that closely matches the experimental value. This outcome confirms the correct modelling of the pressure losses in the circuit. In contrast, during the transient phase introduced by the pump test, the predicted valve opening deviates from the acceptable range, once again highlighting the impact of the simplified control strategy implemented in RELAP5 compared to the real plant. As for CV717, its behaviour is also affected by the differences in control logic. Notably, during experimental sequences O3 and O4, the numerical valve response appears more reactive than the measured one; however, it still reproduces the overall qualitative trend, demonstrating consistency in the general valve behaviour under varying operational scenarios. The analysis now proceeds to the final part of the qualification process, STEP 17, which focuses on the assessment of heat losses. This step is crucial to verify the model's ability to reproduce the global thermal balance of the facility, particularly in configurations where the only heat sink is represented by passive heat exchange with the environment. Again, the relevant test, the monitored key parameters and their acceptance criteria are summarized in Table 61.

***Table 61 STEP 17 parameters***

| Test | Key parameter | Acceptance |
|---|---|---|
| **O2-phase (HEXACOM hot-standby)** | Heat losses | ± 10% |

Figure 157 shows the comparison between the experimentally measured heat losses and those predicted by the numerical model. The result demonstrates a satisfactory agreement, with the numerical prediction falling within the defined acceptance limits. It is worth noting that, unlike the simulation—which assumes a constant and HTC between the facility and the environment—the experimental data exhibit temporal fluctuations. These variations are likely attributable to changes in ambient conditions, such as temperature and air movement, which naturally affect the actual HTC.

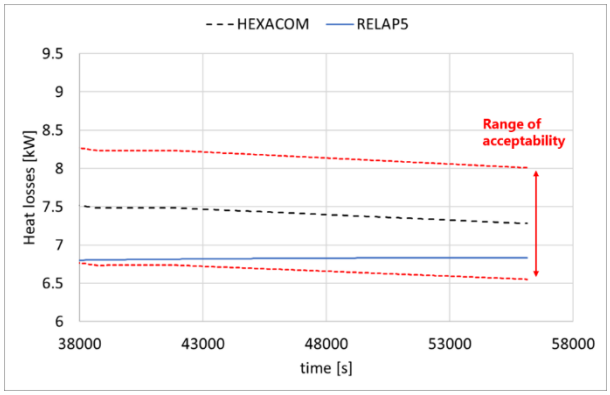


***Figure 157 Experiment vs RELAP5 heat losses***

This discrepancy is expected and does not compromise the overall validity of the model in reproducing the facility's thermal behaviour under steady-state conditions.

### 5.3.5. LBE pre-test analysis

Once the numerical model of HEXACOM was successfully validated—meaning that the RELAP5 input deck passed all the steps of the qualification procedure—the model was employed to carry out a pre-test analysis with LBE as the working fluid.

This analysis simulates the stand-alone operation of HEXACOM coupled with the COMPLOT facility. It is important to recall that COMPLOT was not explicitly modelled in the simulation; only the LBE side of the PHX was included, represented by the control volumes identified by the "1XX" naming convention.

The main objective of the pre-test is to characterize the thermal-hydraulic behaviour of HEXACOM and to investigate its response under an alternative operating mode. In particular, the pre-test aims to reproduce conditions representative of the normal operating regime of MYRRHA. For this reason, the control system was configured as follows:

- CV736 set-point is the mass flow rate crossing the valve itself, fixed at 0.0619 kg/s
- CV717 set-point is the pressure at the top of the SDS, fixed at 15.15 bar
- Air cooler set-point is the PHX water inlet temperature fixed at 196.5 °C
- P712 set-point is the SDS collapsed level fixed at about 60%

The main results of the pre-test analysis, aimed at characterizing the steady-state behaviour of HEXACOM in open loop operation coupled with COMPLOT, are summarized in Table 62, which reports the key parameters at the main reference points of the experimental facility.

The test is configured as follows: LBE from COMPLOT enters the PHX at 275 °C with a mass flow rate of 4.609 kg/s, representative of MYRRHA operating conditions, and transfers a thermal power of 37.39 kW to the secondary water. Considering both the heat transferred to the water and the heat losses of the PHX, the LBE exits the heat exchanger at approximately 219 °C.

The pressure drop on the LBE side of the PHX is about 5 bar, which includes the static head of the LBE. On the water side, the fluid enters at 16 bar and 188 °C and exits in a saturated state with a steam quality of approximately 28%. The pressure drop on the water side of the PHX is around 0.9 bar, consistent with the value obtained in the Stand-Alone test. Since the inlet water temperature to the PHX is below the target setpoint, no airflow is processed through the air cooler.

With the rotational speed of pump P710 set as a boundary condition, a total water flow rate of approximately 0.4 kg/s is established. Of this, about 0.0619 kg/s is directed toward the PHX, while the remaining flow is sent to the SDS. To achieve the required feedwater flow rate, control valve CV736 is adjusted to a normalized flow area of approximately 25%. Additionally, in order to maintain a pressure of 15.15 bar at the top of the SDS, the opening of control valve CV717 is set to 21%.

The make-up line compensates for the steam mass flow released to the environment, maintaining a constant water level in the SDS, with an inflow of about 0.01 kg/s. Finally, the total thermal losses of the HEXACOM facility are estimated to be around 8 kW.

*Table 62 Steady-state characterization of HEXACOM Open Loop operation coupled with COMPLOT*

| Parameter | Unit | RELAP5 |
|---|---|---|
| **LBE inlet temperature (BC)** | °C | 275.00 |
| **LBE outlet temperature** | °C | 219.56 |
| **LBE mass flow rate (BC)** | kg/s | 4.609 |
| **PHX LBE pressure drop** | kPa | 543.38 |
| **PHX water inlet pressure** | bar | 16.09 |
| **PHX water inlet temperature** | °C | 188.11 |
| **PHX water outlet temperature** | °C | 198.93 |
| **PHX water outlet quality** | % | 28.41 |
| **PHX water pressure drop** | kPa | 89.37 |
| **PHX thermal power** | kW | 37.39 |
| **Air cooler inlet temperature (BC)** | °C | 20.00 |
| **Air cooler mass flow rate** | kg/s | 0.00 |
| **P710 velocity (BC)** | rad/s | 111.32 |
| **P710 mass flow rate** | kg/s | 0.41 |
| **Feedwater mass flow rate** | kg/s | 0.0619 |
| **CV736 normalized flow area** | % | 24.72 |
| **Saturated steam mass flow rate** | kg/s | 0.01 |
| **SDS top pressure** | bar | 15.15 |
| **CV717 normalized flow area** | % | 20.65 |
| **W710 thermal power (BC)** | kW | 0.00 |
| **SDS collapsed level** | % | 60.81 |
| **SDS make-up inlet temperature (BC)** | °C | 20.00 |
| **SDS make-up mass flow rate** | kg/s | 0.01 |
| **HEXACOM heat losses** | kW | 7.90 |

# 6. CONCLUSIONS

Thermal–hydraulic analysis plays a central role in the design, safety assessment, and licensing of advanced nuclear reactors. In the context of Generation IV concepts, LFRs present unique challenges and opportunities due to their use of HLMs as primary coolant, high operating temperatures, and reliance on passive safety features. Their thermal–hydraulic behaviour, particularly under accidental scenarios, is governed by complex interactions between buoyancy-driven flows, multi-phase heat transfer, and the large thermal capacities of both structural materials and coolant. Passive safety systems, such as decay heat removal systems, depend on natural circulation and multiple heat transfer mechanisms—including conduction, convection, radiation, and condensation—often in the presence of non-condensable gases. Accurately modelling these processes requires validated numerical tools and a deep understanding of the dominant phenomena across a range of spatial and temporal scales. In this context, and with the goal of contributing to the advancement of state-of-the-art innovative nuclear systems, this thesis has investigated three representative LFR concepts.

The first LFR studied was ALFRED, designed and supported by the FALCON consortium, which includes ANSALDO NUCLEARE, ENEA, and RATEN. Supporting the PIRT analysis performed for ALFRED, a detailed numerical investigation of the reactor's behaviour under three unprotected transient scenarios—Unprotected Loss of Flow, Unprotected Transient of Overpower, and Unprotected Loss of Heat Sink—was carried out using the RELAP5/Mod3.3 STH code. These preliminary simulations provided valuable insights into ALFRED's safety characteristics and dynamic performance. Results indicated that ALFRED exhibits inherent safety features, although further analysis and experimental validation are needed. In the ULOF scenario, the loss of primary flow caused a gradual increase in primary loop temperatures, with the reactor reaching a new equilibrium in about 15 minutes. Clad integrity was preliminarily verified, with peak temperatures below the melting threshold and a calculated time-to-failure exceeding three months. The UTOP scenario highlighted the importance of feedback effects in mitigating power excursions, with a new equilibrium reached in 17 minutes and clad and fuel temperatures remaining safely below melting limits. For the ULOHS case, no equilibrium was reached, and the analysis focused on determining the reactor's grace time based on a cumulative damage fraction approach, yielding values of 36 hours and 20 hours for STAGE 2 and STAGE 3, respectively. While these results are encouraging, limitations such as the use of a point-kinetics neutronic model and the exclusion of heat loss modelling underscore the need for more advanced coupled multi-physics simulations, thermo-mechanical assessments, and uncertainty quantification in future studies.

In the context of ALFRED's innovative DHR system, the SIRIO facility was investigated. A comprehensive review of thermal–hydraulic phenomena related to steam condensation, both with and without non-condensable gases, was conducted. Based on this review, modifications to the condensation models in the RELAP5 source code were implemented by UNIROMA1. These improvements were preliminarily validated against experimental data available in literature, showing significant reductions in deviation from experimental results. The updated RELAP5 version was then applied to simulate SIRIO experiment performed within the PIACE project. Due to substantial changes in ALFRED's design—from the LEADER to the FALCON version—a new scaling analysis was performed for SIRIO within the Euratom LESTO project, ensuring representativeness of the updated reactor design. The scaling preserved NGT volume, IC active length, and thermal power, while neglecting piping volume, an assumption that explains small discrepancies between facility and reactor trends. Steady-state conditions representative of ALFRED STAGE 2 were achieved, and a PLOOP transient was simulated and compared to full-scale behaviour.

The study highlighted the need for both separate-effect tests focusing on IC tube- and pool-side phenomena and integral-effect tests under a broader range of operating conditions once SIRIO's instrumentation is upgraded.

The second LFR examined was the WEC-LFR, designed by Westinghouse Electric Company. Here, the analysis focused on the reactor's innovative PHRS, supported by experiments at the PHRF. Developed under the UK AMR Phase 2 program with international collaboration, the PHRF provided large-scale experimental data on air cooling performance and water-to-air transition dynamics. A RELAP5 model of the PHRF was developed and validated against three natural air convection tests due to data availability constraints. Following successful validation, the model was used for a pre-test simulation of nominal PHRF operation, capturing the expected sequence of phenomena: an initial pool boiling phase followed by dryout, a water-to-air transition at approximately 50 hours marked by a sharp rise in mass flow and temperature drop, and an established long-term natural convection regime.

Complementary to PHRF, the VLF was also analysed. Developed under the UK AMR programme as a key platform for WEC-LFR R&D, the VLF was modelled in RELAP5/Mod3.3. Steady-state and stand-alone component characterisations of the PHE, HX-201, condenser, and FPBS were performed, with calibration as required. Operational and accidental transients were investigated, including a start-up sequence, a shutdown procedure using a simplified on/off valve assumption, and loss-of-heat-sink and loss-of-FPBS-power events. The former showed the facility reaching a new equilibrium in 45 minutes with minimal primary loop impact, while the latter indicated a grace time to lead freezing of about 7 minutes. Future work will extend these analyses to additional scenarios and potential layout refinements.

Detailed studies were also performed on two crucial WEC-LFR RCS components. For the FPBS, a code-to-code comparison between RELAP5 and the ANL-developed subchannel code DASSH was carried out, providing detailed cross-sectional thermal fields and axial coolant temperature profiles. For the PHE, a preliminary RELAP5–ANSYS CFX comparative study of nominal operation was performed. Results showed strong global agreement but local deviations, especially on the water side, likely due to supercritical water property interpolation and generic heat transfer correlations in RELAP5 not consistent with the geometry. Additional tests confirmed the accuracy of RELAP5's 1D heat conduction modelling for this configuration. The analysis supports the RELAP5 model's reliability for the PHE in system-level studies, with recommendations to expand the analysis to the full component and explore improved heat transfer correlations tailored to its geometry and regime supported by VLF experimental results when will be available.

The last LFR investigated was MYRRHA, developed by the Belgian Nuclear Research Centre (SCK CEN). Following a PIRT exercise for MYRRHA, the study focused on its secondary loop, represented and accurately investigated by the HEXACOM experimental facility. A structured, traceable qualification methodology for STH code input decks, developed at SCK CEN, was applied to HEXACOM using RELAP5. Comparisons between qualified and unqualified models against experimental data demonstrated the substantial predictive improvements afforded by input qualification. The facility's behaviour was characterised under Stand-Alone Open Loop and Open Loop coupled with COMPLOT configurations. For the latter, while no experimental data were available, the rigorous qualification process lends confidence to the simulation results. Future work will include post-test analysis once COMPLOT data become available, extension of the qualification framework to transient cases, and application to additional operating conditions.

Overall, this thesis has delivered validated numerical models, improved physical correlations, and robust methodological approaches applicable to a broad range of LFR systems and supporting facilities. The findings demonstrate that accurately predicting passive system behaviour requires not only detailed nodalization and correct boundary conditions but also explicit modelling of phenomena such as radiation exchange in confined cavities and condensation degradation in the presence of non-condensable gases.

In conclusion, the research presented here advances the predictive capability of RELAP5/Mod3.3 and related system codes for LFR safety systems, bridging the gap between experimental evidence and simulation. The models, methods, and improvements developed provide a sound basis for full-scale reactor analysis, safety assessment, and design optimisation. Future developments should focus on coupling system codes with CFD to capture three-dimensional effects, broadening validation datasets to cover a wider range of operating conditions, refining TH models for transient mixed-phase flows, and implementing advanced 3D NK–TH coupling to enable detailed safety analyses in support of the licensing process. Integrating these advancements will support the creation of a comprehensive, reliable simulation framework, enabling the robust design and safety demonstration of next-generation LFR technology.

# LIST OF REFERENCES


[1] IEA (2021), Net Zero by 2050, IEA, Paris https://www.iea.org/reports/net-zero-by-2050

[2] IPCC, 2023: Sections. In: "Climate Change 2023: Synthesis Report. Contribution of Working Groups I, II and III to the Sixth Assessment Report of the Intergovernmental Panel on Climate Change", [Core Writing Team, H. Lee and J. Romero (eds.)]. IPCC, Geneva, Switzerland, pp. 35-115, doi: 10.59327/IPCC/AR6-9789291691647

[3] INTERNATIONAL ATOMIC ENERGY AGENCY, Nuclear Power Reactors in the World, Reference Data Series No. 2, IAEA, Vienna (2024)

[4] INTERNATIONAL ATOMIC ENERGY AGENCY (2025), Power Reactor Information System (PRIS), https://pris.iaea.org/PRIS/

[5] U.S. DOE Nuclear Energy Research Advisory Committee, Generation IV International Forum, "Technology roadmap update for Generation IV nuclear energy systems", USA, 2014. https://www.gen-4.org/gif/jcms/c_60729/technology-roadmap-update-2013

[6] Gen IV International Forum (2020), "Generation IV Goals", https://www.gen-4.org/gif/jcms/c_9502/generation-iv-goals

[7] A. Alemberti, K. Tucek, M. Takahashi, T. Obara, M. Kondo, A. Moiseev, L. Tocheny, C. Smith, I. S. Hwang, Y. Wu, M. Jin, "Lead-cooled Fast Reactor (LFR) System Safety Assessment", https://www.gen-4.org/gif/upload/docs/application/pdf/2020-06/gif_lfr_ssa_june_2020_2020-06-09_17-26-41_202.pdf, GIF, 2020.

[8] F. Tassone, M. E. Ricotti, S. Lorenzi, G. Locatelli, "Economics and finance of lead fast reactors: A systematic literature review", Progress in Nuclear Energy, 174, 105298, 2024. https://doi.org/10.1016/j.pnucene.2024.105298

[9] Alemberti, A., et al., (2017). Status of generation IV lead fast reactor activities. In International Conference on Fast Reactors and Related Fuel Cycles: Next Generation Nuclear Systems for Sustainable Development (FR17) (p. 10). Retrieved January 9, 2025, from https://inis.iaea.org/records/rbzxp-qrw68

[10] Y. G. Dragunov, V. V. Lemekhov, A. V. Moiseev, L. V. Tocheny, A. A. Umansky, "Lead-Cooled Fast-Neutron Reactor (BREST) (Approaches to the closed NFC)", Proceedings of Global 2015, Paris France, September 20-24, 2015, Paper 5435.

[11] Choi, S., et al., (2011). URANUS: Korean lead–bismuth cooled small modular fast reactor activities. In ASME 2011 Small Modular Reactors Symposium (SMR 2011). https://doi.org/10.1115/SMR2011-6650

[12] J. Wallenius, S. Qvist, I. Mickus, S. Bortot, P. Szakalos, J. Ejenstam, "Design of SEALER, a very small lead-cooled reactor for commercial power production in off-grid applications", Nuclear Engineering and Design, 338, pp. 23-33, 2018. https://doi.org/10.1016/j.nucengdes.2018.07.031

[13] Smith, C. F., et al., (2008). SSTAR: The US lead cooled fast reactor (LFR). Journal of Nuclear Materials, 376(3), 255–259. https://doi.org/10.1016/j.jnucmat.2008.02.049

[14] V. S. Smirnov, "Safety features of a power unit with the BREST-OD-300 reactor", International Conference on Fast Reactors and Related Fuel Cycles: Safe Technologies and Sustainable Scenarios, 4-7 March, 2012, Paris, France.

[15] V. V. Orlov, A. I. Filin, A. V. Lopatkin, A. G. Glazov, L. P. Sukhanov, V. I. Volk, P. P. Poluektov, O. A. Ustinov, M. T. Vorontsov, V. F. Leontiev, R. S. Karimov, "The closed on-site fuel cycle of the brest

reactors", Progress in Nuclear Energy, 47 (1-4), pp. 171-177, 2005. https://doi.org/10.1016/j.pnucene.2005.05.017

[16] J. Wallenius, "Status of Blykalla's commercial LFR development in Sweden", Webinar GIF talks with industry series #2, July 17, 2024.

[17] K. Umminger and A. Del Nevo, "Integral Test Facilities and Thermal-Hydraulic System Codes in Nuclear Safety Analysis", *Science and Technology of Nuclear Installations,* pp. 1-3 (2012).

[18] International Atomic Energy Agency, "Safety Assessment for Facilities and Activities", Vienna (2016).

[19] https://nucleus.iaea.org/sites/lmfns/Pages/overviewlfr.aspx. Retrieved in June 2025

[20] Tarantino, Mariano, Massimo Angiolini, Serena Bassini, Sebastiano Cataldo, Chiara Ciantelli, Carlo Cristalli, Alessandro Del Nevo, Ivan Di Piazza, Dario Diamanti, Marica Eboli, and et al. 2021. "Overview on Lead-Cooled Fast Reactor Design and Related Technologies Development in ENEA" Energies 14, no. 16: 5157. https://doi.org/10.3390/en14165157

[21] Pesetti, A., et al., 2018, "ENEA CIRCE-HERO TEST FACILITY: GEOMETRY AND INSTRUMENTATION DESCRIPTION", ENEA report CI-I-R-343, June 2018.

[22] Ivan Di Piazza, Morena Angelucci, Ranieri Marinari, Mariano Tarantino, Nicola Forgione, "Heat transfer on HLM cooled wire-spaced fuel pin bundle simulator in the NACIE-UP facility", Nuclear Engineering and Design, Volume 300, 2016, Pages 256-267. https://doi.org/10.1016/j.nucengdes.2016.02.008.

[23] PIAZZA I. DI, TARANTINO M., AGOSTINI P., GAGGINI P., Helena: An Heavy Liquid Metal Multi-Purpose Loop For Thermal-Hydraulics, Corrosion And Component Test, ICONE22-30784, Praha, CZK, 2014.

[24] Frignani, M., Alemberti, A., Villabruna, G., Grasso, G., Tarantino, M., Constantin, M., Turcu, I., Valeca, S., Di Gabriele, F., & Romanello, V. (2017). FALCON advancements towards the implementation of the ALFRED Project (pag. 10 p.).

[25] M. Constantin, G. Grasso, M. Tarantino, I. Turcu, C. Paunoiu, A. Toma, M. Caramello, M. Frignani, A. Alemberti, D. Diaconu, M. Nitoi, M. Apostol, D. Gugiu, P. Agostini, "The development of the research infrastructure in support of ALFRED demonstrator implementation in Romania", EMERG – Energy. Environment. Efficiency. Resources. Globalization, 7 (1), pp. 123-132, 2021. http://dx.doi.org/10.37410/EMERG.2021.1.10

[26] Fernandez, R. et al. (2021) «MYRRHA Technology and Research Facilities in Support of Heavy Liquid Metal SMR Fast Reactors». Technical Meeting on the Benefits and Challenges of Fast Reactors of the SMR Type, pagg. p. 264–279.

[27] U.S. Nuclear Regulatory Commission. (1989). Quantifying reactor safety margins: Application of code scaling, applicability, and uncertainty evaluation methodology to a large break loss of coolant accident (NUREG/CR 5249). Retrieved February 10, 2025, from https://www.nrc.gov/docs/ML0303/ML030380473.pdf

[28] Boyack, B.E., Wilson, G.E., 2004. Lessons learned in obtaining efficient and sufficient applications of the PIRT process. In: Proceedings of ANS International Meeting on Updates in Best Estimate Methods in Nuclear Installation Safety Analysis (BE-2004), pp. 222–230. Washington, D.C.

[29] Avramova, M. N., & Ivanov, K. N. (2010). Verification, validation and uncertainty quantification in multi-physics modeling for nuclear reactor design and safety analysis. Progress in Nuclear Energy, 52(7), 601–614. https://doi.org/10.1016/j.pnucene.2010.03.009

[30] F. D'Auria, G. M. Galassi, M. Bonuccelli A methodology for the qualification of thermal hydraulic code nodalizations. In proc. of NURETH-6. Grenoble, 1993.

[31] Del Nevo A., Araneo D., D'Auria F., Galassi G. NODALIZATION QUALIFICATION PROCESS OF THE PSB-VVER FACILITY FOR THE CATHARE2 THERMAL-HYDRAULIC CODE 5th International Conference on Nuclear Option in Countries with Small and Medium Electricity Grids-Dubrovnik, Croatia, May 16-20, 2004.

[32] Rozzia D. Procedure for qualification of TH SYS codes nodalization. Internal report number SCK CEN/56952588 - 2025-03-18.

[33] Information Systems Laboratories, "RELAP5/Mod3.3 code manual volume I: code structure, system models, and solution methods", March 2003.

[34] OECD/NEA Nuclear Science Committee, Handbook on Lead-bismuth Eutectic Alloy and Lead Properties, Materials Compatibility, edition, Thermal-hydraulics and Technologies (2015)

[35] M. TARANTINO et al., "Post Test Analysis of ICE Tests", Proc. of 20th Int. Conf. on Nuc. Eng. (ICONE20), Anaheim, CA, USA, July 30–August 3, 2012, Paper No. ICONE20-54952, Vol. 2, pp. 703-712, 10 pages.

[36] R.A. Seban T. Shimazaki, Heat transfer to a fluid flowing turbulently in a smooth pipe with walls at constant temperature, in: California Univ Berkeley Inst of Engineering Research, 1949.

[37] Mikityuk, K. (2009). Heat transfer to liquid metal: Review of data and correlations for tube bundles. Nuclear Engineering and Design, 239(4), 680–687. https://doi.org/10.1016/j.nucengdes.2008.12.014

[38] N. FORGIONE et al., "Post-test simulations for the NACIE-UP benchmark by STH codes", Nuclear Engineering and Design, 353, 110279 (2019); https://doi.org/10.1016/j.nucengdes.2019.110279.

[39] ANSYS CFX-Solver Theory Guide, November 2011.

[40] Atz, Milos, Smith, Micheal A., and Heidet, Florent. Ducted Assembly Steady-State Heat Transfer Software (DASSH) - Theory Manual. Nuclear Engineering Division, Argonne National Laboratory: N. p., 2021. Web. doi:10.2172/1813446

[41] M. Frignani et al. (2017), ALFRED: A Strategic Vision for LFR Deployment, ANS Winter Meeting 2017, Washington, D.C.

[42] E. Bubelis, K. Mikityuk, "Plant data for the safety analysis of the ETDR (ALFRED)", TEC058-2012, LEADER project, 2012.

[43] M. Frignani, A. Alemberti, M. Tarantino, G. Grasso, "ALFRED staged approach", Proceedings of the International Congress on Advances in Nuclear Power Plants (ICAPP 2019), Juan-les-pins, France, May 12-15, 2019.

[44] Alemberti, A., et al., (2020). ALFRED reactor coolant system design. Nuclear Engineering and Design, 370, 110884. https://doi.org/10.1016/j.nucengdes.2020.110884

[45] Frignani, M., et al., (2019a). ALFRED: A revised concept to improve pool related thermal hydraulics. Nuclear Engineering and Design, 355, 110359. https://doi.org/10.1016/j.nucengdes.2019.110359

[46] Grasso, G., et al., (2014). The core design of ALFRED, a demonstrator for the European lead-cooled reactors. Nuclear Engineering and Design, 278, 287–301. https://doi.org/10.1016/j.nucengdes.2014.07.032

[47] Grasso, G., et al., (2019, May). An improved design for the ALFRED core. Paper presented at the International Congress on Advances in Nuclear Power Plants, Juan les Pins, France.

[48] Petrovich, C., et al., (2013). Definition of the ETDR core and neutronic characterization (Lead-cooled European Advanced DEmonstration Reactor – LEADER, Technical Report).

[49] International Atomic Energy Agency. (1991). Safety-related terms for advanced nuclear plants (IAEA-TECDOC-626). IAEA.

[50] Caramello, M., et al., (2017). Thermal hydraulic analysis of a passively controlled DHR system. Progress in Nuclear Engineering, 99, 127–139. https://doi.org/10.1016/j.pnucene.2017.05.015

[51] CORDIS. (n.d.). Advanced Nuclear Safety Evaluation Using Systems (ANSELMUS) Project ID 101061185. Retrieved from https://cordis.europa.eu/project/id/101061185

[52] M. Caramello, G. Khalil Youssef. "ALFRED reference design and initiating events" (Advanced Nuclear Safety Evaluation Using Systems – ANSELMUS, Deliverable 1.2)

[53] Bandini, G., & Polidori, M. (2013). Report on the results of analysis of DEC events for the ETDR (ALFRED) (ENEA EU Contract, Deliverable DEL022, LEADER Project, EU 7th Framework Programme, Grant Agreement No. FP7 249668). Retrieved February 14, 2025, from https://iris.enea.it/bitstream/20.500.12079/7519/1/UTFISSM-P9SZ-007.pdf

[54] G. Khalil Youssef, C. Ciurluini, M. Caramello, F. Lodi, F. Giannetti. "Neutronic and thermal hydraulic analysis of ALFRED during Unprotected transients considering the reactor staged approach". Nuclear Engineering and Design, 444, 114412. https://doi.org/10.1016/j.nucengdes.2025.114412

[55] Information Systems Laboratories, Inc. (2006). RELAP5/MOD3.3 code manual. Volume V: User's guidelines. Nuclear Safety Analysis Division. Prepared for the U.S. Nuclear Regulatory Commission, Division of Systems Research, Office of Nuclear Regulatory Research

[56] International Atomic Energy Agency. (2008). Thermophysical properties of materials for nuclear engineering: A tutorial and collection of data. IAEA. Retrieved February 26, 2025, from https://www-pub.iaea.org/MTCD/Publications/PDF/IAEA-THPH_web.pdf

[57] Luzzi, L., et al., (2014). Modeling and analysis of nuclear fuel pin behavior for innovative lead cooled FBR [Technical Report]. ENEA

[58] Arp, V. D., et al., (1998). Thermophysical properties of helium 4 from 0.8 to 1500 K with pressures to 2000 MPa (Revised) (NIST Tech. Note 1334). National Institute of Standards and Technology. Retrieved January 14, 2025, from https://nvlpubs.nist.gov/nistpubs/Legacy/TN/nbstechnicalnote1334.pdf

[59] American Nuclear Society, ANSI/ANS-5.1-1994, Decay Heat Power in Light Water Reactors, August 23, 1994.

[60] D.A. Brown, et al., ENDF/B-VIII.0: The 8th Major Release of the Nuclear Reaction Data Library with CIELO-project Cross Sections, New Standards and Thermal Scattering Data, Nuclear Data Sheets, 148: pp. 1-142 (2018). https://doi.org/10.1016/j.nds.2018.02.001

[61] Grasso, G., et al., (2018). Stress testing the ALFRED design – Part I: Impact of nuclear data uncertainties on design extension conditions transients. Progress in Nuclear Energy, 106, 372–386. https://doi.org/10.1016/j.pnucene.2018.03.013

[62] Kim, C. S. Thermophysical properties of stainless steel. Argonne National Laboratory. (Prepared for the U.S. Energy Research and Development Administration)

[63] Colebrook, C. F., & White, C. M. (1937). Experiments with fluid friction in roughened pipes. Proceedings of the Royal Society of London. Series A, Mathematical and Physical Sciences, 161(906), 367–381

[64] Idelchik, I. E. (1986). Handbook of hydraulic resistance (2nd ed.). Hemisphere Publishing Corporation

[65] Samanta, P., et al. (2019, June). NRC regulatory history of non-light water reactors (1950–2019). https://doi.org/10.2172/1579511

[66] Topliss, J. R., et al., (1995, July). Measurement and analysis of MOX physical properties. In Proceedings of the Technical Committee Meeting on Recycling of Plutonium and Uranium in Water Reactor Fuel (3–7 July, Newby Bridge, Windermere, United Kingdom)

[67] Lodi, F., & Grasso, G. (2018). Stress testing the ALFRED design – Part III: Safety margins evaluation. Progress in Nuclear Energy, 106, 433–439. https://doi.org/10.1016/j.pnucene.2018.04.003

[68] Lodi, F., (2018). Engineering the Fuel Pin Thermo-Mechanic Code TEMIDE: Validation and Application. ENEA Technical Report XSRS-P000–001

[69] Argonne National Laboratory. (2019, April 26). Analysis of VTR primary pump coastdown [Technical Report]. Nuclear Science and Engineering Division.

[70] International Atomic Energy Agency. (1992). Procedures for conducting probabilistic safety assessments of nuclear power plants (Level 1) (Safety Series No. 50 P 4). IAEA. Retrieved January 21, 2025, from https://www.iaea.org/publications/3759/procedures-for-conducting-probabilistic-safety-assessments-of-nuclear-power-plants-level-1

[71] Waltar A.E., Todd D.R., Tsvetkov, P.V. (Eds), 2011. Fast Spectrum Reactors, Springer, New York.

[72] R. Marinari, M. Tarantino, F.S. Nitti, A. Alemberti, M. Caramello, A. Achilli, R. Ferri, E. Rizzo, F. Giannetti, "SIRIO: an experimental facility for a new heat removal system passively controlled by non-condensable gases," Proceedings of the 2018 26th International Conference on Nuclear Engineering, 6B, pp. 1-10 (2018), London, England, https://doi.org/10.1115/ICONE26-82379

[73] Cassa per i Servizi Energetici e Ambientali (CSEA), "Progetto SIRIO: Sistema di rimozione della potenza di decadimento per reattori nucleari innovativi", 2020. https://www.csea.it/avviso/approvazione-consuntivo-progetto-sirio-bando-b-2014

[74] M. Carelli, L. Conway, M. Dzodzo, A. Maioli, L. Oriani, G. Storrick, B. Petrovic, A. Achilli, G. Cattadori, C. Congiu, R. Ferri, M. Ricotti, D. Papini, F. Bianchi, P. Meloni, S. Monti, F. Berra, D. Grgic, G. Yoder, A. Alemberti, "The SPES3 Experimental Facility Design for the IRIS Reactor Simulation", Science and Technology of Nuclear Installations, 2009, 579430. https://doi.org/10.1155/2009/579430

[75] CORDIS. (n.d.). Passive Isolation Condenser (PIACE) Project ID 847715. Retrieved from https://cordis.europa.eu/project/id/847715

[76] T. Del Moro, F. Giannetti, G. Khalil Youssef, P. Lorusso, M. Caramello, M. T. Cauzzi, M. Tarantino, "Post-Test Analysis of SIRIO Facility Data by System Thermal-Hydraulic Codes for LFR Application", Proceedings of the 20th International Topical meeting on Nuclear Reactor Thermal Hydraulics (NURETH-20), Washington, D.C., August 20-25, 2023. http://dx.doi.org/10.13182/NURETH20-40092

[77] Dynalene Inc, "Dynalene MS-2 technical data sheet", 2020.

[78] J. C. Chen, "Correlation for boiling heat transfer to saturated fluids in convective flow", Industrial & Engineering Chemistry Process Design and Development, 5 (3), 1966. https://doi.org/10.1021/i260019a023

[79] M. G. Cooper, "Heat flow rates in saturated nucleate pool boiling – A wide-ranging examination using reduced properties", Advances in Heat Transfer, 16, pp. 157–239, 1984. https://doi.org/10.1016/S0065-2717(08)70205-3

[80] V. Narcisi, L. Melchiorri, F. Giannetti, G. Caruso, "Assessment of RELAP5-3D for application on in-pool passive removal systems", Proceedings of the 30th European Safety and Reliability Conference and the 15th Probabilistic Safety Assessment and Management Conference, Venice, Italy, 2020.

[81] V. Narcisi, L. Melchiorri, F. Giannetti, "Improvements of RELAP5/Mod3.3 heat transfer capabilities for simulation of in-pool passive power removal systems", Annals of Nuclear Energy, 160, 108436, 2021. https://doi.org/10.1016/j.anucene.2021.108436

[82] R. Ferri, A. Achilli, G. Cattadori, F. Bianchi, P. Meloni, "Design, experiments and Relap5 code calculations for the perseo facility", Nuclear Engineering and Design, 235 (10-12), pp. 1201-1214, 2005. https://doi.org/10.1016/j.nucengdes.2005.02.011

[83] W. Nusselt, "Die Oberflachenkondensation des Wasserdampfes", er. deutsch. Ing. 60, 1916.

[84] S. S. Kutateladze, "Heat transfer theory fundamentals", 1 3, Atomizdat, Moscow/ Arnold Publishers, London/ Academic Press Inc., New York.

[85] F. Blangetti, E. O. Schlunder, "Local Heat Transfer Coefficients of Condensation in a Vertical Tube", Proceedings of the 6th International Heat Transfer Conference, 2, pp. 437-442, 1978.

[86] D. A. Labuntsov, "Heat transfer in film condensation of pure steam on vertical surfaces and horizontal tubes", Teploenergetika, 4 (7), pp. 72-79, 1957.

[87] M. M. Shah. "A General Correlation for Heat Transfer during Film Condensation Inside Pipes", International Journal of Heat and Mass Transfer, 22 (4), pp. 547-556, 1979. https://doi.org/10.1016/0017-9310(79)90058-9

[88] M. M. Shah, "An improved and extended general correlation for heat transfer during condensation in plain tubes", HVAC&R Research, 15 (5), pp. 889–913, 2009. https://doi.org/10.1080/10789669.2009.10390871

[89] D. Papini, A. Cammi, "Modelling of Heat Transfer Phenomena in Vertical and Horizontal Configurations of In-Pool Condensers and Comparison with Experimental Findings", Science and Technology of Nuclear Installations, 2010(1), 815754. https://doi.org/10.1155/2010/815754

[90] A. P. Colburn, O. A. Hougen, "Design of cooler condensers for mixtures of vapors with noncondensing gases", Industrial & Engineering Chemistry, 26 (11), pp. 1178-1182, 1934. https://doi.org/10.1021/ie50299a011

[91] Anderson, N. A., & Mesina, G. L. (2017, June). Improvement of the RELAP5-3D model of condensation in the presence of noncondensables (PowerEnergy2017-3401). In Proceedings of the ASME 2017 Power and Energy Conference (June 26–30, 2017, Charlotte, NC, USA). American Society of Mechanical Engineers.

[92] Caruso, G., Giannetti, F., & Naviglio, A. (2012). Experimental investigation on pure steam and steam–air mixture condensation inside tubes. International Journal of Heat and Technology, 30(2), 77–84. https://doi.org/10.18280/ijht.300211

[93] Siddique, M. (1992). The effects of noncondensable gases on steam condensation under forced convection conditions (Doctoral dissertation, Massachusetts Institute of Technology, Department of Nuclear Engineering). Massachusetts Institute of Technology.

[94] G. Khalil Youssef, T. Del Moro, M. Caramello, M. Tarantino, F. Giannetti, "Re-scaling and Pre-test analysis of SIRIO facility"; "41st UIT International Heat Transfer Conference", Napoli, Italy, June 19-21, 2024

[95] V. Narcisi, F. Giannetti, M. Caramello, G. Caruso, "Preliminary evaluation of ALFRED revised concept under station blackout", Nuclear Engineering Design, vol. 364, art no. 110648, 2020

[96] P. FERRONI et al., "The Westinghouse Lead Fast Reactor: Design Overview and Update on Development Activities," Int. Conf. on Fast Reactors and Related Fuel Cycles: Sustainable Clean Energy for the Future (FR22), Vienna, Austria, April 2022.18.

[97] Stauff, N., Franceschini, F., Ramey, K., Richards, S., Liao, J., Jonson, M., & Ferroni, P. (2025). Core design and performance of the Westinghouse lead fast reactor with $UO_2$ and MOX configurations. Nuclear Engineering and Design, 442, 114266. https://doi.org/10.1016/j.nucengdes.2025.114266

[98] C. Stansbury, et al., An Integrated Design Approach to Address Key Safety Events in the Westinghouse LFR: an Innovative Pool-Type, Liquid Lead-Cooled Fast Reactor. 2022 IAEA International Conference on Topical Issues in Nuclear Installation Safety: Strengthening Safety of Evolutionary and Innovative Reactor Designs. October 2022.

[99] Liao, J., et al., 2021. Development of phenomena identification and ranking table for Westinghouse Lead Fast Reactor's safety, Progress in Nuclear Energy, 131.

[100] Liao, J., Wise, D. L., Wright, R. F., Tatli, E., Ferroni, P., Lee, S. J., Caramello, M., Frignani, M., Howlett, C., Tarantino, M., Grasso, G., 2022. Progress in the Westinghouse LFR safety analysis in support of the UK Advanced Modular Reactor Programme, Proc. 19th International Topical Meeting on Nuclear Reactor Thermal Hydraulics, Brussel, Belgium.

[101] Liao, J. et al., 2023b. Development and demonstration of a reliable fully passive heat removal system for Westinghouse Lead Fast Reactor, Technical Meeting on Reliability Assessment of Passive Heat Removal Systems Used in Advanced Reactor Designs, Vienna, Austria.

[102] "Advanced Modular Reactor (AMR) Feasibility and Development Project," UK Department for Business, Energy & Industrial Strategy; https://www.gov.uk/government/publications/advanced-modular-reactor-amr-feasibility- and-development-project (current as of Aug. 23, 2022).

[103] Caramello, M., Frignani, M., Beaumont, R., Tarantino, M., Liao, J., Wright, R. F., Ferroni, P. (2023). The Passive Heat Removal Facility: Testing and Demonstrating an Innovative Decay Heat Removal System. Nuclear Technology, 210(4), 740–757. https://doi.org/10.1080/00295450.2023.2241731

[104] Jun Liao, Megan Durse, Richard F. Wright, Emre Tatli, Paolo Ferroni, Marco Caramello, Michele Frignani, Giorgio K. Youssef, Rhodri Watkins, Graham Macpherson, "The passive heat removal facility (PHRF) and its first phase experiments", Annals of Nuclear Energy, Volume 213,2025,111132.

[105] M. Caramello, M. Frignani, R. Beaumont, M. Tarantino, C. Stansbury & P. Ferroni (2023): The Versatile Loop Facility: A New Infrastructure for Testing Components and Systems of Lead Fast Reactor Technology, Nuclear Technology, DOI:10.1080/00295450.2023.2181043

[106] S. BASSINI et al., "Oxygen Sensors for Heavy Liquid Metal Coolants: Calibration and Assessment of the Minimum Reading Temperature," J. Nucl. Mater., 486, 197 (2017); https://doi.org/10.1016/j.jnucmat.2017.01.031

[107] Giorgio Khalil Youssef, Marcello Principato, Marco Caramello, Cory Stansbury, Cristiano Ciurluini, Fabio Giannetti,"Pre-test analysis and thermal-hydraulic characterization of the versatile loop facility", Nuclear Engineering and Design, Volume 433,2025,113850

[108] F. W. Dittus, L. M. K. Boelter, "Heat transfer in automobile radiators of the tubular type". The University of California Publications on Engineering 2 (1930) 443–461

[109] R. Lyon, "Liquid metal heat transfer coefficients", Chemical Engineering Progress, vol. 47, no. 2 pp 75-79, 1951.

[110] Kandlikar, S. G., & Grande, W. J. (2003). Evolution of Microchannel Flow Passages-Thermohydraulic Performance and Fabrication Technology. Heat Transfer Engineering, 24(1), 3–17. https://doi.org/10.1080/01457630304040

[111] Khalil Youssef, G.; Missaglia, A.; Caramello, M.; Lorenzi, S.; Ricotti, M.; Ciurluini, C.; Giannetti, F.; "Comparative Analysis of RELAP5 and ANSYS-CFX Simulations for Microchannel Heat

Exchangers: A case study on the VLF Primary Heat Exchanger", “The 21st International Topical Meeting on Nuclear Reactor Thermal Hydraulics (NURETH-21)” Busan, South Korea, August 31 – September 5, 2025

[112] Li, S., Chatoorgoon, V., & Ormiston, S. (2016). "Numerical Instability Study of Supercritical Water Flowing Upward in Two Heated Parallel Channels." Proceedings of The 20th Pacific Basin Nuclear Conference. Springer Singapore. https://link.springer.com/10.1007/978-981-10-2314-9_15

[113] Wagner, W., Cooper, J. R., Dittmann, A., Kijima, J., Kretzschmar, H., Kruse, A., Mareš, R., Oguchi, K., Sato, H., Stöcker, I., Šifner, O., Takaishi, Y., Tanishita, I., Trübenbach, J., and Willkommen, T. (January 1, 2000). "The IAPWS Industrial Formulation 1997 for the Thermodynamic Properties of Water and Steam." ASME. J. Eng. Gas Turbines Power. January 2000; 122(1): 150–184. https://doi.org/10.1115/1.483186

[114] Menter, F. R., 1993. Zonal Two Equation k-w Turbulence Models for Aerodynamic Flows. 24th Fluid Dynamics Conference. 1993, 2906.

[115] Ravindran, P, Sabharwall, P & Anderson, N 2010, Modeling a Printed Circuit Heat Exchanger with RELAP5-3D for the Next Generation Nuclear Plant. https://doi.org/10.2172/1004237

[116] Abderrahim, H. A., Baeten, P., De Bruyn, D., Heyse, J., Schuurmans, P., & Wagemans, J. (2010). MYRRHA, a Multipurpose hYbrid Research Reactor for High-end Applications. Nuclear Physics News, 20(1), 24–28. https://doi.org/10.1080/10506890903178913

[117] Abderrahim, H. A. İ., Kupschus, P., Malambu, E., Benoit, P., Van Tichelen, K., Arien, B., Vermeersch, F., D’hondt, P., Jongen, Y., Ternier, S., & Vandeplassche, D. (2001). MYRRHA: A multipurpose accelerator driven system for research & development. Nuclear Instruments and Methods in Physics Research Section A: Accelerators, Spectrometers, Detectors and Associated Equipment, 463(3), 487–494. https://doi.org/10.1016/S0168-9002(01)00164-4

[118] Bogdán Yamaji, Graham Kennedy, Guy Scheveneels, Tewfik Hamidouche. MYRRHA reference design and initiation events. European Project ANSELMUS, Deliverable 1.3.

[119] Rozzia D. Kennedy G, Mirelli F. et al Development of the HEXACOM Facility for Characterising the Heat Transfer Performance of the MYRRHA PHX in LBE In SESAME international workshop (pp. 1-13). 2019.

[120] G. Khalil Youssef, D. Rozzia, J. Pacio, M. Caramello, C. Ciurluini, F. Giannetti, “Thermal-Hydraulic analysis and characterization of the HEXACOM facility”, Sub. to Annals of Nuclear Energy

[121] Datasheet ProRox WM950, https://rti.rockwool.com/siteassets/tools--documentation/products-industrial/product-data-sheets/english/rw-ti-pds-prorox-wm-950-en.pdf

*La ricerca da cui scaturisce la presente tesi è stata finanziata*
*dall'Unione Europea - Next Generation EU*
*Missione 4, Componente 2, CUP B53C22003670004*